Stress Redistribution in Berea Sandstone Samples Using Acoustic Emission Tomography in the Laboratory

Dennis F. Stevens

Thesis submitted to the faculty of the Virginia Polytechnic Institute and State University in partial fulfillment of the requirements for the degree of

Master of Science
in
Mining and Minerals Engineering

Committee Members:

Dr. Erik Westman, Chair

Dr. Mario G. Karfakis **Dr. Michael E. Karmis**

May 2, 2007
Blacksburg, Virginia

Keywords: Velocity Tomography, Acoustic Emission, Berea Sandstone

Stress Redistribution in Berea Sandstone Samples Using Acoustic Emission Tomography in the Laboratory

Dennis F. Stevens

Abstract

Velocity tomography is a noninvasive technique that can image the interior of a rock structure. To apply tomography to rock specimens, a propagation wave, which acts as a probe, is used. The propagation wave propagates from a source until it reaches a sensor on the surface of the rock specimen. Tomograms can then be generated from the velocity distribution within the rock structure. Areas of higher velocity are typically representative of higher stress concentrations, whereas areas of low velocity can be areas of fracturing. The variation of velocity tomography described in this thesis uses acoustic emissions as sources for the propagation wave. Acoustic emission sources provide advantages over mechanical sources, since the acoustic emission source is generated by the rock as a result of deformation and fracturing.

Velocity tomography of rock structures in the field has numerous applications and advantages. Velocity tomography can be used to monitor rock structures surrounding tunnels and underground openings such as mines. To monitor the rock structure, velocity tomography is used to determine areas of higher stress concentration that may be precursors to rock failure. However, velocity tomography must first be used in a laboratory environment to determine failure in rock samples before being applied to the field.

The research presented includes the unconfined compression strength testing of 19 Berea sandstone samples. These samples were loaded to failure and during the experiment the acoustic emission events within the samples were monitored using a commercial acquisition system manufactured by Engineering Seismology Group (ESG) Canada. Source location software, also produced by ESG, was used for the location of the acoustic emission events. Ray inversions were performed on the data from the experiments to generate tomograms. The tomograms generated display the p-wave

velocity distribution imaged within the Berea sandstone samples with the ultimate goal of being able to predict rock failure.

Based on the experiments discussed in this thesis it can be inferred that velocity tomography is a useful tool for imaging the inside of the Berea sandstone samples. Precursors of rock failure could not be determined in this early stage of research. However, the tomograms do image the p-wave velocity distribution and do show a gradual progression of the p-wave velocity from the initial velocity model to higher velocities. Results of these 19 experiments do provide reasonable confidence in the method and warrant pursuit of further research to refine and improve this method of monitoring velocity tomography.

Acknowledgements

First, I would like to thank my advisor, Dr. Erik Westman, for all of his support, advice, guidance and awarding me the opportunity to pursue this research. I would also like to thank my committee members, Dr. Mario Karfakis and Dr. Michael Karmis, for their guidance and support through the last year of performing this research. I would like to also thank the National Science Foundation for their funding and for giving me the opportunity to pursue this research.

I would like to thank all of my family and friends, especially Michelle Stevens, Frederick Stevens, Frances Stevens and Elaine Morazzani, without all of your support I would have never been able to complete this last year. I would also like to thank Jennifer Johnson, Kramer Luxbacher, Kevin Andrews, Adam Schaum and Kara Smith with whom I have spent this past year of graduate school with and for providing me with advice and support.

Finally, I would like to thank everyone in the Department of Mining and Minerals Engineering for making this department seem more like a home than a school and always being there for support and help whenever it was needed.

Table of Contents

List of Figures

List of Tables

Chapter 1: Introduction

A major safety consideration in the underground coal mining industry has been rock failure and the methods for predicting and preventing these failures. The demand for coal and the depleting of minable deposits has resulted in a need for underground coal mines to go deeper. With the ever increasing depths that coal mines are reaching, the possibility of rock failure increases as well. In 2005, fourteen fatalities occurred in the underground coal mining industry, with nine of those fatalities caused by failure of roof, rib, face, or back (MSHA 2006; NMA 2006). Figure 1.1 displays the fatalities that have occurred in the underground coal mining industry from 2002 to 2007 and also shows the amount of fatalities that occur due to fall of roof, rib, face or back.

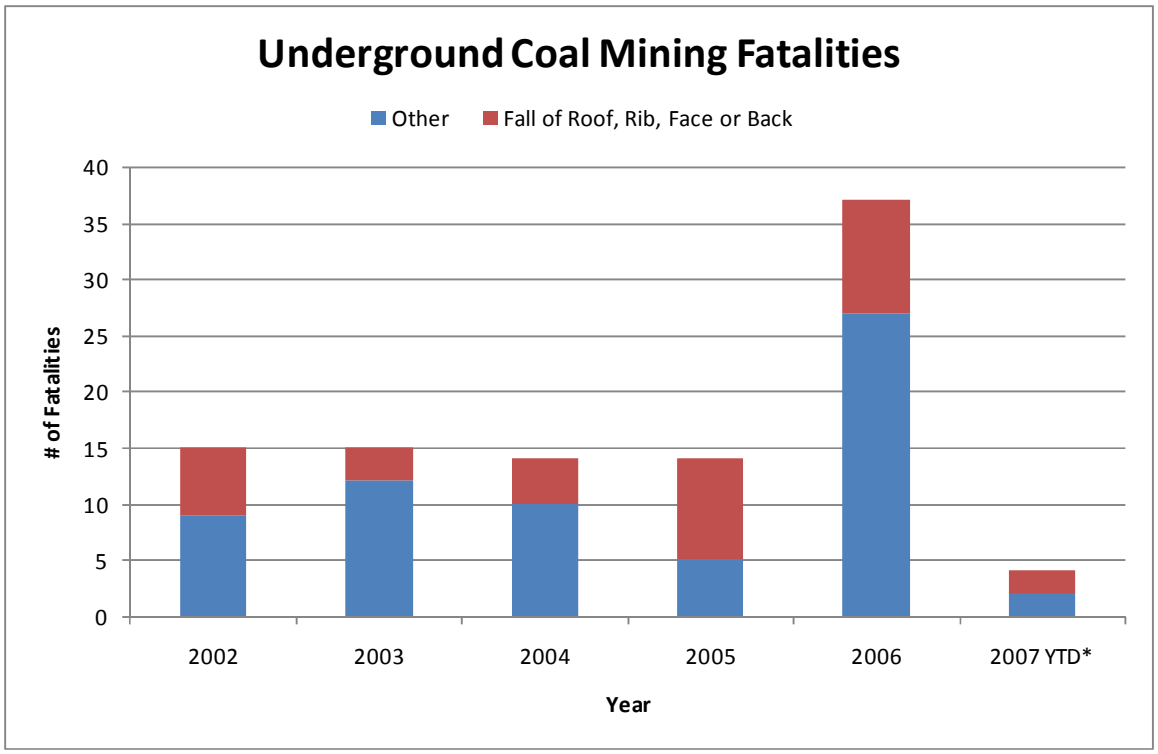

Figure 1.1: Underground Coal Mining Fatalities in the United States from 2002 – 2007 (MSHA 2006; NMA 2006)

Aside from the over whelming safety issues that arise from rock failure, the underground coal mining industry typically incurs production loss when rock failures occur. The coal industry on average has produced 1063 million short tons since 1990, which underground coal mining accounts for 36.6 % of this production. The electrical

*YTD refers to March 13, 2007

demand for the United States requires on average 866 million short tons, leaving very little room for production loss in the coal industry. Figure 1.2 displays coal production in the United States from 1990 to 2005 as well as the amount that underground and surface coal mining produced for each year.

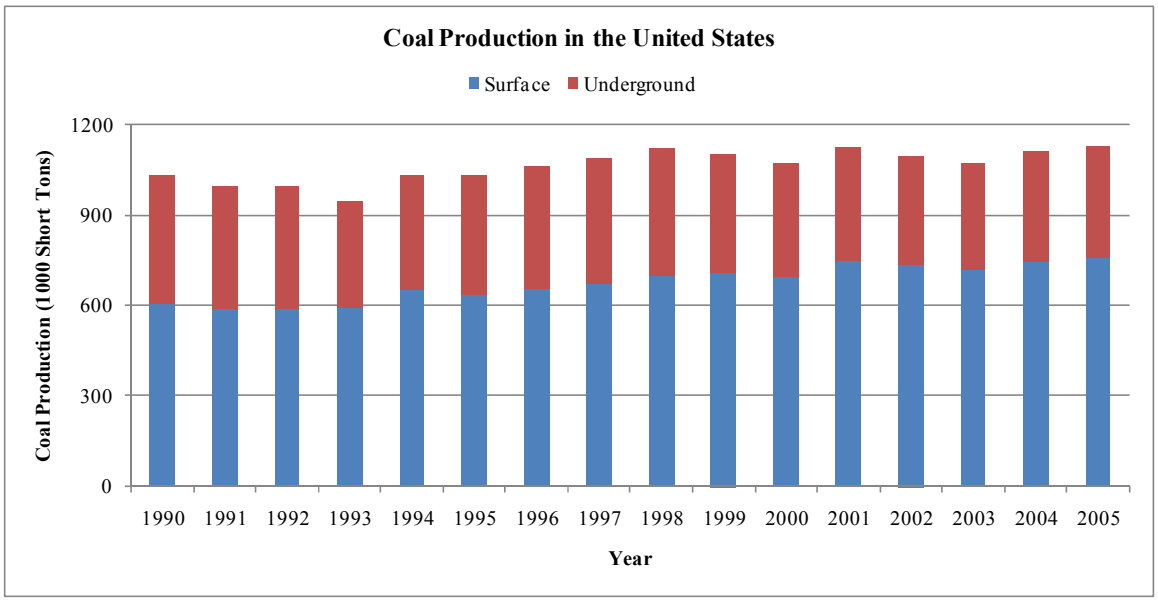

Figure 1.2: Coal Production in the United States from 1990 to 2005

The safety and production issues that arise from rock failure have been problematic in the mining industry. There have been several methods developed to predict rock mass failure, including numerical modeling, empirical methods and rating systems. The purpose of the presented research is to use a non-invasive technique, tomography, too image the rock mass. In tomography, a probe is passed through the specimen to image the specimen two or three dimensionally. To apply tomography to rock specimens, a propagation wave, which acts as the probe, is used. The propagation wave propagates from the source, which can be micro-fracturing, until it reaches a sensor on the surface of the rock specimen.

The research presented generates tomograms for 19 Berea sandstone samples that were subjected to unconfined compression strength testing. The acoustic emissions were monitored using a commercial system, manufactured by Engineering Seismology Group (ESG) Canada, which locates the source of the acoustic emission event. With the acoustic emission event location, primary wave travel-time and the receiver location, the

velocity of the propagation wave can be determined. The determined velocity can then be analyzed and displayed using tomography, by performing ray inversions to determine velocity distribution. The tomograms created from this process were then used to determine whether trends are present in the forming of the failure plane within the tested samples that could be considered precursors of failure occurrence, therefore creating a method of failure prediction.

Chapter 2: Literature Review

2.1 Failure in Rock Masses

2.1.1 Rock Composition

In order to begin understanding failure in rock masses the composition and structure of rock itself must be known. Rock is defined by Hartman and Mutmansky (2002) as "any naturally formed aggregate of one or more types of mineral particles (Hartman and Mutmansky 2002)." Unlike other engineering materials, rock is a conglomerate of different minerals and heterogeneous due to the presence of discontinuities within the rock structure. These discontinuities, which can be joints, bedding planes, fissures, etc., tend to be the factor that causes failure to occur within a rock structure when load is applied (Zhang 2005).

2.1.2 Rock Mechanics & Stress-Strain Curve

Due to the nature of rock, the creation of a novel concentration in engineering was created with the intention of studying the failure phenomenon of rock known as rock mechanics. Goodman explains rock mechanics as "dealing with the properties of rocks and the methods required for design of rock-related components (Goodman 1980)." Therefore, rock mechanics is applied in attempts to understand and reasonably predict the effect of rock properties and the discontinuities within the rock that cause failure.

The effect discontinuities have on an axial loaded rock specimen can be explained using the Stress-Strain Curve. To generate the Stress-Strain Curve for a rock specimen requires the calculation of two variables, stress and strain. Herget (1988) defines stress as the force, or load, applied per unit area on the rock specimen. Deformation of the rock specimen occurs as a result of the stress and is a dimensionless quantity, commonly called strain, which is defined as the change in length per the total length of the rock structure (Herget 1988). Figure 2.1 below depicts a typical Stress-Strain curve for a uniaxially loaded rock specimen.

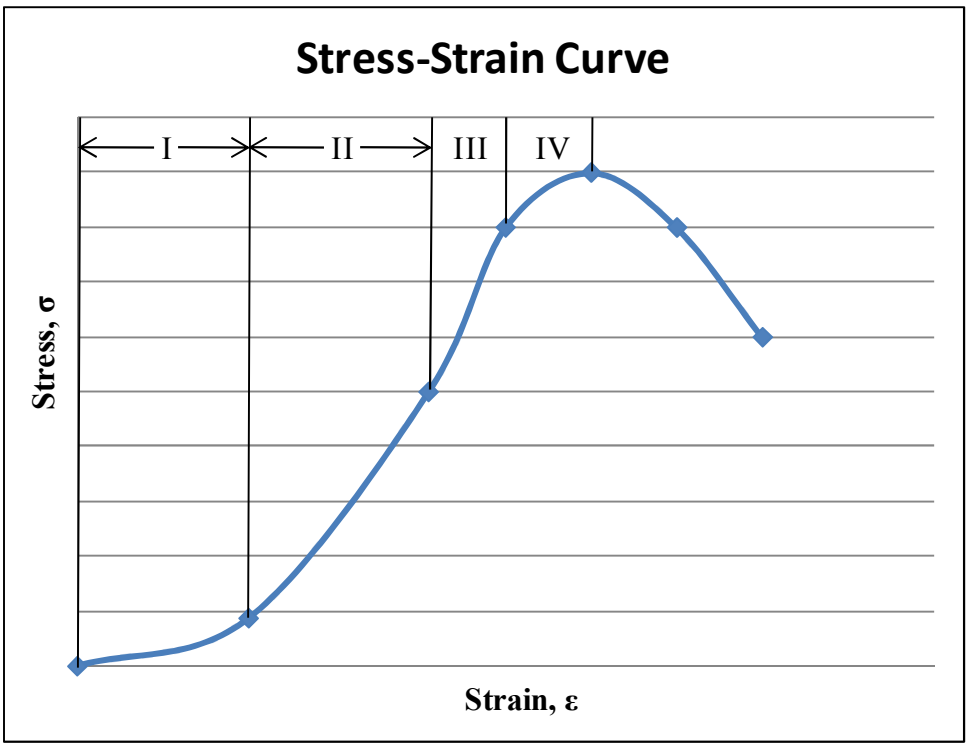

Figure 2.1: Typical Stress-Strain Curve for a Uniaxially Compressed Rock Specimen

The Stress-Strain Curve can be divided into four stages, as shown in Figure 2.1. These four stages can be used to describe the behavior of the rock specimen at that portion of the Stress-Strain Curve. The different stages of the Stress-Strain Curve include three nonlinear portions, stages I, III and IV, and a linear portion, stage II.

Stage I of the Stress-Strain Curve is the first of the non-linear portions of the curve. The non-linear portion is considered to exhibit an inelastic behavior based on the theory of elasticity. The theory of elasticity states that when a material is loaded and upon unloading, the strain incurred by the material due to loading returns to zero. Therefore, when a material behaves elastically the changes incurred during loading are reversible (Jaeger 1979). Stage I's strain, upon unloading, will not return to zero thus exhibits behavior opposite to this, referred to as inelastic. The closing of discontinuities such as pore space, fissures and preexisting cracks within the rock specimen will also occur during this stage. Due to the closing of discontinuities, there will also be an increase in the elastic stress wave velocity within the rock specimen (Nur and Simmons 1969; Hardy and Kim 1971; Jones and Murrell 1989).

Stage II of the Stress-Strain Curve will be reached when the rock specimen reaches a state of stress causing all the discontinuities to close. However, according to

Carlson and Gangi to close all discontinuities within a rock specimen required a pressure in excess of 500 MPa in some rock types (Carlson and Gangi 1985). Stage II of the Stress-Strain Curve is typically strongly linear, which is representative of the rock specimen demonstrating elastic behavior as already explained. Also, a linear relationship between the axial stress and lateral strain and the axial stress and axial strain are experienced by the rock specimen, during this stage (Goodman 1980). The ladder portion of stage II marks the beginning of microcrack formation and propagation, which leads into Stage III.

At around two-thirds of the maximum strength of the rock specimen, stage III of the Stress-Strain Curve will begin (Jaeger 1979). Stage III strongly demonstrates a non-linear curve, as shown in Figure 2.1. During stage III, the lateral strain experienced by the rock specimen will begin to increase relative to axial strain, which leads to the rock specimen exhibiting a behavior called hysteresis (Goodman 1980). Hysteresis within a material is representative of irreversible damage occurring, which upon unloading the specimen will not return back to its original shape (Jaeger 1979). The forming of new micro cracks begins to increase in this stage, where the cracks will form and extend parallel to the applied load. The cracks forming during stage III are also considered to be stable, implying that with every increment of load the cracks extend a finite length (Goodman 1980). A decrease in the elastic stress wave velocity also occurs due to the newly fragmented internal structure of the rock specimen (Paterson and Wong 2005).

Microcrack formation and propagation will continue within the rock specimen and lead into Stage IV with an increase in the density of cracks occurring. These cracks will begin to combine until the newly formed fractures create a failure plane. Failure will occur within the rock specimen along this failure plane once the maximum stress of the rock has been reached (Goodman 1980). The maximum stress of the rock specimen is considered to be the peak of the Stress-Strain Curve, which can be seen in Figure 2.1 (Jaeger 1979).

2.2 Review of Classification and Failure Methods

2.2.1 Rock Mass Classification Systems

Rock mass classification systems are a common method of determining rock characteristics that can be used with failure prediction methods. There are a number of rock mass classifications that are practiced by engineers all over the world. Classification systems are used to aid in engineering design by grouping similar rock types in an attempt to determine the similarities and differences present. Therefore, rock mass classifications are based off of case histories and require periodic updating (Bieniawski 1989). As already stated there are numerous rock mass classification systems in use, but ones of particular interest that will be reviewed in this thesis are the Rock Quality Designation (RQD), Rock Mass Rating (RMR) System and the Q-System.

The rock quality designation (RQD) classification system was first proposed in 1967 by D. U. Deere. The RQD system was developed with the intention of generating a means of determining rock quality information in the field (Deere, Hendron et al. 1967). The purpose behind this system was to classify and determine rock mass areas that required more exploratory work. The system accomplishes this by incorporating only sound pieces of cored rock that have a length greater than 100 mm (4 in.) (Bieniawski 1989). The calculation performed for the RQD system sums the rock cores of length greater than 100 mm (4 in.) and divides this amount by the total length of the drill run, as shown below in Equation 2.1.

$$RQD = \frac{\sum Length\ of\ Core\ Pieces}{Total\ Core\ Run\ Length} \times 100\% \qquad (2.1)$$

Upon performing the previous calculation the resulting percentage can be used with Table 2.1, which was proposed by Deere (1968). Table 2.1 shows the relationship expected between the RQD index, which is the percentage attained from equation 2.1, and the engineering quality of the rock mass being examined.

Table 2.1: RQD Index Table (after Deere 1968)

RQD Index Table	
RQD %	Rock Quality
<25	Very Poor
25 - 50	Poor
50 - 75	Fair
75 - 90	Good
90 - 100	Excellent

The Rock Mass Rating (RMR) system is commonly referred to as the geomechanics classification and was developed by Bieniawski in 1973. The RMR system requires the use of six parameters in order to classify a rock structure. The six parameters required according to Bieniawski (1989) are the uniaxial compressive strength of the rock mass, RQD, spacing of discontinuities, condition of discontinuities, groundwater conditions, and the orientation of discontinuities. The rock mass then has to be separated into closely uniform regions. Measurements taken in the field will then be used to determine the parameters mentioned before. These parameters are then used along with various tables and charts developed by Bieniawski from case histories to determine the RMR Rating. The tables and charts used to determine the RMR rating can be found in a book authored by Bieniawski, titled *Engineering Rock Mass Classifications*.

The Q-System, according to Bieniawski (1989), represents a major contribution to rock mass classification. As already stated, rock mass classifications are based off of case histories and the Q-System is based off over 200 tunnel case histories. The Q-System was developed in 1974, by Barton, Lien and Lunde (Bieniawski 1989). Like the other rock mass classification systems, the Q-System determines, through numerical assessment, the rock quality of the rock mass being evaluated. The value determined from the Q-System can be between the values of 0.001 to 1000 on a logarithmic scale. This value can be determined from Equation 2.2 and be used with the database of case histories to determine the tunnel support needed in a rock mass to prevent failure.

$$Q = \frac{RQD}{J_n} \times \frac{J_r}{J_a} \times \frac{J_W}{SRF} \qquad (2.2)$$

2.2.2 Numerical Modeling

Numerical modeling has been used in the mining industry extensively for failure prediction within rock. This is accomplished by creating mathematical or computational models that recreate the rock body being examined. The model is then used to test load scenarios that can be possible real world situations. Analyses of these scenarios can be used to determine the rock body's resistance to failure. This method of failure prediction has become more extensively used with the development of computers that allow for multiple scenarios to be run and the best solution found in a fraction of the time that it took to run one scenario by hand (Hoek 2007).

There are numerous numerical modeling methods employed for rock mechanics problems, but these methods can be broken down into three commonly used methods. The three most common methods are the continuum method, discrete method and hybrid continuum/discrete method (Jing and Hudson 2002). The choice on which model to use in rock mechanics is based on a number of factors such as the rock type, structural discontinuities and material properties of the rock mass being modeled (Hoek 2007).

The continuum method of numerical modeling uses the assumption that the modeled structure is continuous and can be divided into interconnected elements. Within the continuum method there are a number of methods that are based off of the continuum assumption, which are the finite difference method, the finite element method and the boundary element method. The choice of using the continuum modeling method over other methods is highly dependent on the structure being modeled. For the continuum method to accurately model the structure, the structure needs to be continuous with very little fracturing and large scale displacement of blocks not present (Jing and Hudson 2002). Therefore, if the rock structure being modeled has a large number of discontinuities and these discontinuities will cause the rock structure to not displace as a single entity than this method of modeling will not provide an adequate model.

The discrete method of numerical modeling uses the assumption that the modeled structure is not continuous and is delineated by joints (Ku, Lin et al. 2004). Methods of modeling that are based off of the discontinuum method include the discrete element method and the discrete fracture network methods. This method of modeling can

perform reasonably when the modeled structure has a moderate amount of fracturing and when large scale displacements of blocks are expected (Jing and Hudson 2002).

There is no particular advantage that makes the previous two methods better than the other, which leads to the hybrid/continuum method. The hybrid/continuum method uses characteristics of both, the continuum and discrete methods, and eliminates some of the disadvantages associated with using these methods. However, a disadvantage arises when using this method. Issues arise at the interfaces of the two methods, due to the transition from one method to the other (Jing and Hudson 2002).

2.2.3 Empirical Failure Prediction Methods

Several failure criterions have been created with the intention of understanding and predicting the failure of rock, especially in the situation where there are combined states of stress being applied to rock. One such criterion that can be used to predict rock failure is the Coulomb-Mohr criterion, which relates shear and normal stress to rock failure.

The first component to the Coulomb-Mohr criterion is the Coulomb criterion. The Coulomb criterion was created by Coulomb in 1773 according to Herget. The criterion was based off the idea that shear stress that caused failure within the rock was resisted by two things. The first was the cohesion of the material and second by a constant multiplied by a normal stress described by Coulomb as the coefficient of friction. Using the coefficient of friction along with the cohesion of the material Coulomb proposed to describe failure in a linear relationship as shown in equation 2.3:

$$\tau = S_0 + \mu\sigma \qquad (2.3)$$

Using the criterion proposed by Coulomb it was suggested that when the shear stress experienced by the rock touched on or above this failure envelope, which is created on a plot of shear stress versus normal stress, as shown in Figure 2.2, that the material was predicted to fail (Dowling 2007).

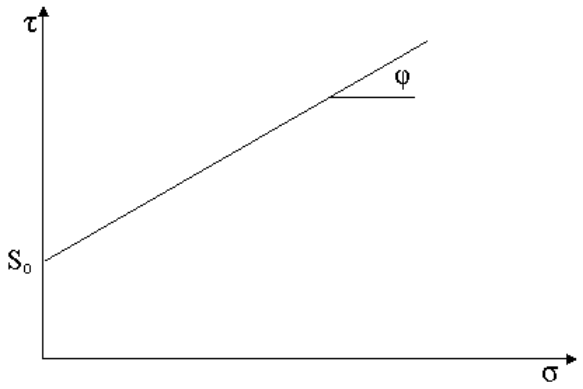

Figure 2.2: Example of the Coulomb Failure Criterion

The second component to the Coulomb-Mohr criterion is Mohr's circle. Mohr's circle is used to represent stress relationships in a graphical manner on a plot of shear stress versus normal stress. This manner of representing stress relationships was first discovered by Culmann, in 1866, and was developed by Mohr, in 1882, which is who the method is named after (Parry 2004). Equations 2.2 and 2.3 are used to determine the principal normal stresses and principal shear stress based on the stress being applied to the material.

$$\sigma_1, \sigma_2 = \frac{\sigma_x + \sigma_y}{2} \pm \sqrt{\left(\frac{\sigma_x - \sigma_y}{2}\right)^2 + (\tau_{xy})^2} \tag{2.2}$$

$$\tau_3 = \sqrt{\left(\frac{\sigma_x - \sigma_y}{2}\right)^2 + (\tau_{xy})^2} \tag{2.3}$$

Equation 2.2 can be used to calculate the maximum and minimum values of the principal normal stresses that will be experienced by the rock specimen being examined. The maximum shear stress that can occur within the rock specimen can be determined from Equation 2.3. The principal normal stresses and principal shear stress experienced by the material are used to generate points on Mohr's circle (Dowling 2007). Mohr's circle, as shown in Figure 2.3, can be used to estimate the state of stress present at different angles of failure for the material being examined.

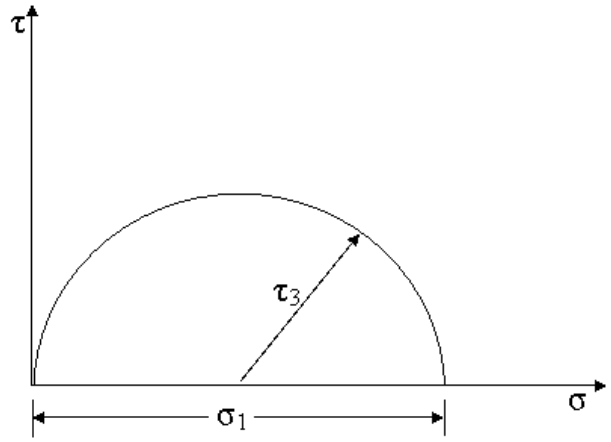

Figure 2.3: Example of Mohr's Circle for Uniaxial Loading

The Coulomb-Mohr Failure Criterion was proposed by Mohr in 1900. Mohr proposed that the stresses at failure can be related by a function, which can be a straight or curved line. The straight line can be used for describing situations of compression, such as uniaxial loading, and the curved line can be used in situations where a transition is needed between compressive to tensile stresses. The Coulomb criterion, as already stated, implies a linear relationship between shear and normal stress that lead to failure, which can be used along with Mohr's circle to define a boundary that if crossed failure is expected to occur. The concept with using the Mohr-Coulomb failure criterion is that if any combination of stresses experienced by the rock specimen touch or exceed the failure envelope than failure will occur within the rock specimen (Dowling 2007). An example of the point at which failure will occur according to the Mohr-Coulomb failure criterion is shown in Figure 2.4.

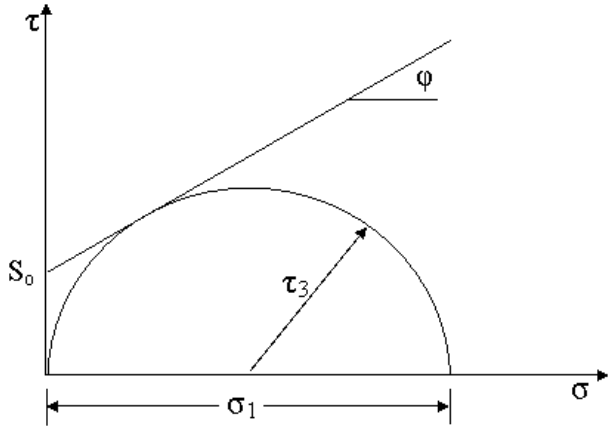

Figure 2.4: Coulomb Failure Criterion with Mohr's Circle for Uniaxial Loading

In 1920, Griffith proposed a failure criterion that assumed the initial presence of microfractures within a crystalline material. The presence of these microfractures governs the strength of brittle materials, such as rock (Paterson and Wong 2005). The Griffith's failure criterion, compared to the Mohr-Coulomb failure criterion, provides a more accurate estimation of material strength in the tensile region of failure by applying a parabola to the behavior in this region as opposed to a straight line (Goodman 1980).

Griffith's failure criterion suggests that the existing microcracks have a uniform elliptical shape within the material. Stress concentrations located at the tips of the elliptical cracks propagate out through the material and eventually cause ultimate failure to occur on the macroscopic level. The failure criterion, proposed by Griffith, has been backed by results from experimental work on glass (Jumikis 1983). The application of Griffith's failure criterion to failure in rocks has little physical basis if the principal stresses experience are compressive (Goodman 1980). However, the Griffith's failure criterion does provide a good insight into the process of how cracks propagate within a rock specimen and ultimately coalesce into a failure plane causing the rock specimen to fail (Paterson and Wong 2005).

2.3 Acoustic Emissions

2.3.1 Discovery of the Presence of Acoustic Emissions

The study of acoustic emissions, also known as microseismic activity, has been around since the late 1930s, when the presence of acoustic emissions was discovered. Credit for the discovery of acoustic emissions has to go to two U.S. Bureau of Mines employees named L. Obert and W.I. Duvall. Obert and Duvall discovered the presence of acoustic emissions while they were performing sonic studies in a rock burst prone mine. The sonic technique that Obert and Duvall were using required the use of two transducers. One of the transducers acted as a source, which created a mechanical signal, and the second acted as a receiver that monitored the mechanical signal and modifications that occurred as a result of stress changes or characteristics of the rock. While performing these tests on a rock pillar within a mine, Obert and Duvall removed the transducer creating the mechanical signal and discovered that they were still detecting

signals using the remaining transducer. Obert and Duvall than determined that the signals being received were being generated by the pillar. This led to the birth of the acoustic emission technique of monitoring, which are the self generated signals within a material (H. Reginald Hardy 2003).

2.3.2 Acoustic Emission Sources

Acoustic emissions, as already stated, are sounds that are generated by rock failure and deformation. These sounds are at times audible, but frequently they are on the sub-audible range due to the sound's low amplitude or high frequency, and sometimes both (Choudhury, Raina et al. 2004). In geological materials, such as rock, the activity that occurs within the rock that causes acoustic emissions is related to the deformation and failure of rock. Therefore, acoustic emissions can occur on the micro-level, macro-level and the mega level as dislocations, twinning, grain boundary movements and by fractures (H. Reginald Hardy 2003). The magnitude and number of acoustic emissions, as crack generation and growth are occurring, begin to show an increase during stage III of the stress-strain curve, Figure 2.1 (Goodman 1980).

2.3.3 Methods of Monitoring Acoustic Emissions

The sounds generated by rock, due to deformation or failure, propagate through the rock as elastic stress waves. These waves travel from the point of origin, the acoustic emission source, to the boundary of the rock. There are two waves of particular interest that are created by the acoustic emission source. The first is a primary wave (p-wave), where the particles within the medium will move in a compressive and expansive motion with the wave front. The second is referred to as a secondary wave (s-wave) and is much slower than the primary wave, but has a much larger destructive force. The particles within the medium also move in a shear up and down motion as the wave front of the propagation wave of the secondary wave passes through the medium (Paterson and Wong 2005).

In order to monitor the acoustic emission when it reaches the boundary of the rock a transducer has to be used. The transducer will monitor the acoustic emission waveform

and with the use of other equipment and computer software, that will be explained later in the section, the acoustic emission waveform can be monitored, recorded and displayed for analyses (H. Reginald Hardy 2003). Figure 2.5 shows an example of a typical acoustic emission waveform that can be analyzed.

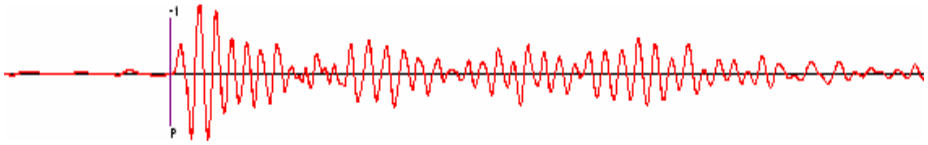

Figure 2.5: Example of an Acoustic Emission Wavelet

In order to monitor acoustic emissions the following equipment is needed:

- transducer,
- preamplifier
- band pass filter
- method to record, display and analyze the generated waveforms

To adequately monitor acoustic emissions a suitable transducer is needed. Depending on the application, i.e. field or lab, the chosen transducer needs to be able to monitor the frequency of the acoustic emissions. Hardy proposes, based on previous experiments on geologic materials, that the frequency of the acoustic emission waveforms in the field can be in the range of 10^0 to 10^5 Hz, whereas in the lab the acoustic emission waveforms can be in the range of 10^3 to 10^6 (H. Reginald Hardy 2003).

In acoustic emission experiments an array of transducers is typically used to allow for the location of the acoustic emission event. In an array of transducers, each transducer will pick up an independent signal from an acoustic emission that can be used for locating the acoustic emission source. In order to solve for the source location a minimum of four transducers is needed (ESG 2006). Array size and placement are also important factors to consider for source location determination. Error increases or decreases depending on the manner in which the array is arranged. If the transducer array is small and monitoring a small area then the error associated with source location is also small, whereas if the array is larger than a larger area can be monitored but the error will also be larger. Ideally the array should be large enough and placed to allow for the acoustic emission event source to be located in the middle of the array. As the events

move away from the center of this array the error will also increase (H. Reginald Hardy 2003).

The final components needed for an acoustic emission monitoring system are a preamplifier, a band pass filter and a method of recording the generated waveforms. Pre-amplifiers are needed for monitoring acoustic emissions to amplify the transducer signal without introducing distortion or noise to the waveforms. The transducer signal requires amplification due to their relatively small output, which are typically in units of microvolts. A band pass filter is used to filter out extraneous high and low frequency signals, which are considered background noise (H. Reginald Hardy 2003). Finally, a method of recording, displaying and analyzing the generated waveforms is needed, which there are various software programs that are capable of this. The software used in these experiments is the Hyperion Seismic Software Suite and is produced by Engineering Seismology Group (ESG) Canada.

2.3.4 Locating Acoustic Emission Sources and their Magnitude

The importance of source location lies in the fact that in order to accurately and efficiently analyze a propagation wave, the location of the origin of the wave needs to be known. Source location in a laboratory environment, as opposed to a field environment, is considerably easier for a few reasons. First, the source location deals with only one material and also the geometry of the specimen is known. However, due to the size of the specimen being tested in the laboratory the location of the transducers need to be very accurately known (H. Reginald Hardy 1977).

To locate acoustic emission sources, the arrival times for the source have to be known as well as some assumptions made. There are two major assumptions that are made in the locating of acoustic emission sources. First the travel path of the elastic stress wave is assumed to be a straight line. Second, the velocity of the propagation wave is assumed to be constant for the material being used (Riefenberg 1988). The determination of the source location, given the previous assumptions, requires that the arrival time difference to be calculated between every transducer and the first hit transducer. Using the arrival time differences, array geometry and the velocity of the

wave traveling through the medium, the source location of the acoustic emission can be found (H. Reginald Hardy 2003).

2.4 Tomography

2.4.1 Background

Before discussing the theory behind tomography, the problem that required the creation of tomography will be presented. With many solids, such as the human body, manmade structures or geologic structures, the interior of the body can contain an anomaly that is causing a problem. Under normal circumstances this anomaly can only be determined through cutting open the solid and exposing the anomaly, but with tomography the anomaly can be imaged noninvasively. This leads to the anomaly being examined without using destructive means.

The first application of tomography was done in 1917 by Johann Radon. Radon proposed that the density of an object could be determined if the total density of every line passing through the object was known. This was done by assuming that the lines contained various points through the material and the densities at these points were known. X-rays can be used to determine the total density along the line of travel that the x-ray takes. Using x-rays along with Radon's theory allows for a method of imaging a body noninvasively, which is referred to as tomography (Markoe 2006).

2.4.2 Fields of Application

Since tomography's original application by Radon, tomography has been adapted and applied to a multitude of applications. These applications include the medical field, agriculture and for imaging various materials for construction purposes.

Tomography has been used extensively in the medical field to image various areas of the human body. One such application is Computerized axial tomography (CAT). CAT is a diagnostic procedure used in the medical field to image the interior of the body using x-rays. This procedure produces a detailed image of the interior of the body without blurring due to the presence of overlapping tissue (Hounsfield 1973).

X-ray computerized tomography (CT) has also been used in the agriculture industry (Heeraman, Hopmans et al. 1997; Pierret, Capowiez et al. 1999; Lontoc-Roy, Dutilleul et al. 2006). X-ray CT was used by Lontoc-Roy et al. to image the root structure of a crop species, maize, in different soil-moisture combinations. The results from the X-ray CT scanning were then used to reconstruct the root system of the plant species 3-dimensionally, to determine the effect of the soil-moisture environment on the root system of the plant species (Lontoc-Roy, Dutilleul et al. 2006).

The imaging of various construction materials has also been done using tomography (Masad, Jandhyala et al. 2002; Hiltunen, Cho et al. 2004; Clarke 2006; Gopalakrishnan, Ceylan et al. 2006). Gopalakrishnan et al. uses X-ray computed tomography to image asphalt materials. Studies of the asphalt samples were performed at the Center for Nondestructive Evaluation (CNDE) using the in house CT system. The system was used to determine air-void distribution and internal structure evolution through laboratory tests in an attempt to create a better understanding of asphalt behavior to build more durable and longer lasting roads (Gopalakrishnan, Ceylan et al. 2006).

2.4.3 Velocity Tomography

A variation of tomography that is used extensively in geology and mining is seismic tomography. Seismic tomography, as opposed to X-ray CT, uses pressure waves to image the interior of the body being examined (Westman 2004). This is accomplished through analyzing some aspect of the pressure wave, which can be diffraction, attenuation, p-wave velocity and s-wave velocity of the seismic wave or a combination of the four. Velocity tomography will be discussed over diffraction and attenuation tomography because these methods require the input of an artificial signal or that the original signal input is known. Monitoring acoustic emissions, which is the application being performed in this thesis, does not allow for the original source input signal to be known since it is self-generated by the rock specimen. For that reason velocity tomography will be discussed in more detail in this thesis.

Velocity tomography involves the analysis of the time it takes the pressure wave, which can be the p-wave or s-wave, to reach an appropriate transducer from the wave's point of origin. This concept is illustrated by a sample waveform, shown in Figure 2.6,

which shows an input signal created by an artificial source and the time it takes for the wave to travel from the source to the receiver.

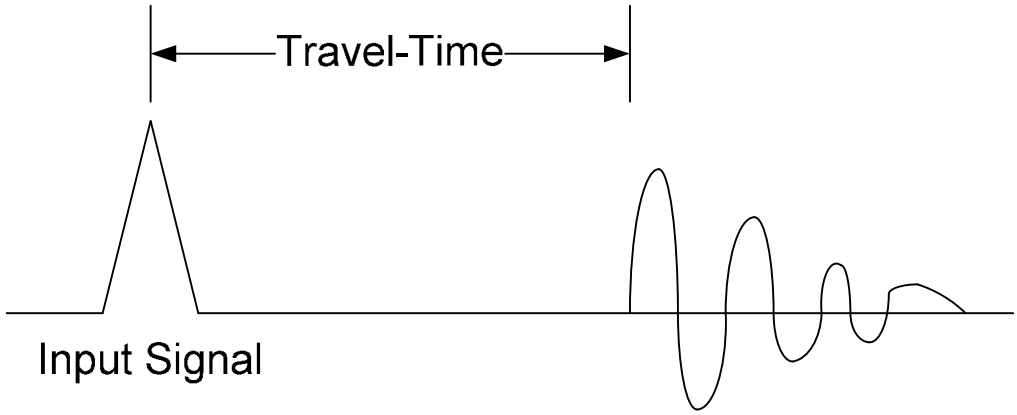

Figure 2.6: Sample Waveform demonstrating Travel-time from the source to receiver

The source of the waveform can be either artificially created using a source or can be self generated by the material, such as an acoustic emission. With the location of the source and receiver known, the distance between the two points can be determined by assuming a straight line path of the wave, which will be referred to as a raypath. The amount of time required for the wave to travel from the source to the receiver along with the ray distance can be used to determine the velocity of the wave. The velocity is calculated fairly easily by computing the quotient of distance divided by travel-time. A simple example showing the path that a pressure wave travels from a source to a receiver is shown in Figure 2.7.

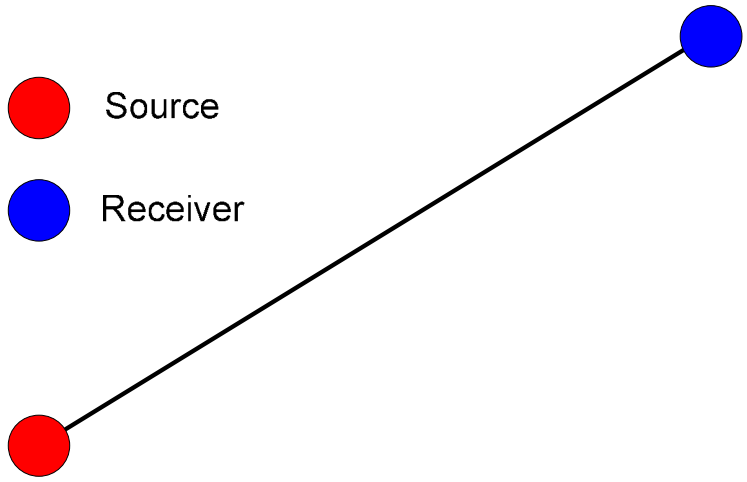

Figure 2.7: Pressure Wave Path from Source to Receiver

The theory of tomography, which was proposed by Radon (1917), is that a value for the raypath as a whole is known. In this application, the value for the raypath is velocity. Tomography involves separating the material being examined into grid cells, for a two-dimensional situation, and voxels, for a three-dimensional situation. Figure 2.8 shows the wave path of Figure 2.7 separated into grid cells of equivalent size.

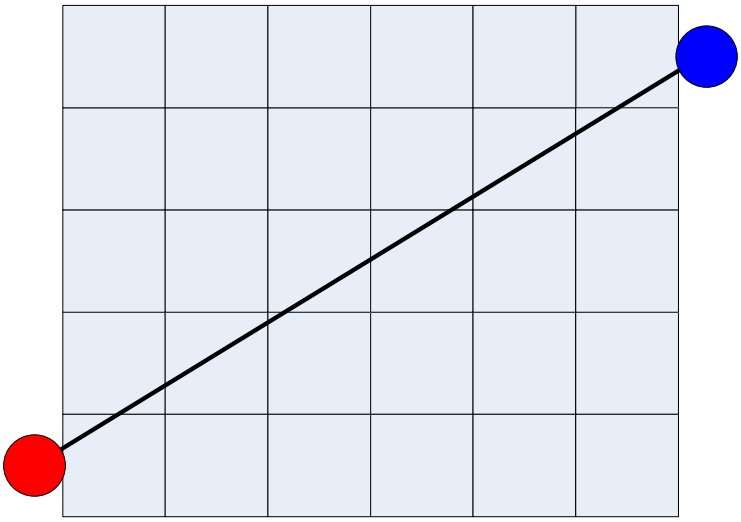

Figure 2.8: Wave Path separated into corresponding grid cells

The time, distance and velocity are all known for the raypath as a whole, but are not known for the individual grid cells or voxels that the ray has been divided into. The distance of the ray contained within each gird cell can be easily determined, but the determination of time and velocity in each grid cell requires the application of an iterative technique that applies an inversion to the raypath. Upon application of the raypath inversion, the velocity distribution along the material will change due to the presence of anomalies (Westman 2004). The resulting velocity distribution is then displayed graphically and referred to as a tomogram. Figure 2.9 shows the wave path of Figure 2.7 after a raypath inversion is performed and areas of different velocities have been determined, where areas of red are higher velocities.

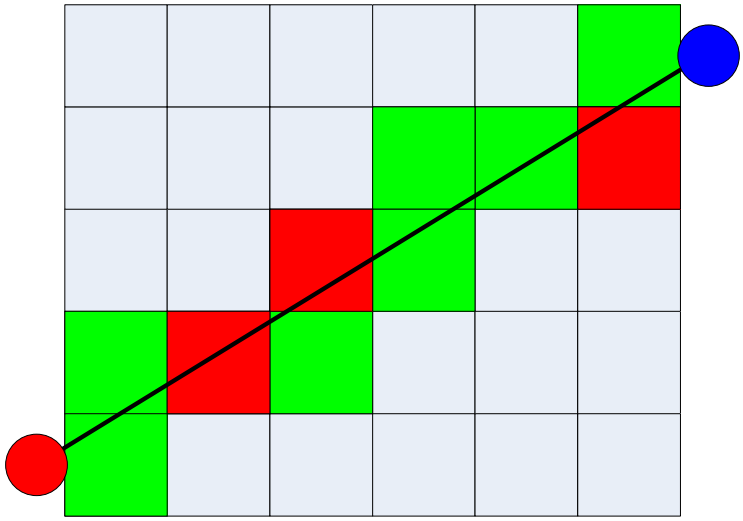

Figure 2.9: Velocity Distribution after Performing a Ray Inversion

In a non-uniform material, such as rock, the velocity of the pressure wave will change as a result of the presence of discontinuities, voids and cracks. The determination of areas of high and low velocity in rock can be used to determine the internal structure of the rock. Areas of increased velocity within a rock specimen are indicative of the presence of higher compression stresses due to a denser rock structure. Areas of lower velocity are representative of areas of void space, cracks and the opening and propagation of cracks (Meglis, Chow et al. 2005). For imaging these low and high velocity area, the use of p-wave travel-times tends to show a bias toward the high velocity regions as opposed to the low velocity regions compared to s-wave travel-times (Jackson and Tweeton 1994; Vasco, Peterson et al. 1995). Regardless of this fact the p-wave travel-times will be used in this thesis due to the ease with which arrival times are chosen for p-waves and also the p-wave arrival times are used for the location of the source mechanism of the pressure wave as well. Therefore, this thesis employs the analysis of the p-wave travel-times monitored during the uniaxial loading of circular Berea sandstone samples, which will be discussed further in the next chapter.

Chapter 3: Instrumentation & Experimental Procedure

3.1 Laboratory Procedure

3.1.1 Introduction

In order to gain a greater understanding of rock failure, uniaxial compression tests were conducted on cylindrical samples of Berea sandstone in a laboratory environment. An array of piezoelelectric transducers were attached to the Berea sandstone samples prior to testing and these sensors were in turn connected to an ultrasonic data acquisition system. The ultrasonic data acquisition system used is capable of monitoring, measuring and storing information on the acoustic emission events that are generated by the rock sample due to deformation.

3.1.2 Statistically Significant Sample Size

A minimum number of experiments had to be conducted to ensure that the results drawn from the experiments would be statistically significant so they could be adequately applied to predict the behavior of future experiments. Therefore, the number of samples had to be large enough to find the range that would contain the true compressional strength of the samples. For any experiment sample size is recommended to be at least five or more samples tested. Therefore, five experiments were conducted and the results from these five experiments were used to calculate the required sample size according to an equation proposed by Ott & Longnecker (2001), which is

$$n = \frac{(z_{\alpha/2})^2 \sigma^2}{(W/2)^2} \qquad (3.1)$$

where, n = statistically significant sample size
z = desired confidence level
σ = population estimated standard deviation
W = tolerable error.

This equation along with some assumed constants were used to calculate the required number of experiments. The constants used were confidence level and tolerable error. A confidence level of 95 % and a tolerable error of 2.59 MPa (375 psi) were used for calculation of sample size. The sample size needed to achieve a statistically significant amount was found to be 19 experiments. The sample dimensions along with the compressional strengths calculated for each sample are shown in Table 3.1.

Table 3.1: Berea Sandstone Sample Dimensions and Compressional Strength

Experiment #	Length (in)	Diameter (in)	Peak Load (Kips)	C_o (psi)	C_o (MPa)
1	5.089	2.014	25.100	7879	54
2	5.045	2.015	26.070	8175	56
3	5.139	1.982	22.937	7434	51
4	5.170	1.983	25.104	8128	56
5	5.122	2.011	26.312	8284	57
6	5.156	2.014	26.890	8441	58
7	5.007	2.011	27.140	8545	59
8	5.002	2.011	22.467	7073	49
9	5.062	2.013	23.790	7475	52
10	5.164	2.011	26.860	8457	58
11	5.136	2.013	27.704	8705	60
12	5.055	2.013	22.780	7158	49
13	5.166	2.012	27.606	8683	60
14	5.059	2.012	27.325	8594	59
15	5.136	2.012	27.570	8671	60
16	5.090	2.011	26.923	8476	58
17	5.084	2.012	22.479	7070	49
18	5.133	2.012	26.040	8190	56
19	5.062	2.011	26.233	8259	57

3.1.2 ASTM Specification for Unconfined Compressive Strength Testing

To conduct the uniaxial compression test on the Berea sandstone samples there was a large amount of sample preparation required to meet the ASTM Specification D2938 for unconfined compressive strength tests. The samples that were tested had approximate dimensions of 2 inches in diameter and 5 inches in length. These sample dimensions were used to meet the requirement that the samples had to be right circular cylinders with a sample diameter larger than 2.126 inches (54mm) and a length to diameter ratio of 2.0 – 2.5. Table 3.2 shows the dimensions of the nineteen samples tested and the corresponding length to diameter ratio for each sample (Farmer 1983).

Table 3.2: Sample Dimenstions and Length to Diameter Ratios

Experiment #	Length (in)	Diameter (in)	Length/Diameter
1	5.089	2.014	2.5
2	5.045	2.015	2.5
3	5.139	1.982	2.6
4	5.170	1.983	2.6
5	5.122	2.011	2.5
6	5.156	2.014	2.6
7	5.007	2.011	2.5
8	5.002	2.011	2.5
9	5.062	2.013	2.5
10	5.164	2.011	2.6
11	5.136	2.013	2.6
12	5.055	2.013	2.5
13	5.166	2.012	2.6
14	5.059	2.012	2.5
15	5.136	2.012	2.6
16	5.090	2.011	2.5
17	5.084	2.012	2.5
18	5.133	2.012	2.6
19	5.062	2.011	2.5

The sample diameter used was actually 2 inches for each experiment as opposed to 2.126 inches. From Table 3.2 it can be determined that experiment 3, 4, 6, 10, 11, 13, 15 and 18 did not meet the ASTM specification for unconfined compressive strength testing. Unfortunately, due to the amount of transducers that were placed on the samples the length had to be as large as possible to accommodate the transducers. Therefore, the length to diameter ratio was slightly off for some samples to meet this requirement. The samples that did not meet this requirement were still tested, but not as much confidence will be instilled in the results from these experiments later in the thesis.

The final specifications that the samples had to meet according to ASTM standards was that the sides of the samples should be smooth and free of irregularities and the ends of the sample should be cut parallel to the longitudinal axis of the sample to within 0.001 inches (0.025 mm). The next section of this thesis will discuss the actual procedure used for preparing the samples for the unconfined compressive strength tests.

3.1.3 Sample Preparation

The Berea sandstone samples used for the experiments were prepared from large rectangular blocks attained from Cleveland Quarries with dimensions measuring roughly

13x13x6 inches. Prior preparation of the rectangular blocks before they were received included grinding of the top and bottom of the blocks so they would be easier to handle and work with the equipment. An example of one of the Berea sandstone blocks used for the experiments is shown in Figure 3.1.

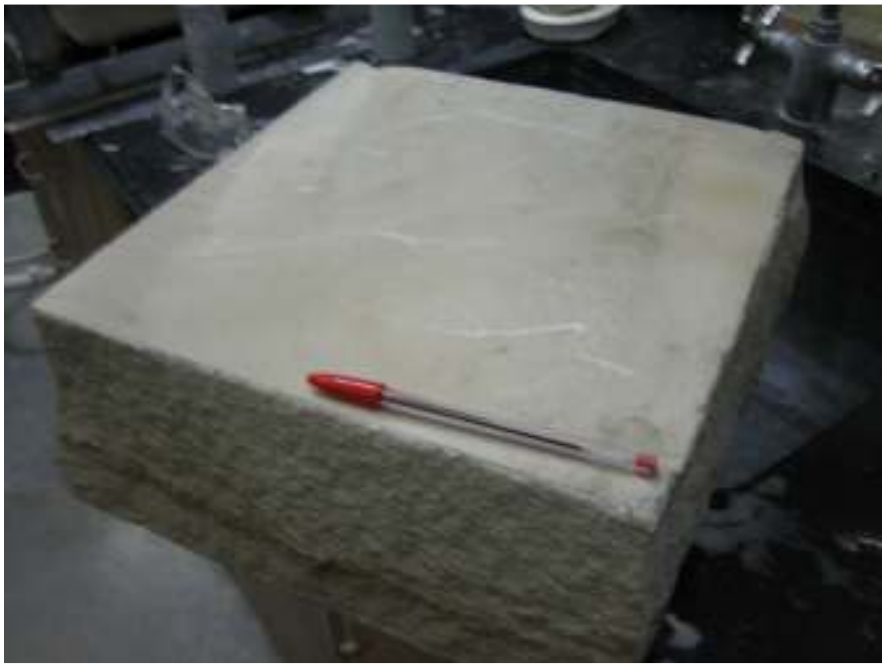

Figure 3.1: Rectangular Block of Berea Sandstone Used for Samples

To meet the first requirement of the ASTM specifications, which was that the samples had to be right circular cylinders, a modified milling machine was used. The milling machine used was equipped with a two inch diameter diamond tipped drill bit for coring the samples from the rectangular block of Berea sandstone. The milling machine was also modified with a water flushing system, which allowed for easier coring of the samples and also to suppress dust emission. The milling machine used for coring the Berea sandstone samples is shown in Figure 3.2.

Figure 3.2: Modified Milling Machine for Coring Rock Samples

Once the samples were cored using the milling machine, a tile saw equipped with a diamond tipped saw blade was used to attain the desired length of the samples, which was approximately five inches. The tile saw is also equipped with a water flushing system to allow for easier cutting and to minimize dust emission. Figure 3.3 shows the tile saw used for reducing the Berea sandstone sample lengths.

Figure 3.3: Tile Saw used for Sample Length Reduction

The final specification for the unconfined compressive strength testing of the Berea sandstone samples required the surfaces of the samples to be parallel within 0.001 inches (0.127 mm). A water flushed grinding machine was used to grind the surfaces of the samples to meet the specification along with a granite reference block that was used to measure the difference between the two parallel surfaces. The grinding machine used for sample preparation is shown in Figure 3.4. Upon completion of all preparation for the Berea sandstone samples were allowed to dry at room temperature for at least a 24 hour period before the transducers were attached to the sample.

Figure 3.4: Rock Core Grinding Machine

3.1.3 Placement of Sensors

The Berea sandstone samples, after having ample time for drying, were measured to get the exact diameter and length of each sample to within 0.001 inches using a dial caliper. This was accomplished by taking five measurements of diameter and length and averaging the measurements. The samples were then marked to show where the piezoelelectric transducers would be placed. The placement of the sensors remained uniform on all 19 samples tested. The sensors were placed in such a way that they created a suitable array around the sample to provide adequate coverage of the sample for monitoring the resulting acoustic emissions. There were sixteen piezoelelectric

transducers glued on the sample at 30, 60, 120,150, 210, 240, 300 & 330 degrees around the sample in columns of two. Figure 3.5 is a schematic of the transducer array used for the 19 experiments.

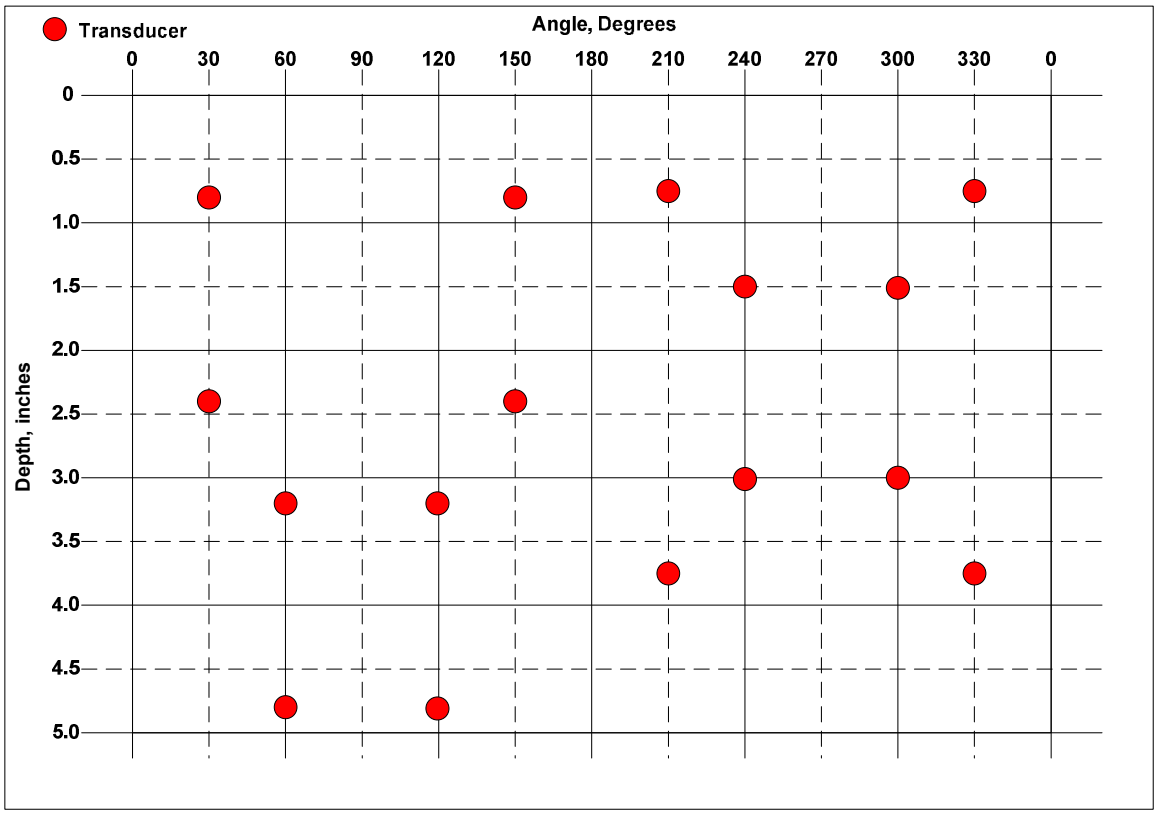

Figure 3.5: Sensor Configuration Schematic

The attachment of the piezoelelectric transducers to the Berea sandstone sample required a couplant. The purpose of the couplant is to fill in any air gaps between the piezoelelectric transducers and the rock core to allow the ultrasonic wave to reach the transducer. The couplant that was chosen for the experiment was super glue. Super glue was chosen based on it easy use for attaching the sensors and after the experiment the sensors could be cleaned using a debonder agent without causing damage to the piezoelelectric transducers. Figure 3.6 & 3.7 show the marks made for the piezoelelectric transducers positions on Berea sandstone and the piezoelelectric transducers actually attached to a Berea sandstone sample, respectively.

Figure 3.6: Sensor Locations on Berea Sandstone Sample

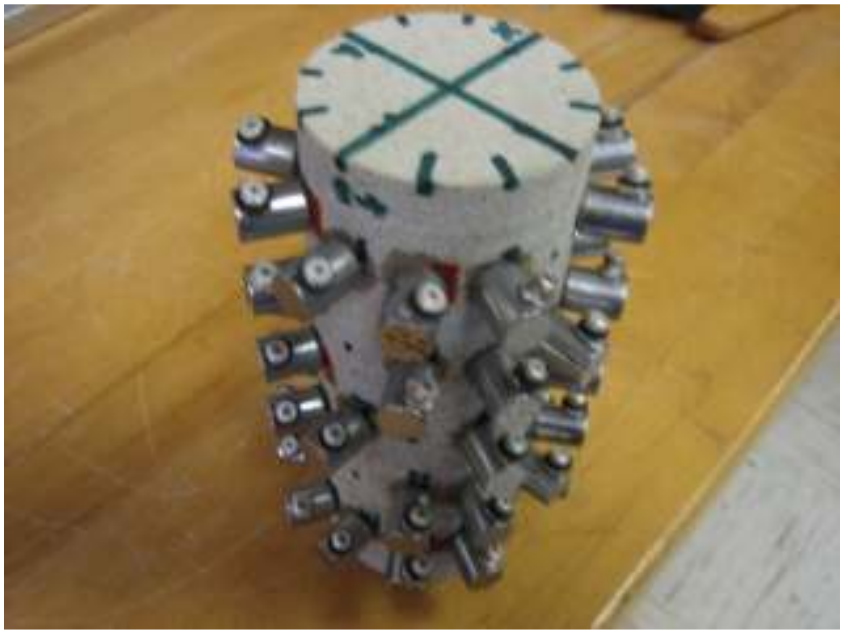

Figure 3.7: Sensors Attached to a Berea Sandstone Sample

3.1.4 Sample Loading

In order to conduct the uniaxial compression tests on the Berea sandstone samples a Materials Testing System (MTS) load frame equipped with a million pound load cell was used to conduct the experiments. The samples were positioned in the center of the

loading platform with a 2 inch diameter platen placed on top of the sample to allow the piezoelelectric transducer's wires for the ultrasonic data acquisition system to clear the loading platen. A schematic of how the sample is placed in the MTS loading platform is shown in Figure 3.8.

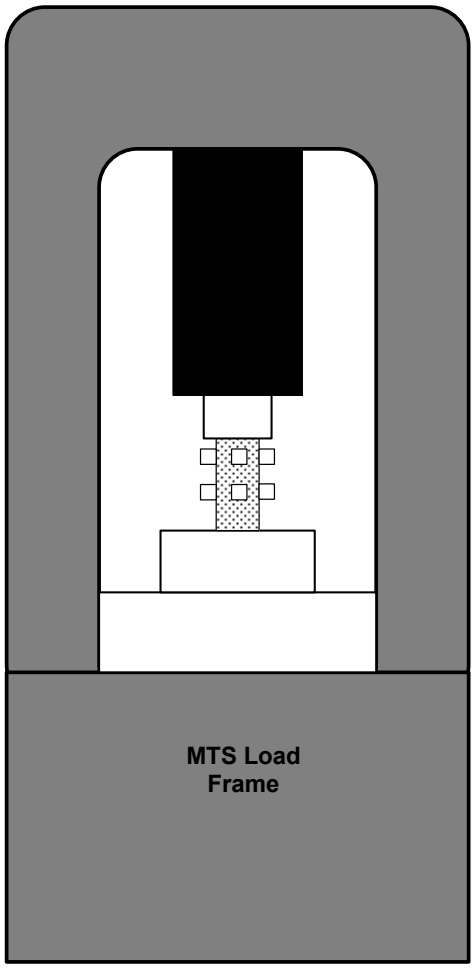

Figure 3.8: Schematic of Sample Placement in MTS Load Frame

Once the sample was placed within the MTS load frame, the sample was loaded at a controlled displacement rate of 0.003 mm/sec until failure occurred. The displacement of the MTS load frame was controlled by a computer using a LabVIEW environment. During the sample experiment, the loading of the sample was paused every 2000 pounds of load applied to allow for sample data to be taken and recorded for an active tomography experiment that was being conducted simultaneously as the acoustic emission experiments. The sample was tested in this manner until the sample ultimately failed, which an example of a failed Berea sandstone sample is shown in Figure 3.9.

Figure 3.9: Failed Berea Sandstone Sample

3.2 Acquisition System

The acquisition system used for the 19 experiments is a commercial system manufactured by Engineering Seismology Group (ESG) Canada. The acquisition system is the ESG Hyperion Ultrasonic System, which is shown in Figure 3.10. The acquisition system is capable of 14 bit resolution and sample rates up to 10 MHz. The included windows based software that came with the system allows for real time monitoring through 16 channels (piezoelectric sensors) and is capable of filtering events by setting a threshold trigger value and the number of channels needed to trigger.

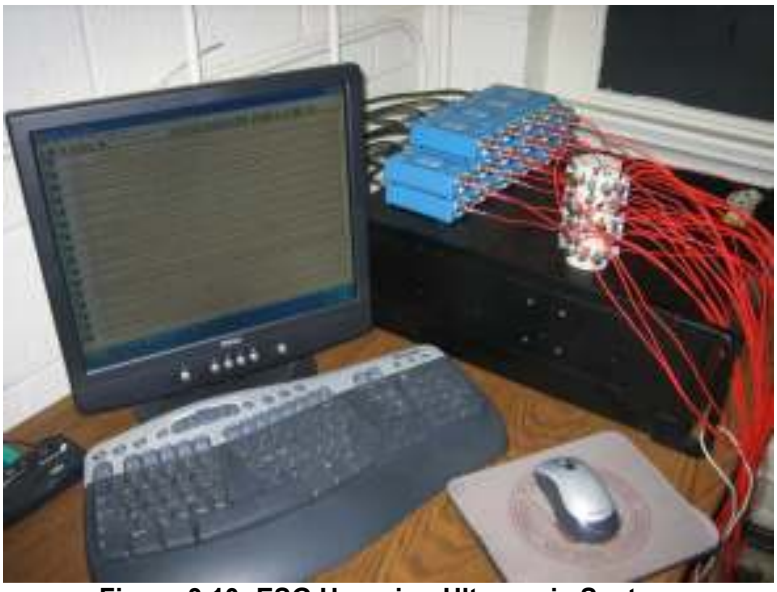

Figure 3.10: ESG Hyperion Ultrasonic System

3.2.1 Analog to Digital Card Interfaces

The Hyperion Ultrasonic System includes two 8-channel ISA Analog/Digital boards. The role of the ISA Analog/Digital boards is to convert the analog signals, which are the output from the piezoelectric sensors, to a digital format that can be used by the computer system. The ISA Analog/Digital boards also allow the monitoring system to record multiple events in a short time period by acting as a buffer to store the analog data from the piezoelectric sensors. While the analog data is stored in the buffer, the ISA Analog/Digital cards apply a user preset trigger to the analog data to determine if the amplitude of the data is beyond the trigger threshold and meets the requirements for an event. This process allows for the filtering out of unnecessary data from later processing. A schematic showing the location of the Analog/Digital cards is shown in Figure 3.11.

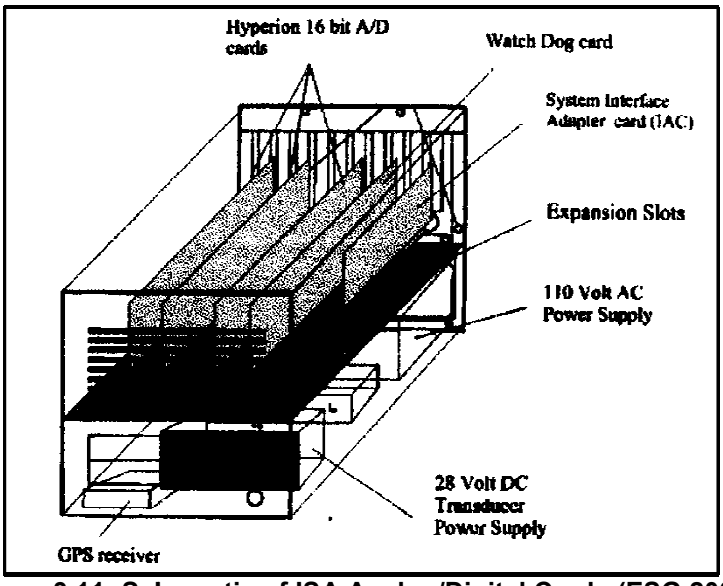

Figure 3.11: Schematic of ISA Analog/Digital Cards (ESG 2006)

3.2.2 Pre-Amplifiers

Sixteen pre-amplifiers were included with the Hyperion Ultrasonic System and were each attached to a corresponding piezoelectric sensor. The pre-amplifiers used are model #1220A and are manufactured by Physical Acoustics Corporation (PAC). The role of the pre-amplifiers in the Hyperion Ultrasonic System is to amplify the relatively small output from the piezoelectric sensors, which are on the order of micro-volts. The pre-amplifiers actually amplify the output from the piezoelectric sensors without introducing significant amounts of noise and distortion to the data. Figure 3.12 shows one of the PAC 1220A pre-amplifiers used in the experiments.

Figure 3.12: PAC 1220A Pre-Amplifier

3.2.3 Sensors

The Hyperion Ultrasonic System uses sixteen piezoelectric transducers as the means to connect the system to the rock sample being tested. Piezoelectric transducers typically contain a piezoelectric crystal, which converts movement to an electrical signal that is amplified by the pre-amplifier and then sent to the ISA Analog/Digital boards to be processed. Piezoelectric transducers also have another application as source mechanisms, where they convert an electrical signal to movement. The 16 Piezoelectric transducers used for the experiments are manufactured by Physical Acoustics Corporation (PAC) and the model used is the Micro-80. The Micro-80 was chosen for the experiments based mainly on its size, which is small enough to allow for more than 50 sensors to be attached to a two inch diameter sample.

3.3 Monitoring Procedure

The procedure employed for monitoring the acoustic emissions generated by the Berea sandstone samples included the setting of many parameters that the Hyperion Ultrasonic System operated based off of and also required the presence of a user to pause the monitoring process at certain times. For all 19 experiments, the ESG program, UltrACQ, was used for the real-time monitoring of the acoustic emission events. UltrACQ was set to record all events that triggered more than six piezoelectric transducers that exceeded the triggering threshold within a moving 4096 microsecond time frame. At the beginning of every experiment UltrACQ was triggered once before every experiment to ensure that the system and piezoelectric transducers were all working correctly. Figure 3.9 shows the window displayed when using the UltrACQ software with the Hyperion Ultrasonic System.

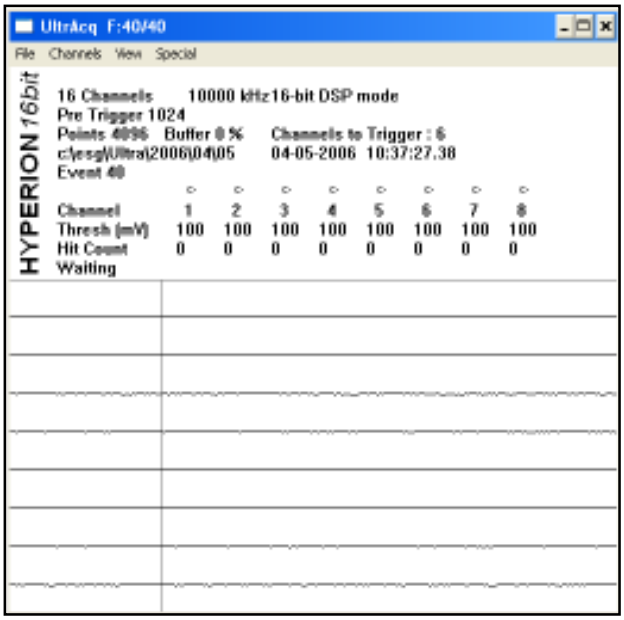

Figure 3.13: UltrACQ Software Used with Hyperion Ultrasonic System

Once the system was found to be operating correctly, a uniaxial compressive strength test was performed on the Berea sandstone sample being tested. The sample was loaded at a controlled displacement and paused every 2000 pounds of load. At this point the Hyperion Ultrasonic System was paused to allow for another ultrasonic acquisition system to be run that uses active sources. The Hyperion Ultrasonic System was paused due to the interference with monitoring acoustic emission caused by the active sources from the other acquisition system. During the period when the system was paused, the number of events occurring up to that point were recorded and used later to create tomograms reflecting different loads applied to the Berea sandstone samples. During this time the threshold value of the system may have been adjusted due to the decreasing amount of unusable waveforms that occurred at higher loads. This process was repeated for all 19 Berea sandstone samples. The data attained from these experiments was processed and used to generate tomograms, which will be explained in more detail in the next chapter.

Chapter 4 – Data Reconciliation and Analysis

There were a number of steps and computer programs used to analyze and display the data obtained from the 19 Berea sandstone experiments. The programs used for the analysis include WaveVIS, SeisProc Tree, LabVIEW, Microsoft Excel, GeoTOM and RockWorks 2004. The following sections explain the steps and how each program was used to lead to the generation of the tomograms for all 19 experiments

4.1 Arrival Time Picking & Source Location

The events recorded during the 19 Berea sandstone experiments using UltrACQ, were displayed and analyzed using another ESG program called WaveVIS. WaveVIS is a waveform visualization and seismic wave picker software suite. WaveVIS allows for the visualization of all 16 peizoelectric sensors used for the experiment and also utilizes the use of user defined processors that allow for the automated determination of the seismic wave arrival time at each sensor for each event. Figure 4.1 shows the window displayed when using the WaveVIS software.

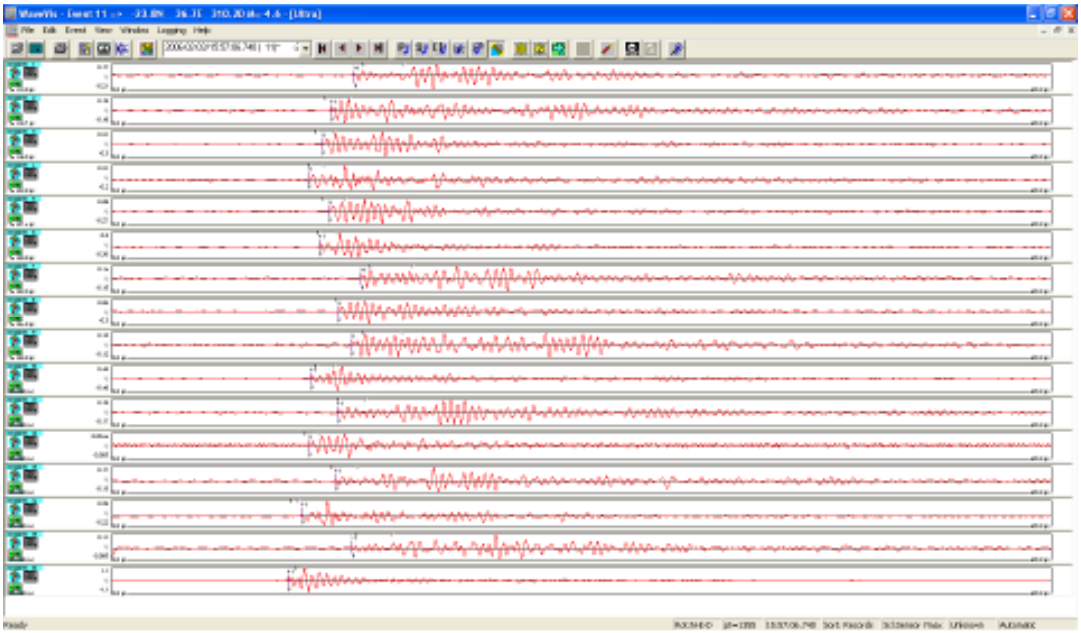

Figure 4.1: WaveVIS Software Used with Hyperion Ultrasonic System

In order to use the processor function of WaveVIS another ESG program, called Seisproc Tree, is used by the user to create custom picker and source location algorithms, while still allowing for user defined input in the form of boundaries and material properties. The algorithm used for the 19 experiments used a p-wave picker function with a moving window and the simplex source location method to determine the location of the source of the acoustic emission. The Geiger source location method was used as well for locating the acoustic emission sources by refining the locations determined by the Simplex method. The parameters used for the locating the acoustic emission source include a uniform velocity of 8000 feet per second and confining the location of the sources to the boundary of the sample being tested.

4.2 Data Reconciliation & Travel-time Determination

WaveVIS outputs two text files, which are the acoustic emission event locations and the p-wave arrival time picks for every sensor in every event. A program was developed that converts the data from these two files along with another text file created by the user containing the sensor locations to a more usable format. The program also requires the input of the number of triggered events and the number of located events. Both of these parameters can be easily determined using the WaveVIS program mentioned in the previous section. The program developed was created using LabVIEW. The LabVIEW program takes the data from all the text files and combines this data into one text file, where every line contains the source location, a sensor location and the corresponding p-wave arrival time for that combination. Figure 4.2 shows the input window displayed when using the developed LabVIEW program.

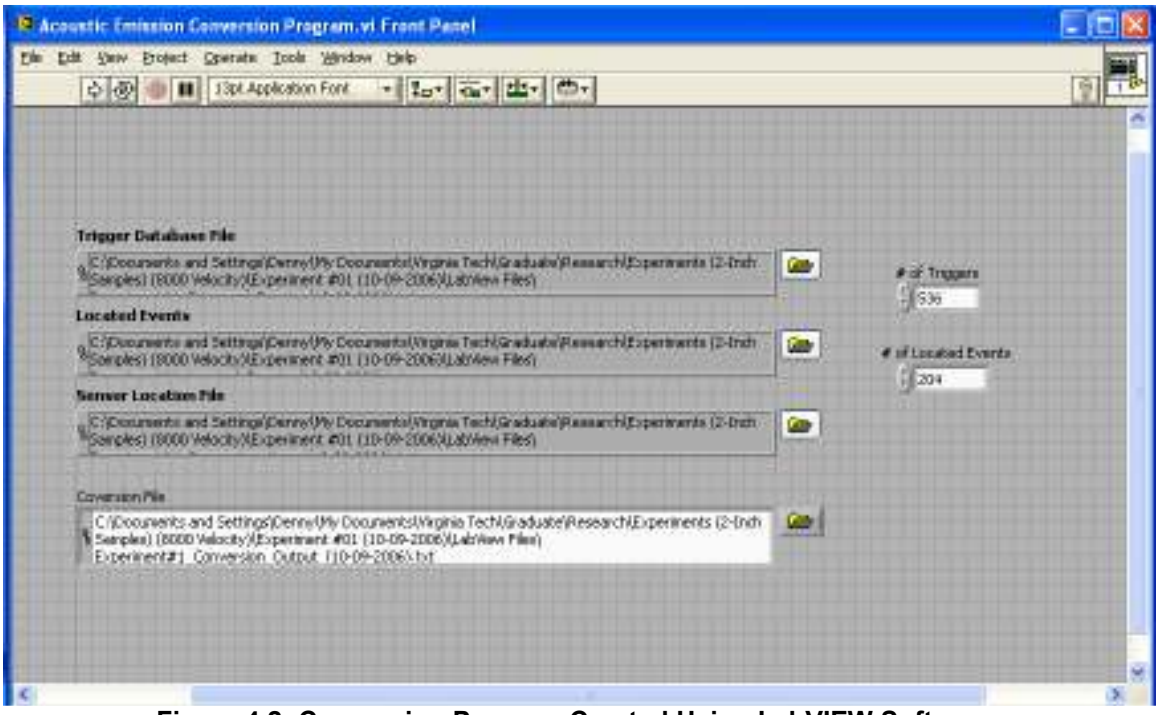

Figure 4.2: Conversion Program Created Using LabVIEW Software

The output file from LabVIEW, then requires the adjustment of the arrival times to determine the travel-times. This step is required because in the process of source location, the actual time the acoustic emission occurred is not known. Therefore, the first hit sensor is used to determine the travel-time by assuming a straight ray path and uniform velocity from the acoustic emission source to the first hit sensor. The arrival time difference between the first hit sensor to every other sensor in the event is then added to the travel-time to determine the travel-time for the remaining sensors. This step of data reconciliation is performed using Microsoft Excel and the process used to determine the travel-times is outlined in the flowchart of Figure 4.3.

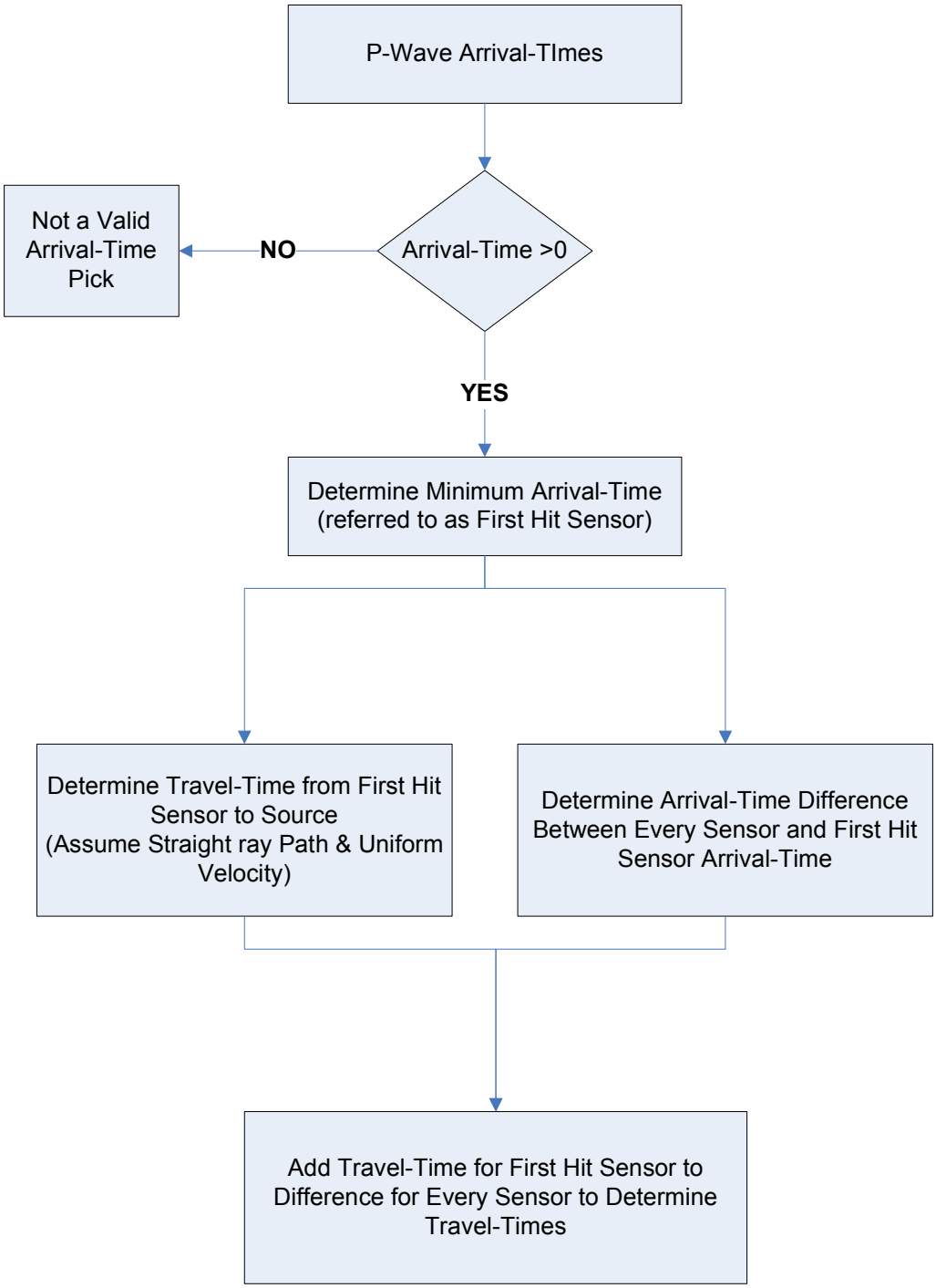

Figure 4.3: Flowchart for Travel-Time Determination Using Microsoft Excel

The usefulness of this data reconciliation method is shown in the improvement of the linear correlation of the data on a travel-time versus distance plot. For the 19 experiments the correlation found with the arrival-times was typically less than one

percent, whereas after the adjustment of the arrival-times to attain the travel-times increased the linear correlation to 70 – 80 %, after removing outliers and events that were located outside the boundary of the sample. Outliers were easily seen once the travel-times were determined due to the fact that they would have travel-times much larger than the other events. If an outlier was removed from the data all picks that corresponded with that event were removed as well, since every arrival-time pick was used in the determination of the source location. The correlation coefficient of each event was also determined and if this value was smaller than 40 % than the event was removed as well. Using this method of data reconciliation also allowed for the checking of the accuracy of the picks determined by WaveVIS. Figure 4.4 and 4.5 shows the arrival-times and the travel-times for experiment #2 versus distance, respectively.

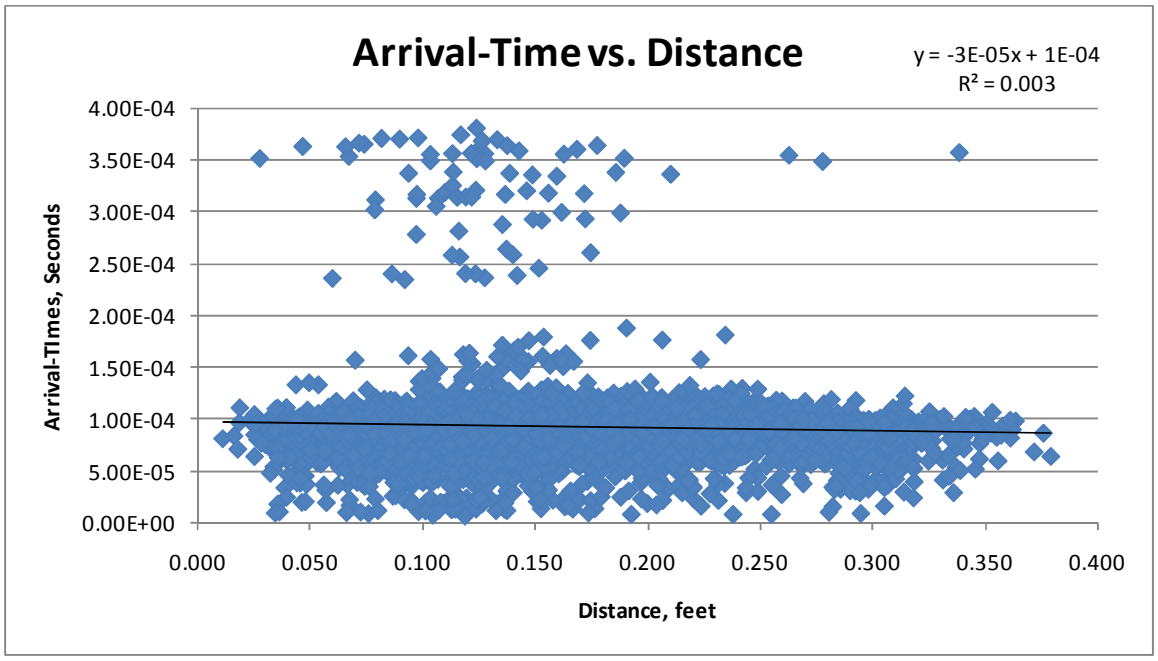

Figure 4.4: Plot of Arrival-Times versus Distance for Experiment #2

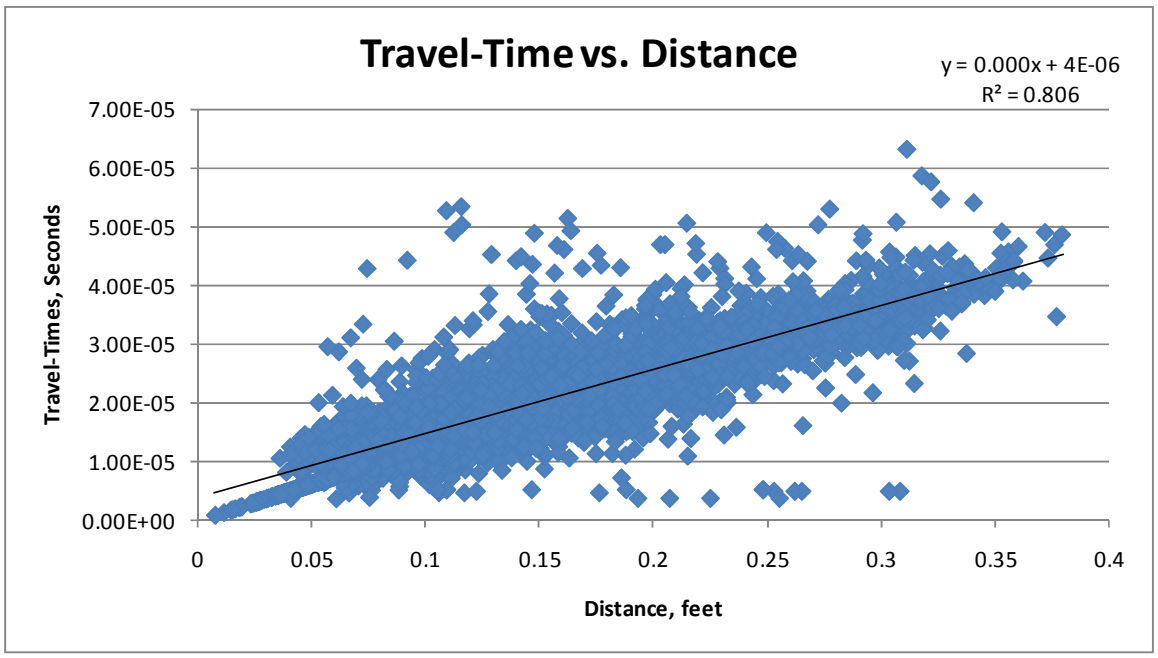

Figure 4.5: Adjusted Travel-Times versus Distance Plot for Experiment #2

4.3 Inversion

The source and receiver locations along with the corresponding travel-times were exported from excel to a text file for determination of velocity distribution within the Berea sandstone samples. Velocity distribution within the samples is of importance because the propagation wave velocities within the sample can be used for inference of stress redistribution within the sample. To determine the velocities within the samples, ray inversions were performed on the text files using a commercial software package called GeoTOM. GeoTOM is an iterative inversion program that inverts the rays for slowness using the SIRT algorithm, which is an acronym for Simultaneous Iterative Reconstruction Technique.

GeoTOM requires the input of certain parameters as well as a model file to adequately perform the ray inversions. GeoTOM determines the velocity distribution by separating the structure into nodes, commonly called pixels in 2-d and voxels in 3-d. The defining of the boundaries of the structures and the number of nodes the structure is split into are required parameters needed for the inversions of the rays and is defined in the model file created.

Ray inversions were then performed using GeoTOM with 10 iterations performed for both straight and curved rays. GeoTOM outputs the velocity distribution of the structure in slices that can be viewed two dimensionally and also allows for the exporting of the nodes in a dat file format. Figure 4.7 shows the velocity distribution of one slice of experiment#2 in the x-y plane.

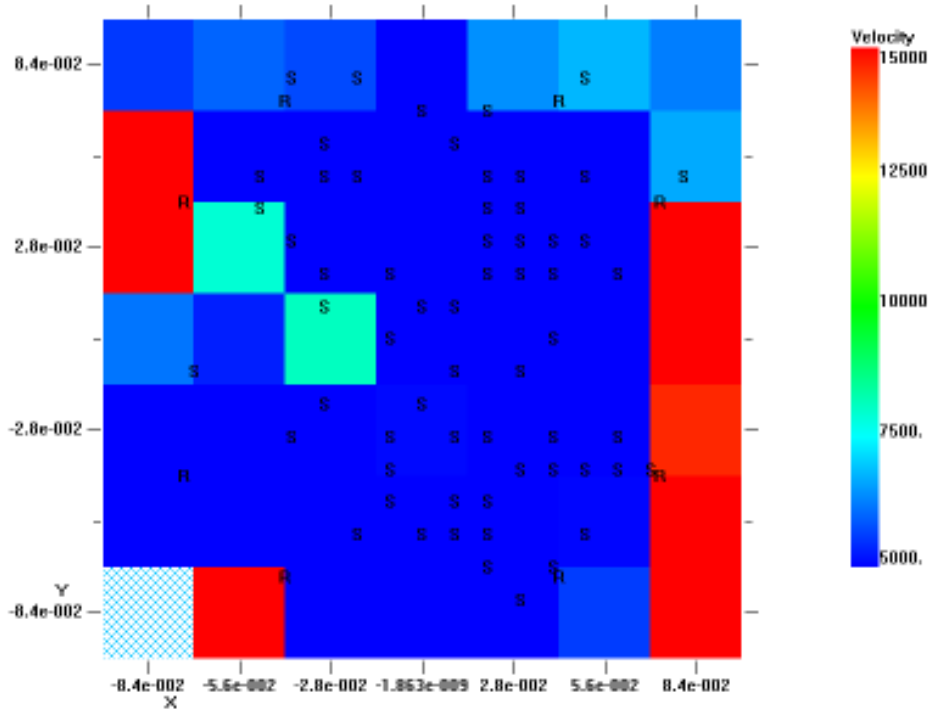

Figure 4.7: Velocity Distribution Slice in X-Y Plane at a Load of 52.0 MPa

4.4 Three-Dimensional Modeling

Due to the poor graphic output of GeoTOM, the velocity distributions of the samples are exported and displayed using RockWorks 2004. RockWorks 2004 allows for the combining of the velocity distribution slices and the viewing of these slices three dimensionally.

The exported dat files from GeoTOM are filtered to remove all nodes that contain less than 5 rays per node or if the velocity is equal to 5000 ft/s or 15000 ft/s. Nodes with less than 5 rays were removed to eliminate artifacts, which can cause inaccurate velocity distributions in the structure due to the higher influence of the rays within the node.

Nodes with velocity values of 5000 ft/s or 15000 ft/s were removed because these were the minimum and maximum values for velocity defined in GeoTOM. If the velocity values calculated in GeoTOM were lower or higher than these set limits they were set to the minimum or maximum velocity value. Therefore, these values were removed to prevent misleading high or low velocity distributions. This process is completed using Microsoft excel prior to importing the dat file into RockWorks 2004.

The dat file is imported into the geological utilities menu of RockWorks 2004 and a model is generated with the value for each node being the velocity. RockWorks 2004 requires the input of the project dimensions, which is the geometry of the sample, and interpolates the values of nodes with no values using an inverse-distance isotropic algorithm. The generated model is square in shape as opposed to circular like the Berea sandstone samples so a distance filter is applied to the model and assigns a zero velocity for all nodes outside the boundaries of the samples. The model is then filtered to remove the nodes that do not fall between velocities of 5000 – 15000 feet per second. The legend for the tomograms was set to display 5000 ft/s to 13000 ft/s due to the velocity distributions in the Berea Sandstone samples having only a few velocities larger than 13000 ft/s. Figure 4.8 shows the tomogram generated for Experiment#2 at a load of 24000 pounds.

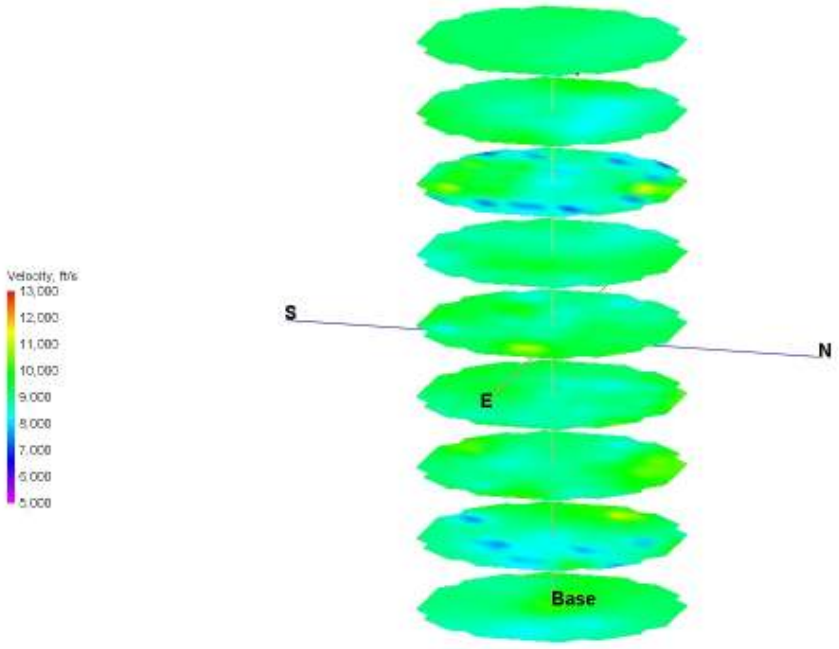

Figure 4.8: RockWorks Tomogram Generated for Experiment #2 at a Load of 52.0 MPa

This process was repeated to create tomograms for every 2000 pounds of load applied to the Berea sandstone samples. The tomograms were then sliced horizontally every 0.05 feet and oriented with the major failure plane perpendicular to the paper. The failure plane is also oriented so that the failure plane is sloping down from the top right corner to the bottom left. This process was repeated for all 19 Berea sandstone samples tested.

Chapter 5: Experimental Results

For every experiment the locations of the acoustic emissions for the entire experiment were plotted along with tomograms for every load. Since passive sources, acoustic emissions, were used for the travel-time tomography not every load pause had sufficient data for generation of a tomogram. The following sections present results for Berea Sandstone Experiment #2. These sections include a plot of the acoustic emission source locations, load pause tomograms, travel-time versus distance plot, plot relating acoustic emission activity to the stress-strain curve of the tested sample and a plot relating the stress-strain curve and p-wave velocity.

5.1 Travel-Time versus Distance Plots

The arrival-time versus distance plot for Experiment #2 is shown in Figure 5.1. Figure 5.2 contains the adjusted travel-time versus distance plot for Experiment #2. Table 5.1 summarizes the information for the data reconciliation for experiment #2. Appendix A contains the arrival-time and travel-time plots for all 19 experiments conducted. The correlation coefficient from the arrival-time plot was 4.7 %, but upon performing the previously explained data reconciliation was improved to 80.6 % for the travel-time plot. This was accomplished by performing the required data reconciliation and by removing 39 rays out of 8140 rays, which were considered to be outliers. Based on the high correlation coefficient of the travel-time data and removal of a minimal amount of rays, there was a high level of confidence in this experiment over the other 18 experiments.

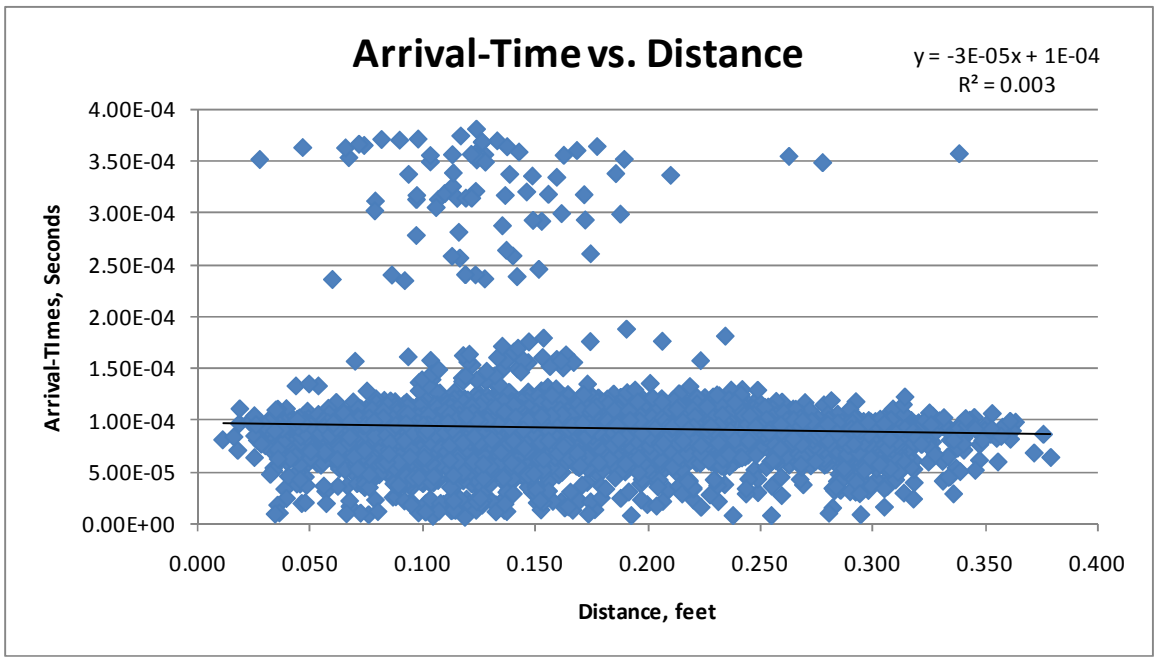

Figure 5.1: Experiment #2 Arrival-Time Versus Distance Plot

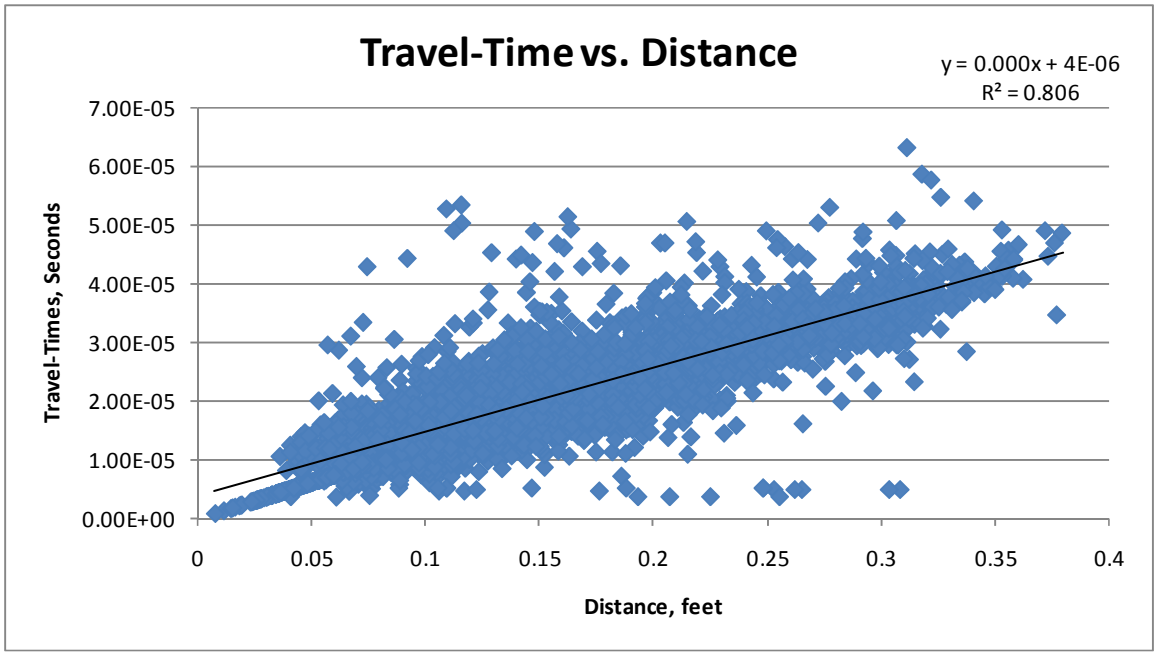

Figure 5.2: Experiment #2 Travel-Time Versus Distance Plot

Table 5.1: Data Reconciliation Summary Statistics for Experiment #2

Experiment #2	
Arrival-Time R^2	4.70%
Number of Arrival-Time Rays	8142
Travel-Time R^2	80.60%
Number of Travel-Time Rays	8101
Number of Rays Eliminated	41

5.2 Acoustic Emission & Wave Velocity Plots

Table 5.2 summarizes the acoustic emission and loading, by load pause, for Experiment #2. The stress-strain curve plotted against the number of acoustic emission events that occurred in Experiment #2 is shown in Figure 5.3. Figure 5.4 plots the average velocity for every load pause against the stress-strain curve. The average velocities in Figure 5.4 also contain error bars that show one standard deviation for each load pause's velocities. Appendix B contains the acoustic emission and wave velocity plots for all 19 experiments conducted.

The acoustic emission activity monitored during the experiment shows a gradual increase up to 4403 psi, where the acoustic emission activity begins to increasingly large amounts in the same load interval of 2000 lbs. The average velocity within each load pause was found to have a fairly consistent behavior with very little large increases in velocity. Experiment #2 does have a large increase in velocity at 8175 psi, but this is considered to be due to the sample being close to failure and the difficulty involved with recording reasonable acoustic emission events so close to failure.

Table 5.2: Experiment #2 Acoustic Emission Activity & Loading Summary Statistics

Experiment #2									
Load Pause	Strain	Stress (psi)	Stress (MPa)	Number of Triggered Events	Number of Located Events	Thresh (mV)	Ave. Vel. (ft/s)	Std. Dev. (ft/s)	% Variation
0	0.00000	0	0.0	0	N/A	200	N/A	N/A	N/A
1	0.00147	627	4.3	6	4	200	7586	940	12.4
2	0.00245	1261	8.7	7	7	200	7541	902	12.0
3	0.00309	1888	13.0	18	18	200	7429	934	12.6
4	0.00358	2509	17.3	28	26	200	7681	983	12.8
5	0.00406	3148	21.7	32	30	200	7621	1163	15.3
6	0.00447	3769	26.0	32	29	200	7428	1104	14.9
7	0.00482	4403	30.4	37	35	200	7409	1104	14.9
8	0.00524	5024	34.6	74	61	200	7559	1221	16.2
9	0.00560	5657	39.0	87	59	200	7446	1425	19.1
10	0.00597	6278	43.3	158	81	200	7633	1473	19.3
11	0.00638	6918	47.7	225	102	200	7713	1842	23.9
12	0.00674	7539	52.0	200	81	200	7873	4010	50.9
13	0.00734	8153	56.2	216	89	200	7841	3837	48.9
14	0.00740	8175	56.4	81	20	200	8534	5448	63.8

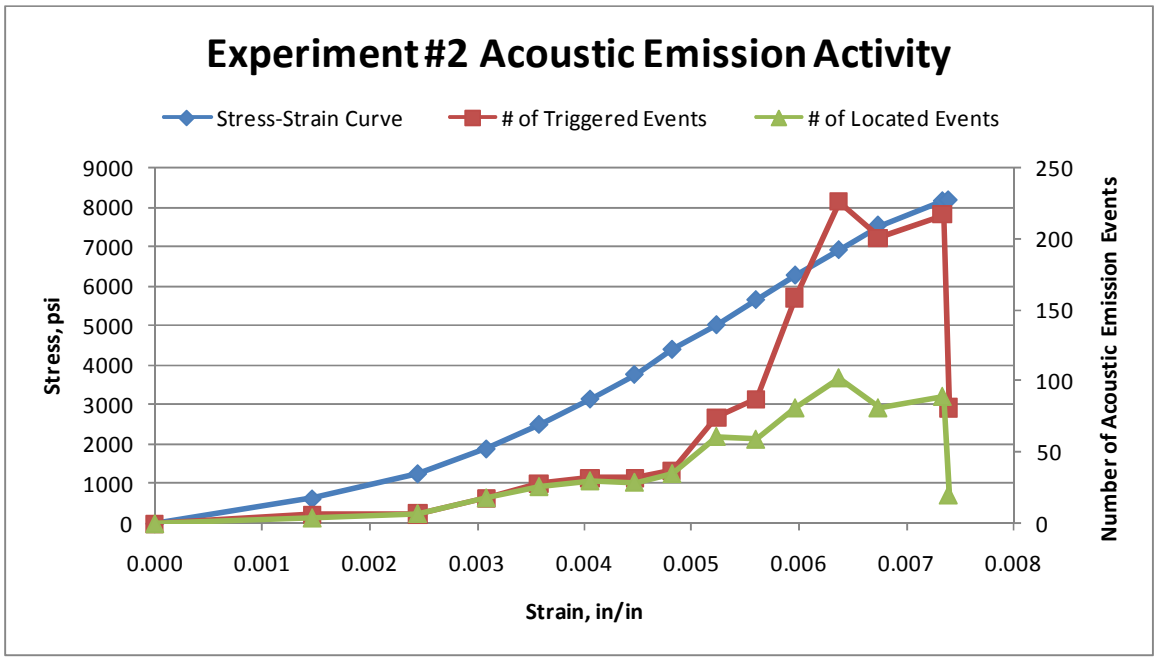

Figure 5.3: Plot of Stress-Strain Curve & Acoustic Emission Activity for Experiment #2

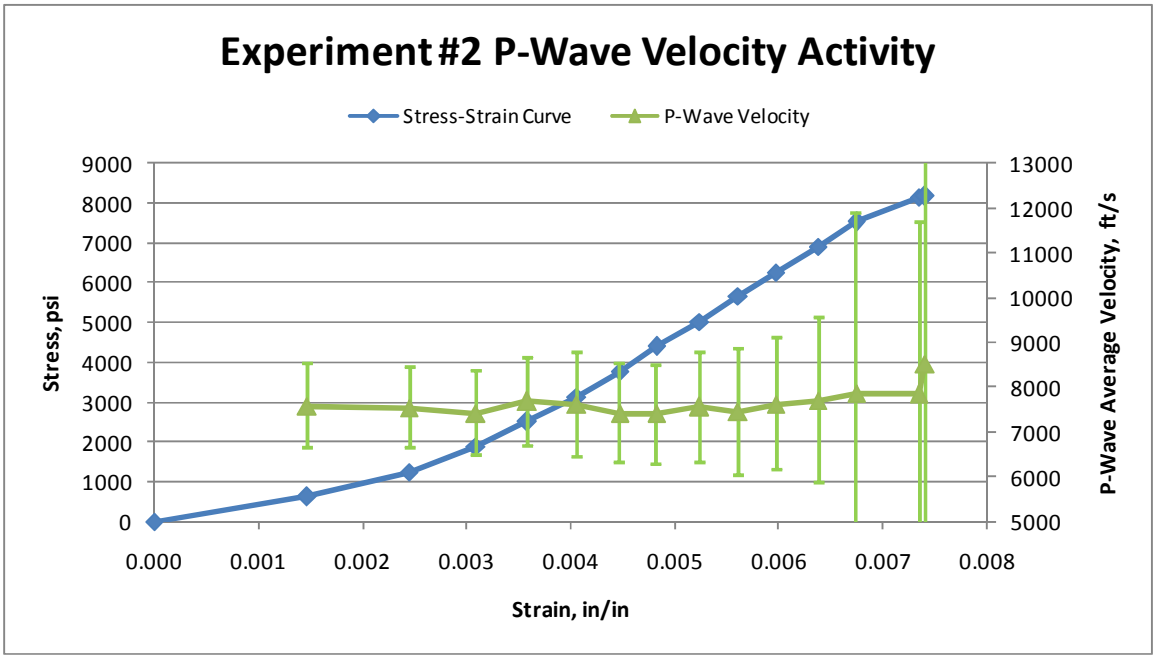

Figure 5.4: Plot of Stress-Strain Curve & P-Wave Velocity for Experiment #2

5.3 Display of Tomograms

The acoustic emission locations for Experiment #2 are shown in Figure 5.5. The tomograms generated for the load pauses for Experiment #2 are shown in Figures 5.6 – 5.19. These tomograms have been rotated 165 degrees counter clockwise from the North axis. This allows for the failure plane to be perpendicular to the page. The failure plane also dips down from the upper right corner to the bottom left corner, which is the manner used to display all tomograms in this thesis. Figure 5.20 shows the failed Berea sandstone sample used in Experiment #2 oriented in the same manner as the tomograms.

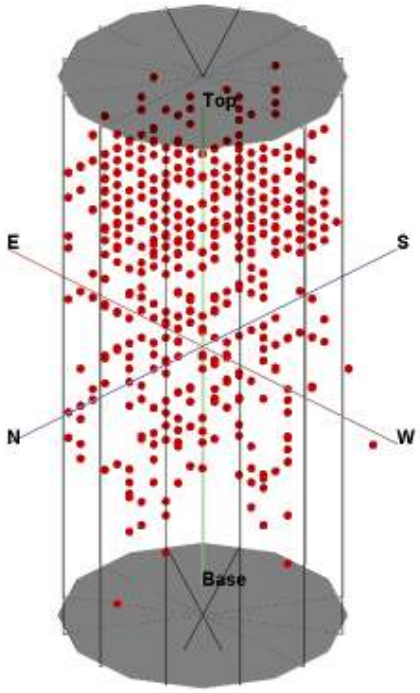

Figure 5.5: Acoustic Emission Locations for Experiment #2

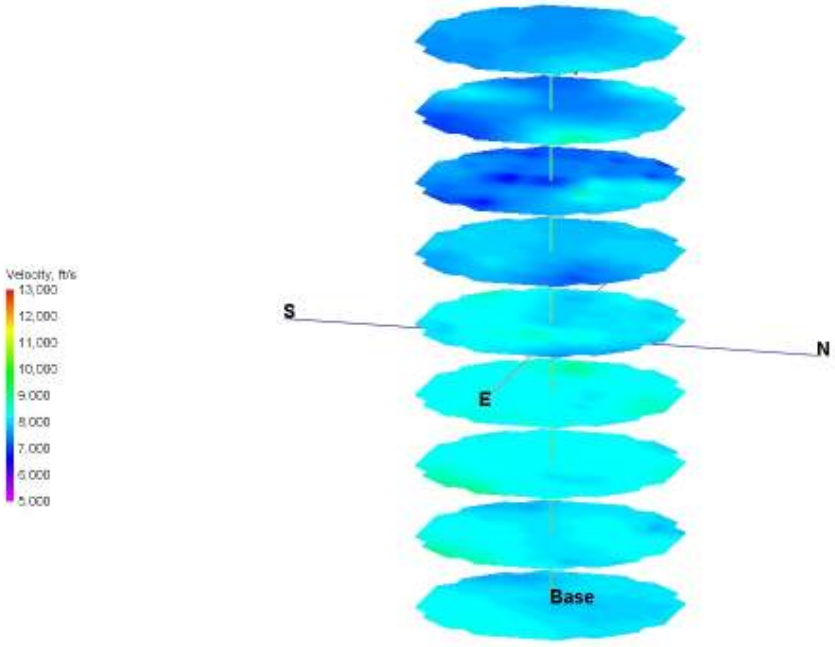

Figure 5.6: Experiment #2 Tomogram at 4.3 MPa of Load

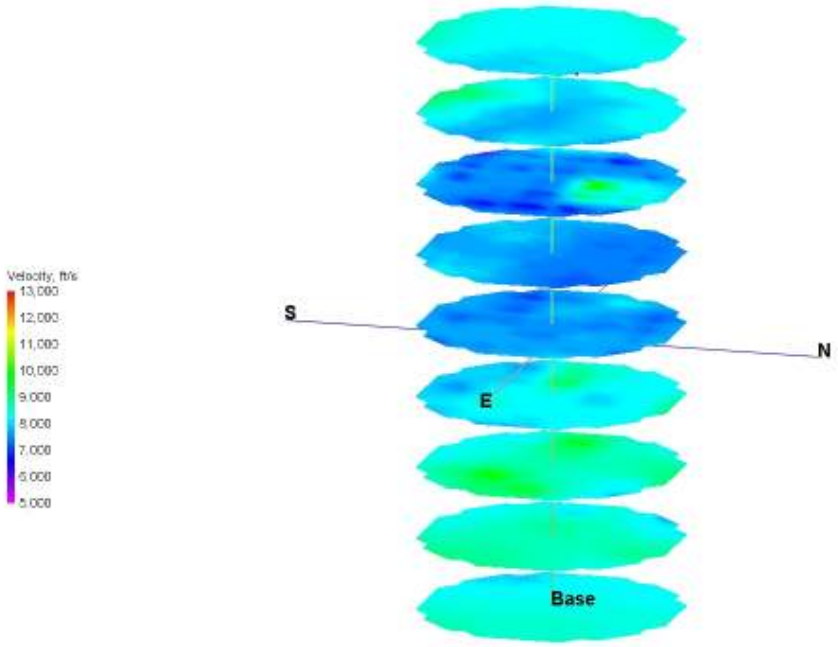

Figure 5.7: Experiment #2 Tomogram at 8.7 MPa of Load

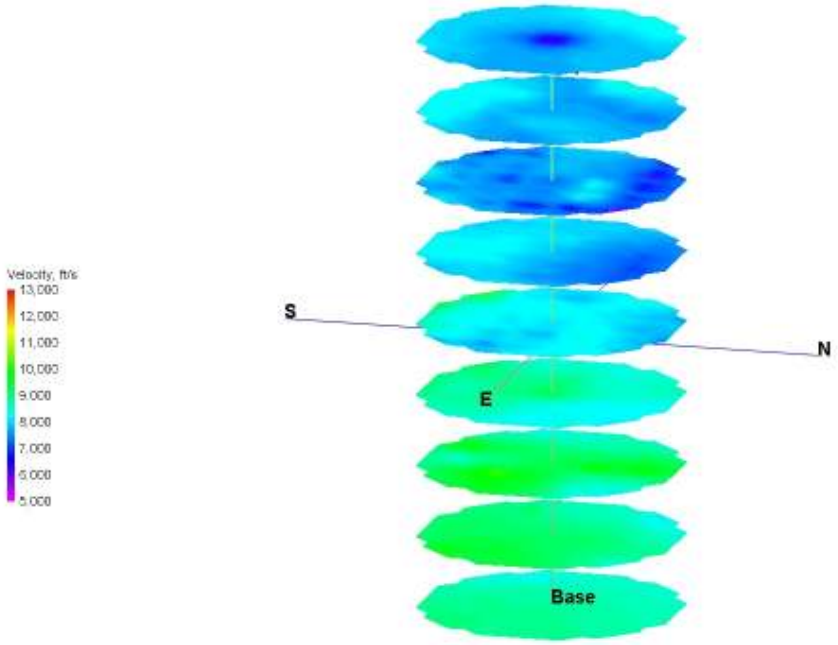

Figure 5.8: Experiment #2 Tomogram at 13.0 MPa of Load

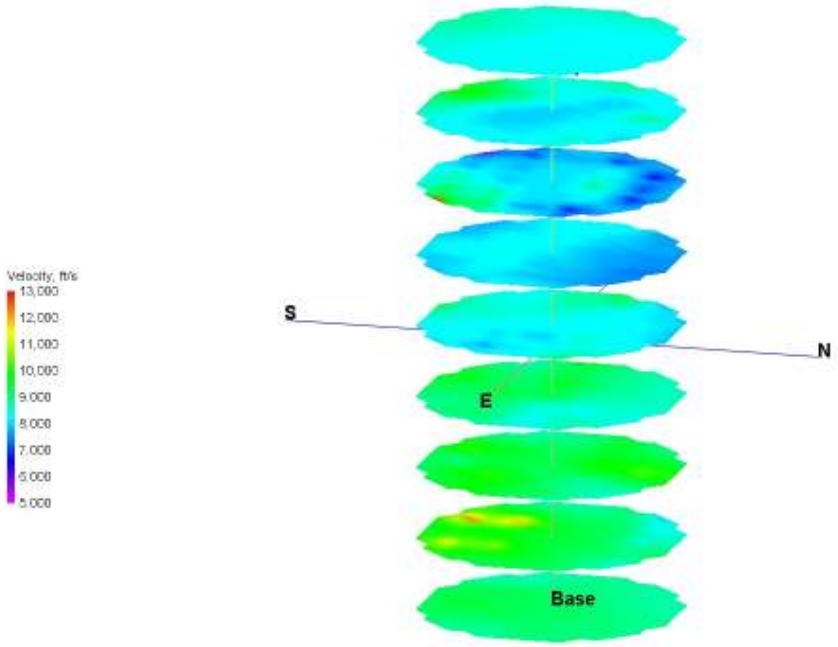

Figure 5.9: Experiment #2 Tomogram at 17.3 MPa of Load

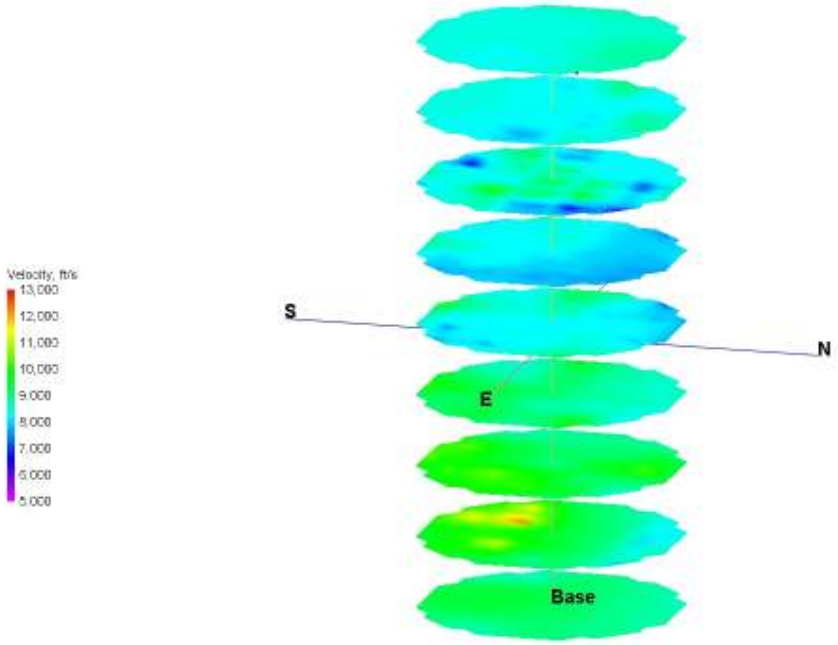

Figure 5.10: Experiment #2 Tomogram at 21.7 MPa of Load

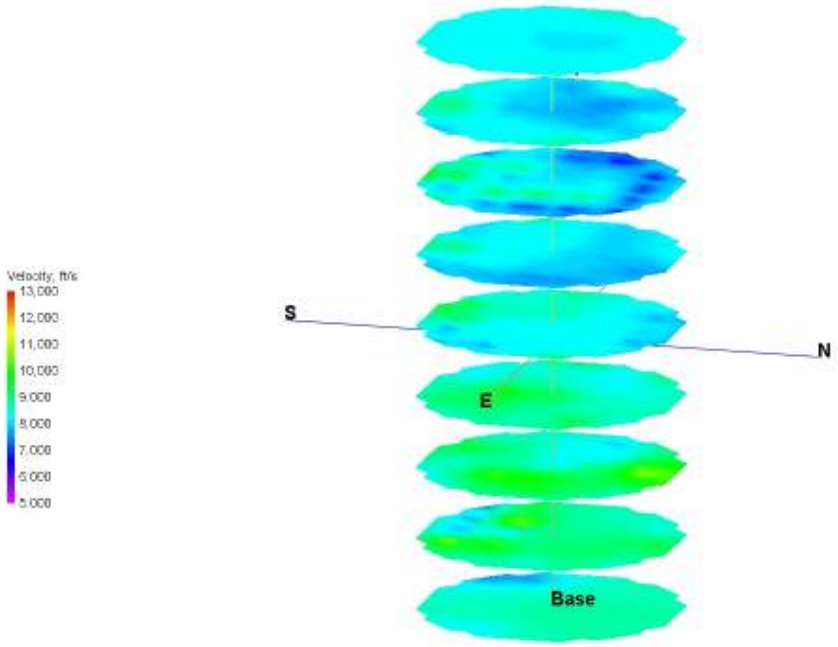

Figure 5.11: Experiment #2 Tomogram at 26.0 MPa of Load

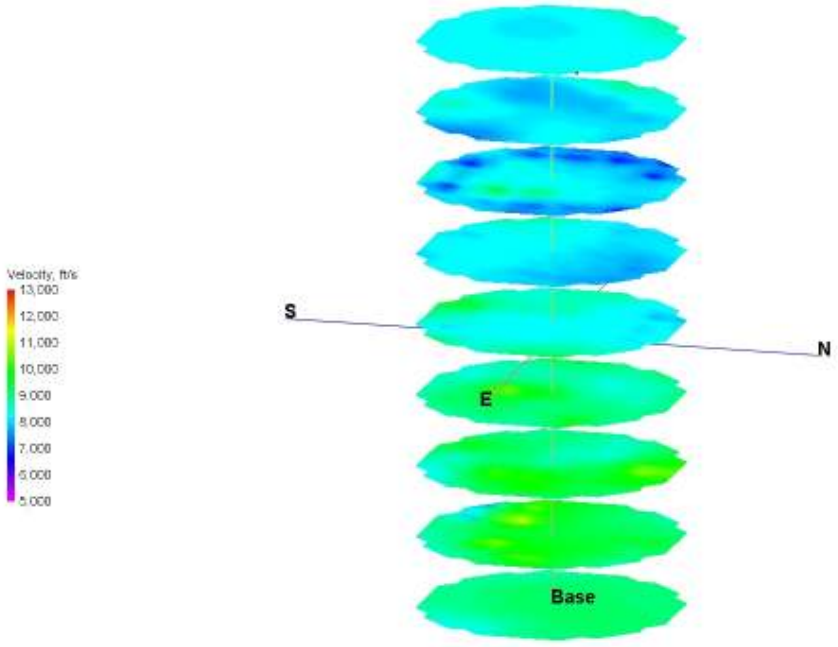

Figure 5.12: Experiment #2 Tomogram at 30.4 MPa of Load

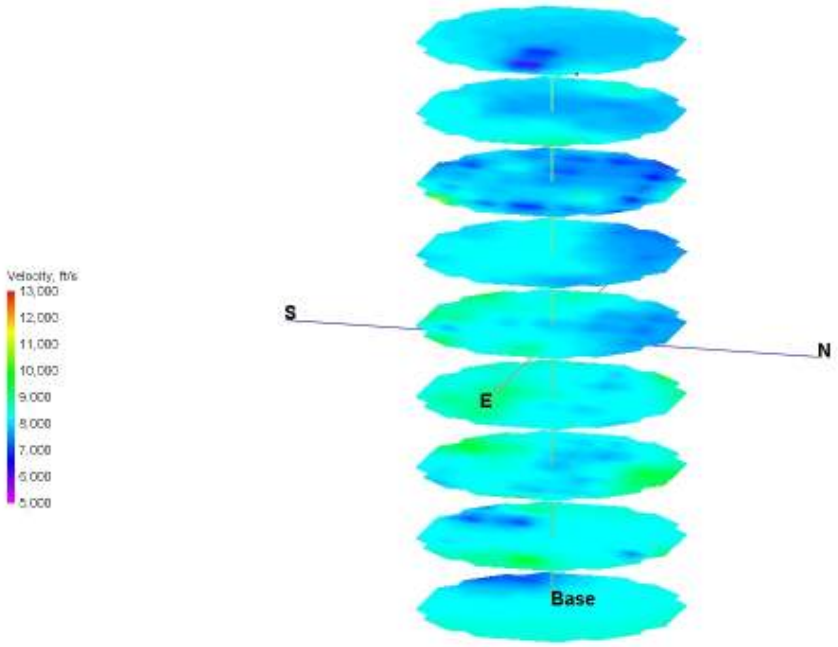

Figure 5.13: Experiment #2 Tomogram at 34.6 MPa of Load

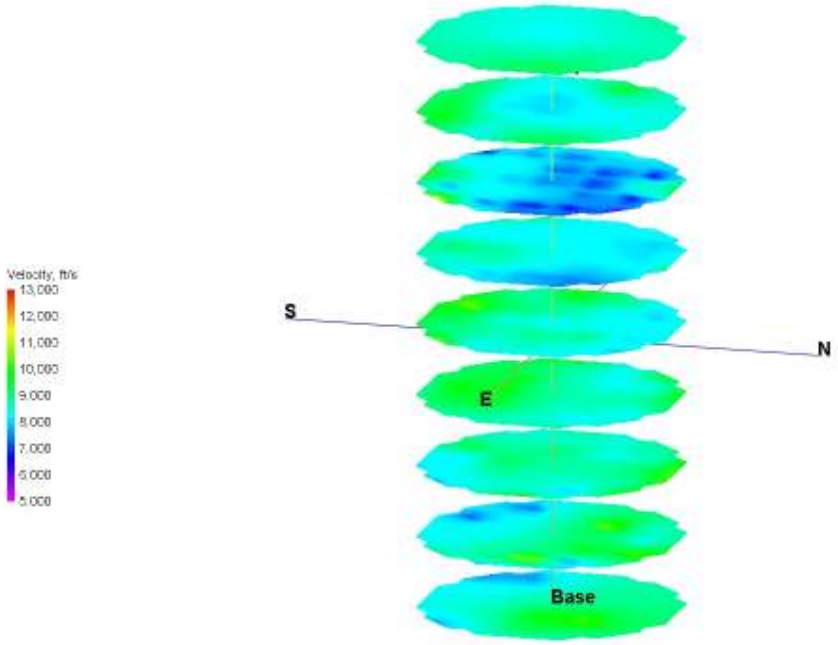

Figure 5.14: Experiment #2 Tomogram at 39.0 MPa of Load

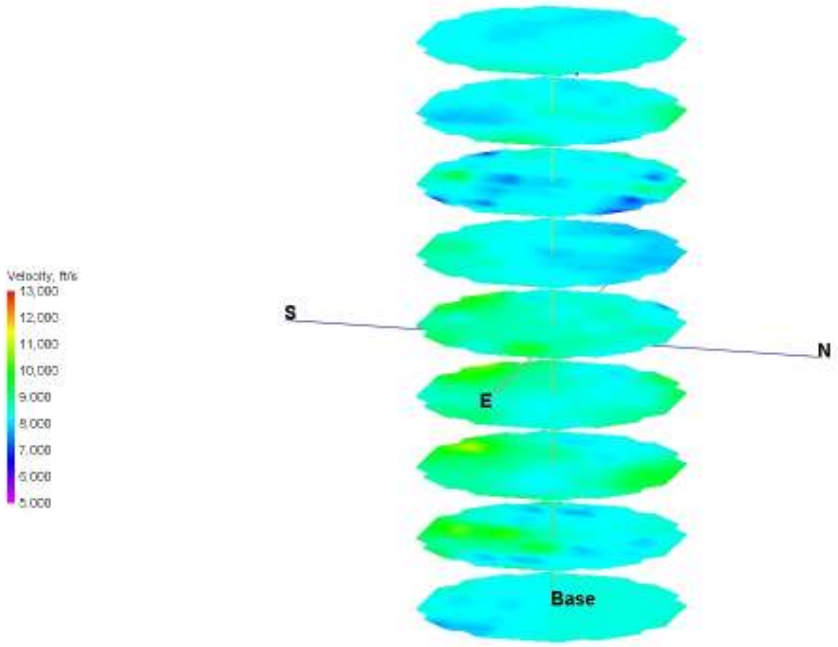

Figure 5.15: Experiment #2 Tomogram at 43.3 MPa of Load

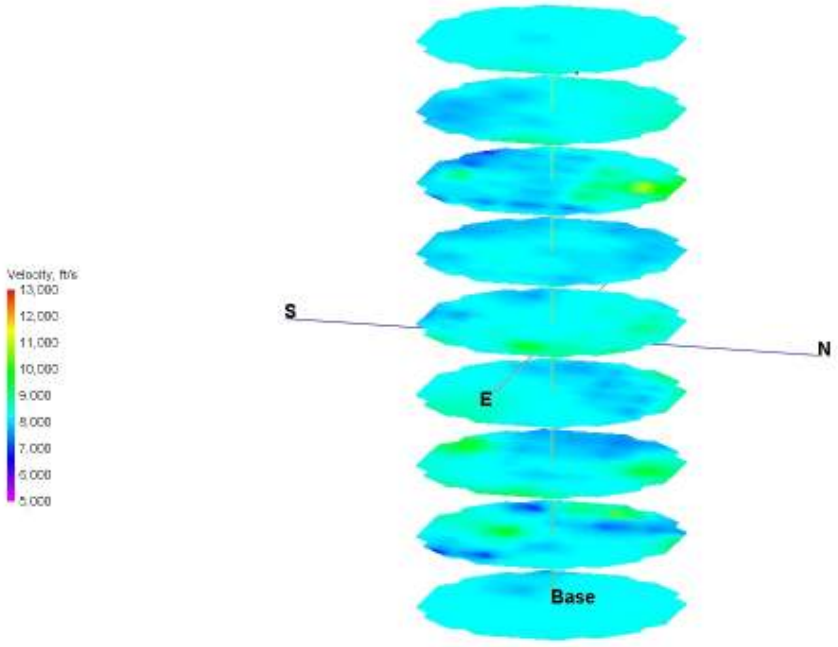

Figure 5.16: Experiment #2 Tomogram at 47.7 MPa of Load

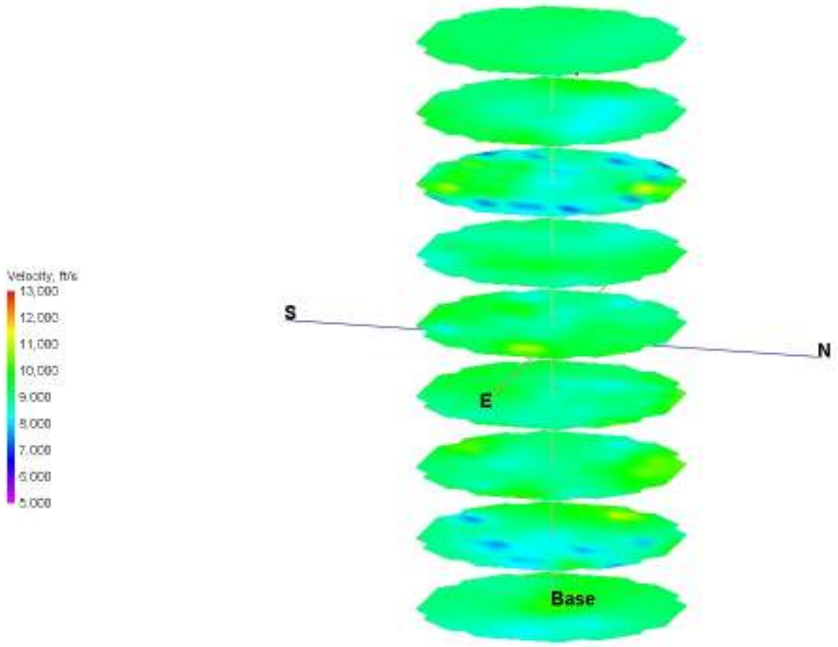

Figure 5.17: Experiment #2 Tomogram at 52.0 MPa of Load

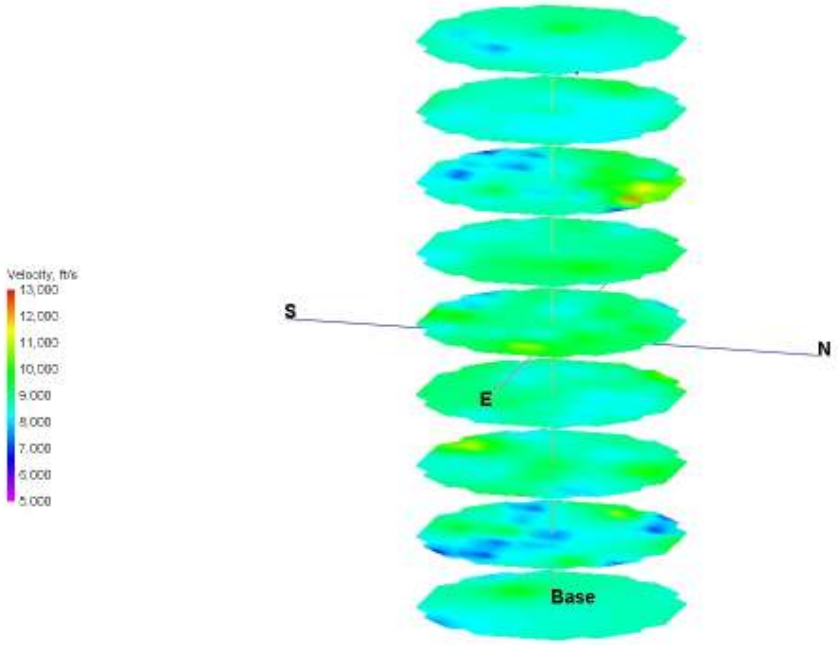

Figure 5.18: Experiment #2 Tomogram at 56.2 MPa of Load

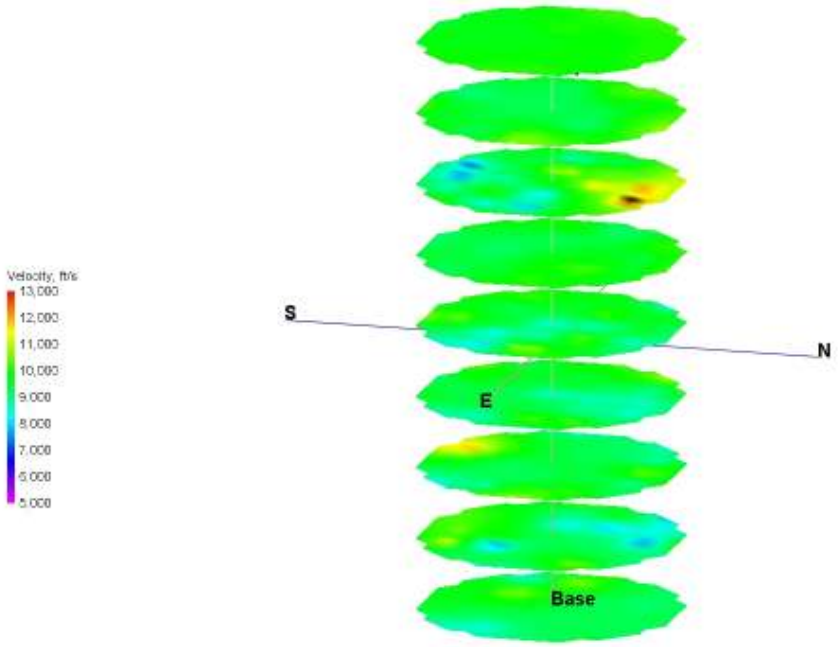

Figure 5.19: Experiment #2 Tomogram at 56.4 MPa of Load

Figure 5.20: Failed Berea Sandstone Sample from Experiment #2

Experiment #2 was chosen for discussion based on a few reasons. First, Experiment #2 provides data to generate tomograms for all load pauses conducted. This allows for the velocity distribution to be analyzed without any missing tomograms for load pauses that did not have sufficient sources. Secondly, Experiment #2 was chosen based on the travel-time versus distance plot. The correlation of the travel-time data for Experiment #2 was 80.6 %, while only having to remove 39 rays, of the 8140 rays calculated for Experiment #2. Appendix C contains the tomograms for all 19 experiments conducted.

The tomograms generated in this thesis show a reasonable progression of changing velocity distribution with increasing load. These progressions are seen usually in the tomograms prior to failure. For example, in the Experiment #2 tomograms Figures 5.2 through 5.11 show a gradual progression of the velocity distribution in the high velocity areas, but Figure 5.12 does not follow with this gradual progression. Figure 5.12 actually has an abrupt change back to nearly uniform velocity and then again shows a gradual progression through the remaining tomograms to failure.

From the analysis of the tomograms for Experiment #2, as well as the other experiments, it can be determined that the gradual progression of stress redistribution can be imaged within the sample using acoustic emission travel-time tomography. However, the results at this early stage do not provide significant support to determine when failure will occur in the Berea sandstone samples or for the determination of the plane of failure within the sample.

Determination of when failure will occur and the location of the failure plane cannot be extrapolated from the tomograms as is due to a few issues. First, past research done by Meglis, Chow, et. al (2005) shows that areas of increased velocity within a rock specimen are indicative of the presence of higher compressional stresses due to a denser rock structure, whereas areas of lower velocity are representative of areas of void space, cracks and the opening and propagation of cracks. From this it is known that areas of higher velocity are areas of higher stress, but the determination of the stress being experienced in these high velocity areas cannot be determined at this time. Second, the Hyperion Ultrasonic Acquisition system used for monitoring the acoustic emissions performs excellent for collecting the waveforms. However, the software used to calculate

the location of the acoustic emission sources was meant to be used in field studies and not the laboratory. Therefore, software specifically for the laboratory needs to be used to check the accuracy of the ESG software for locating in a laboratory environment.

Chapter 6: Conclusions & Recommendations

Acoustic emission velocity tomograms have been generated for 19 Berea sandstone samples subjected to unconfined compression strength testing. To attain the data for the tomograms, a commercial acquisition system produced by Engineering Seismology Group (ESG) Canada was used for the monitoring of the acoustic emissions, as well as using software provided with the system to locate the source of the acoustic emissions.

The generated tomograms provided a reasonable progression of changing p-wave velocity distribution with increasing load. However, the progression of the tomograms becomes more abrupt as opposed to gradual when the sample reaches higher load applications. The results attained at this early stage do not provide significant support to determine when failure will occur in the Berea sandstone samples or for the determination of the plane of failure within the sample. This is due primarily to the inability to relate the actual stress occurring within the sample to the p-wave velocity. Also the Hyperion Ultrasonic System, produced by ESG, proves to be an excellent data acquisition system for monitoring and recording the acoustic emission events, but the Hyperion Software Suite that is included with the system does not provide necessary accuracy for locating the acoustic emission events in a laboratory environment. The inefficiency of the system is due to the system being meant for field work as opposed to a laboratory environment.

Further research resulting from the study of acoustic emission activity within Berea sandstone presented in this thesis can be primarily concentrated in improving the tomograms. The Hyperion Ultrasonic Acquisition System appears to be capable of sufficiently monitoring and recording the acoustic emission events, however the Hyperion Suite that is included with the system is not sufficient for a laboratory environment. The Hyperion Suite software can locate acoustic emission sources to an accuracy of 3.048 mm (0.01 feet), whereas an accuracy of 1 mm (0.003 ft) is needed in the laboratory. The accuracy of the p-wave arrival-time picks is the most important step in the process to locating the acoustic emission sources and to generating a tomogram. Therefore, the Hyperion Suite software, which also utilizes a p-wave arrival time picker,

should be tested against other p-wave arrival-time picker software that is available to determine the picker programs accuracy and efficiency.

Besides the primary areas just mentioned, there are also other areas of further research that could be very beneficial to the development of acoustic emission tomography. The first area is performing more experiments not only on Berea sandstone, but on other rock types. The purpose in pursuing this type of research would be to determine the tomogram behavior in different rock types. The tomogram behavior from different rock types can then be used to determine if there is a similarity in the tomogram behavior between the different rock types. Also, performing laboratory tests with a pre-cut failure plane within the specimen would be highly beneficial to determine the accuracy of the acquisition system and also to gain a better understanding of the behavior expected in tomograms around an area of failure. Lastly, research could be performed to upgrade the acquisition system to provide tomograms as the specimen is being tested to aid in the ultimate goal of this research, which is to predict rock failure.

In closing, acoustic emission tomography has shown the capability of being able to monitor the p-wave velocity distribution within samples of Berea sandstone. At this time, this method of tomography was not capable to be used for failure prediction or for determining the plane of failure within the Berea sandstone samples. Acoustic emission tomography does show promise to being a valuable tool for monitoring rock failure due to the ability to noninvasively monitor a rock at a local point, while still being able to draw conclusions about the entire rock structure.

References

Bieniawski, Z. T. (1989). *Engineering rock mass classifications: a complete manual for engineers and geologists in mining, civil, and petroleum engineering*. New York, John Wiley & Sons, Inc.

Carlson RL, Gangi AF (1985) "Effect of cracks on the pressure dependence of P wave velocities in crystalline rocks". *Journal of Geophysical Research* 90:8675-8684

Choudhury, P. B., A. K. Raina, et al. (2004). "Crown pillar stability assessment in an underground copper mine using acoustic emission." *International Journal of Rock Mechanics and Mining Sciences* 41(3): 399-400.

Clarke, C. R. (2006). "Monitoring Long-Term Subgrade Moisture Changes with Electrical Resistivity Tomography." *Unsaturated Soils 2006*, Carefree, Arizona, USA, ASCE.

Deere, D. U., A. J. Hendron, et al. (1967). "Design of Surface and Near Surface Construction in Rock." *Proc. 8th U.S. Symposium on Rock Mechanics*. New York, AIME**:** 237-302.

Dowling, N. E. (2007). *Mechanical Behavior of Materials*. Upper Saddle River, Pearson Prentice Hall.

ESG (2006). *Hyperion Software User's Guide - Ver. 11.0*. Kingston.

Farmer, I. (1983). *Engineering Behavior of Rocks*. New York, Chapman and Hall.

Goodman, R. E. (1980). *Introduction to Rock Mechanics*. New York, John Wiley & Sons.

Gopalakrishnan, K., H. Ceylan, et al. (2006). "Characterization of Asphalt Materials Using X-ray High-Resolution Computed Tomography Imaging Techniques." *Airfield and Highway Pavements 2006*, Atlanta, Georgia, USA, ASCE.

H. Reginald Hardy, J. (1977). "Emergence of Acoustic Emission/Microseismic Activity as a tool in Geomechanics." *Acoustic Emission/Microseimic Activity in Geologic Structures and Materials*. Pennsylvania State University, Trans Tech S.A.

H. Reginald Hardy, J. (2003). *Acoustic Emission/Microseismic Activity*. The Netherlands, A.A. Balkema Publishers.

Hardy HR, Kim YS (1971). Monitoring crack closure in geologic materials using ultrasonic techniques. In: Rock fracture. Proc. Int. Symp. Rock Mech., Nancy, pp Paper I-3 (17pp)

Hartman, H. L. and J. M. Mutmansky (2002). *Introductory Mining Engineering*. Hoboken, John Wiley & Sons, Inc.

Heeraman, D. A., J. W. Hopmans, et al. (1997). "Three-dimensional imaging of plant roots in situ with X-ray computed tomography." *Plant Soil* 189: 167-179.

Herget, G. (1988). *Stresses in Rock*. Brookfield, A.A. Balkema Publishers.

Hiltunen, D. R., G.-C. Cho, et al. (2004). "Investigation of a Bridge Foundation Site in Karst Terrane via Seismic Crosshole Tomography." *GeoTrans 2004*, Los Angeles, California, USA, ASCE.

Hoek, E. (2007). "Practical Rock Engineering." Roscience.

Hounsfield, G. N. (1973). "Computerized transverse axial scanning (tomography). Part 1: Description of System." *British Journal of Radiology* 46: 1016-22.

Jackson, M. J. and D. R. Tweeton (1994). "Migratom - Geophysical Tomography Using Wavefront Migration and Fuzzy Constraints: Report of Investigations 9497." United States Department of the Interior: Bureau of Mines.

Jaeger, J. C. (1979). *Fundamentals of Rock Mechanics*. London, Chapman and Hall Ltd.

Jing, L. and J. A. Hudson (2002). "Numerical methods in rock mechanics." *International Journal of Rock Mechanics and Mining Sciences* 39(4): 409-427.

Jones C, Murrell SAF (1989) “Acoustic compressional wave velocity and dilatancy in triaxially stressed rocks”. In: *Maury V, Fourmaintraux D (eds) Rock at great depth*. A. A. Balkema, Rotterdam, 1, pp 241-247

Jumikis, A. R. (1983). *Rock Mechanics*. Rockport, Trans Tech Publications.

Ku, C.-Y., J.-S. Lin, et al. (2004). "Modeling of jointed rock masses using a combined equivalentcontinuum and discrete approach." *International Journal of Rock Mechanics and Mining Sciences* 41(Supplement 1): 402-407.

Lontoc-Roy, M., P. Dutilleul, et al. (2006). "Advances in the acquisition and analysis of CT scan data to isolate a crop root system from the soil medium and quantify root system complexity in 3-D space." *Geoderma* 137(1-2): 231-241.

Markoe, A. (2006). *Analytic Tomography*. Cambridge, Cambridge University Press.

Masad, E., V. K. Jandhyala, et al. (2002). "Characterization of Air Void Distribution in Asphalt Mixes using X-ray Computed Tomography." *Journal of Materials in Civil Engineering* 14(2): 122-129.

Meglis, I. L., T. Chow, et al. (2005). "Assessing in situ microcrack damage using ultrasonic velocity tomography." *International Journal of Rock Mechanics and Mining Sciences* 42(1): 25-34.

MSHA. (2006). "Mining Industry Accident, Injuries, Employment, and Production Statistics." Retrieved March 19, 2007, from www.msha.gov.

NMA. (2006). "Facts about Coal." Retrieved March 19, 2007, from www.nma.org.

Nur A, Simmons G (1969) Stress-induced velocity anisotropy in rock: an experimental study. Journal of Geophysical Research 74:6667-6674

Ott, R. L. and M. Longnecker (2001). *An Introduction to Statistical Methods and Data Analysis*. Pacific Grove, Duxbury.

Parry, R. H. G. (2004). *Mohr Circles, Stress Paths and Geotechnics*. New York, Spon Press.

Paterson, M. S. and T.-f. Wong (2005). *Experimental Rock Deformation - The Brittle Field*. Netherlands, Springer-Verlag Berlin Heidelberg.

Pierret, A., Y. Capowiez, et al. (1999). "X-ray computed tomography to quantify tree rooting spatial distributions." *Geoderma* 90: 307-326.

Riefenberg, J. (1988). "A Simplex Method-Based algorithm for source location of microseismic events associated with underground mining." *Rock Mechanics as a Guide for Efficient Utilization of Natural Resources*. West Virginia University, A.A. Balkema.

Vasco, D. W., J. J. E. Peterson, et al. (1995). "Beyond ray tomography: Wavepaths and Fresnel volumes." *Geophysics* 60(6): 1790-1804.

Westman, E. C. (2004). "Use of Tomography for Inference of Stress Redistribution in Rock." *IEEE Transactions on Industry Applications* 40(5): 1413-1417.

Zhang, L. (2005). *Engineering Properties of Rocks*. San Diego, Elsevier Inc.

Appendix A: Arrival-Time & Travel-Time Plots

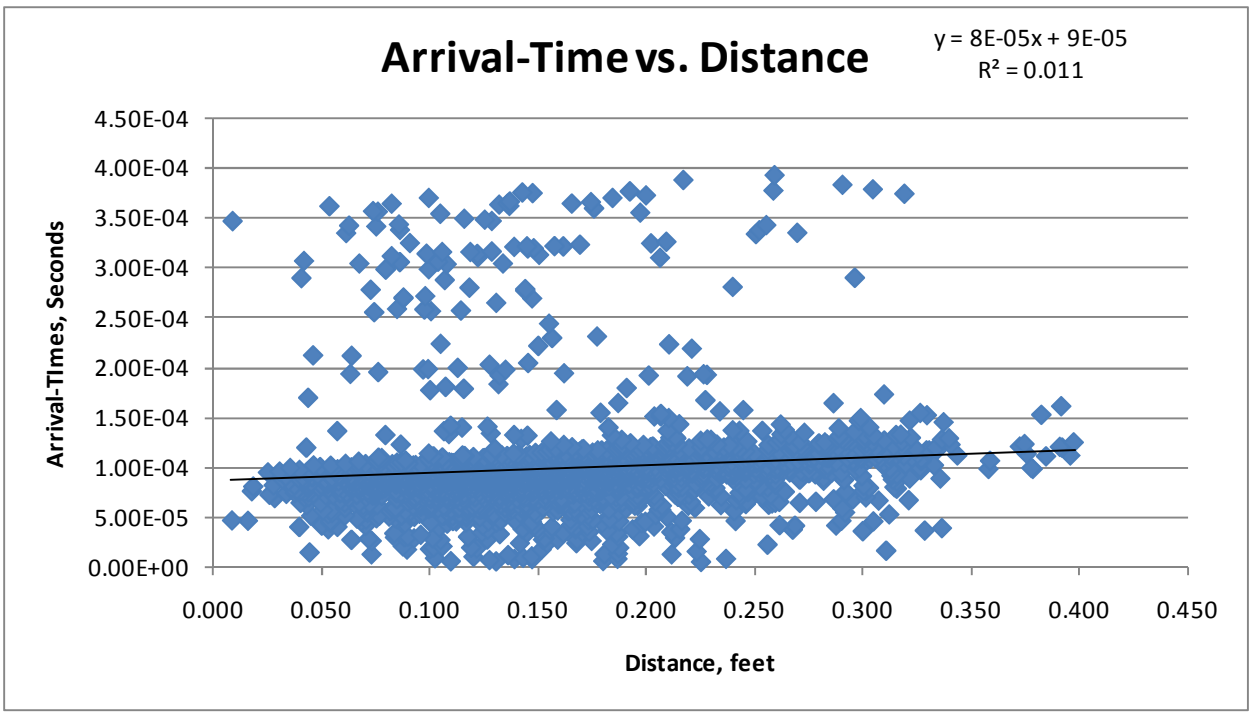

Figure A.1: Experiment #1 Arrival-Time Versus Distance Plot

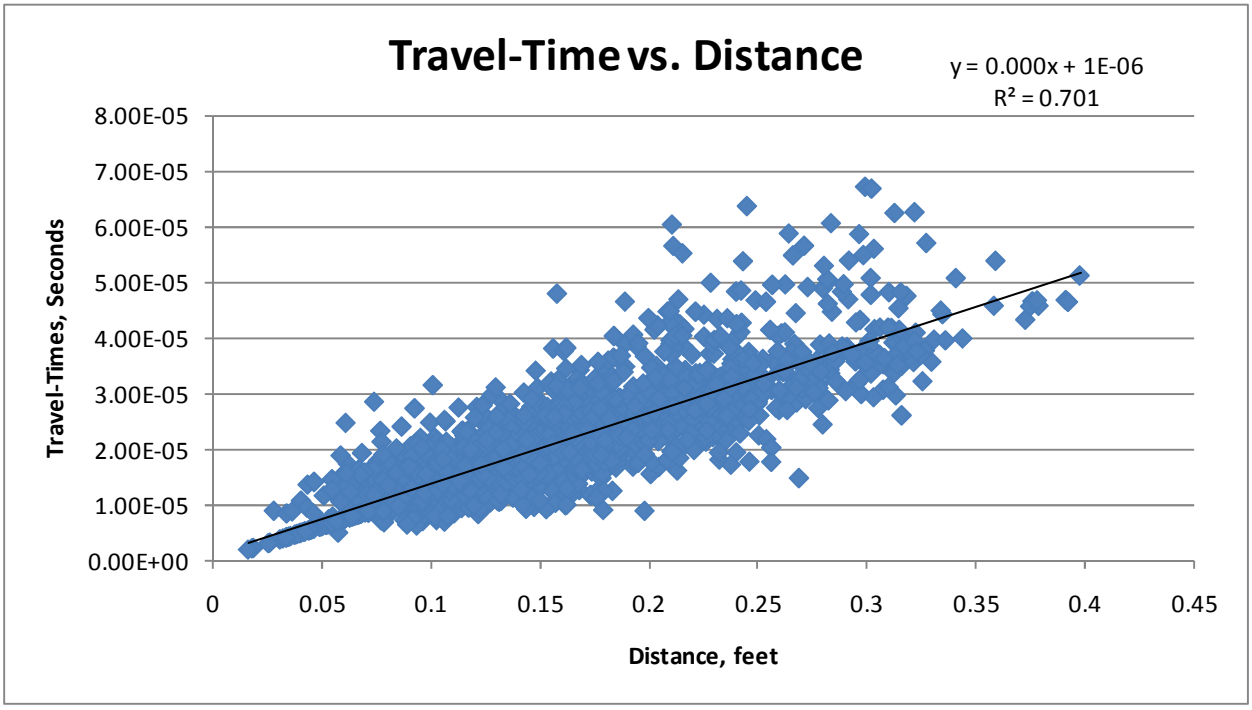

Figure A.2: Experiment #1 Travel-Time Versus Distance Plot

Table A.1: Data Reconciliation Summary Statistics for Experiment #1

Experiment #1	
Arrival-Time R^2	1.10%
Number of Arrival-Time Rays	2757
Travel-Time R^2	70.10%
Number of Travel-Time Rays	2047
Number of Rays Eliminated	710

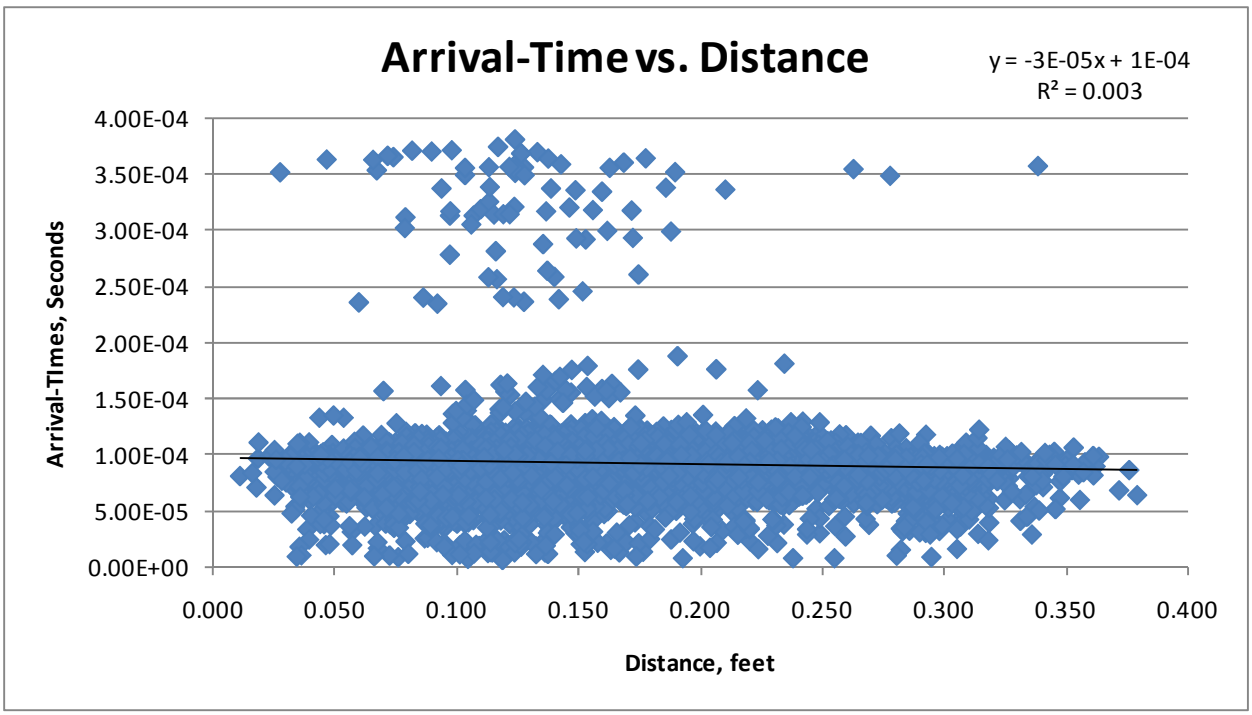

Figure A.3: Experiment #2 Arrival-Time Versus Distance Plot

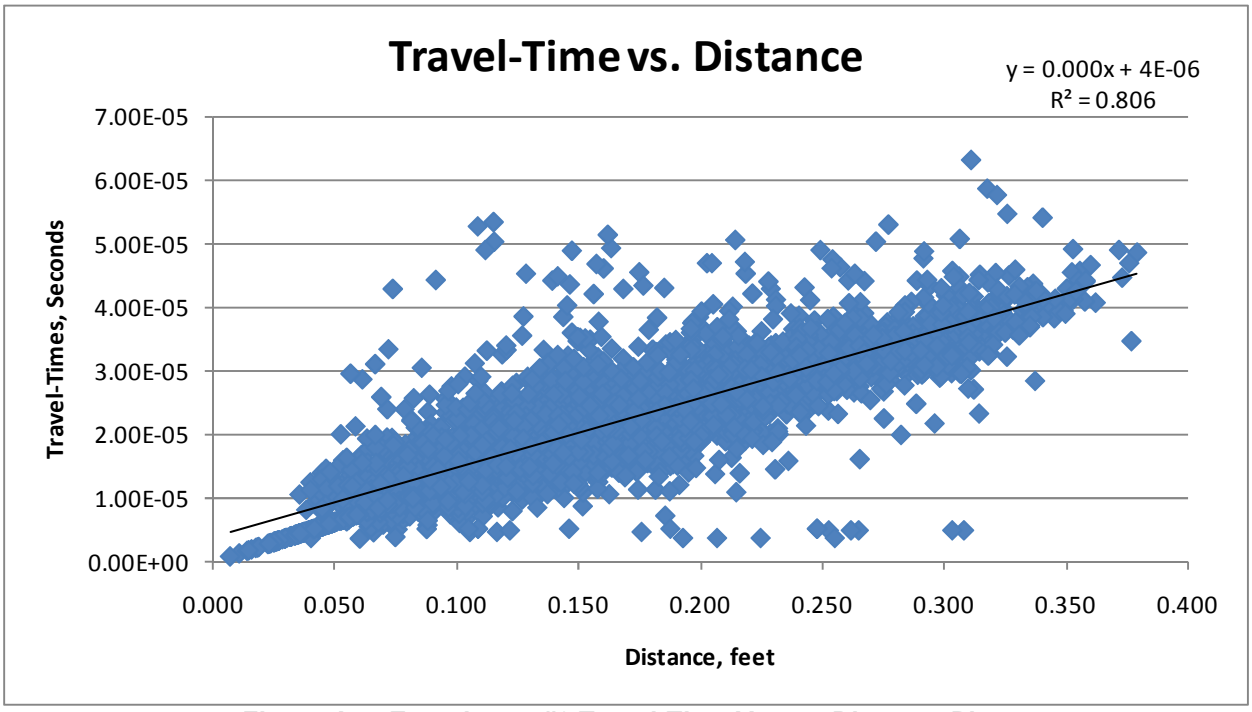

Figure A.4: Experiment #2 Travel-Time Versus Distance Plot

Table A.2: Data Reconciliation Summary Statistics for Experiment #2

Experiment #2	
Arrival-Time R^2	4.70%
Number of Arrival-Time Rays	8142
Travel-Time R^2	80.60%
Number of Travel-Time Rays	8101
Number of Rays Eliminated	41

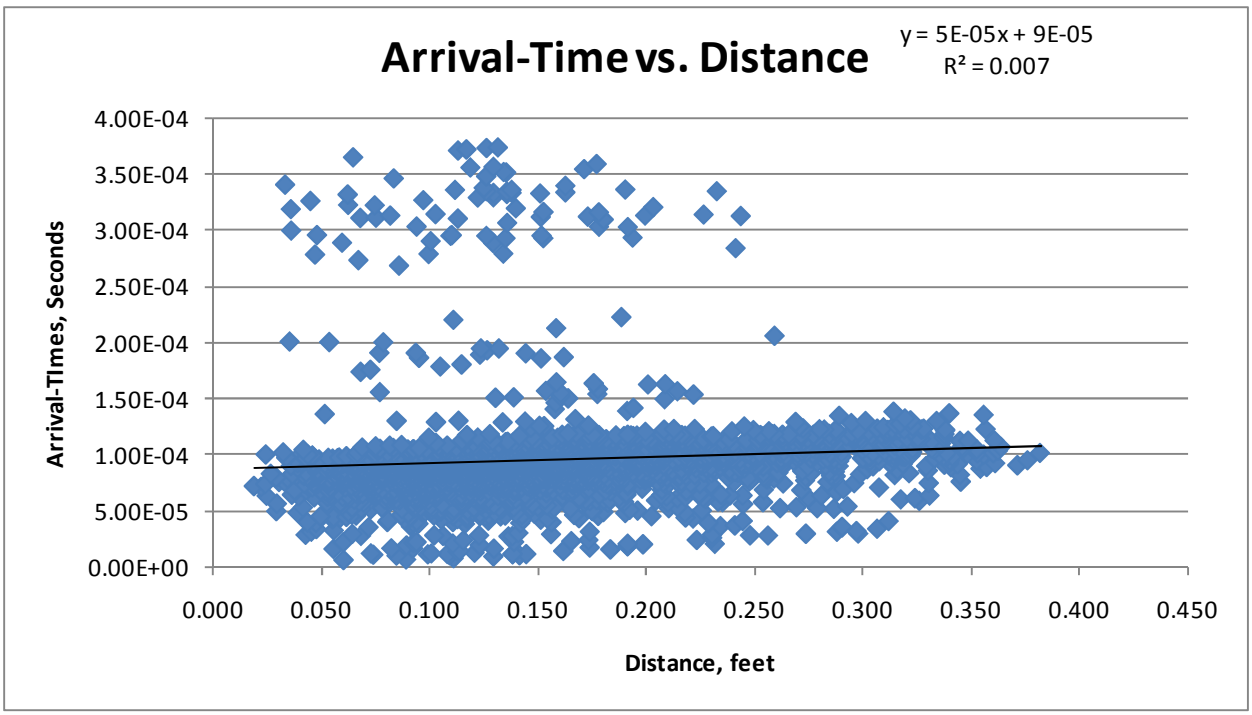

Figure A.5: Experiment #3 Arrival-Time Versus Distance Plot

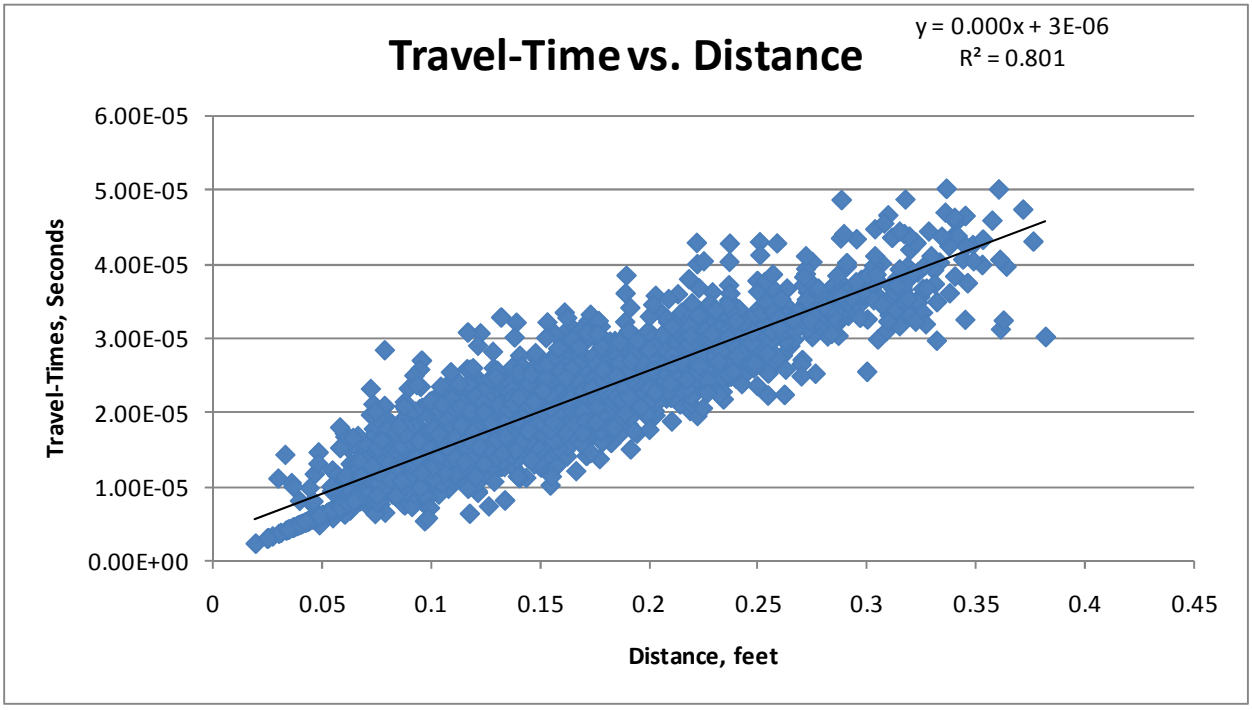

Figure A.6: Experiment #3 Travel-Time Versus Distance Plot

Table A.3: Data Reconciliation Summary Statistics for Experiment #3

Experiment #3	
Arrival-Time R^2	0.70%
Number of Arrival-Time Rays	2903
Travel-Time R^2	80.10%
Number of Travel-Time Rays	2624
Number of Rays Eliminated	279

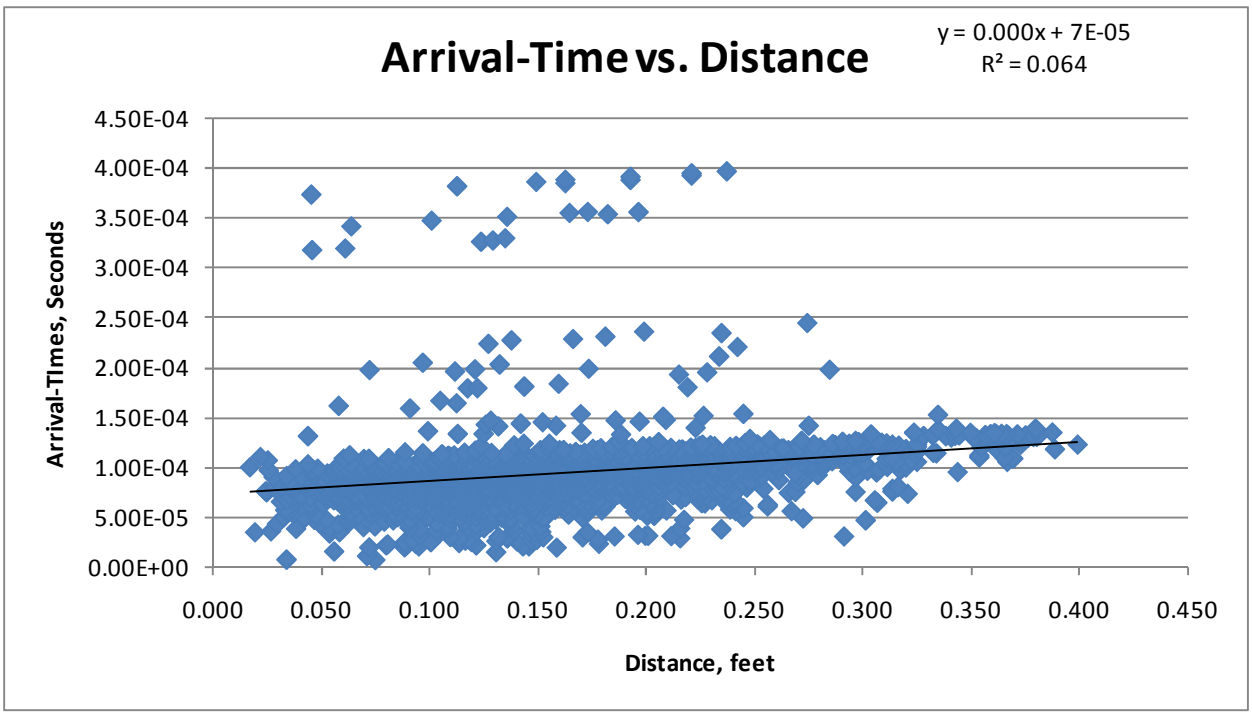

Figure A.7: Experiment #4 Arrival-Time Versus Distance Plot

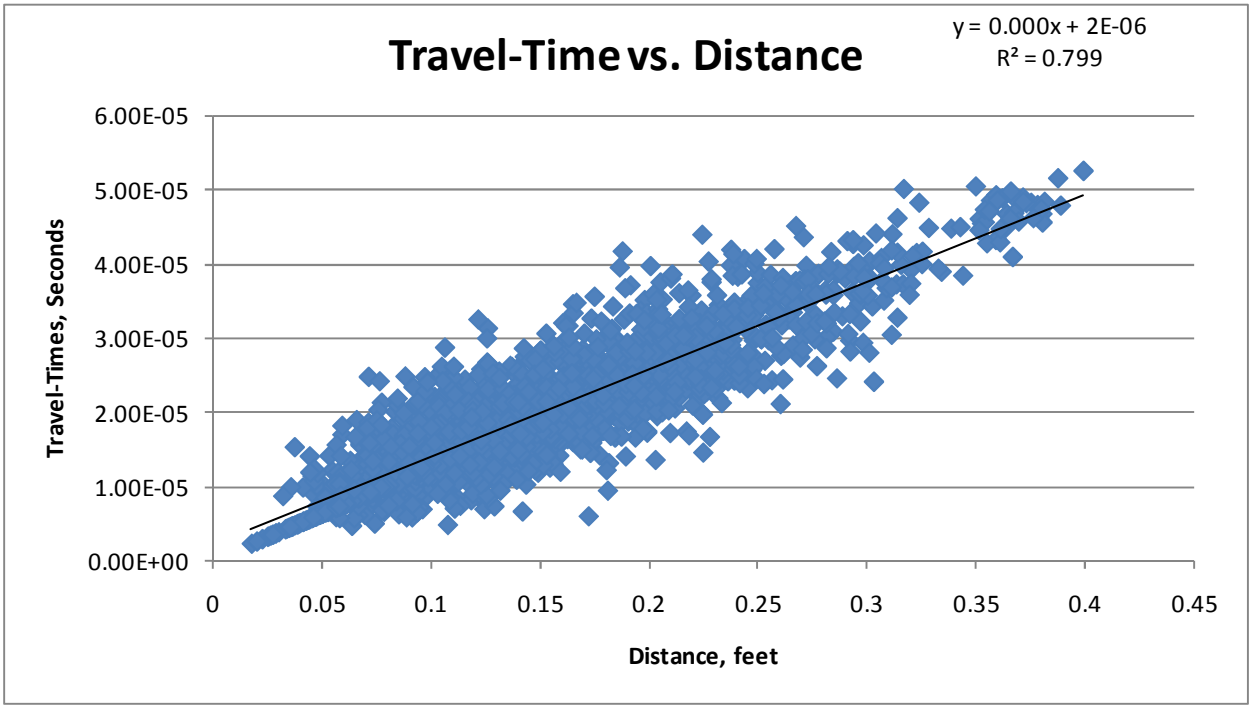

Figure A.8: Experiment #4 Travel-Time Versus Distance Plot

Table A.4: Data Reconciliation Summary Statistics for Experiment #4

Experiment #4	
Arrival-Time R^2	6.40%
Number of Arrival-Time Rays	2713
Travel-Time R^2	79.90%
Number of Travel-Time Rays	2521
Number of Rays Eliminated	192

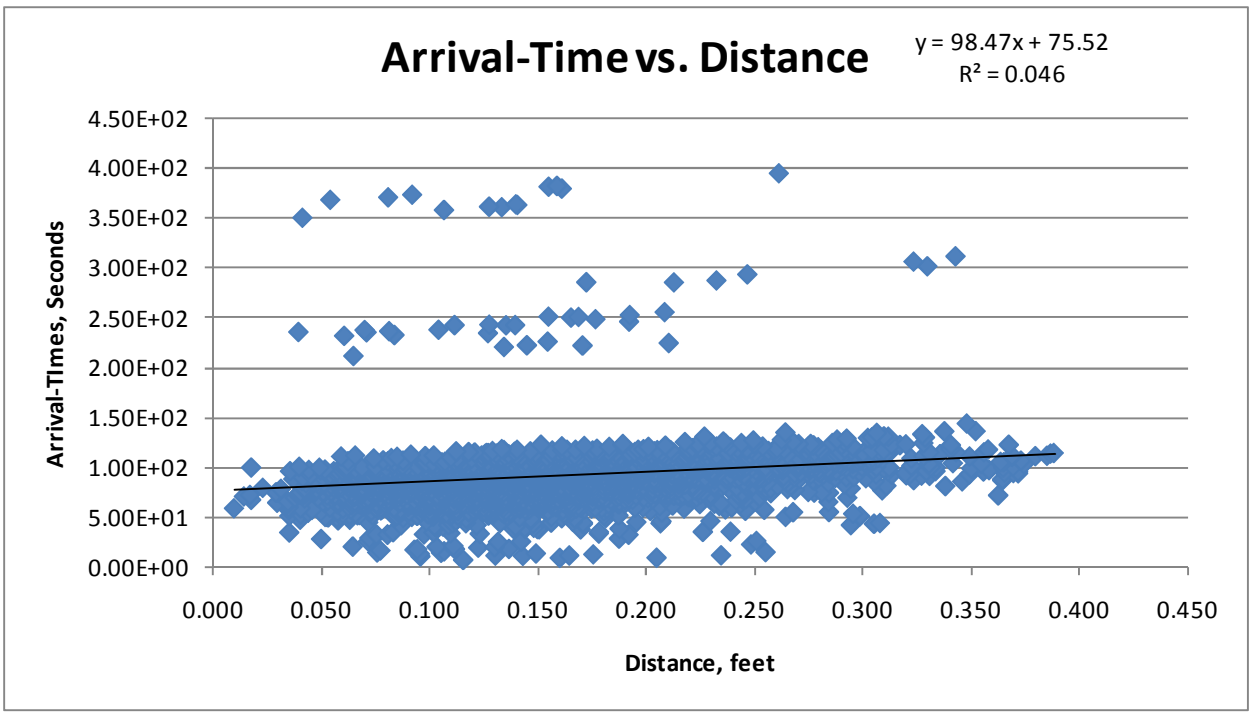

Figure A.9: Experiment #5 Arrival-Time Versus Distance Plot

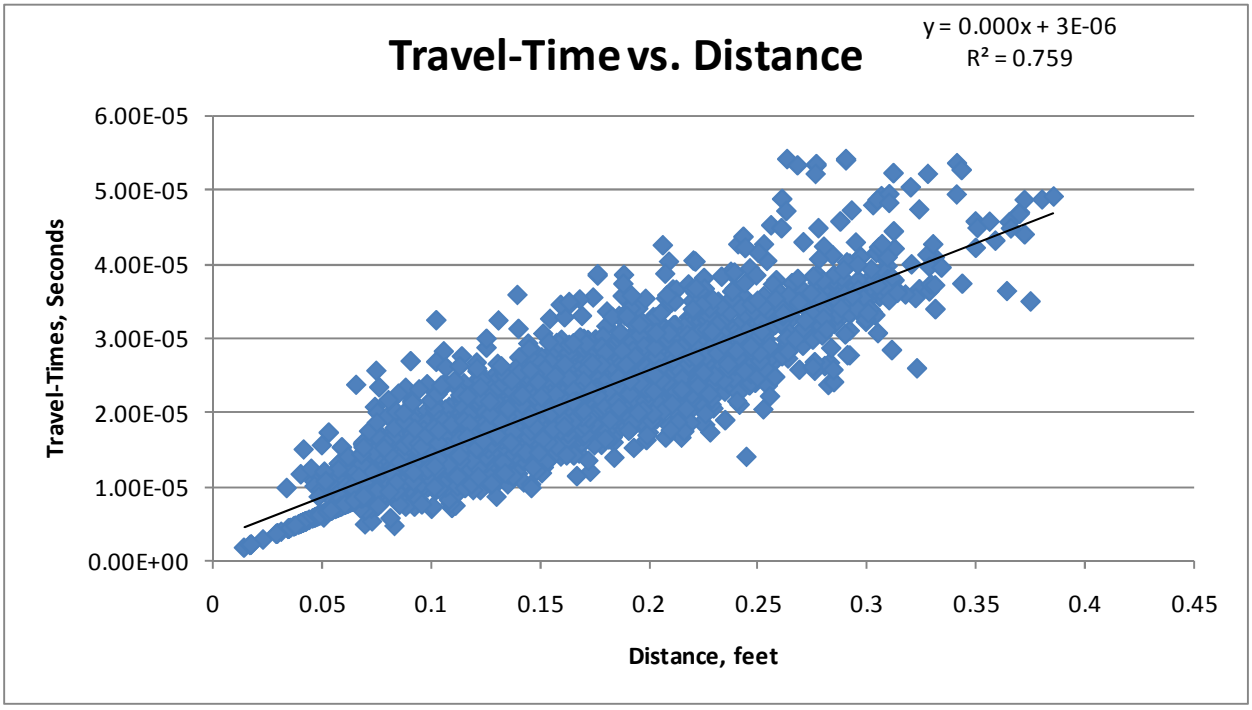

Figure A.10: Experiment #5 Travel-Time Versus Distance Plot

Table A.5: Data Reconciliation Summary Statistics for Experiment #5

Experiment #5	
Arrival-Time R^2	4.60%
Number of Arrival-Time Rays	3160
Travel-Time R^2	75.90%
Number of Travel-Time Rays	2919
Number of Rays Eliminated	241

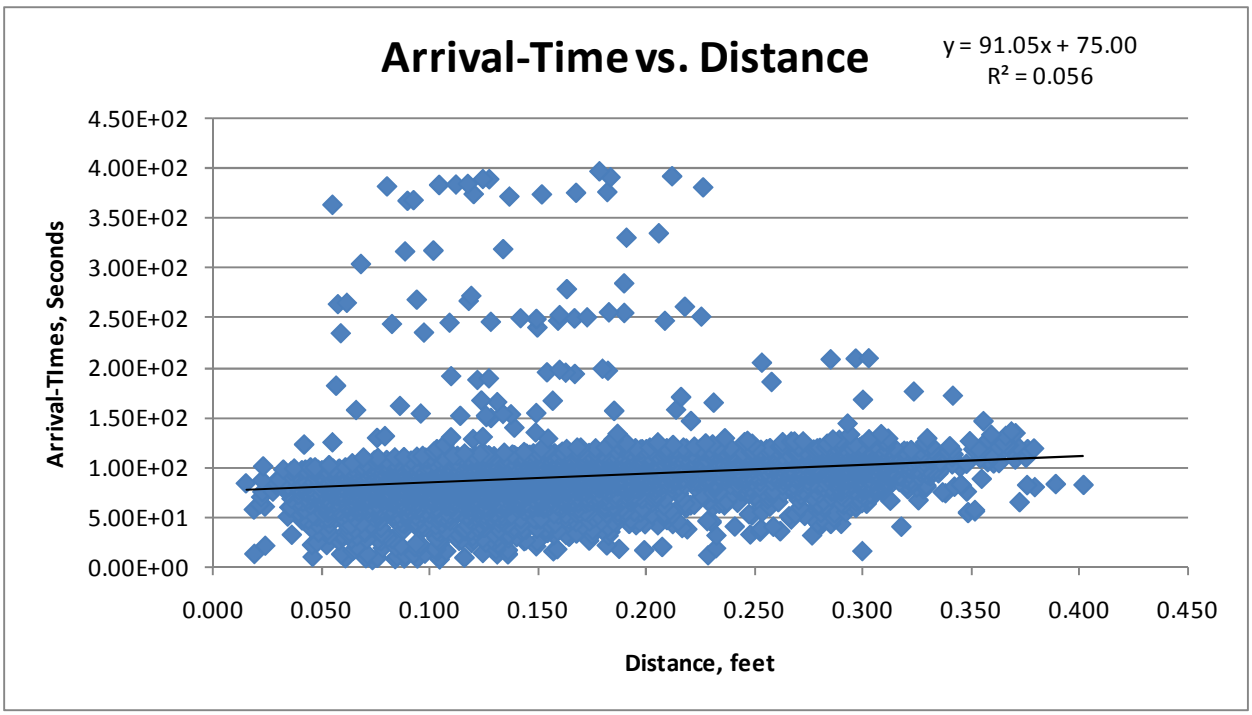

Figure A.11: Experiment #6 Arrival-Time Versus Distance Plot

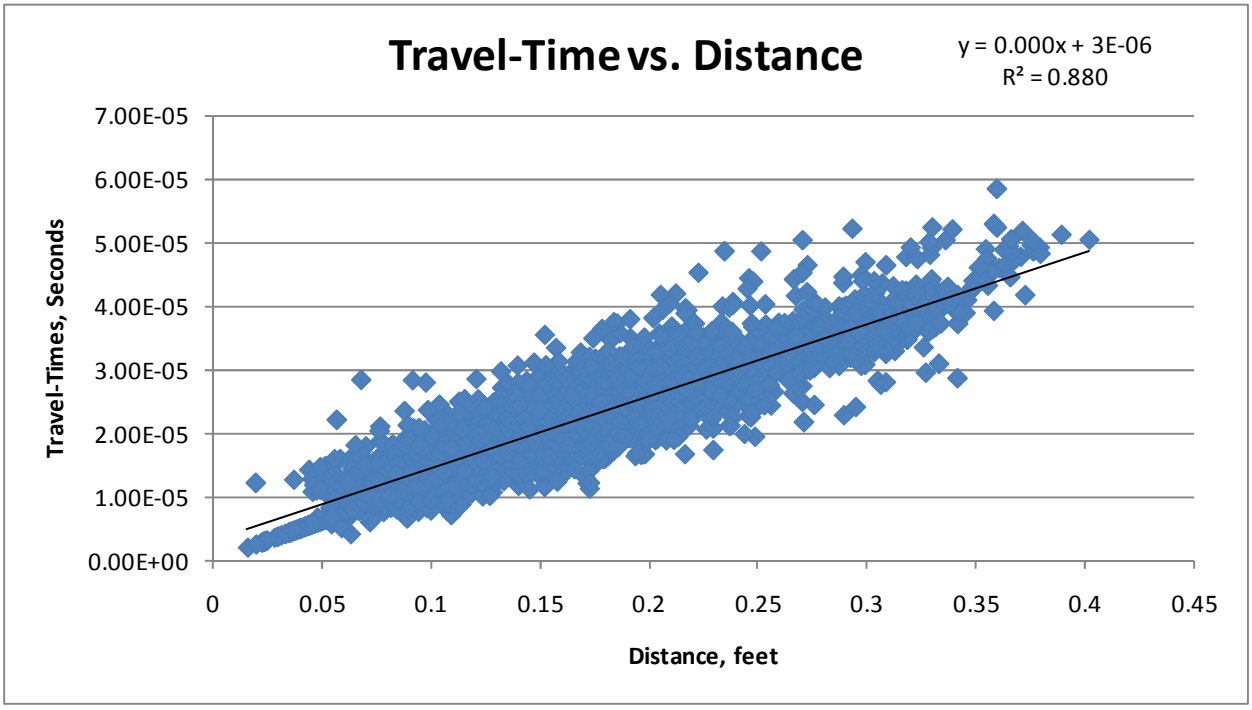

Figure A.12: Experiment #6 Travel-Time Versus Distance Plot

Table A.6: Data Reconciliation Summary Statistics for Experiment #6

Experiment #6	
Arrival-Time R^2	5.60%
Number of Arrival-Time Rays	5526
Travel-Time R^2	88.00%
Number of Travel-Time Rays	5309
Number of Rays Eliminated	217

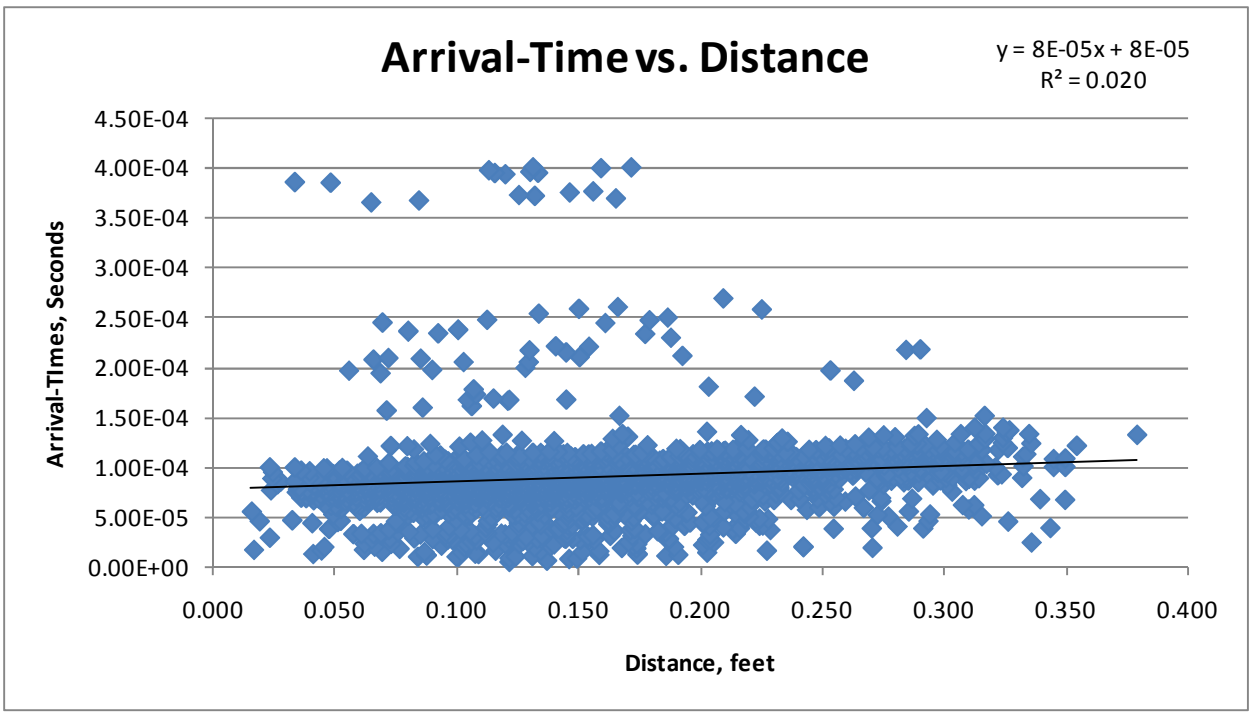

Figure A.13: Experiment #7 Arrival-Time Versus Distance Plot

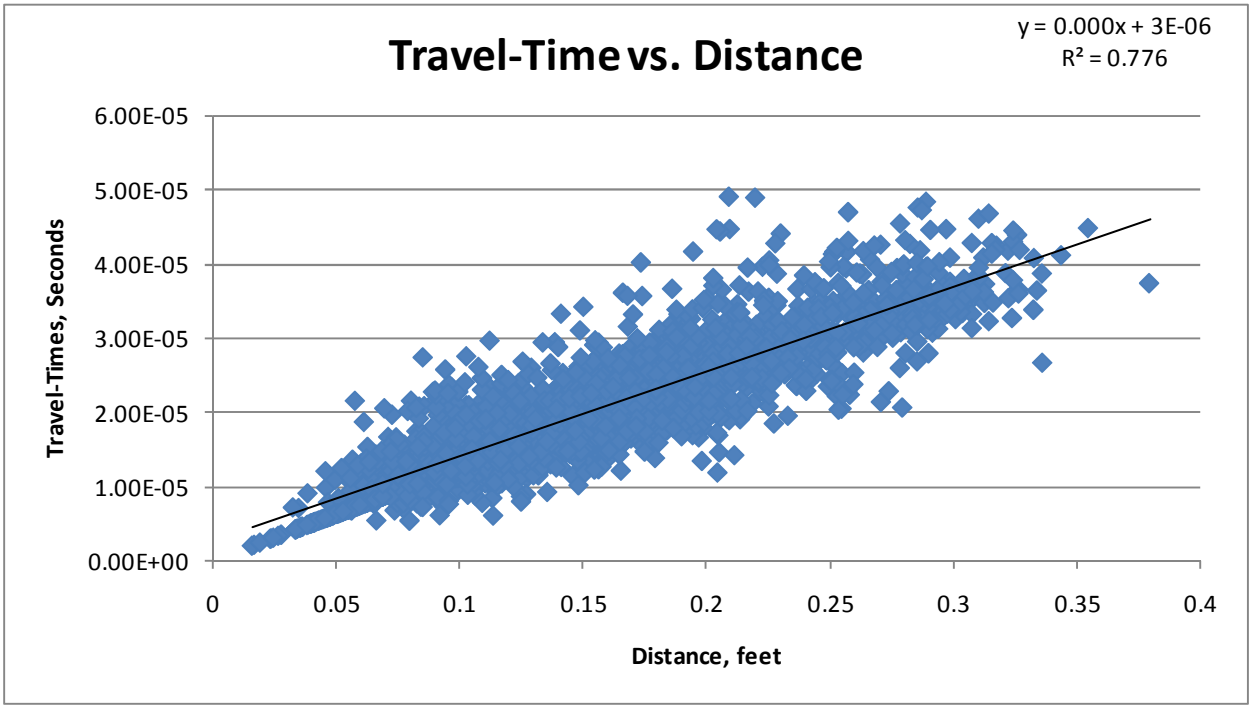

Figure A.14: Experiment #7 Travel-Time Versus Distance Plot

Table A.7: Data Reconciliation Summary Statistics for Experiment #7

Experiment #7	
Arrival-Time R^2	2.00%
Number of Arrival-Time Rays	2847
Travel-Time R^2	77.60%
Number of Travel-Time Rays	2684
Number of Rays Eliminated	163

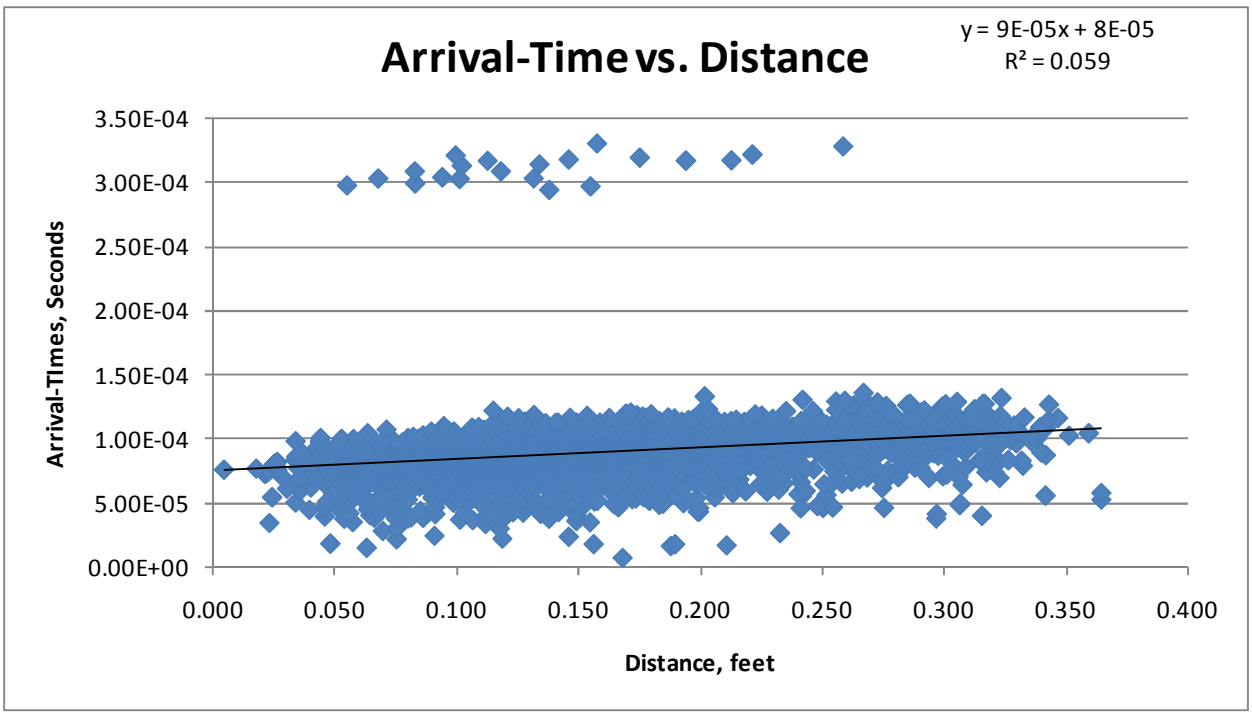

Figure A.15: Experiment #8 Arrival-Time Versus Distance Plot

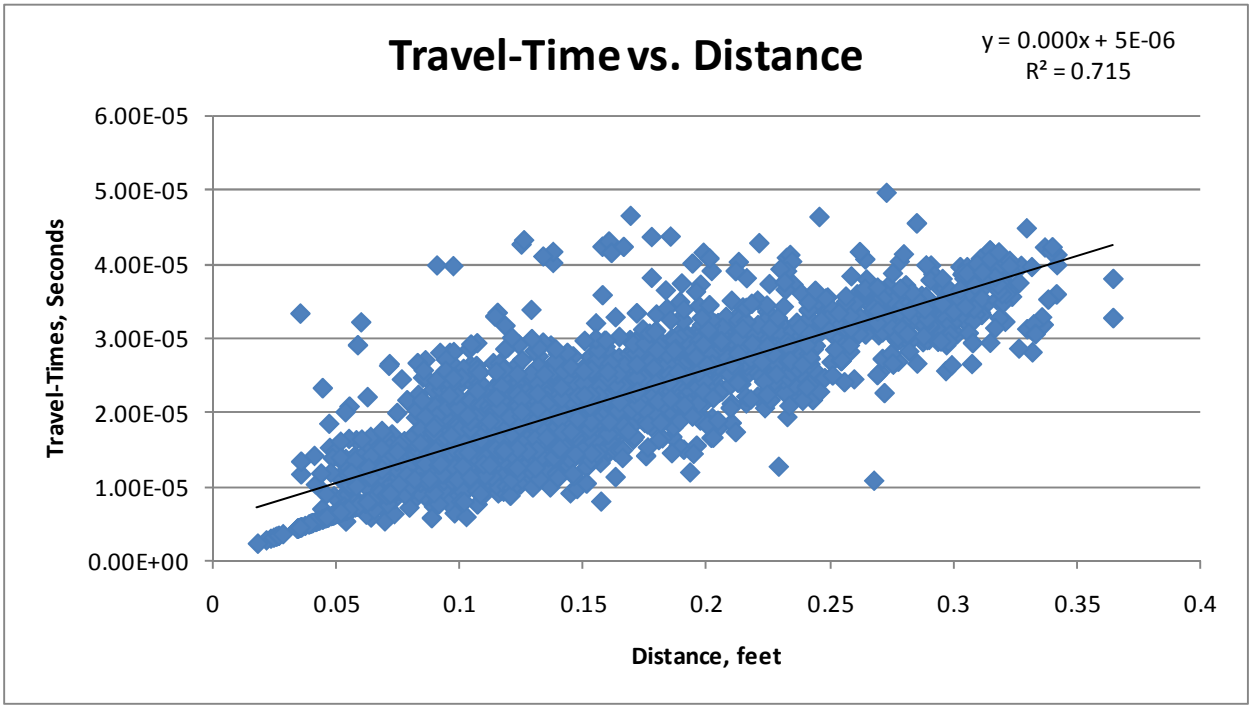

Figure A.16: Experiment #8 Travel-Time Versus Distance Plot

Table A.8: Data Reconciliation Summary Statistics for Experiment #8

Experiment #8	
Arrival-Time R^2	5.90%
Number of Arrival-Time Rays	3097
Travel-Time R^2	71.50%
Number of Travel-Time Rays	2885
Number of Rays Eliminated	212

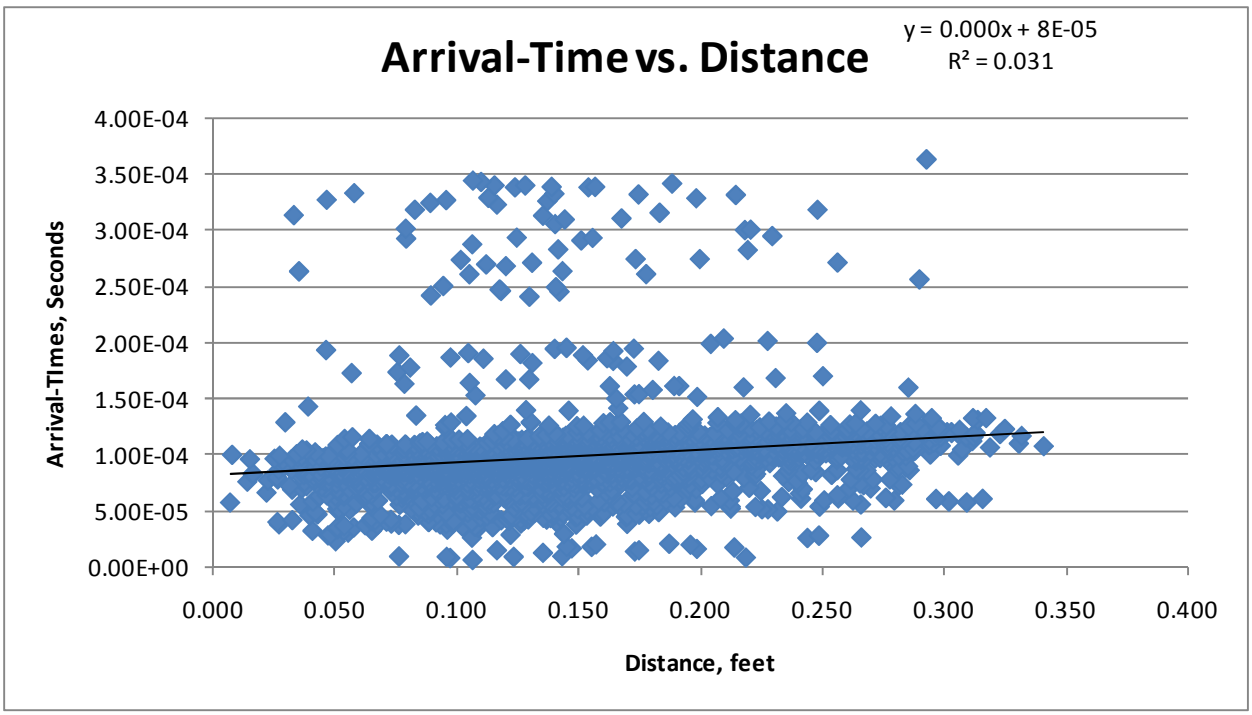

Figure A.17: Experiment #9 Arrival-Time Versus Distance Plot

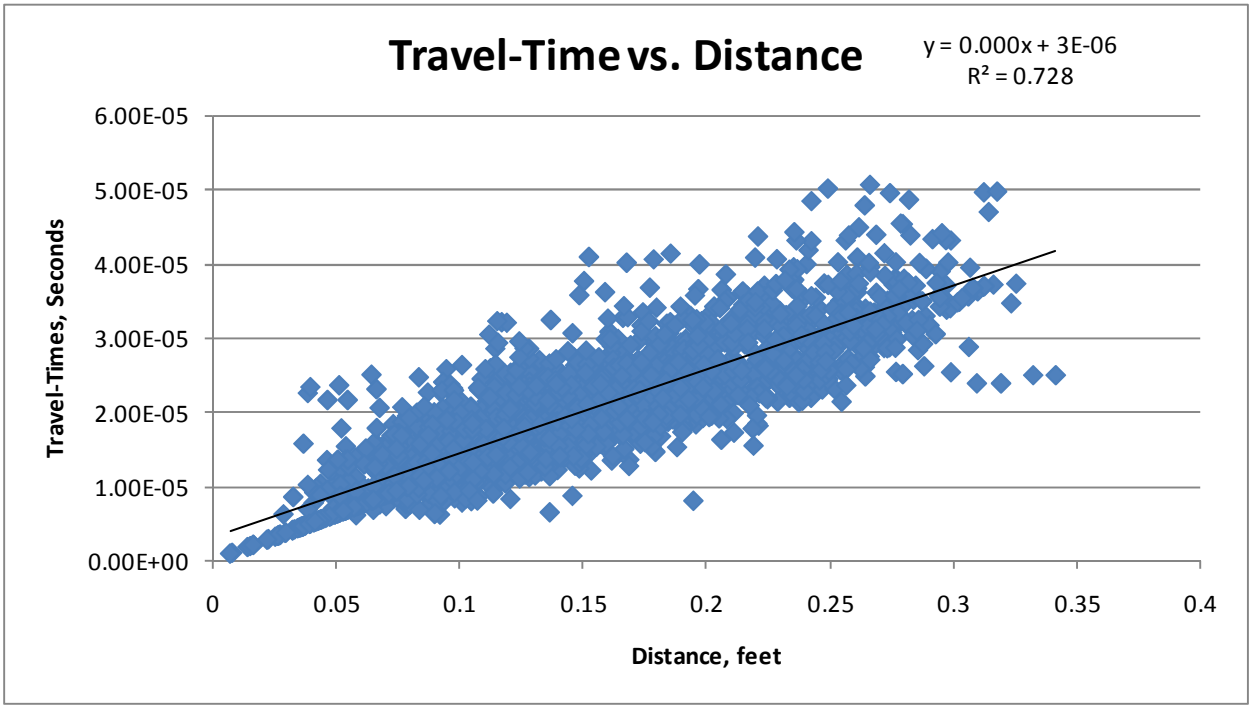

Figure A.18: Experiment #9 Travel-Time Versus Distance Plot

Table A.9: Data Reconciliation Summary Statistics for Experiment #9

Experiment #9	
Arrival-Time R^2	3.10%
Number of Arrival-Time Rays	2883
Travel-Time R^2	72.80%
Number of Travel-Time Rays	2754
Number of Rays Eliminated	129

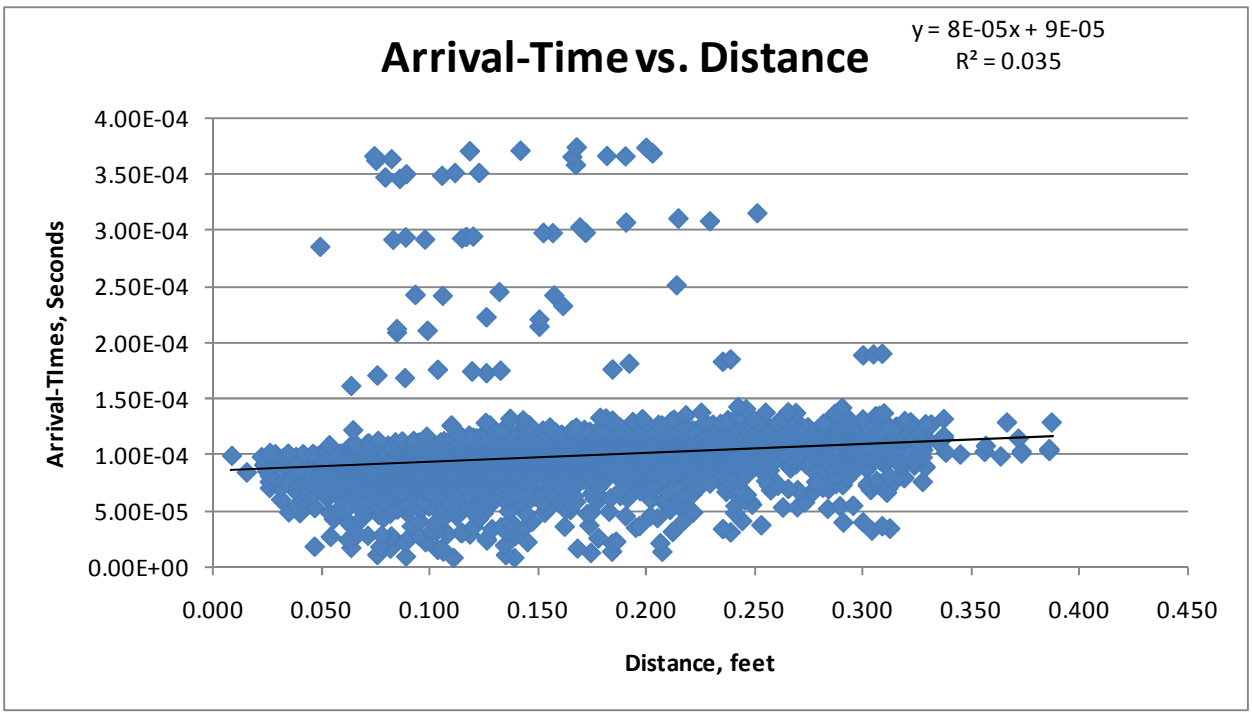

Figure A.19: Experiment #10 Arrival-Time Versus Distance Plot

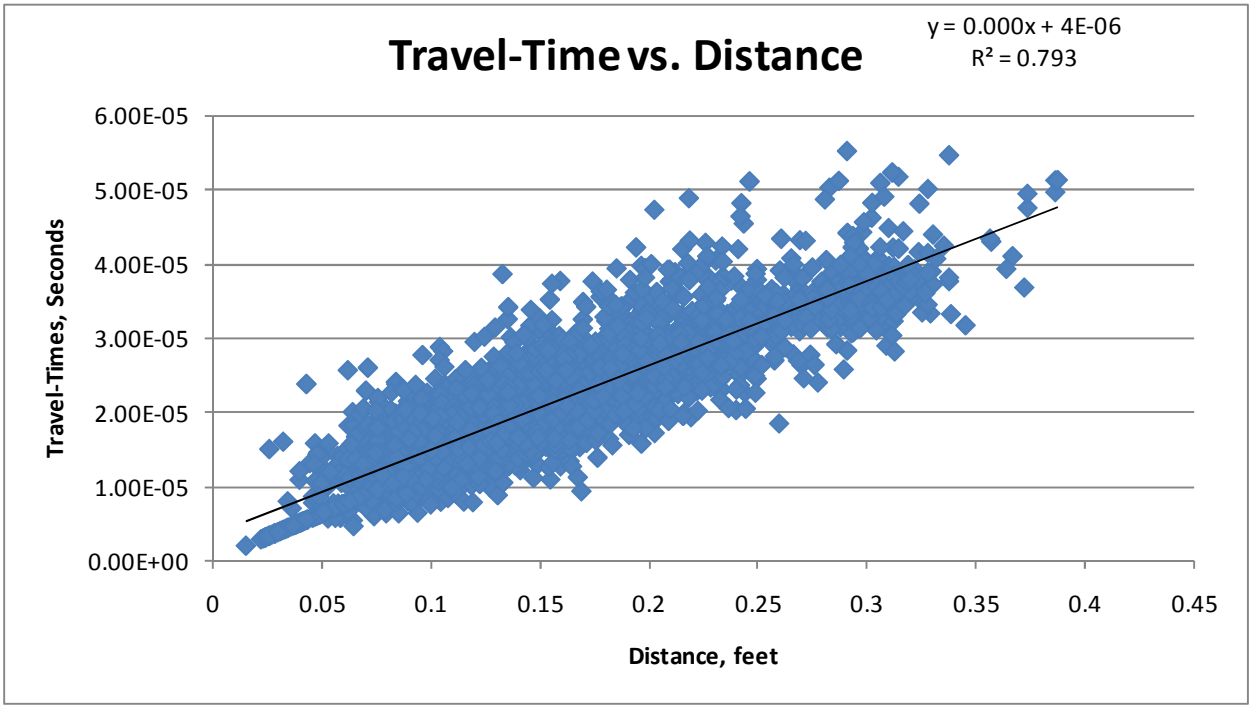

Figure A.20: Experiment #10 Travel-Time Versus Distance Plot

Table A.10: Data Reconciliation Summary Statistics for Experiment #10

Experiment #10	
Arrival-Time R^2	3.50%
Number of Arrival-Time Rays	3811
Travel-Time R^2	79.30%
Number of Travel-Time Rays	3565
Number of Rays Eliminated	246

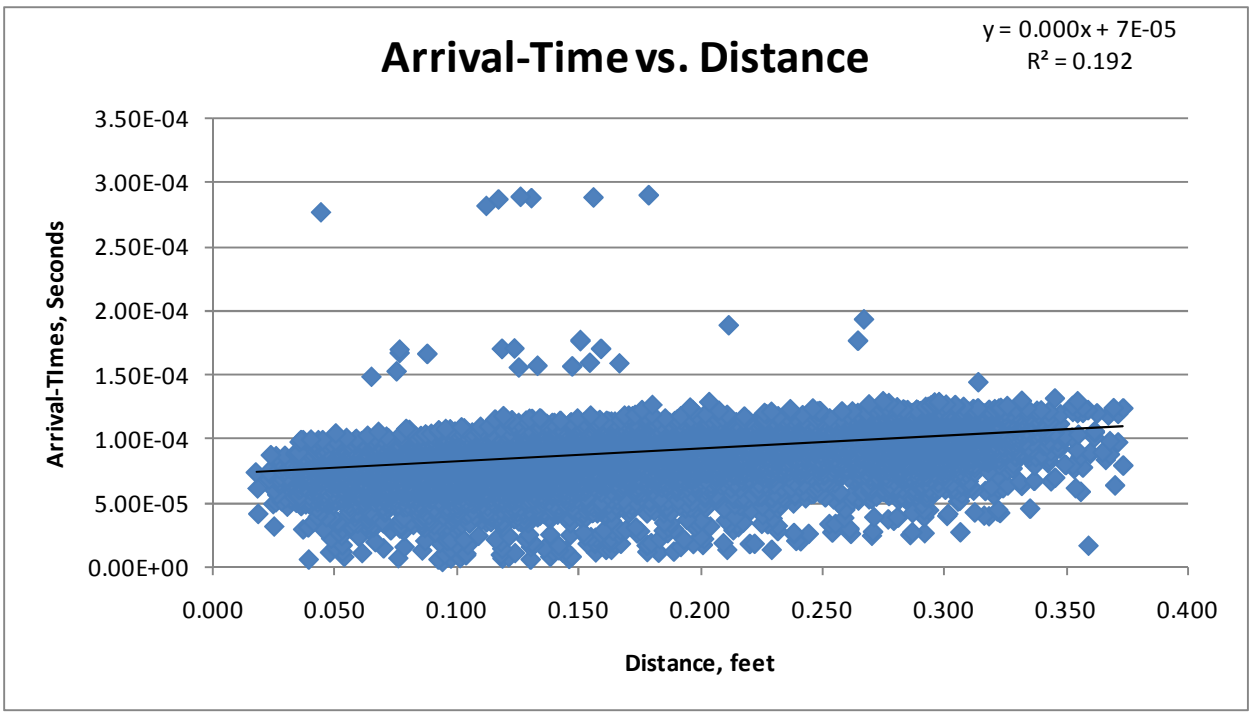

Figure A.21: Experiment #11 Arrival-Time Versus Distance Plot

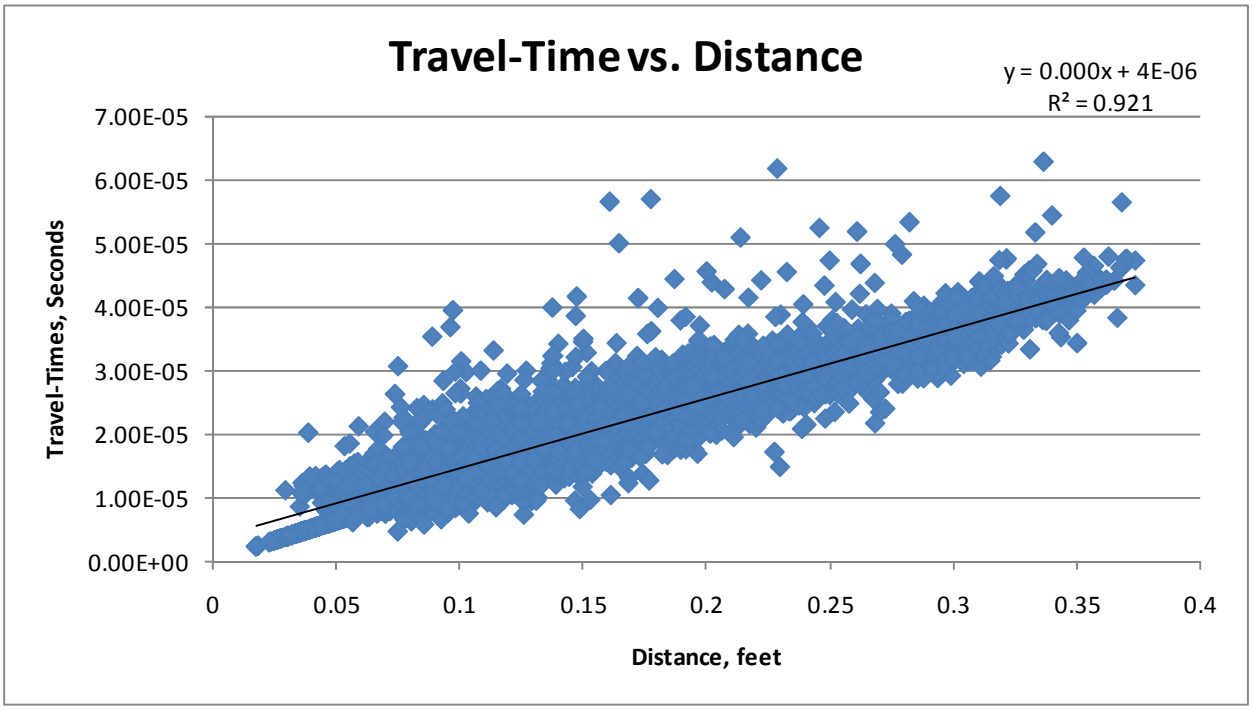

Figure A.22: Experiment #11 Travel-Time Versus Distance Plot

Table A.11: Data Reconciliation Summary Statistics for Experiment #11

Experiment #11	
Arrival-Time R^2	2.90%
Number of Arrival-Time Rays	14962
Travel-Time R^2	92.10%
Number of Travel-Time Rays	14750
Number of Rays Eliminated	212

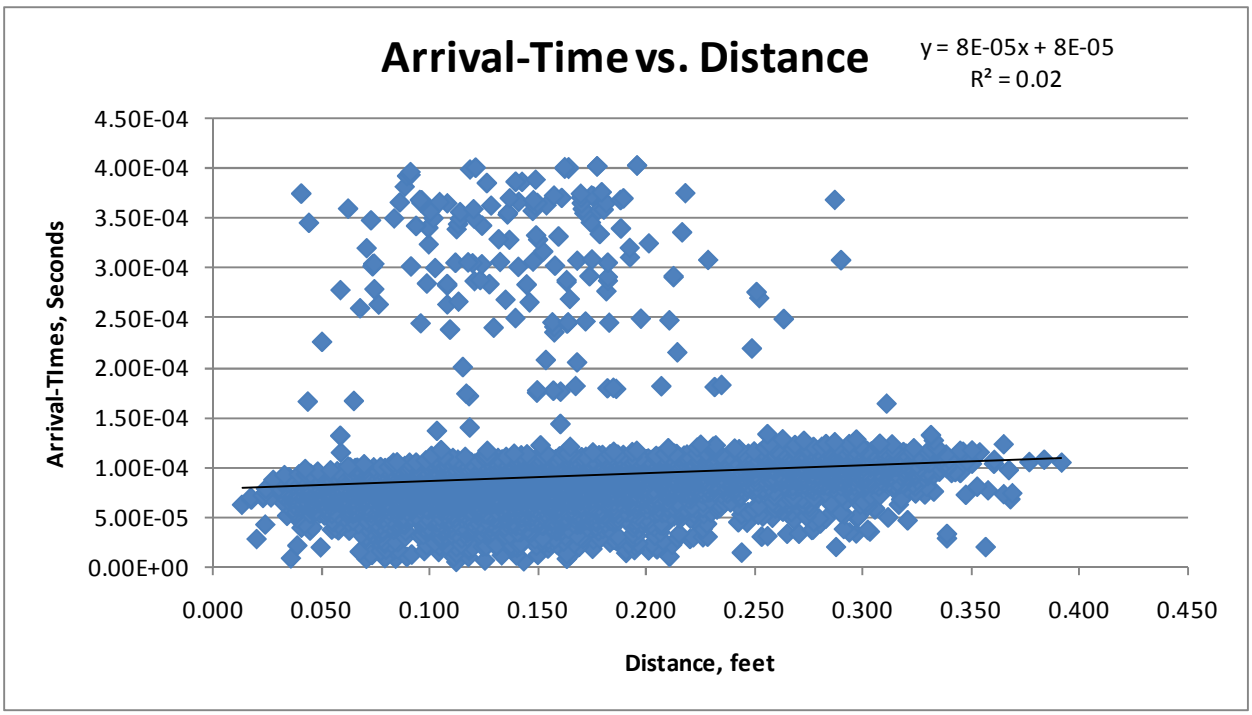

Figure A.23: Experiment #12 Arrival-Time Versus Distance Plot

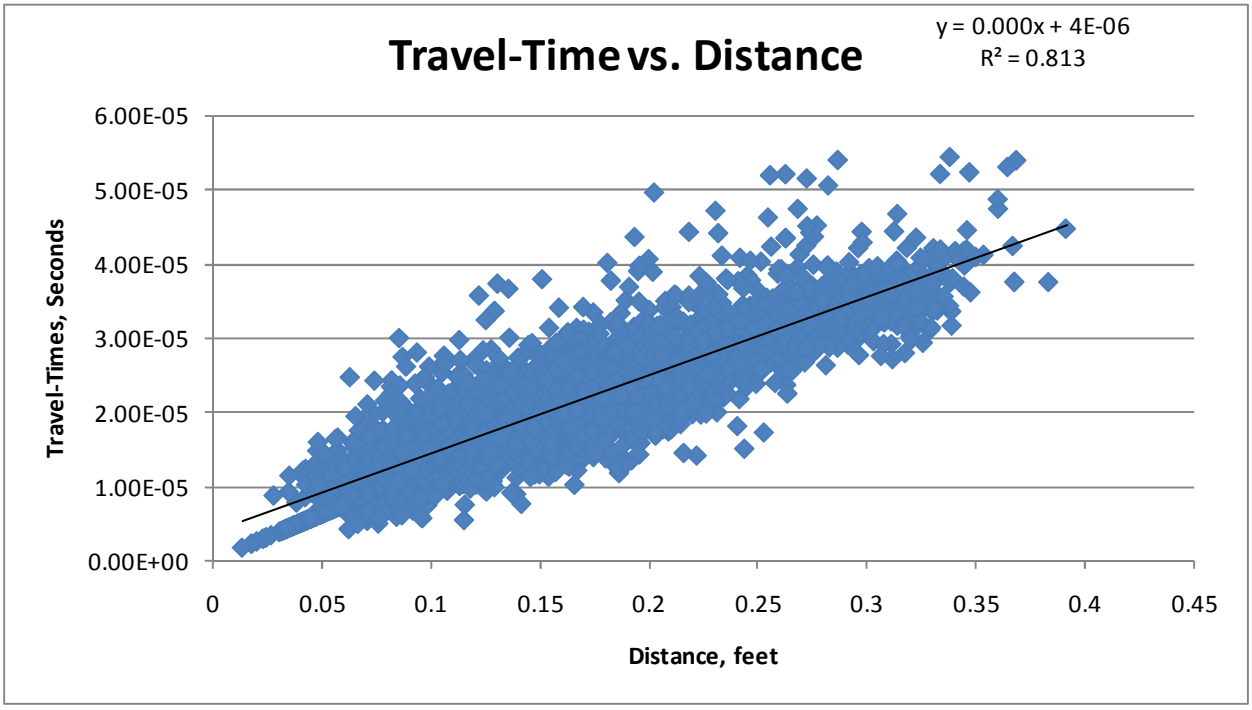

Figure A.24: Experiment #12 Travel-Time Versus Distance Plot

Table A.12: Data Reconciliation Summary Statistics for Experiment #12

Experiment #12	
Arrival-Time R^2	2.00%
Number of Arrival-Time Rays	7185
Travel-Time R^2	81.30%
Number of Travel-Time Rays	6445
Number of Rays Eliminated	740

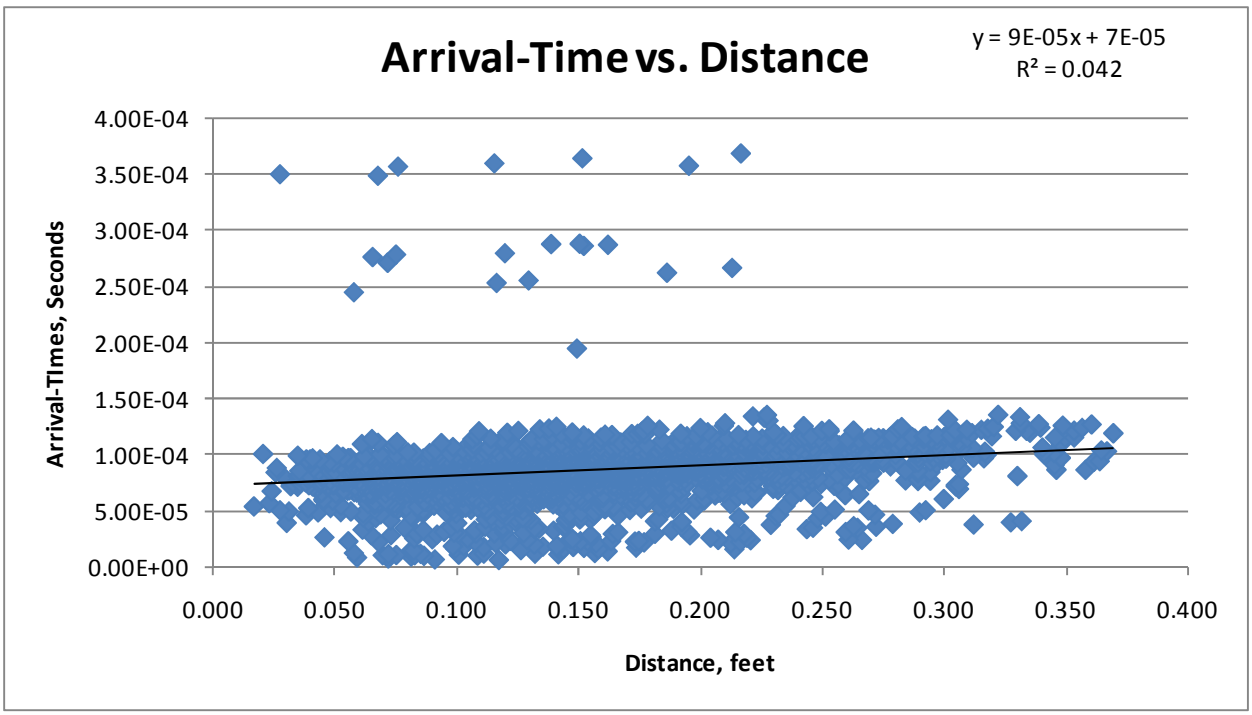

Figure A.25: Experiment #13 Arrival-Time Versus Distance Plot

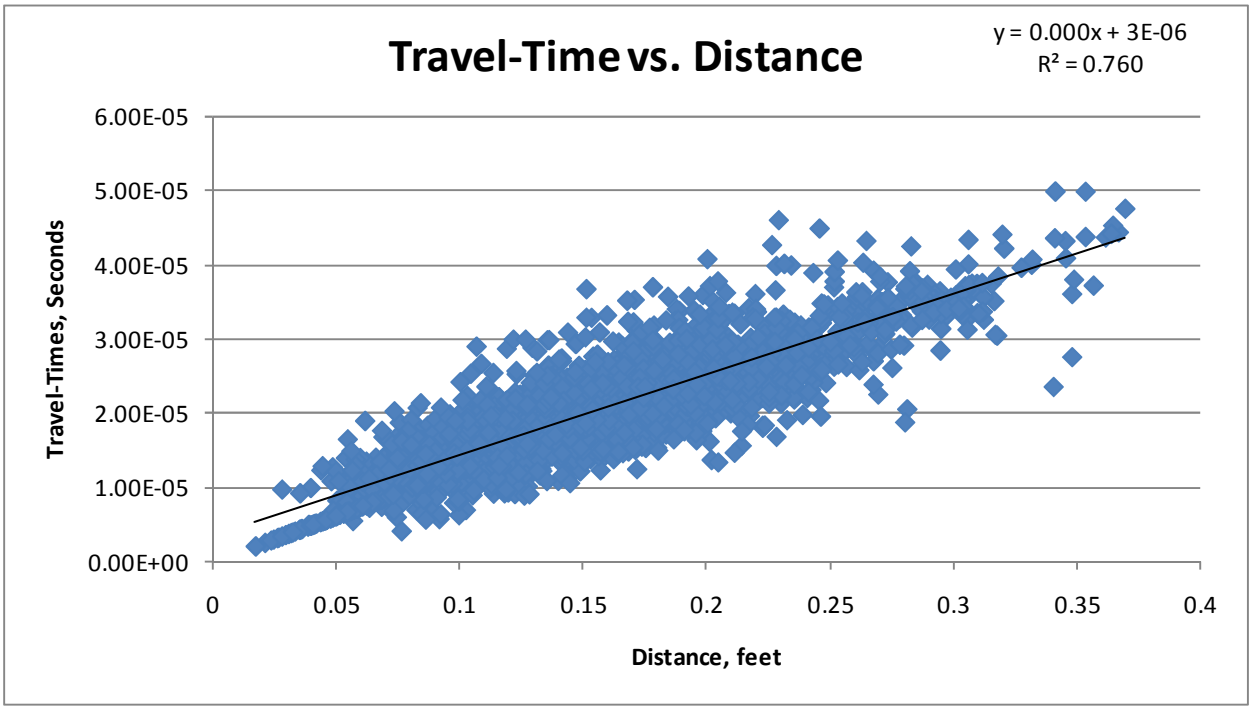

Figure A.26: Experiment #13 Travel-Time Versus Distance Plot

Table A.13: Data Reconciliation Summary Statistics for Experiment #13

Experiment #13	
Arrival-Time R^2	4.20%
Number of Arrival-Time Rays	2823
Travel-Time R^2	76.00%
Number of Travel-Time Rays	2642
Number of Rays Eliminated	181

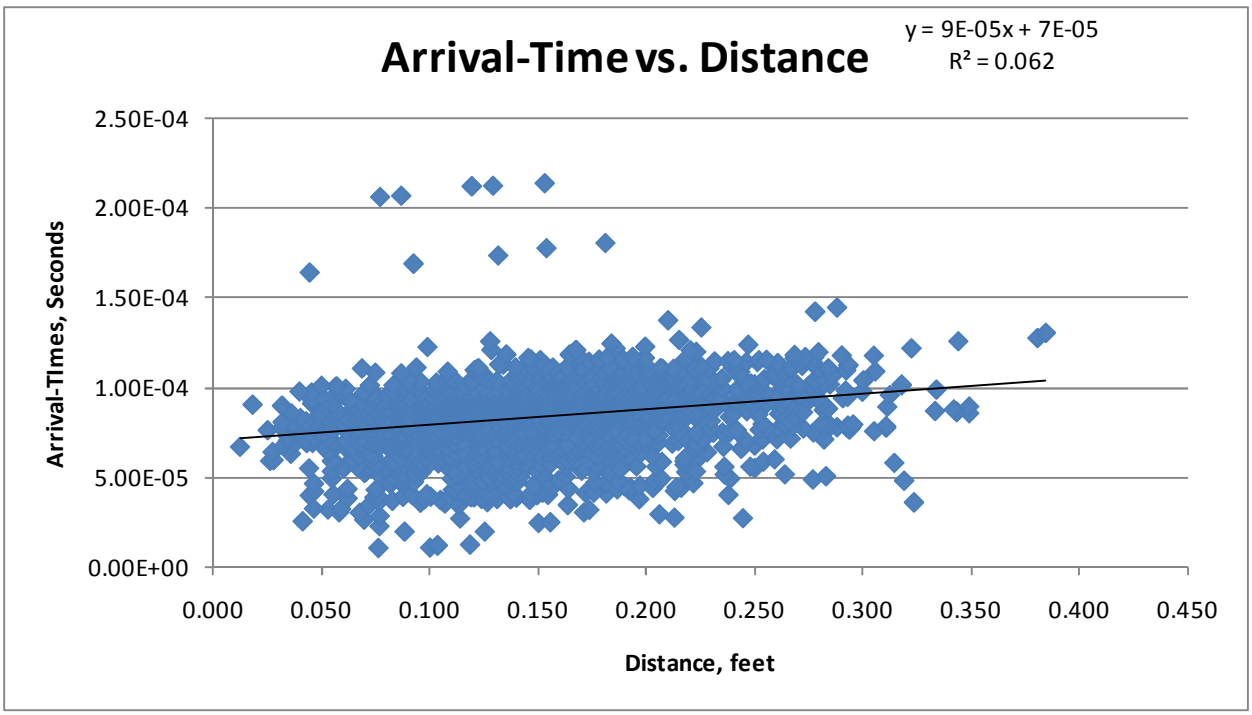

Figure A.27: Experiment #14 Arrival-Time Versus Distance Plot

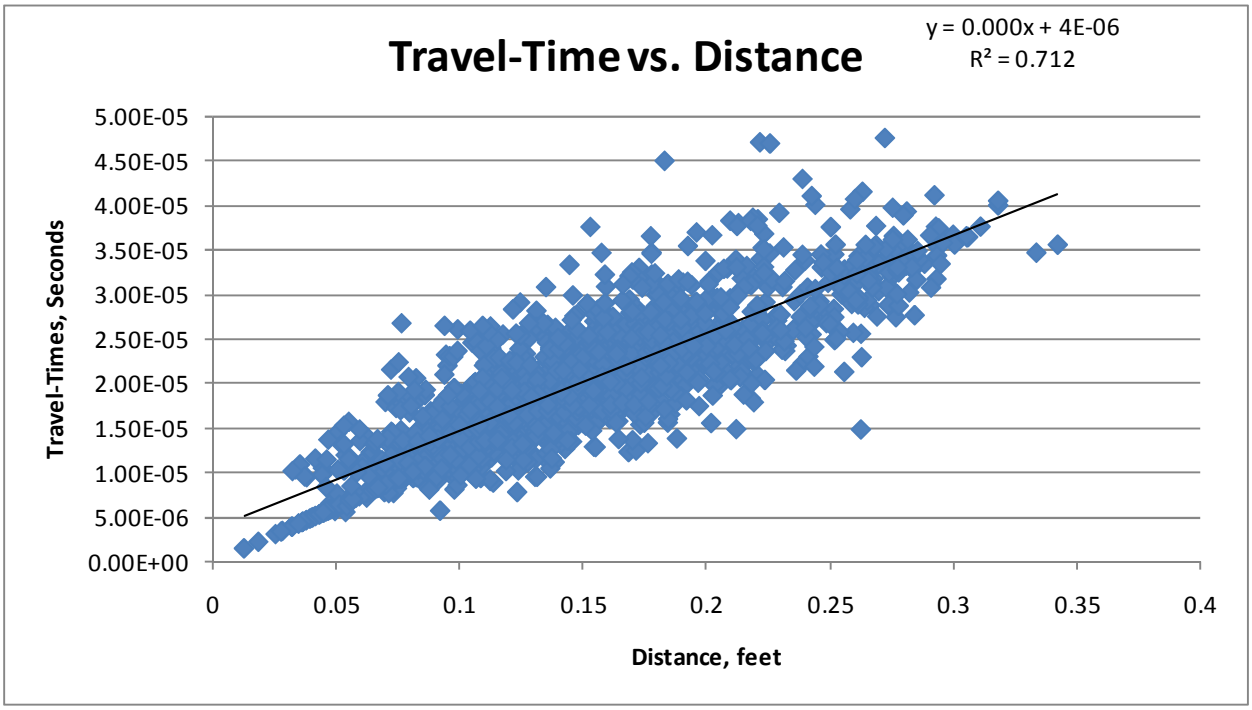

Figure A.28: Experiment #14 Travel-Time Versus Distance Plot

Table A.14: Data Reconciliation Summary Statistics for Experiment #14

Experiment #14	
Arrival-Time R^2	6.20%
Number of Arrival-Time Rays	1972
Travel-Time R^2	71.20%
Number of Travel-Time Rays	1824
Number of Rays Eliminated	148

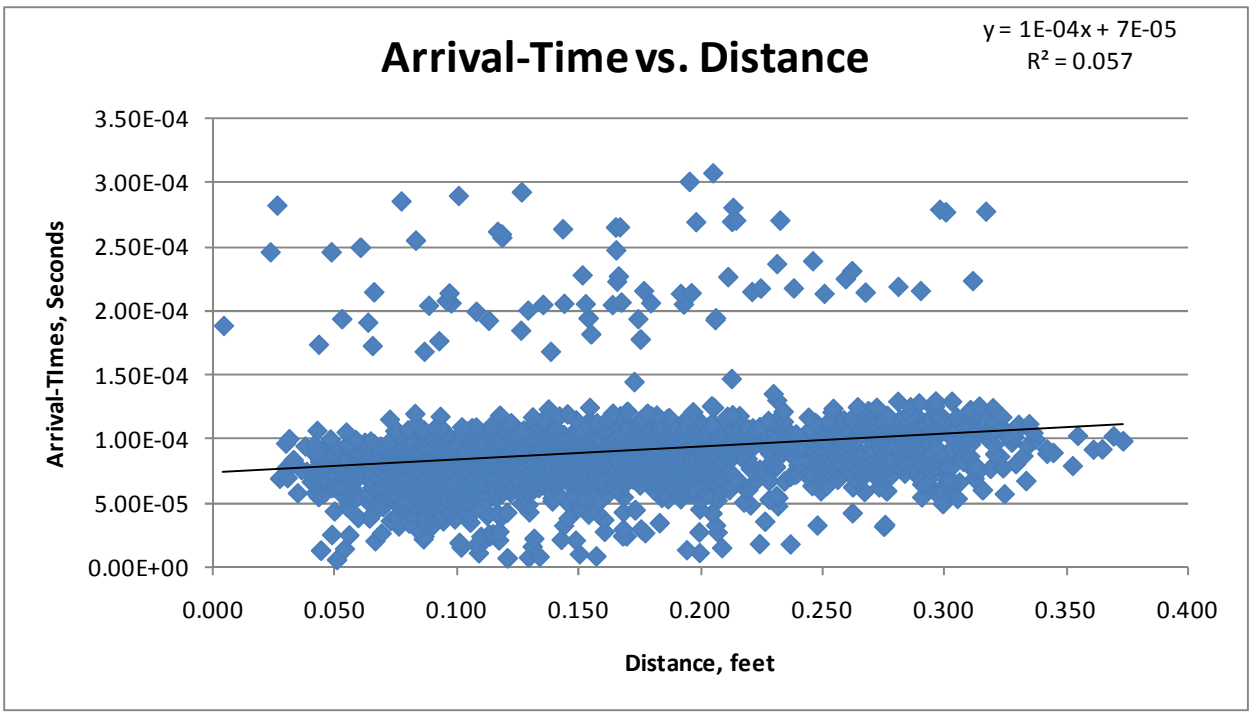

Figure A.29: Experiment #15 Arrival-Time Versus Distance Plot

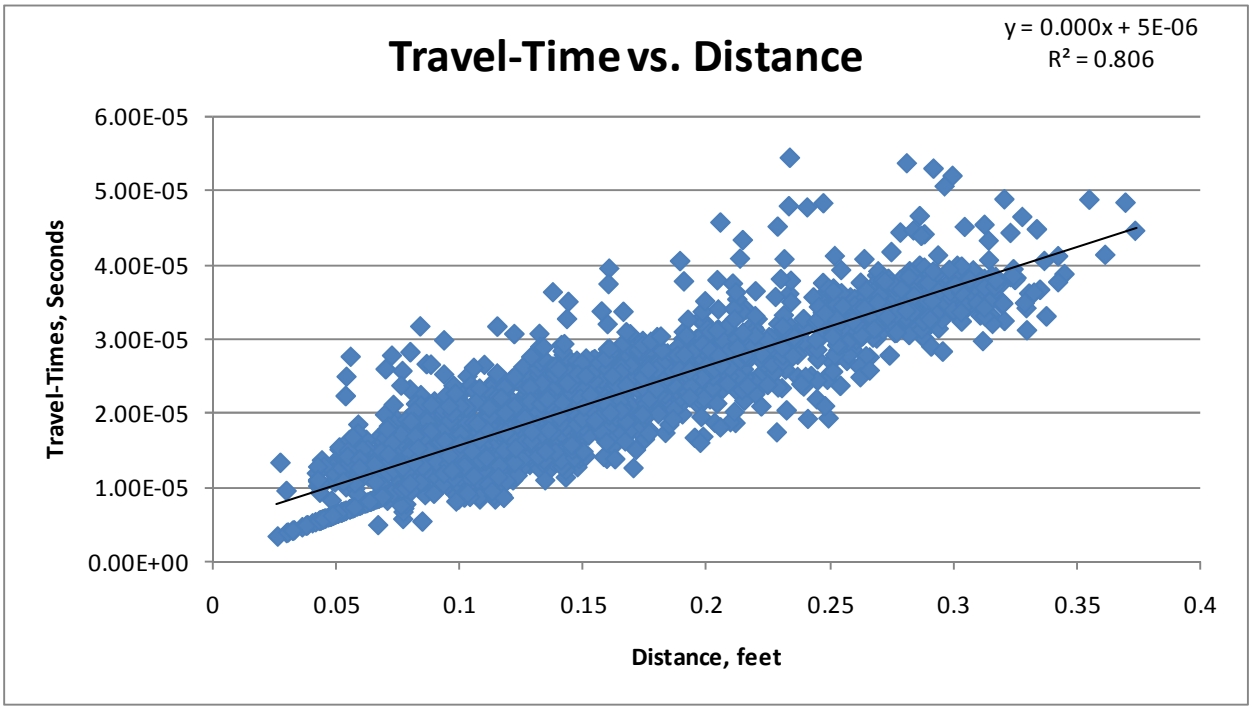

Figure A.30: Experiment #15 Travel-Time Versus Distance Plot

Table A.15: Data Reconciliation Summary Statistics for Experiment #15

Experiment #15	
Arrival-Time R^2	5.70%
Number of Arrival-Time Rays	2728
Travel-Time R^2	80.60%
Number of Travel-Time Rays	2599
Number of Rays Eliminated	129

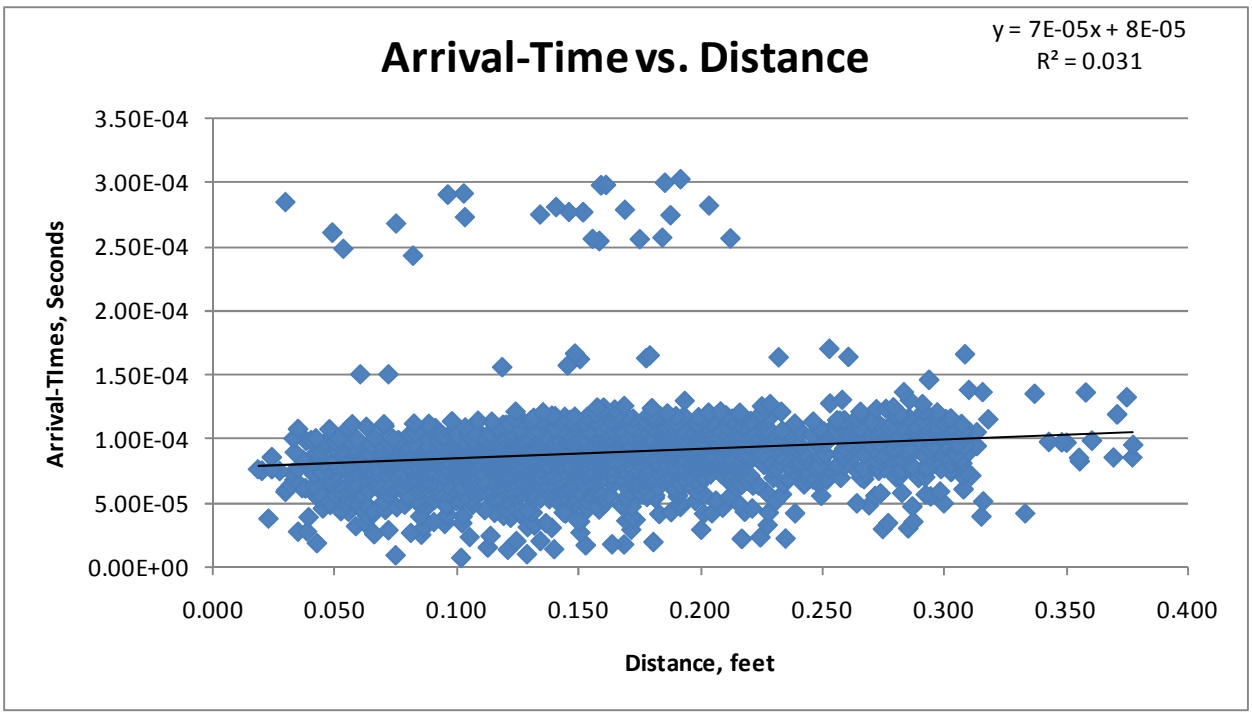

Figure A.31: Experiment #16 Arrival-Time Versus Distance Plot

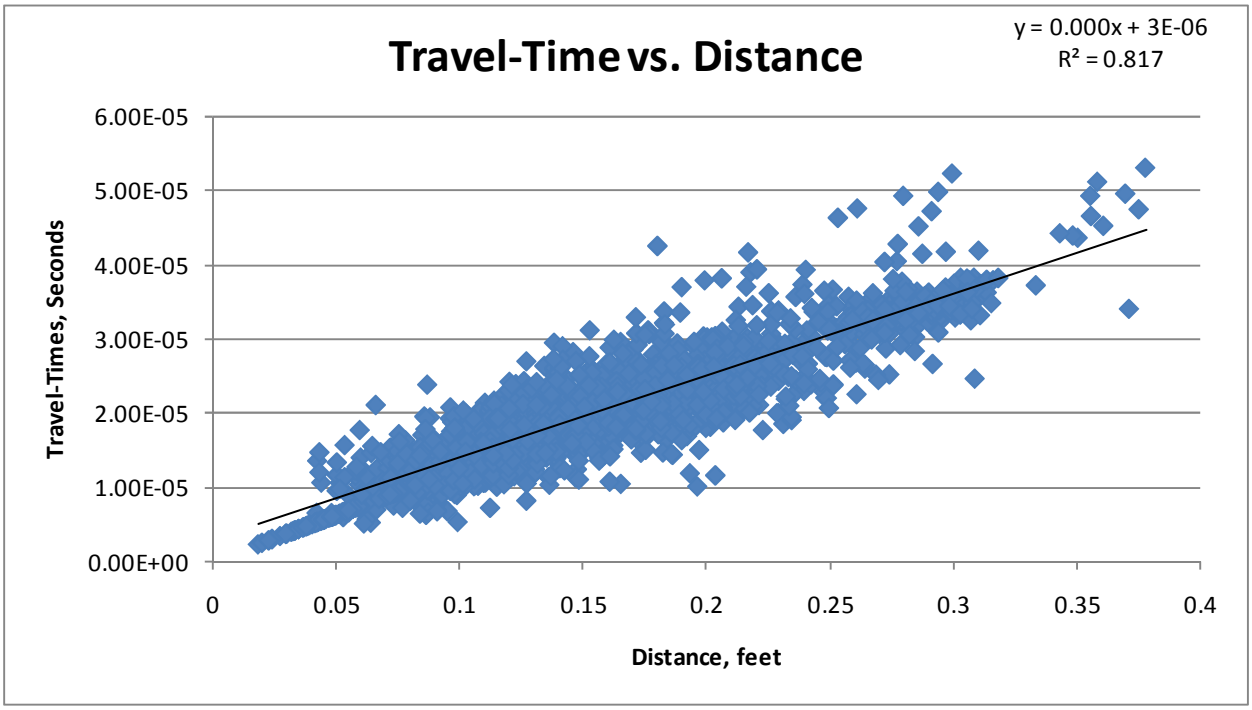

Figure A.32: Experiment #16 Travel-Time Versus Distance Plot

Table A.16: Data Reconciliation Summary Statistics for Experiment #16

Experiment #16	
Arrival-Time R^2	3.10%
Number of Arrival-Time Rays	2286
Travel-Time R^2	81.70%
Number of Travel-Time Rays	2201
Number of Rays Eliminated	85

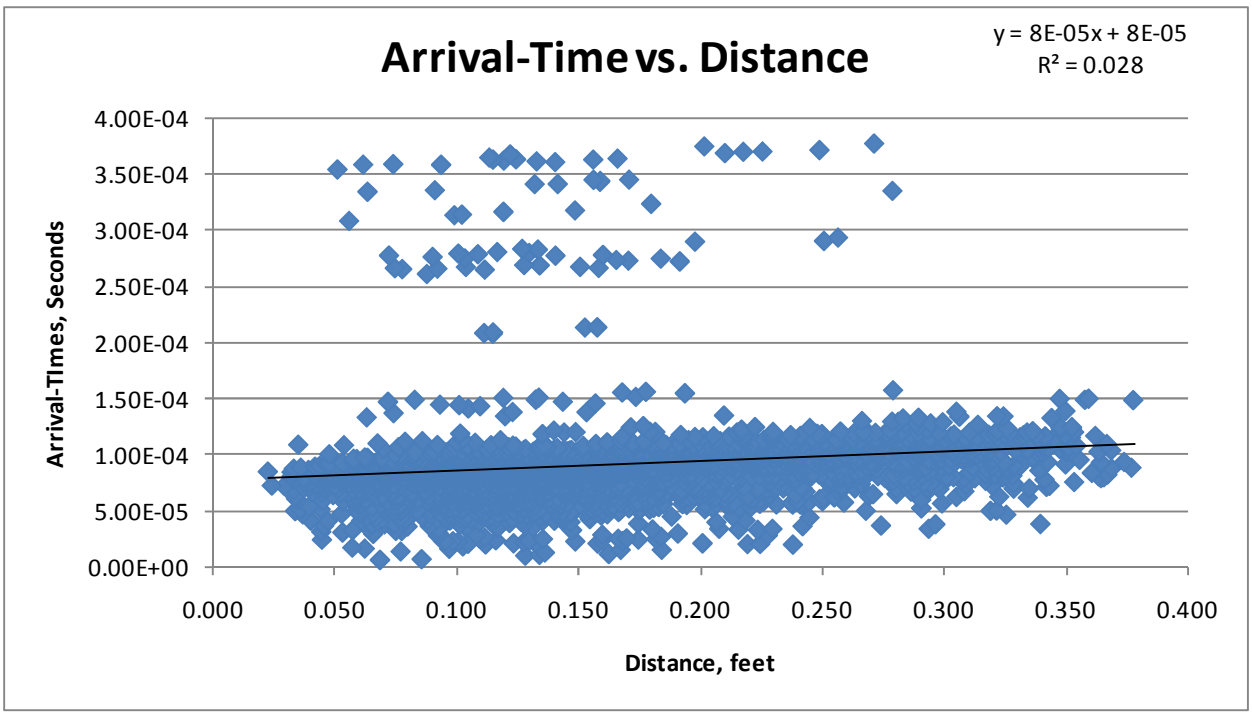

Figure A.33: Experiment #17 Arrival-Time Versus Distance Plot

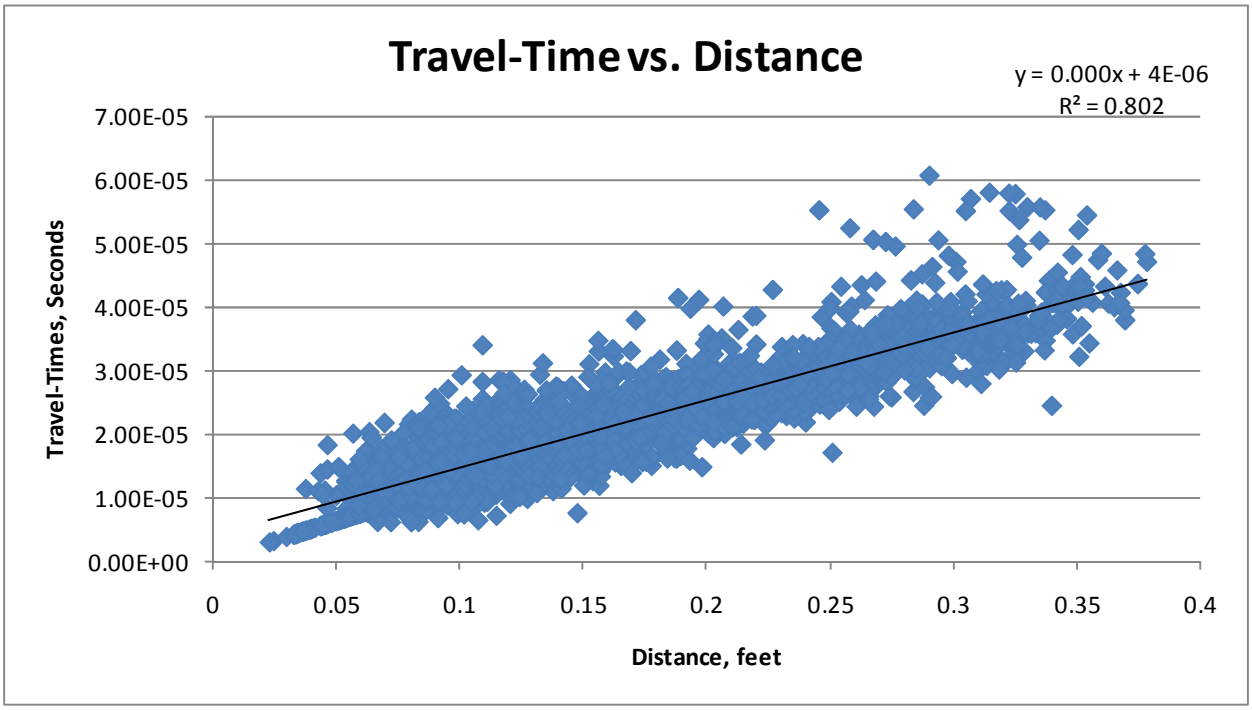

Figure A.34: Experiment #17 Travel-Time Versus Distance Plot

Table A.17: Data Reconciliation Summary Statistics for Experiment #17

Experiment #17	
Arrival-Time R^2	2.80%
Number of Arrival-Time Rays	3658
Travel-Time R^2	80.20%
Number of Travel-Time Rays	3525
Number of Rays Eliminated	133

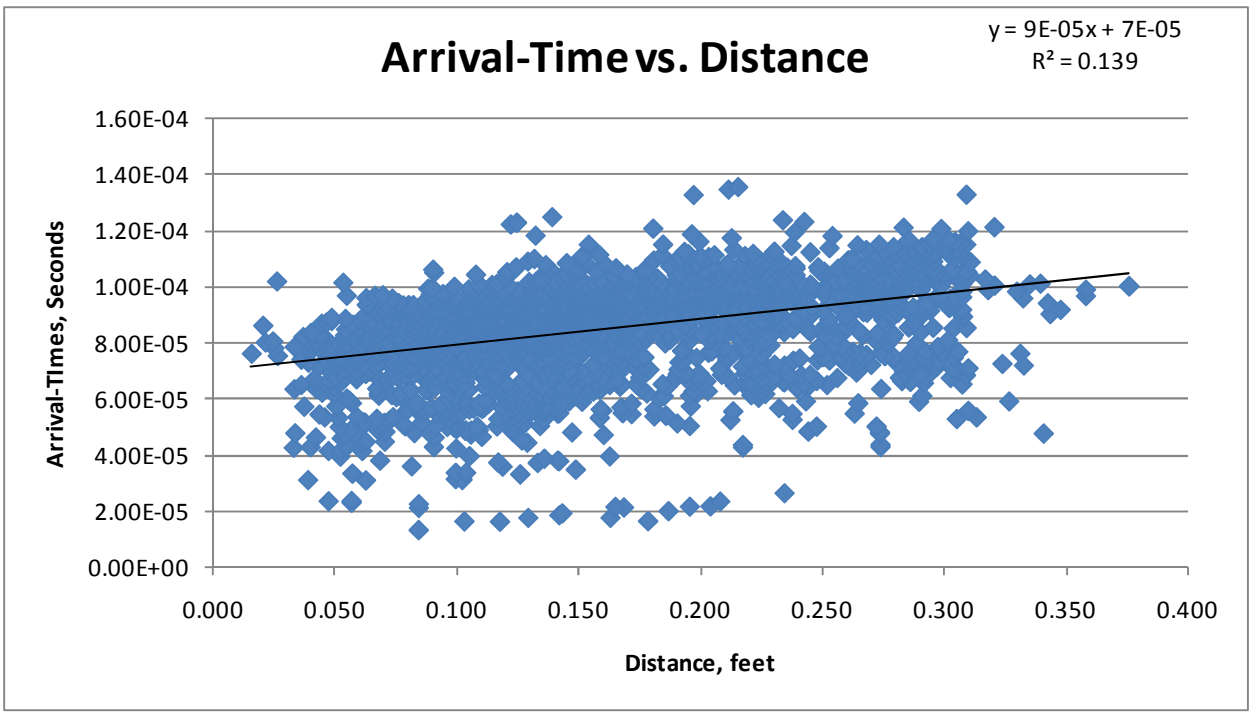

Figure A.35: Experiment #18 Arrival-Time Versus Distance Plot

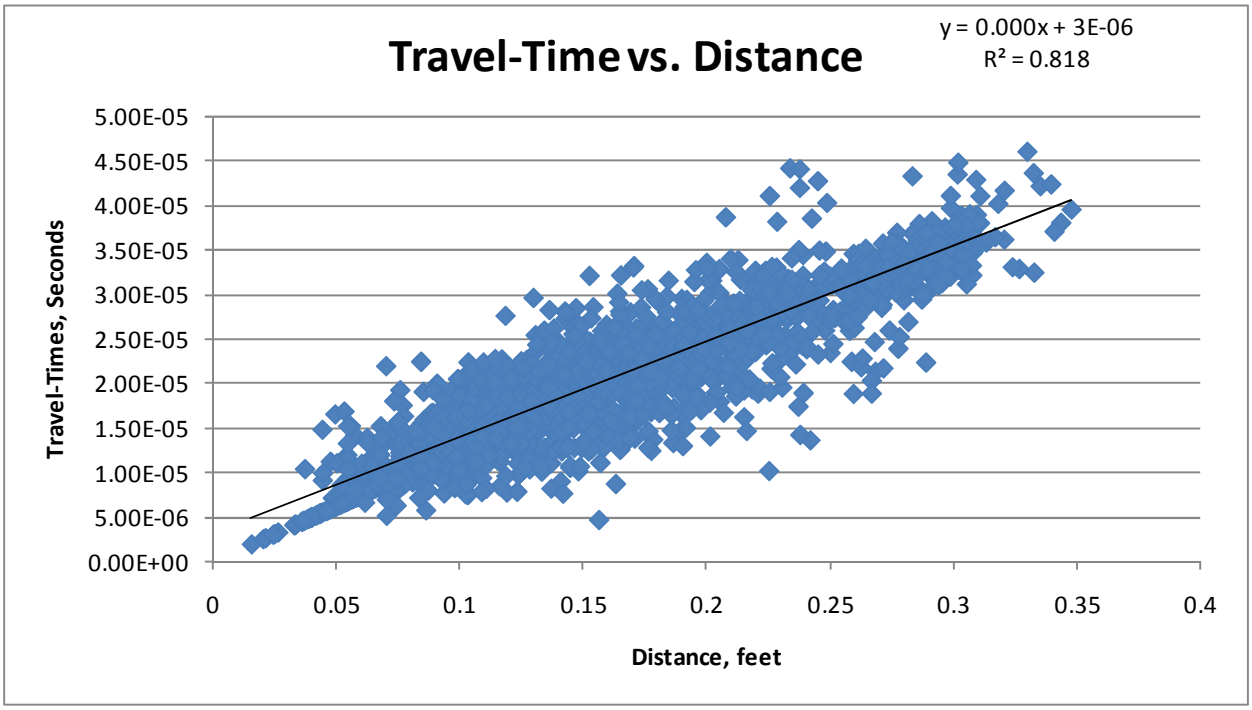

Figure A.36: Experiment #18 Travel-Time Versus Distance Plot

Table A.18: Data Reconciliation Summary Statistics for Experiment #18

Experiment #18	
Arrival-Time R^2	13.90%
Number of Arrival-Time Rays	2449
Travel-Time R^2	81.80%
Number of Travel-Time Rays	2280
Number of Rays Eliminated	169

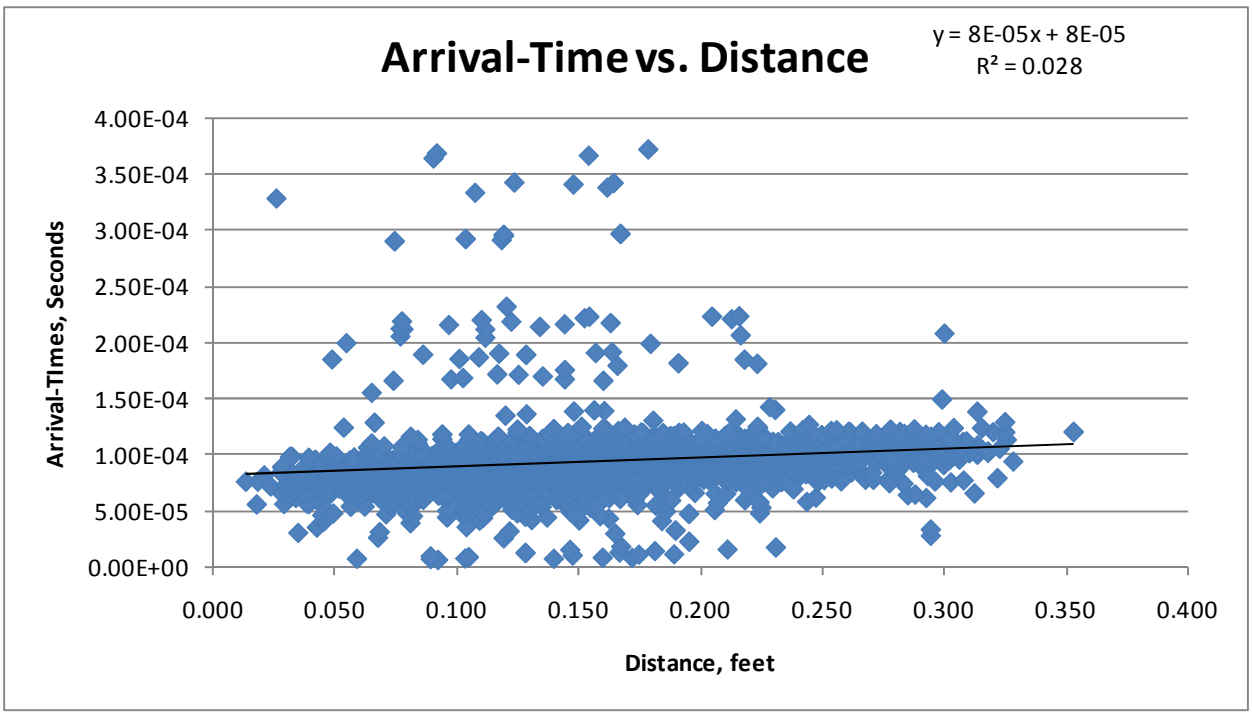

Figure A.37: Experiment #19 Arrival-Time Versus Distance Plot

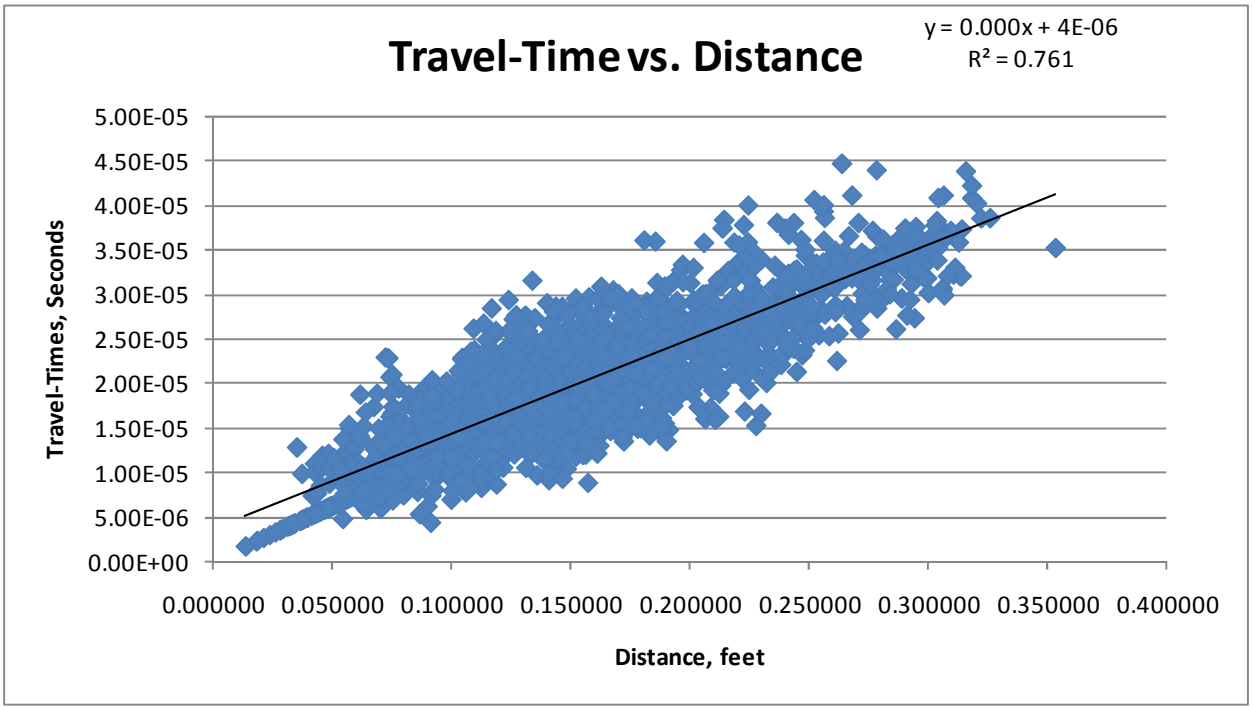

Figure A.38: Experiment #19 Travel-Time Versus Distance Plot

Table A.19: Data Reconciliation Summary Statistics for Experiment #19

Experiment #19	
Arrival-Time R^2	11.40%
Number of Arrival-Time Rays	2686
Travel-Time R^2	76.10%
Number of Travel-Time Rays	2398
Number of Rays Eliminated	288

Appendix B: Acoustic Emission & Wave Velocity Plots

Table B.1: Experiment #1 Acoustic Emission Activity & Loading Summary Statistics

Experiment #1									
Load Pause	Strain	Stress (psi)	Stress (MPa)	Number of Triggered Events	Number of Located Events	Thresh (mV)	Ave. Vel. (ft/s)	Std. Dev. (ft/s)	% Variation
0	0.00000	0	0.0	0	N/A	175	N/A	N/A	N/A
1	0.00094	634	4.4	28	3	175	8044	721	9.0
2	0.00191	1262	8.7	2	2	175	8019	888	11.1
3	0.00258	1896	13.1	0	N/A	175	N/A	N/A	N/A
4	0.00315	2517	17.4	4	2	175	6528	1092	16.7
5	0.00361	3152	21.7	0	N/A	175	N/A	N/A	N/A
6	0.00405	3786	26.1	6	3	175	7347	1190	16.2
7	0.00446	4395	30.3	52	8	175	8185	1405	17.2
8	0.00490	5054	34.8	195	21	175	7674	1988	25.9
9	0.00529	5663	39.0	38	15	175	8158	1950	23.9
10	0.00568	6284	43.3	124	28	200	7754	2102	27.1
11	0.00613	6912	47.7	152	35	200	7601	2050	27.0
12	0.00663	7546	52.0	120	24	200	7537	1858	24.6
13	0.00711	7880	54.3	141	20	200	7788	2088	26.8

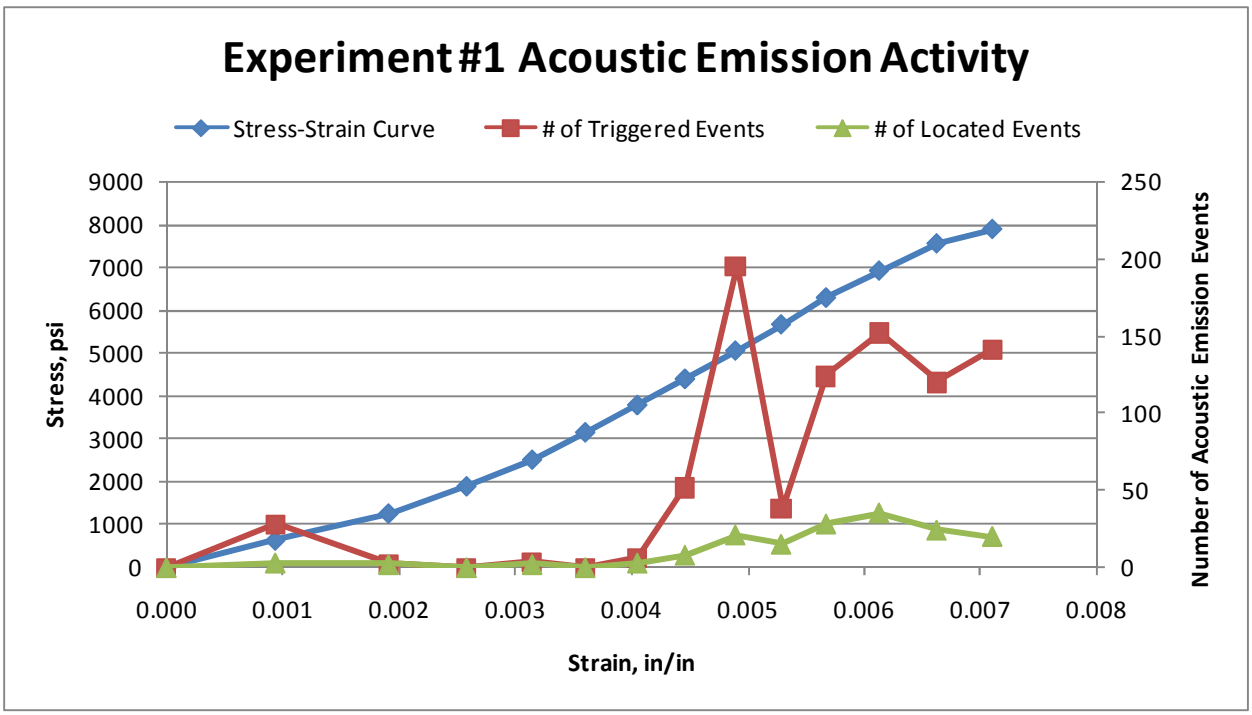

Figure B.1: Plot of Stress-Strain Curve & Acoustic Emission Activity for Experiment #1

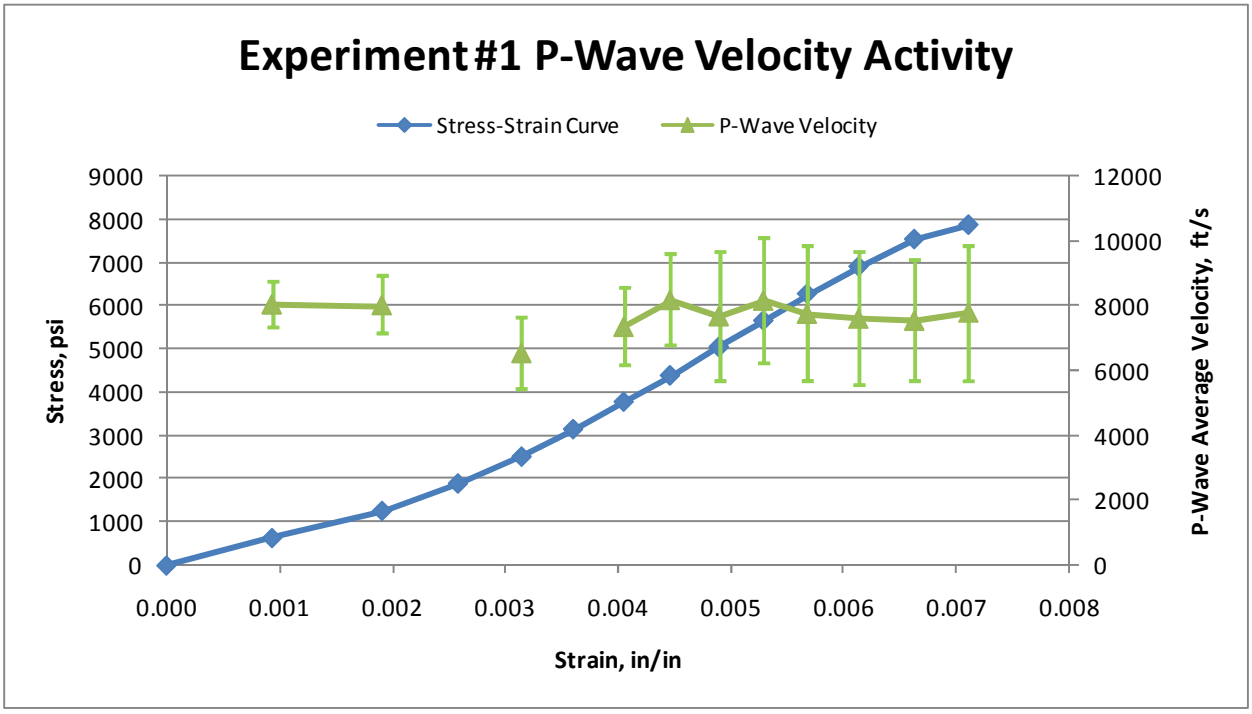

Figure B.2: Plot of Stress-Strain Curve & P-Wave Velocity for Experiment #1

Table B.2: Experiment #2 Acoustic Emission Activity & Loading Summary Statistics

Experiment #2									
Load Pause	Strain	Stress (psi)	Stress (MPa)	Number of Triggered Events	Number of Located Events	Thresh (mV)	Ave. Vel. (ft/s)	Std. Dev. (ft/s)	% Variation
0	0.00000	0	0.0	0	N/A	200	N/A	N/A	N/A
1	0.00147	627	4.3	6	4	200	7586	940	12.4
2	0.00245	1261	8.7	7	7	200	7541	902	12.0
3	0.00309	1888	13.0	18	18	200	7429	934	12.6
4	0.00358	2509	17.3	28	26	200	7681	983	12.8
5	0.00406	3148	21.7	32	30	200	7621	1163	15.3
6	0.00447	3769	26.0	32	29	200	7428	1104	14.9
7	0.00482	4403	30.4	37	35	200	7409	1104	14.9
8	0.00524	5024	34.6	74	61	200	7559	1221	16.2
9	0.00560	5657	39.0	87	59	200	7446	1425	19.1
10	0.00597	6278	43.3	158	81	200	7633	1473	19.3
11	0.00638	6918	47.7	225	102	200	7713	1842	23.9
12	0.00674	7539	52.0	200	81	200	7873	4010	50.9
13	0.00734	8153	56.2	216	89	200	7841	3837	48.9
14	0.00740	8175	56.4	81	20	200	8534	5448	63.8

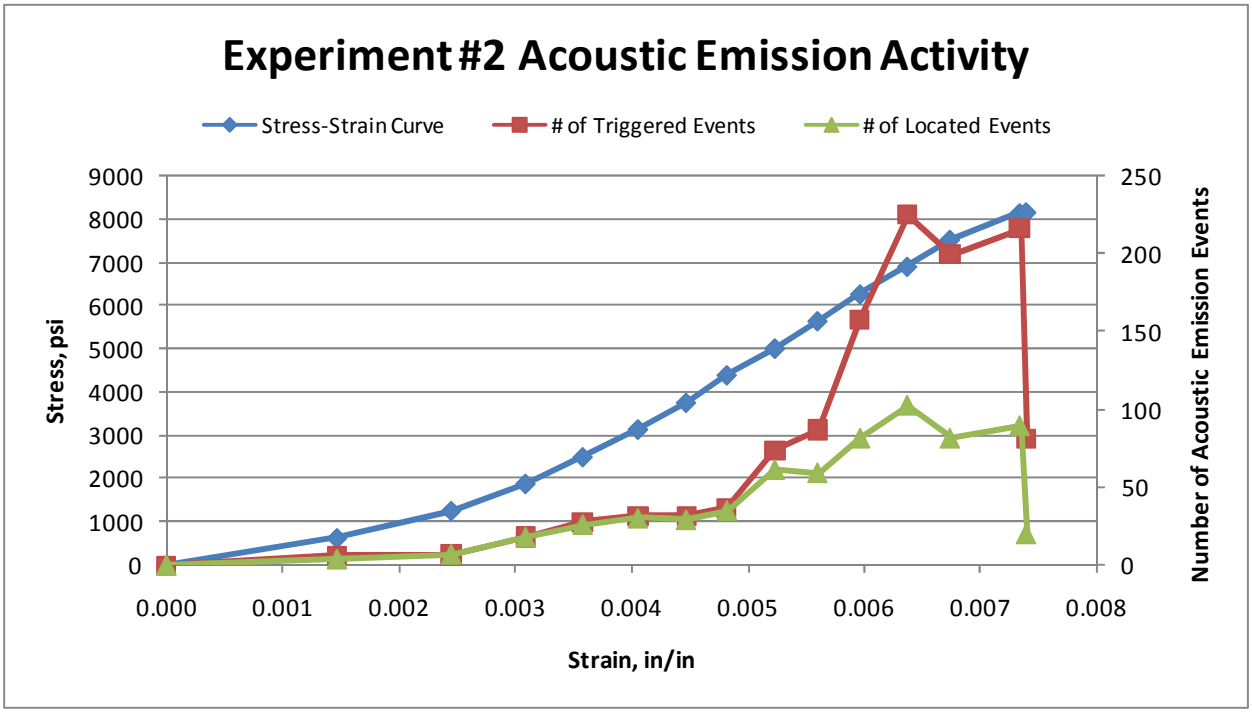

Figure B.3: Plot of Stress-Strain Curve & Acoustic Emission Activity for Experiment #2

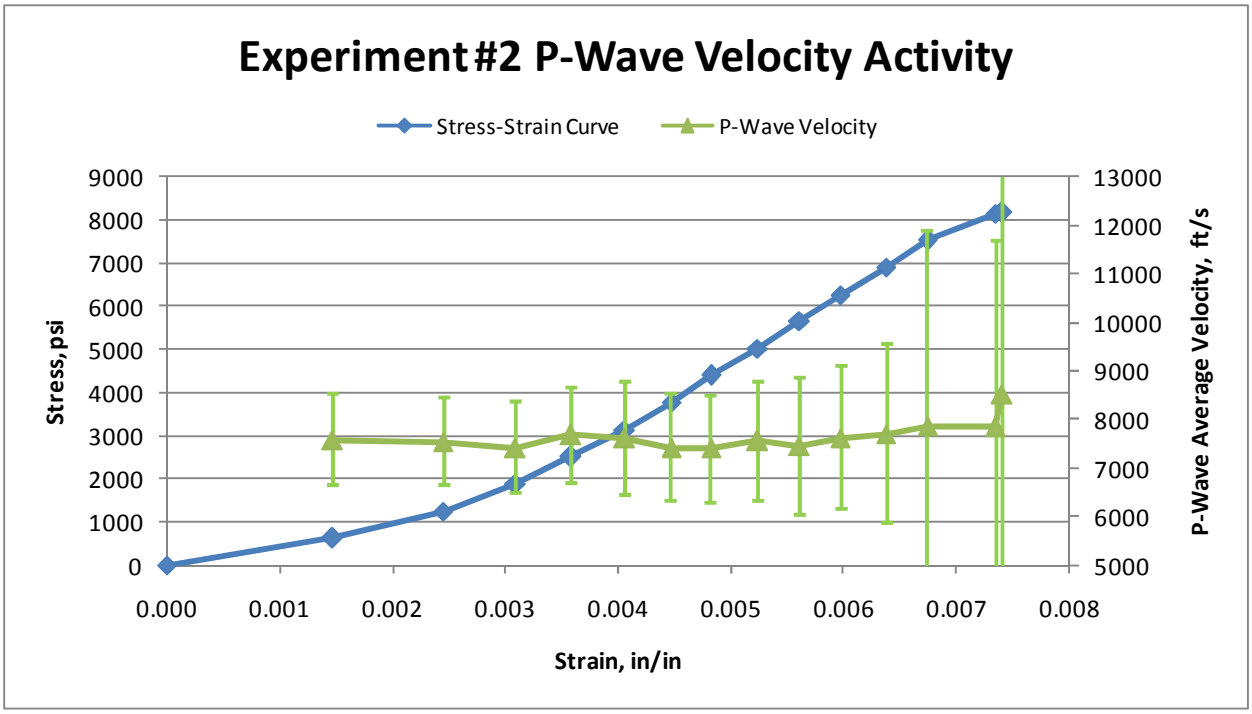

Figure B.4: Plot of Stress-Strain Curve & P-Wave Velocity for Experiment #2

Table B.3: Experiment #3 Acoustic Emission Activity & Loading Summary Statistics

Experiment #3									
Load Pause	Strain	Stress (psi)	Stress (MPa)	Number of Triggered Events	Number of Located Events	Thresh (mV)	Ave. Vel. (ft/s)	Std. Dev. (ft/s)	% Variation
0	0.00000	0	0.0	0	N/A	200	N/A	N/A	N/A
1	0.00205	655	4.5	36	5	200	7925	762	9.6
2	0.00303	1316	9.1	2	2	200	7712	467	6.1
3	0.00372	1958	13.5	1	1	200	7509	471	6.3
4	0.00427	2612	18.0	2	0	200	N/A	N/A	N/A
5	0.00475	3254	22.4	0	N/A	200	N/A	N/A	N/A
6	0.00522	3902	26.9	5	5	200	7669	1534	20.0
7	0.00560	4544	31.3	7	4	200	7721	1534	19.9
8	0.00602	5199	35.8	26	15	200	7794	1507	19.3
9	0.00639	5847	40.3	37	23	200	7794	1696	21.8
10	0.00683	6489	44.7	100	56	200	7564	1485	19.6
11	0.00735	7144	49.3	226	101	200	7408	1489	20.1
12	0.00756	7434	51.3	131	38	200	7816	1766	22.6

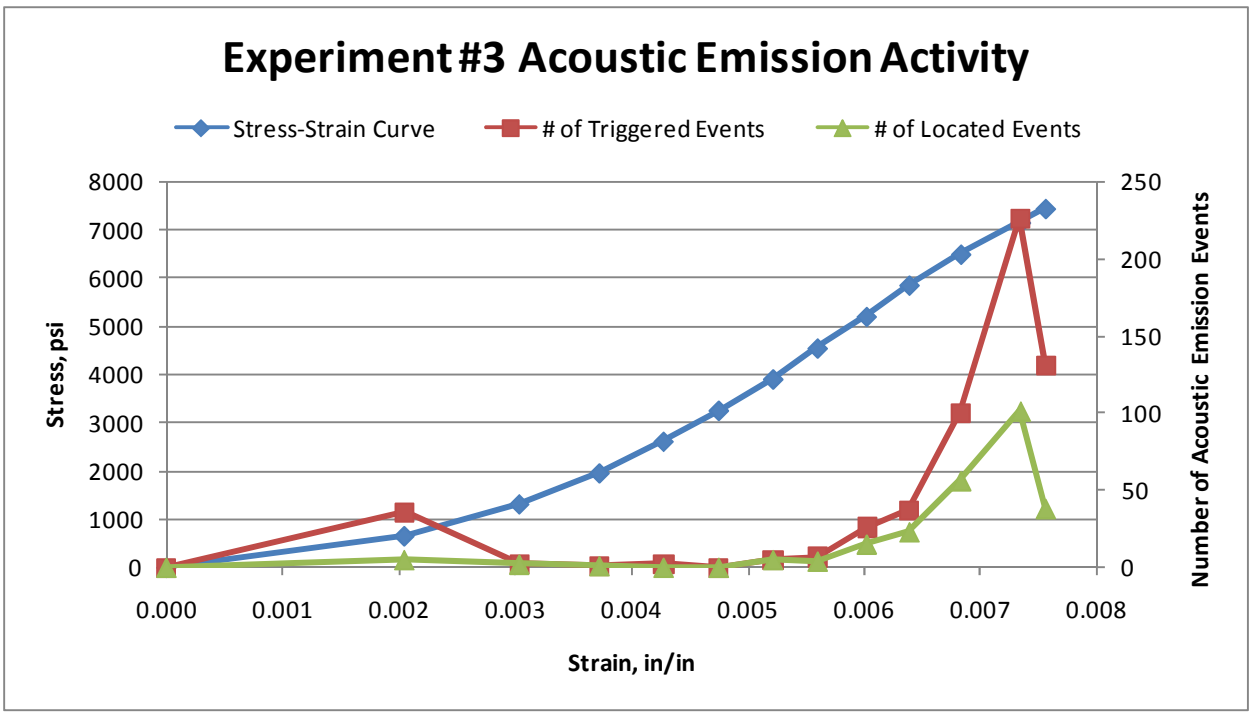

Figure B.5: Plot of Stress-Strain Curve & Acoustic Emission Activity for Experiment #3

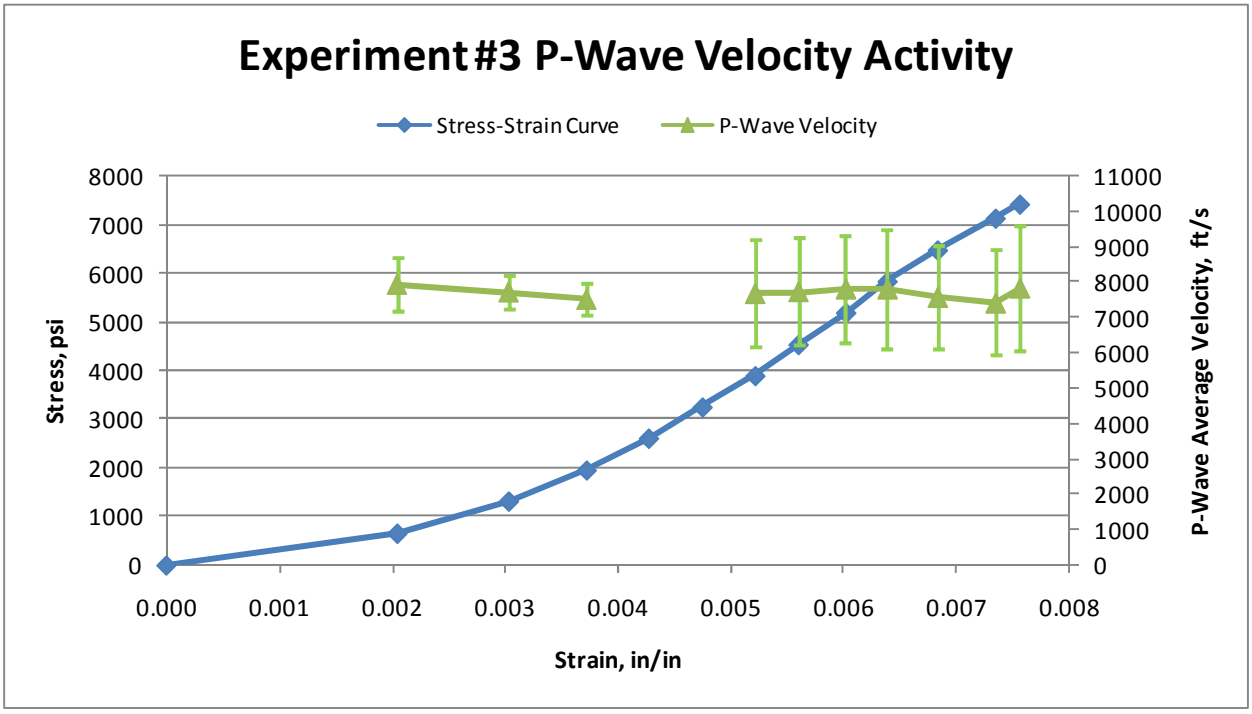

Figure B.6: Plot of Stress-Strain Curve & P-Wave Velocity for Experiment #3

Table B.4: Experiment #4 Acoustic Emission Activity & Loading Summary Statistics

Experiment #4									
Load Pause	Strain	Stress (psi)	Stress (MPa)	Number of Triggered Events	Number of Located Events	Thresh (mV)	Ave. Vel. (ft/s)	Std. Dev. (ft/s)	% Variation
0	0.00000	0	0.0	0	N/A	200	N/A	N/A	N/A
1	0.00092	654	4.5	35	15	200	7558	610	8.1
2	0.00188	1302	9.0	2	1	200	7599	480	6.3
3	0.00254	1956	13.5	0	N/A	200	N/A	N/A	N/A
4	0.00310	2597	17.9	1	0	200	N/A	N/A	N/A
5	0.00355	3257	22.5	0	N/A	200	N/A	N/A	N/A
6	0.00399	3898	26.9	0	N/A	200	N/A	N/A	N/A
7	0.00439	4533	31.3	2	2	200	7420	1607	21.7
8	0.00482	5200	35.9	6	5	200	7542	1594	21.1
9	0.00521	5835	40.2	34	10	200	8401	1810	21.5
10	0.00559	6482	44.7	128	36	200	7753	1544	19.9
11	0.00604	7123	49.1	226	53	200	7672	1528	19.9
12	0.00653	7771	53.6	223	84	200	7783	2162	27.8
13	0.00700	8128	56.0	207	32	200	7685	1882	24.5

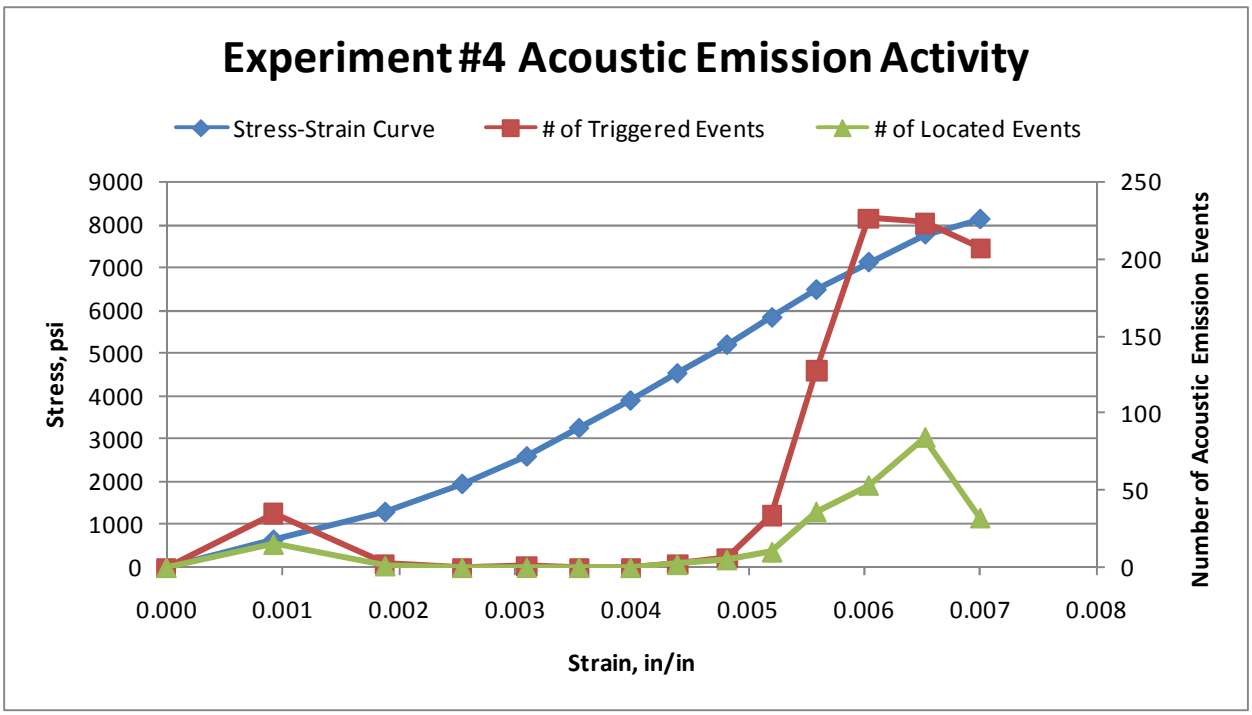

Figure B.7: Plot of Stress-Strain Curve & Acoustic Emission Activity for Experiment #4

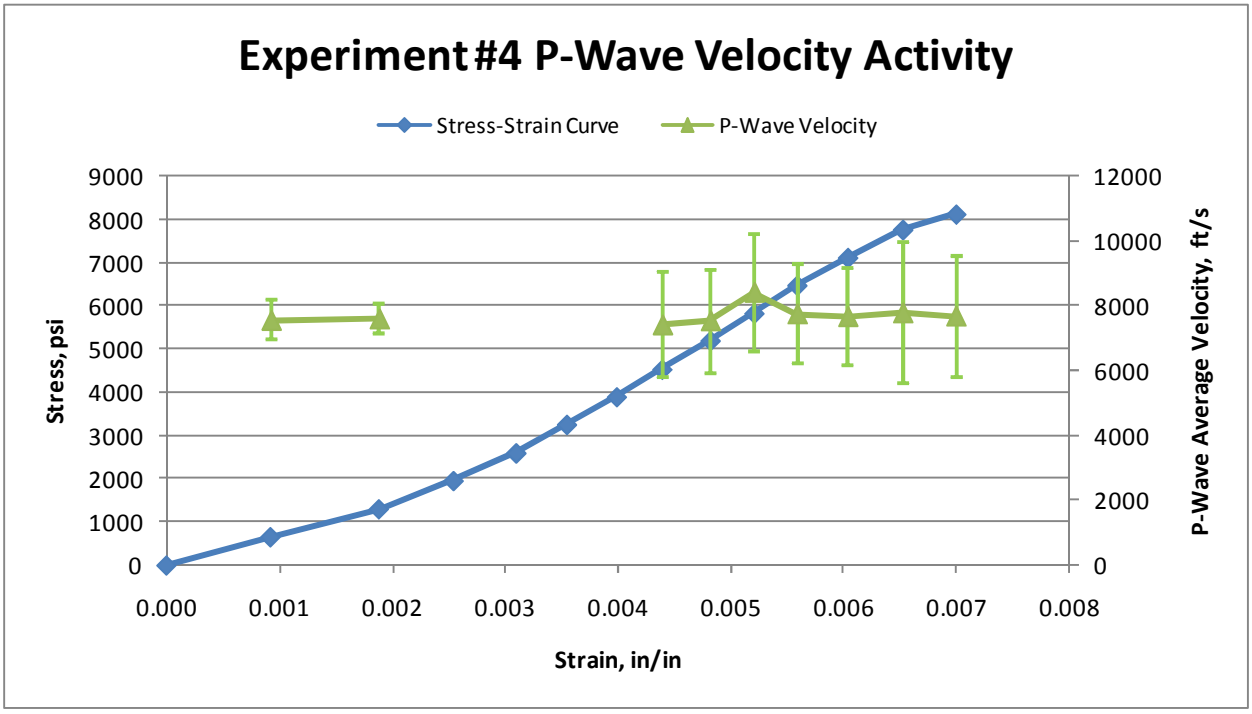

Figure B.8: Plot of Stress-Strain Curve & P-Wave Velocity for Experiment #4

Table B.5: Experiment #5 Acoustic Emission Activity & Loading Summary Statistics

Experiment #5									
Load Pause	Strain	Stress (psi)	Stress (MPa)	Number of Triggered Events	Number of Located Events	Thresh (mV)	Ave. Vel. (ft/s)	Std. Dev. (ft/s)	% Variation
0	0.00000	0	0.0	0	N/A	200	N/A	N/A	N/A
1	0.00187	630	4.3	26	0	200	6783	1615	23.8
2	0.00281	1272	8.8	2	2	200	7836	422	5.4
3	0.00351	1895	13.1	1	1	200	7740	1038	13.4
4	0.00406	2538	17.5	1	1	200	7307	738	10.1
5	0.00452	3155	21.8	2	2	200	7150	750	10.5
6	0.00497	3797	26.2	6	6	200	7720	955	12.4
7	0.00535	4420	30.5	9	6	200	7687	1481	19.3
8	0.00576	5037	34.7	70	17	200	7894	1639	20.8
9	0.00611	5680	39.2	91	14	200	7452	1485	19.9
10	0.00647	6309	43.5	62	27	200	7743	1597	20.6
11	0.00686	6933	47.8	45	26	225	7928	1544	19.5
12	0.00728	7562	52.1	88	48	225	7543	1609	21.3
13	0.00783	8192	56.5	124	64	225	7766	1805	23.2
14	0.00785	8284	57.1	173	23	225	8028	1661	20.7

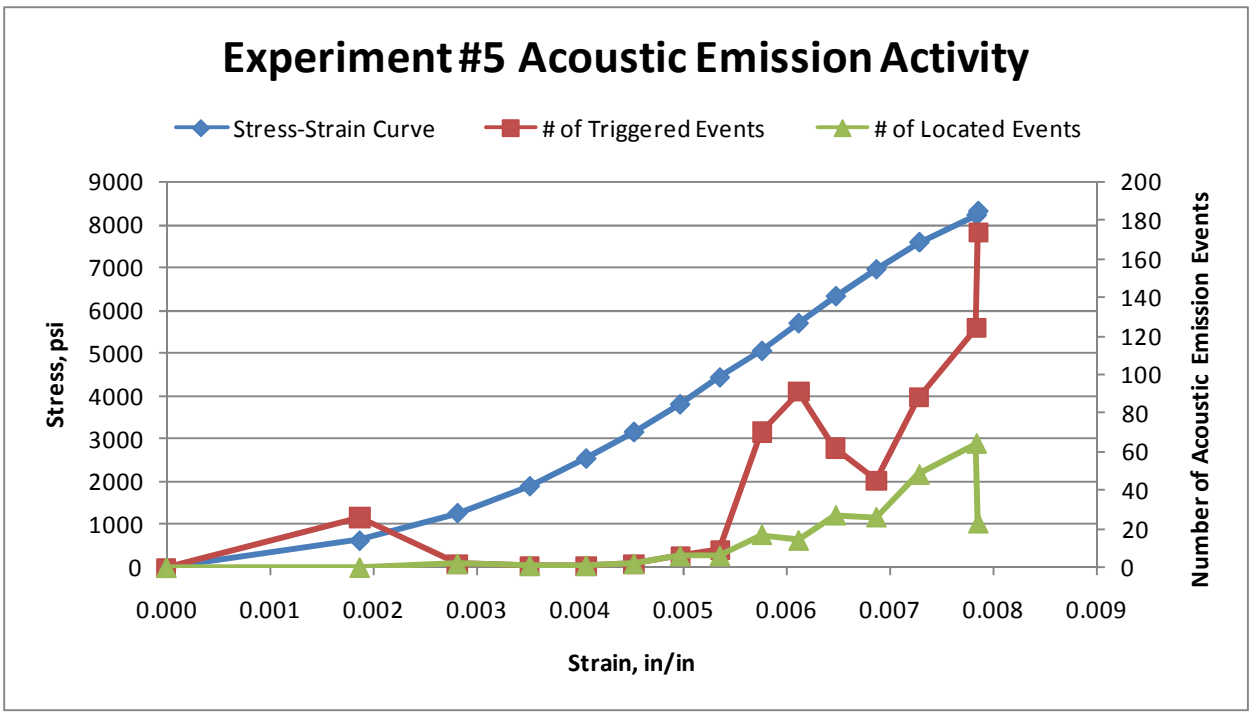

Figure B.9: Plot of Stress-Strain Curve & Acoustic Emission Activity for Experiment #5

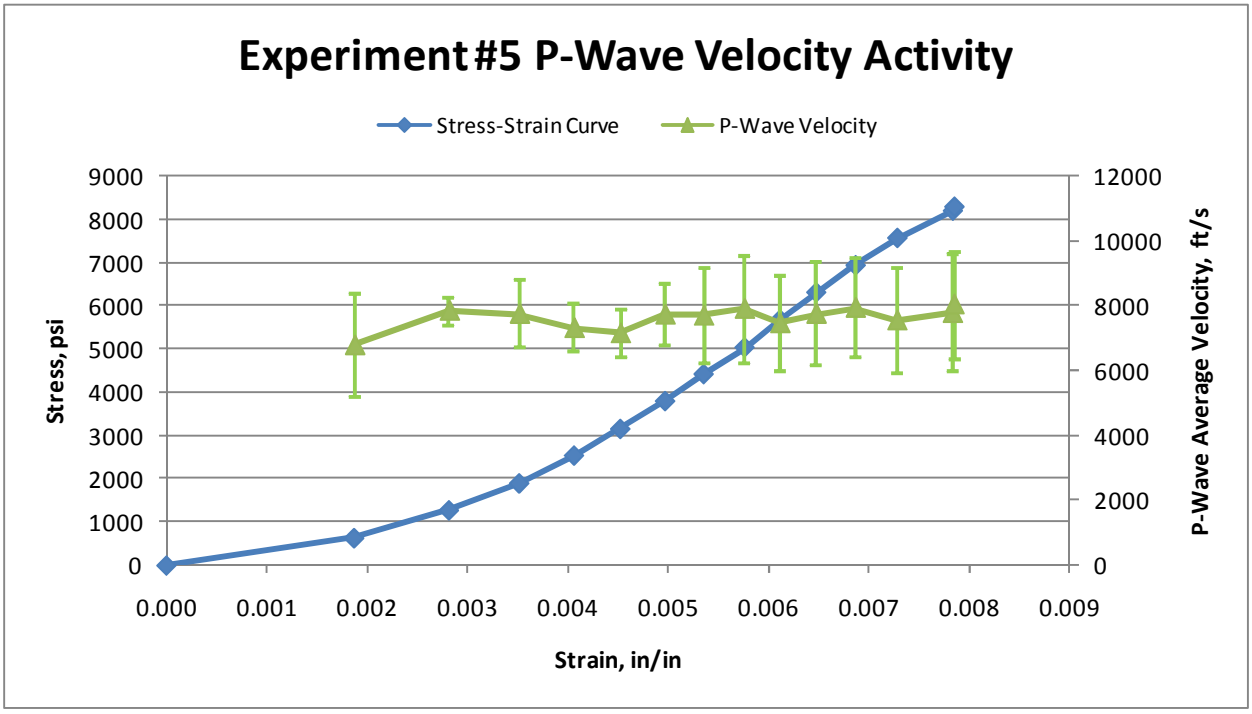

Figure B.10: Plot of Stress-Strain Curve & P-Wave Velocity for Experiment #5

Table B.6: Experiment #6 Acoustic Emission Activity & Loading Summary Statistics

Experiment #6									
Load Pause	Strain	Stress (psi)	Stress (MPa)	Number of Triggered Events	Number of Located Events	Thresh (mV)	Ave. Vel. (ft/s)	Std. Dev. (ft/s)	% Variation
0	0.00000	0	0.0	0	N/A	225	N/A	N/A	N/A
1	0.00127	628	4.3	12	0	225	N/A	N/A	N/A
2	0.00227	1256	8.7	9	7	225	7675	763	9.9
3	0.00297	1890	13.0	10	10	225	7606	860	11.3
4	0.00353	2517	17.4	17	15	225	7283	867	11.9
5	0.00400	3139	21.6	17	13	225	7250	957	13.2
6	0.00444	3773	26.0	20	20	225	7486	974	13.0
7	0.00485	4413	30.4	29	24	225	7493	1017	13.6
8	0.00522	5029	34.7	40	29	225	7657	914	11.9
9	0.00561	5663	39.0	53	39	225	7566	1115	14.7
10	0.00599	6291	43.4	96	67	225	7666	1354	17.7
11	0.00638	6931	47.8	106	57	225	7436	1180	15.9
12	0.00679	7546	52.0	165	66	250	7630	1349	17.7
13	0.00729	8174	56.4	150	70	250	7430	1608	21.6
14	0.00764	8439	58.2	181	47	250	7671	1570	20.5

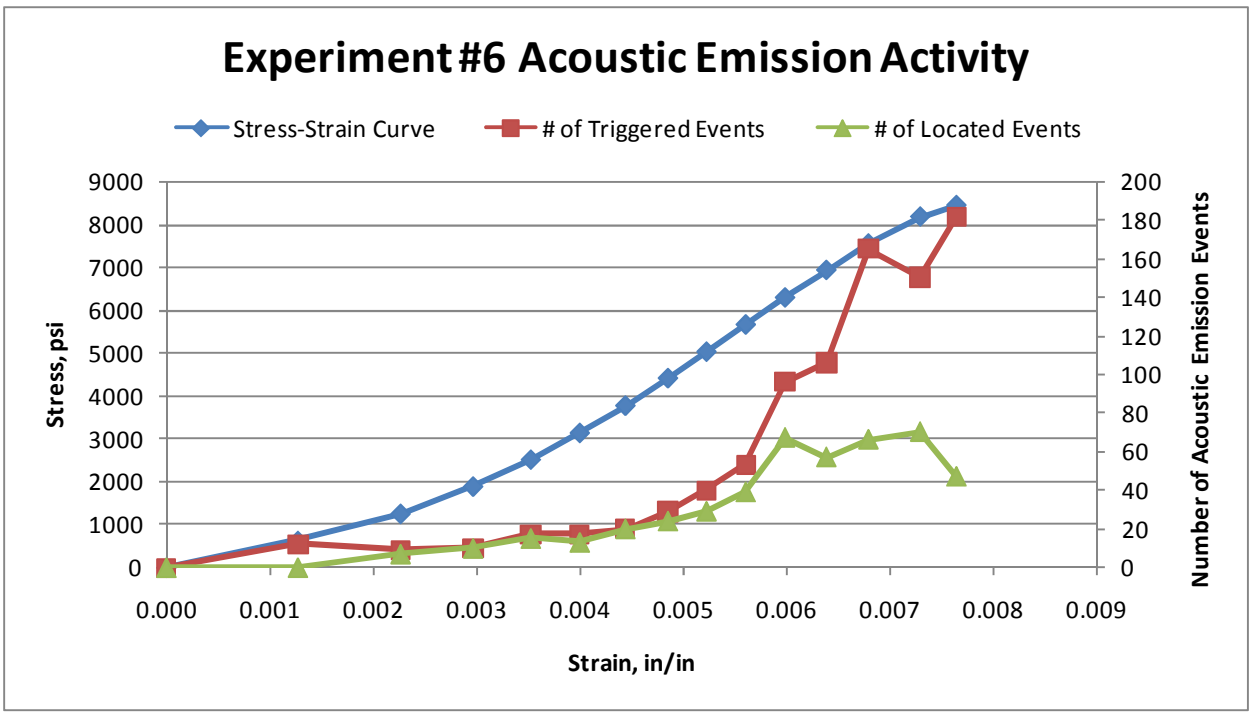

Figure B.11: Plot of Stress-Strain Curve & Acoustic Emission Activity for Experiment #6

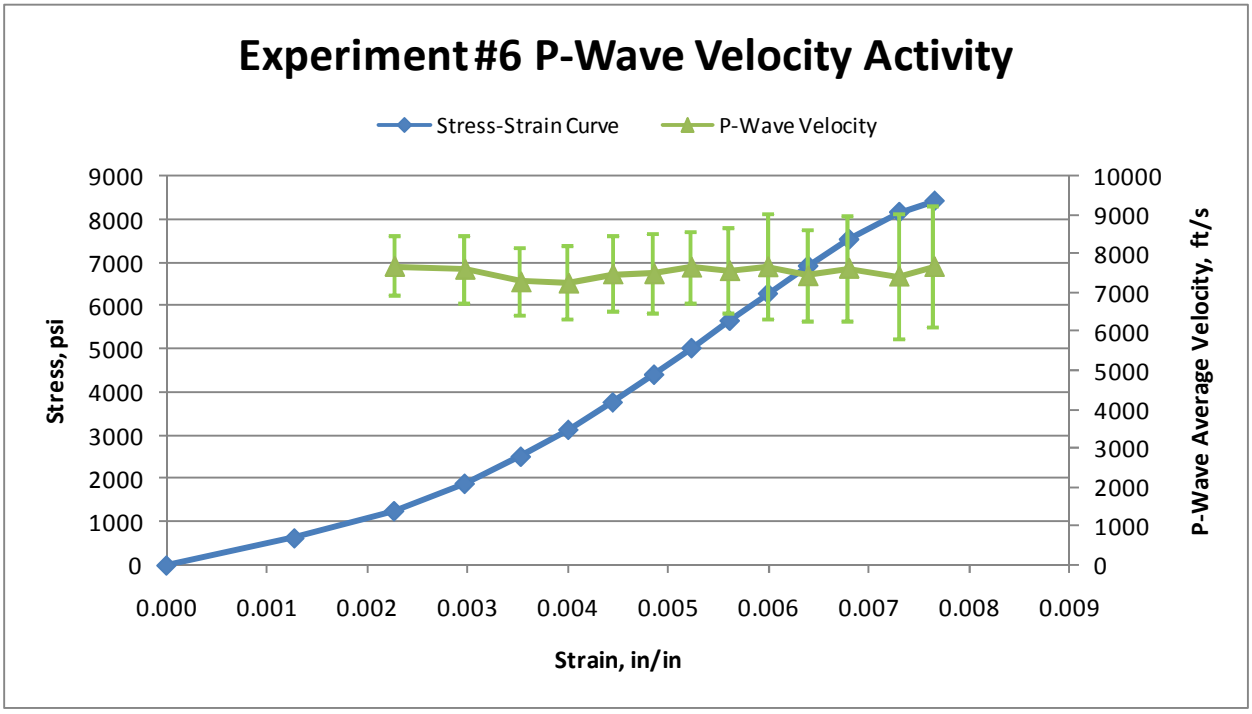

Figure B.12: Plot of Stress-Strain Curve & P-Wave Velocity for Experiment #6

Table B.7: Experiment #7 Acoustic Emission Activity & Loading Summary Statistics

Experiment #7									
Load Pause	Strain	Stress (psi)	Stress (MPa)	Number of Triggered Events	Number of Located Events	Thresh (mV)	Ave. Vel. (ft/s)	Std. Dev. (ft/s)	% Variation
0	0.00000	0	0.0	0	N/A	225	N/A	N/A	N/A
1	0.00061	636	4.4	0	N/A	225	N/A	N/A	N/A
2	0.00131	1266	8.7	0	N/A	175	8052	1739	21.6
3	0.00195	1902	13.1	3	2	225	6977	1023	14.7
4	0.00249	2538	17.5	2	2	225	6977	1023	14.7
5	0.00296	3174	21.9	3	3	225	7214	956	13.3
6	0.00337	3784	26.1	0	N/A	225	N/A	N/A	N/A
7	0.00376	4420	30.5	4	4	225	8018	1376	17.2
8	0.00414	5044	34.8	6	5	225	7269	1090	15.0
9	0.00451	5680	39.2	12	5	225	8436	1521	18.0
10	0.00489	6316	43.5	81	22	250	8015	1504	18.8
11	0.00526	6939	47.8	40	21	250	7647	1222	16.0
12	0.00568	7569	52.2	101	46	250	7620	1546	20.3
13	0.00618	8198	56.5	152	62	250	7803	1573	20.2
14	0.00667	8545	58.9	192	70	250	7639	1771	23.2

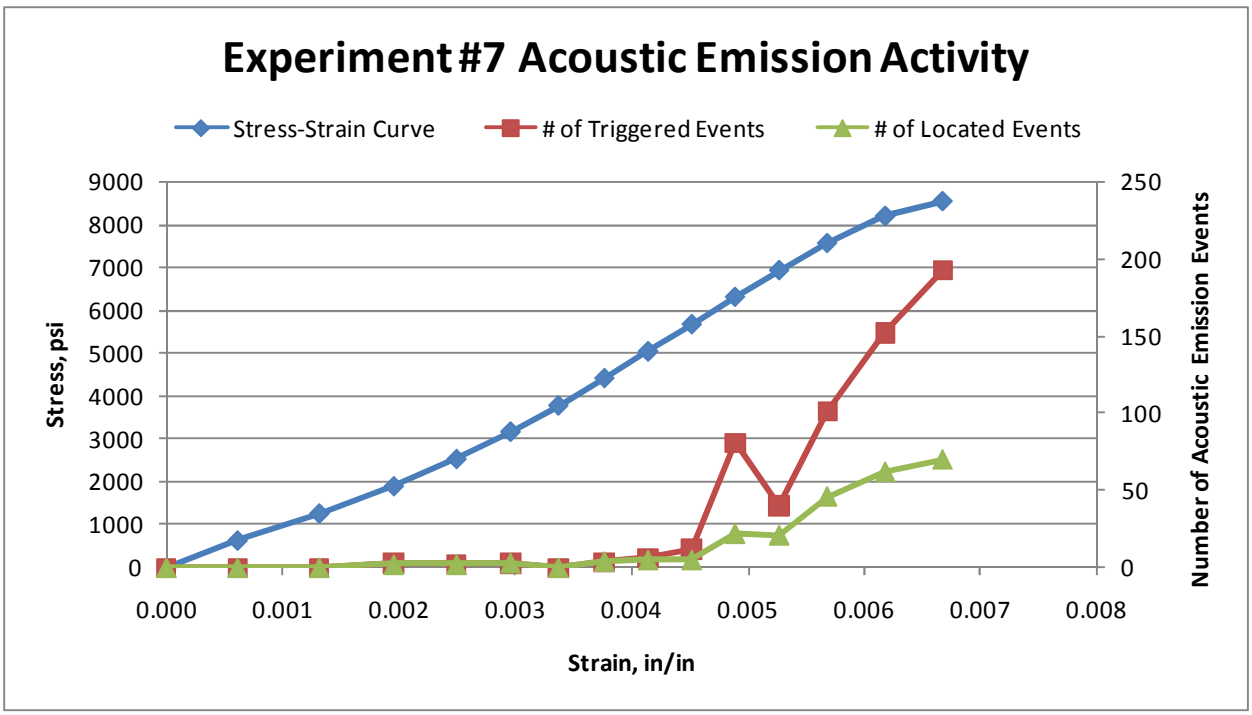

Figure B.13: Plot of Stress-Strain Curve & Acoustic Emission Activity for Experiment #7

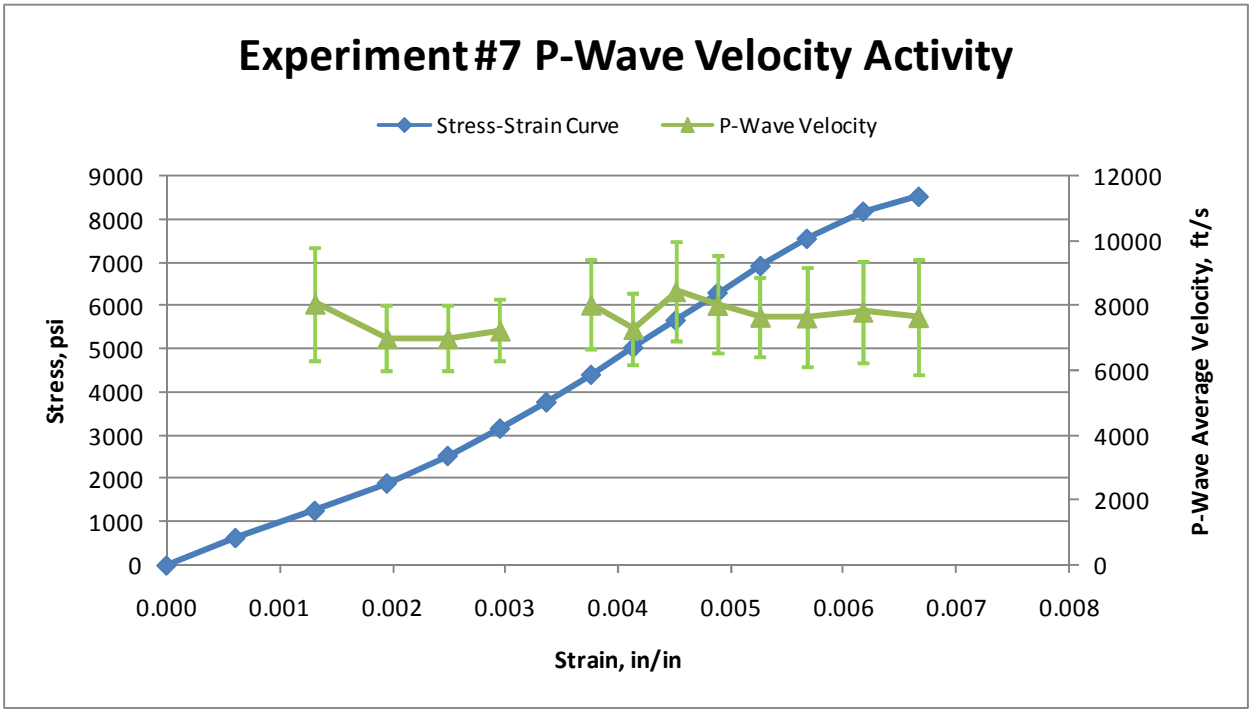

Figure B.14: Plot of Stress-Strain Curve & P-Wave Velocity for Experiment #7

Table B.8: Experiment #8 Acoustic Emission Activity & Loading Summary Statistics

Experiment #8									
Load Pause	Strain	Stress (psi)	Stress (MPa)	Number of Triggered Events	Number of Located Events	Thresh (mV)	Ave. Vel. (ft/s)	Std. Dev. (ft/s)	% Variation
0	0.00000	0	0.0	0	N/A	225	N/A	N/A	N/A
1	0.00135	642	4.4	0	N/A	225	N/A	N/A	N/A
2	0.00231	1259	8.7	0	N/A	225	N/A	N/A	N/A
3	0.00299	1895	13.1	0	N/A	225	N/A	N/A	N/A
4	0.00356	2544	17.5	0	N/A	225	N/A	N/A	N/A
5	0.00403	3155	21.8	0	N/A	225	N/A	N/A	N/A
6	0.00446	3791	26.1	0	N/A	225	N/A	N/A	N/A
7	0.00487	4414	30.4	3	2	225	7105	764	10.7
8	0.00526	5050	34.8	9	8	225	7691	1482	19.3
9	0.00565	5673	39.1	21	18	225	7668	2132	27.8
10	0.00603	6309	43.5	51	44	225	7698	1671	21.7
11	0.00645	6933	47.8	116	90	225	7326	1800	24.6
12	0.00669	7073	48.8	135	64	225	7256	1750	24.1

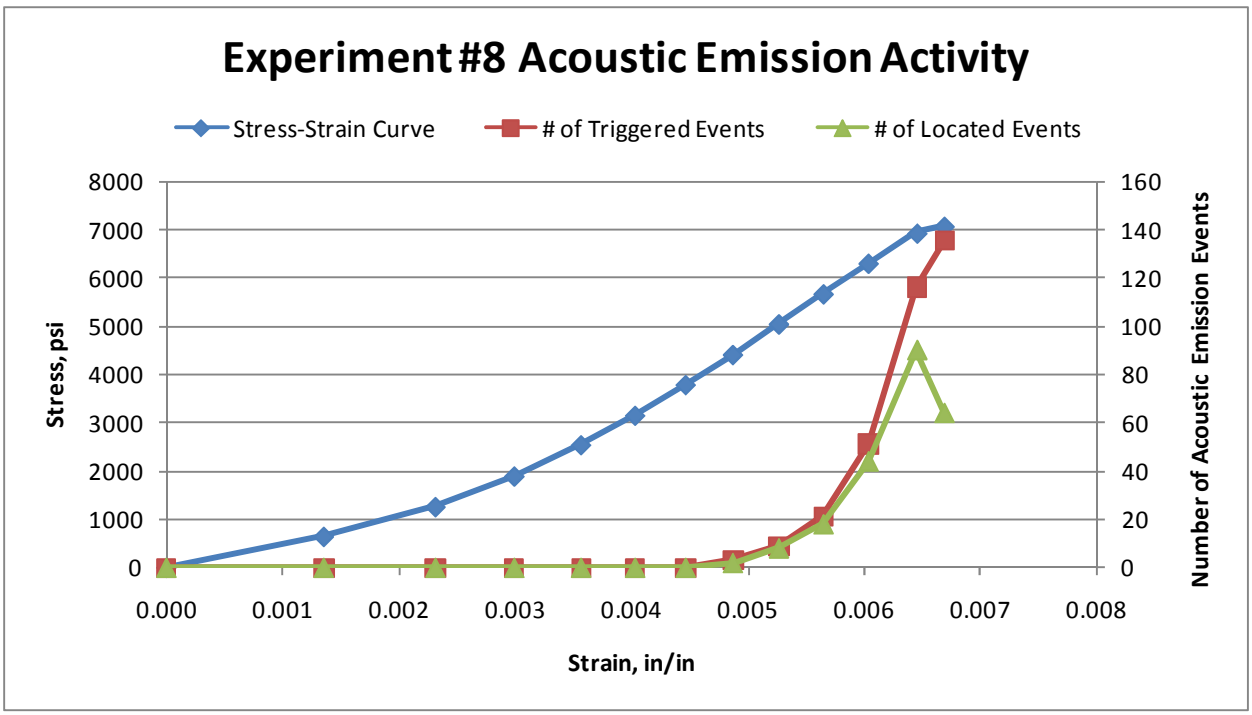

Figure B.15: Plot of Stress-Strain Curve & Acoustic Emission Activity for Experiment #8

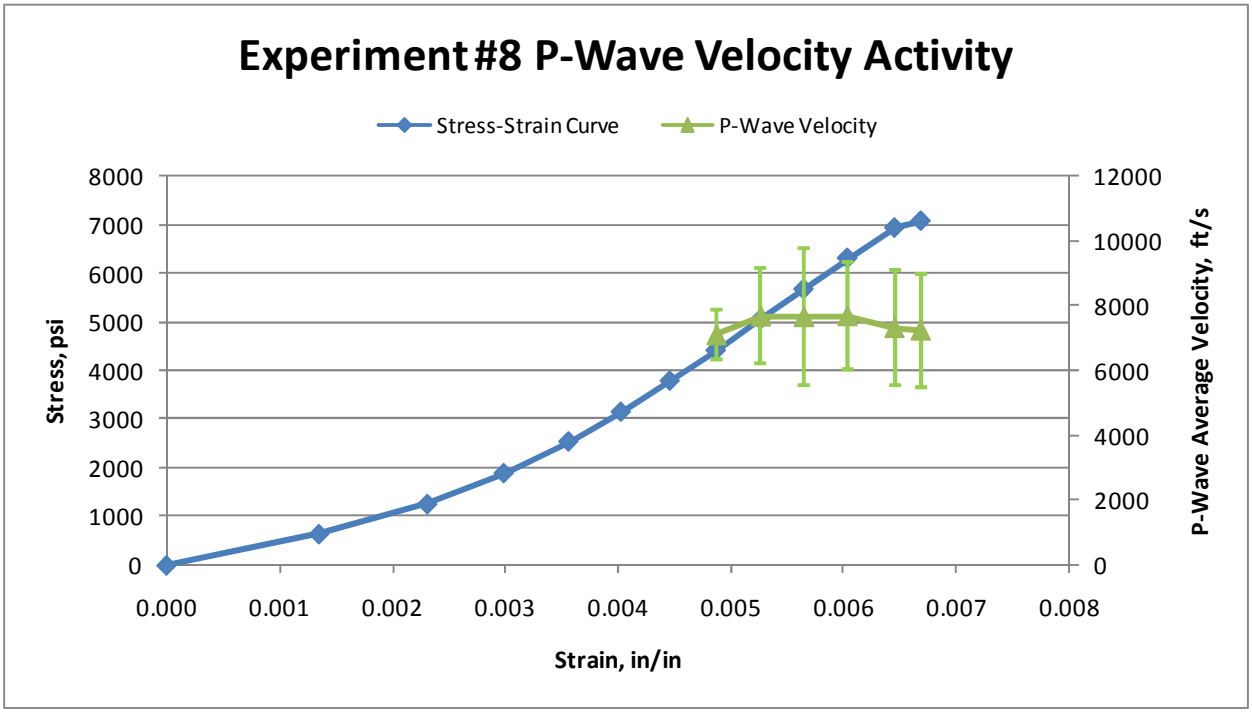

Figure B.16: Plot of Stress-Strain Curve & P-Wave Velocity for Experiment #8

Table B.9: Experiment #9 Acoustic Emission Activity & Loading Summary Statistics

Experiment #9									
Load Pause	Strain	Stress (psi)	Stress (MPa)	Number of Triggered Events	Number of Located Events	Thresh (mV)	Ave. Vel. (ft/s)	Std. Dev. (ft/s)	% Variation
0	0.00000	0	0.0	0	N/A	225	N/A	N/A	N/A
1	0.00163	628	4.3	11	N/A	225	N/A	N/A	N/A
2	0.00263	1263	8.7	0	N/A	225	N/A	N/A	N/A
3	0.00336	1885	13.0	0	N/A	225	N/A	N/A	N/A
4	0.00394	2520	17.4	0	N/A	225	N/A	N/A	N/A
5	0.00446	3155	21.8	0	N/A	225	N/A	N/A	N/A
6	0.00493	3802	26.2	3	1	225	8502	620	7.3
7	0.00536	4418	30.5	1	1	225	6240	1165	18.7
8	0.00577	5046	34.8	18	12	225	7532	1394	18.5
9	0.00617	5668	39.1	34	21	225	7722	1291	16.7
10	0.00657	6291	43.4	121	68	225	7608	1574	20.7
11	0.00700	6925	47.7	160	63	225	7529	1780	23.6
12	0.00737	7474	51.5	195	74	225	7487	1722	23.0

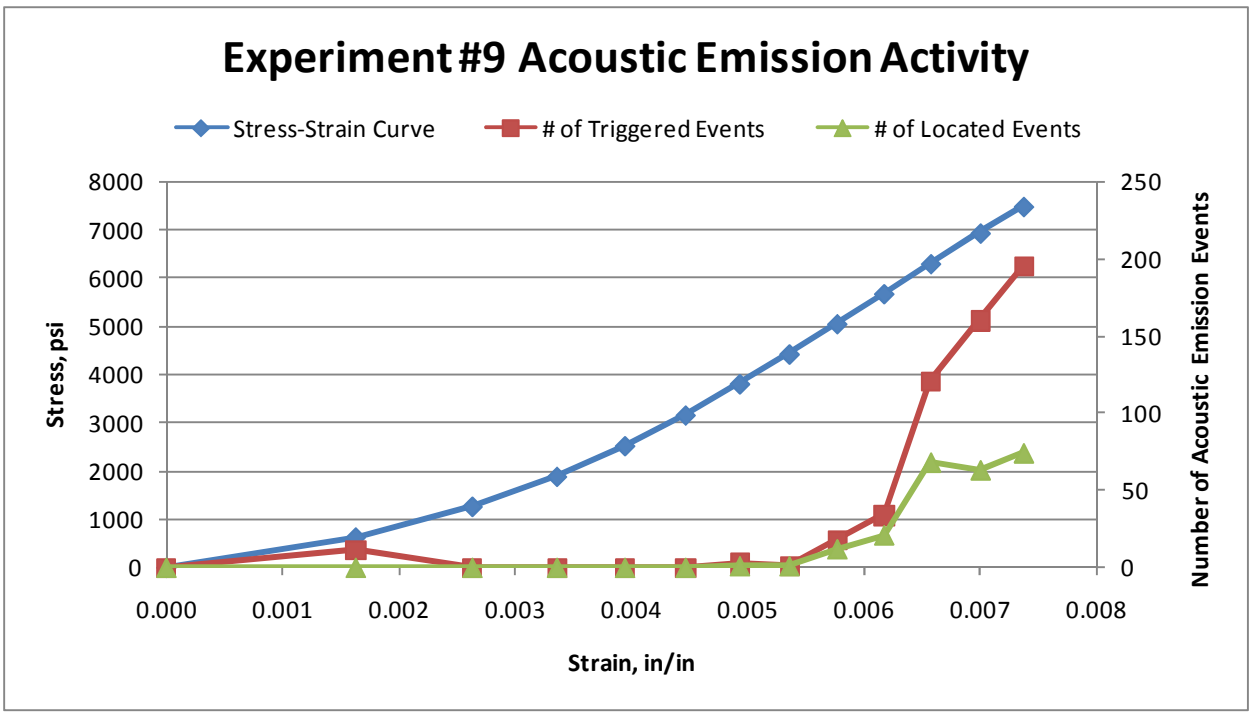

Figure B.17: Plot of Stress-Strain Curve & Acoustic Emission Activity for Experiment #9

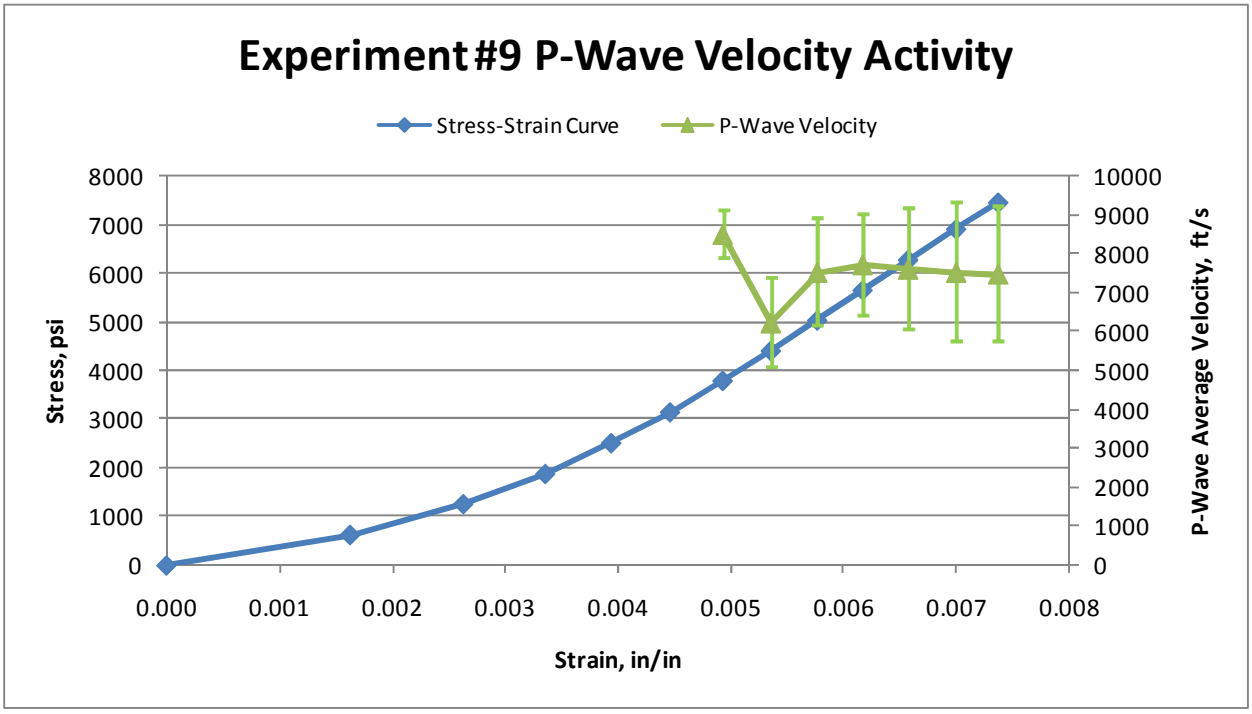

Figure B.18: Plot of Stress-Strain Curve & P-Wave Velocity for Experiment #9

Table B.10: Experiment #10 Acoustic Emission Activity & Loading Summary Statistics

Experiment #10									
Load Pause	Strain	Stress (psi)	Stress (MPa)	Number of Triggered Events	Number of Located Events	Thresh (mV)	Ave. Vel. (ft/s)	Std. Dev. (ft/s)	% Variation
0	0.00000	0	0.0	0	N/A	225	N/A	N/A	N/A
1	0.00140	630	4.3	3	0	225	N/A	N/A	N/A
2	0.00237	1272	8.8	0	N/A	225	N/A	N/A	N/A
3	0.00305	1895	13.1	0	N/A	225	N/A	N/A	N/A
4	0.00360	2525	17.4	1	1	225	6711	989	14.7
5	0.00409	3155	21.8	6	5	225	6964	1234	17.7
6	0.00452	3791	26.1	2	2	225	8478	1143	13.5
7	0.00492	4408	30.4	10	4	225	7350	930	12.7
8	0.00531	5044	34.8	55	21	225	7660	1374	17.9
9	0.00569	5673	39.1	87	21	250	7506	1714	22.8
10	0.00607	6309	43.5	171	35	250	7487	1548	20.7
11	0.00647	6958	48.0	154	39	275	7452	1553	20.8
12	0.00686	7556	52.1	155	58	325	7513	1644	21.9
13	0.00735	8192	56.5	113	60	325	7238	1459	20.2
14	0.00764	8457	58.3	136	60	325	7458	1625	21.8

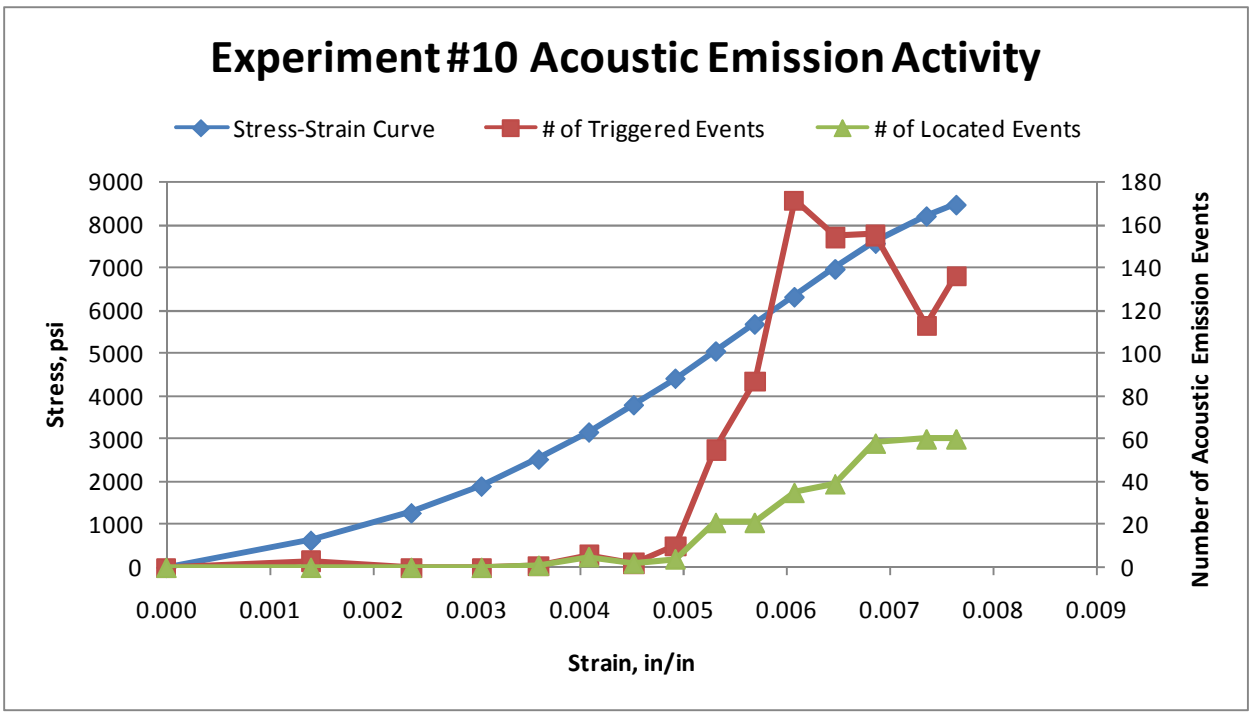

Figure B.19: Plot of Stress-Strain Curve & Acoustic Emission Activity for Experiment #10

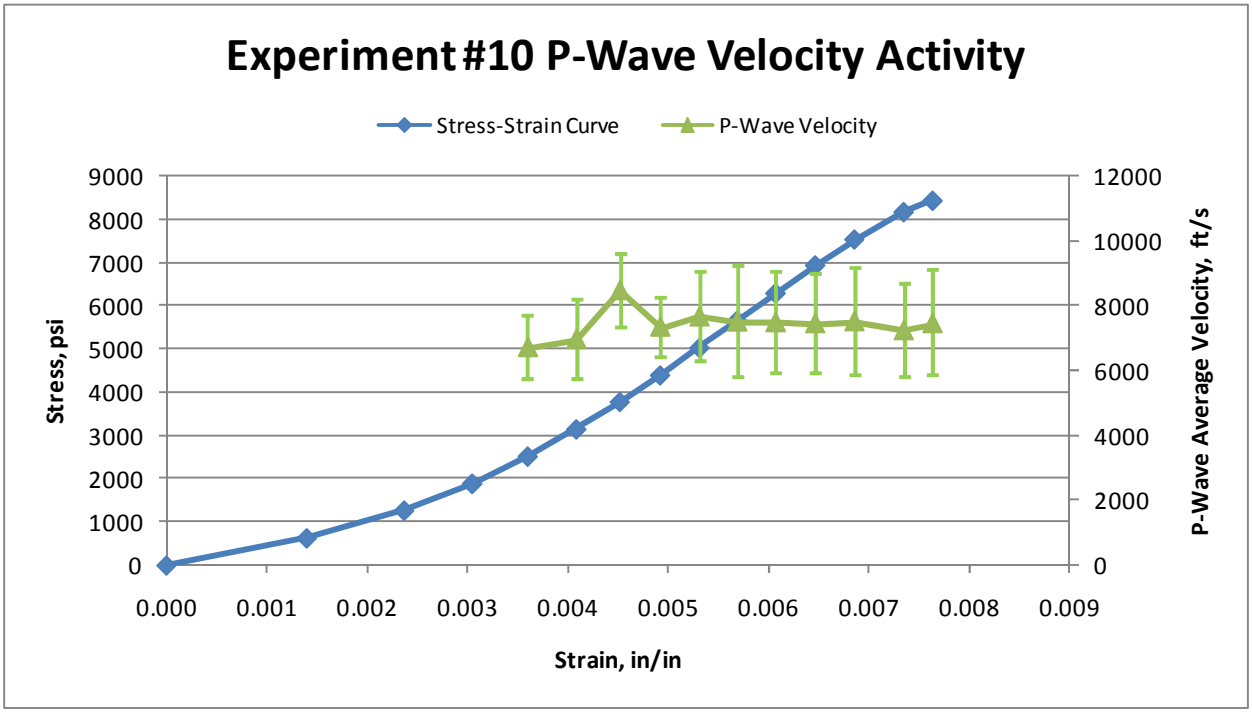

Figure B.20: Plot of Stress-Strain Curve & P-Wave Velocity for Experiment #10

Table B.11: Experiment #11 Acoustic Emission Activity & Loading Summary Statistics

Experiment #11									
Load Pause	Strain	Stress (psi)	Stress (MPa)	Number of Triggered Events	Number of Located Events	Thresh (mV)	Ave. Vel. (ft/s)	Std. Dev. (ft/s)	% Variation
0	0.00000	0	0.0	0	N/A	225	N/A	N/A	N/A
1	0.00123	628	4.3	1	N/A	225	N/A	N/A	N/A
2	0.00203	1257	8.7	24	23	225	7506	716	9.5
3	0.00266	1892	13.0	54	47	225	7555	1005	13.3
4	0.00321	2520	17.4	87	85	225	7634	821	10.8
5	0.00367	3148	21.7	94	87	225	7568	826	10.9
6	0.00409	3783	26.1	88	81	225	7665	936	12.2
7	0.00449	4418	30.5	94	85	225	7556	898	11.9
8	0.00486	5034	34.7	87	77	225	7616	901	11.8
9	0.00523	5656	39.0	99	84	225	7506	1000	13.3
10	0.00560	6303	43.5	122	87	225	7443	1152	15.5
11	0.00597	6925	47.7	83	60	275	7460	1119	15.0
12	0.00637	7560	52.1	71	55	275	7520	1255	16.7
13	0.00682	8176	56.4	146	117	325	7499	1256	16.8
14	0.00741	8705	60.0	164	83	325	7591	1470	19.4

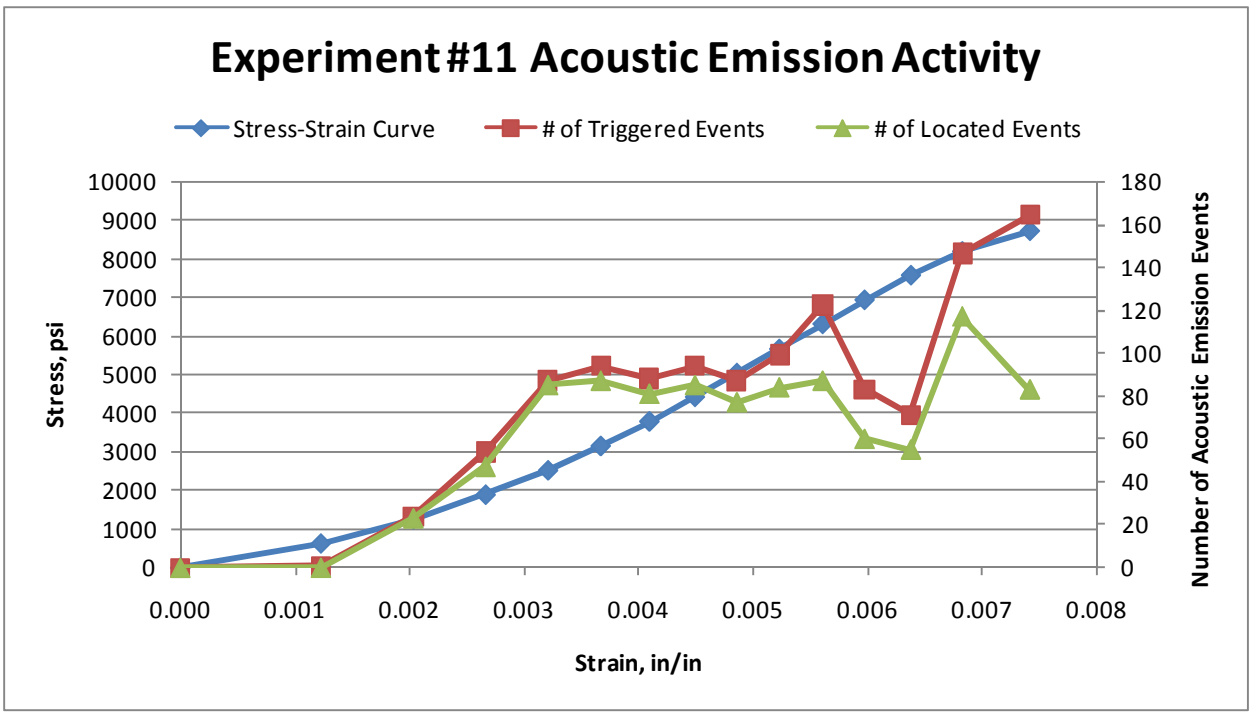

Figure B.21: Plot of Stress-Strain Curve & Acoustic Emission Activity for Experiment #11

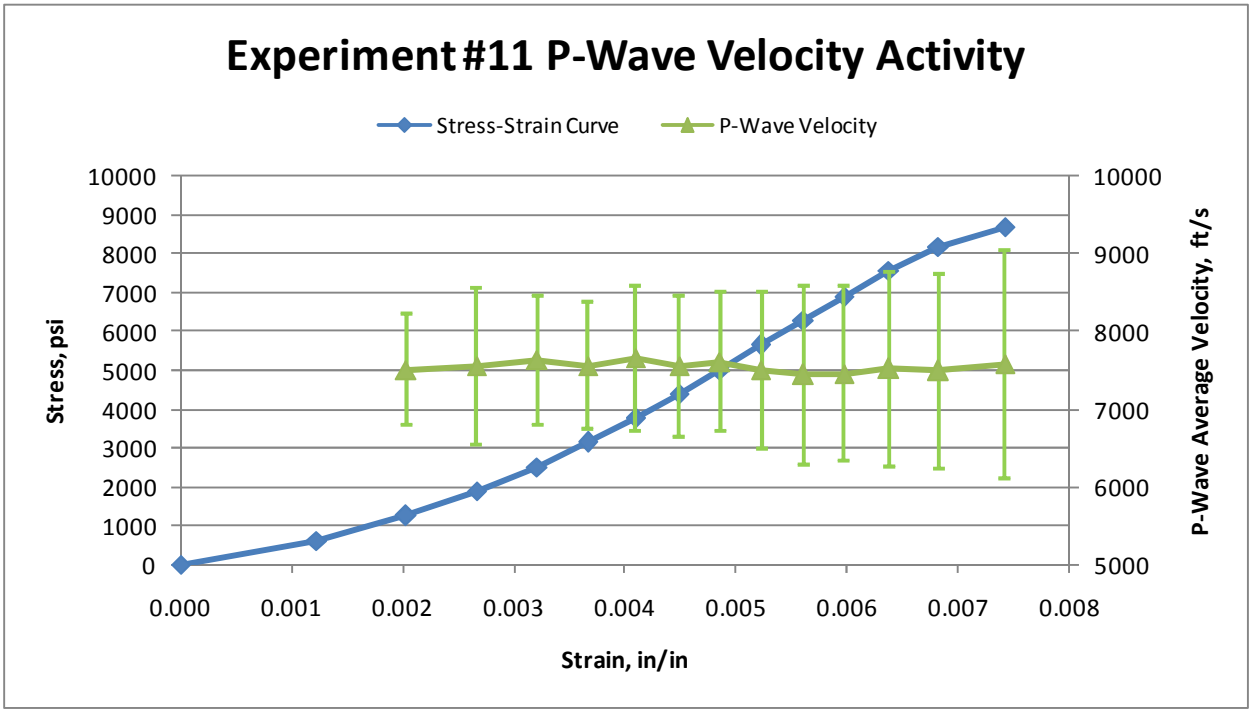

Figure B.22: Plot of Stress-Strain Curve & P-Wave Velocity for Experiment #11

Table B.12: Experiment #12 Acoustic Emission Activity & Loading Summary Statistics

Experiment #12									
Load Pause	Strain	Stress (psi)	Stress (MPa)	Number of Triggered Events	Number of Located Events	Thresh (mV)	Ave. Vel. (ft/s)	Std. Dev. (ft/s)	% Variation
0	0.00000	0	0.0	0	N/A	225	N/A	N/A	N/A
1	0.00155	635	4.4	4	N/A	225	N/A	N/A	N/A
2	0.00233	1263	8.7	3	N/A	225	N/A	N/A	N/A
3	0.00288	1892	13.0	3	3	225	7991	775	9.7
4	0.00335	2526	17.4	8	6	225	7744	1130	14.6
5	0.00379	3167	21.8	21	16	225	7715	1187	15.4
6	0.00423	3808	26.3	29	24	225	7676	1315	17.1
7	0.00461	4405	30.4	45	35	225	7620	1237	16.2
8	0.00502	5034	34.7	84	65	275	7584	1344	17.7
9	0.00542	5668	39.1	48	40	275	7691	1236	16.1
10	0.00582	6297	43.4	85	69	275	7562	1480	19.6
11	0.00627	6932	47.8	106	65	325	7517	1560	20.8
12	0.00649	7157	49.3	409	148	325	8102	1815	22.4

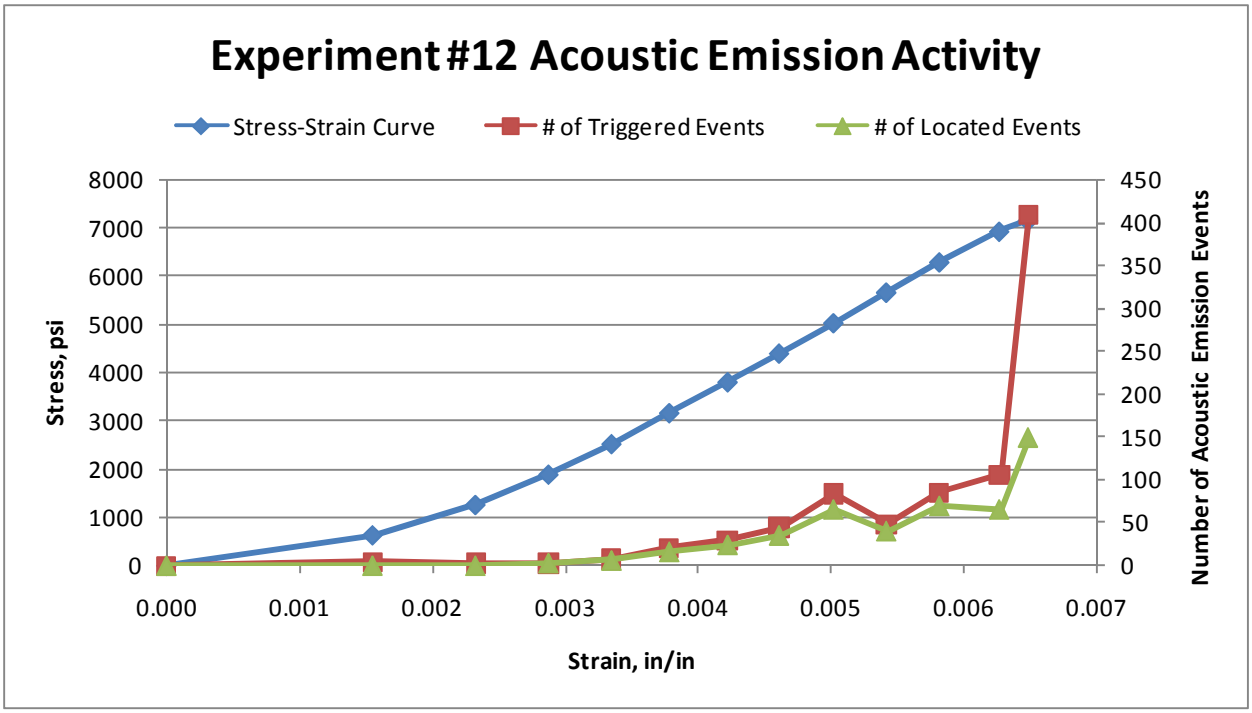

Figure B.23: Plot of Stress-Strain Curve & Acoustic Emission Activity for Experiment #12

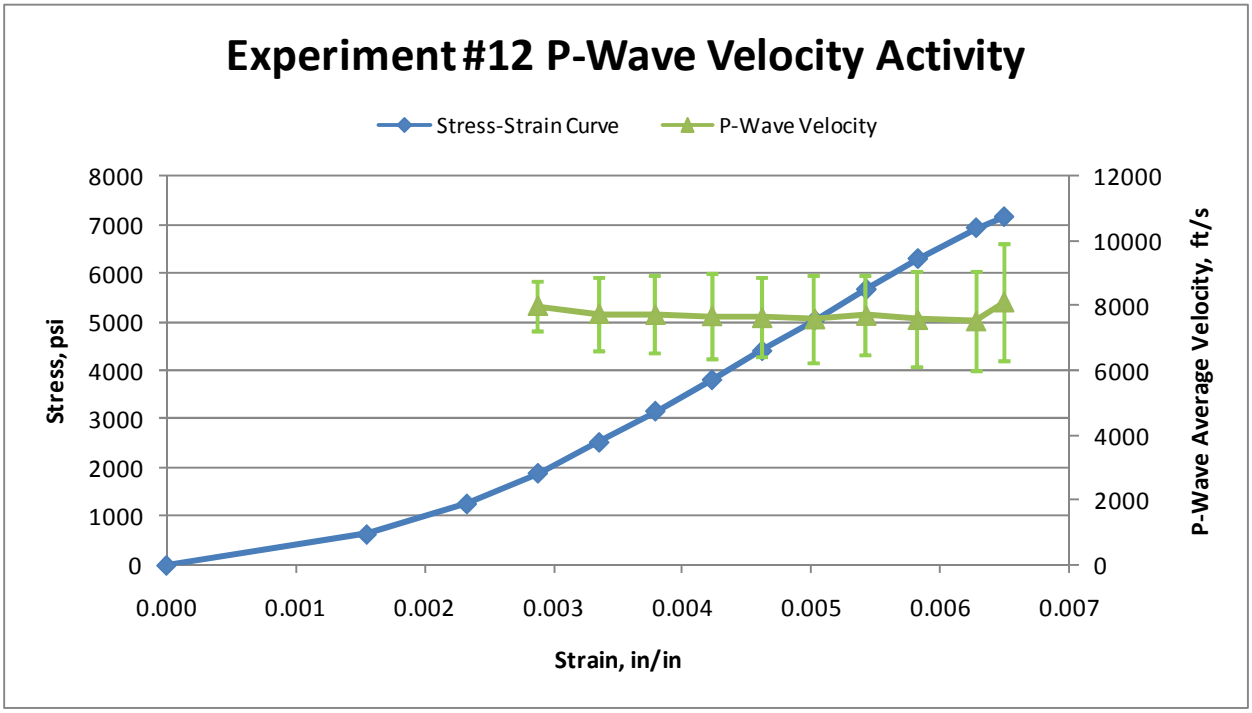

Figure B.24: Plot of Stress-Strain Curve & P-Wave Velocity for Experiment #12

Table B.13: Experiment #13 Acoustic Emission Activity & Loading Summary Statistics

Experiment #13									
Load Pause	Strain	Stress (psi)	Stress (MPa)	Number of Triggered Events	Number of Located Events	Thresh (mV)	Ave. Vel. (ft/s)	Std. Dev. (ft/s)	% Variation
0	0.00000	0	0.0	0	N/A	225	N/A	N/A	N/A
1	0.00059	629	4.3	0	N/A	225	N/A	N/A	N/A
2	0.00161	1271	8.8	1	1	225	7171	1098	15.3
3	0.00232	1893	13.1	2	1	225	7608	851	11.2
4	0.00288	2529	17.4	1	1	225	7643	653	8.5
5	0.00334	3152	21.7	0	N/A	225	N/A	N/A	N/A
6	0.00377	3793	26.2	1	1	225	6820	1069	15.7
7	0.00415	4422	30.5	2	2	225	7930	1031	13.0
8	0.00453	5045	34.8	5	4	225	8398	1365	16.3
9	0.00491	5687	39.2	14	11	250	7429	1390	18.7
10	0.00527	6297	43.4	16	14	250	7703	1324	17.2
11	0.00564	6920	47.7	36	27	250	7703	1343	17.4
12	0.00605	7555	52.1	47	36	275	7745	1672	21.6
13	0.00653	8190	56.5	82	54	325	7515	1503	20.0
14	0.00692	8683	59.9	144	51	325	8003	1923	24.0

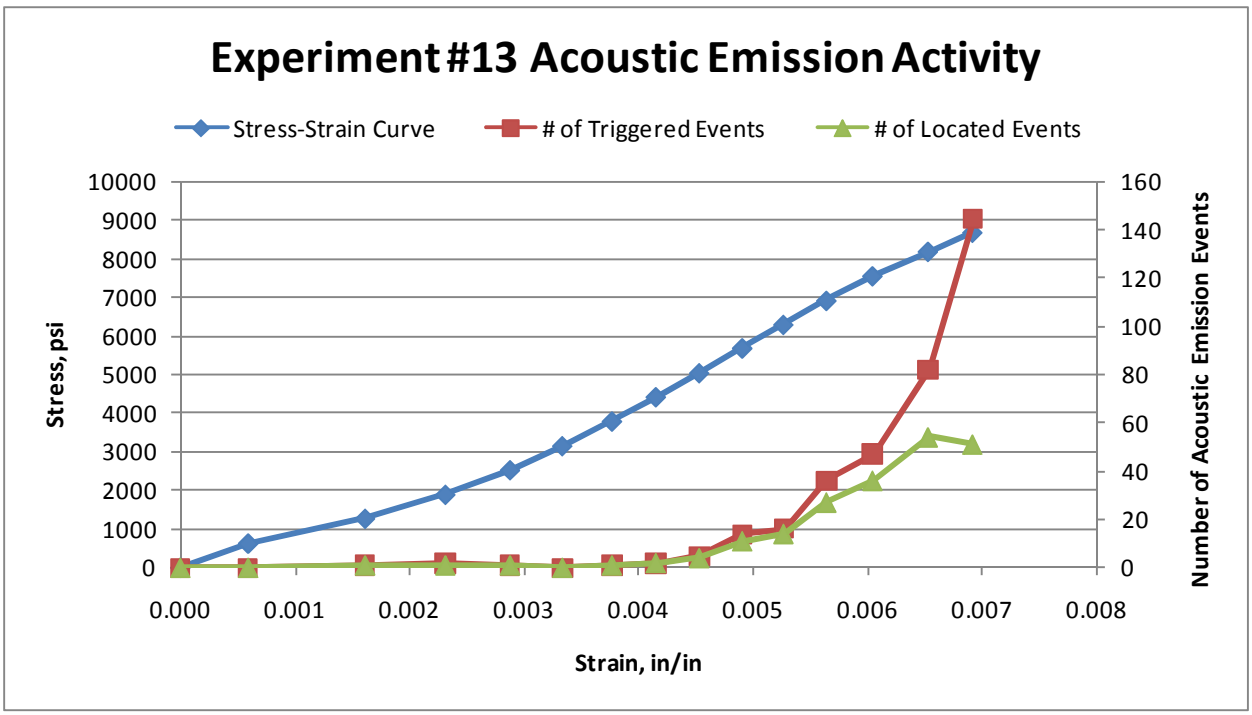

Figure B.25: Plot of Stress-Strain Curve & Acoustic Emission Activity for Experiment #13

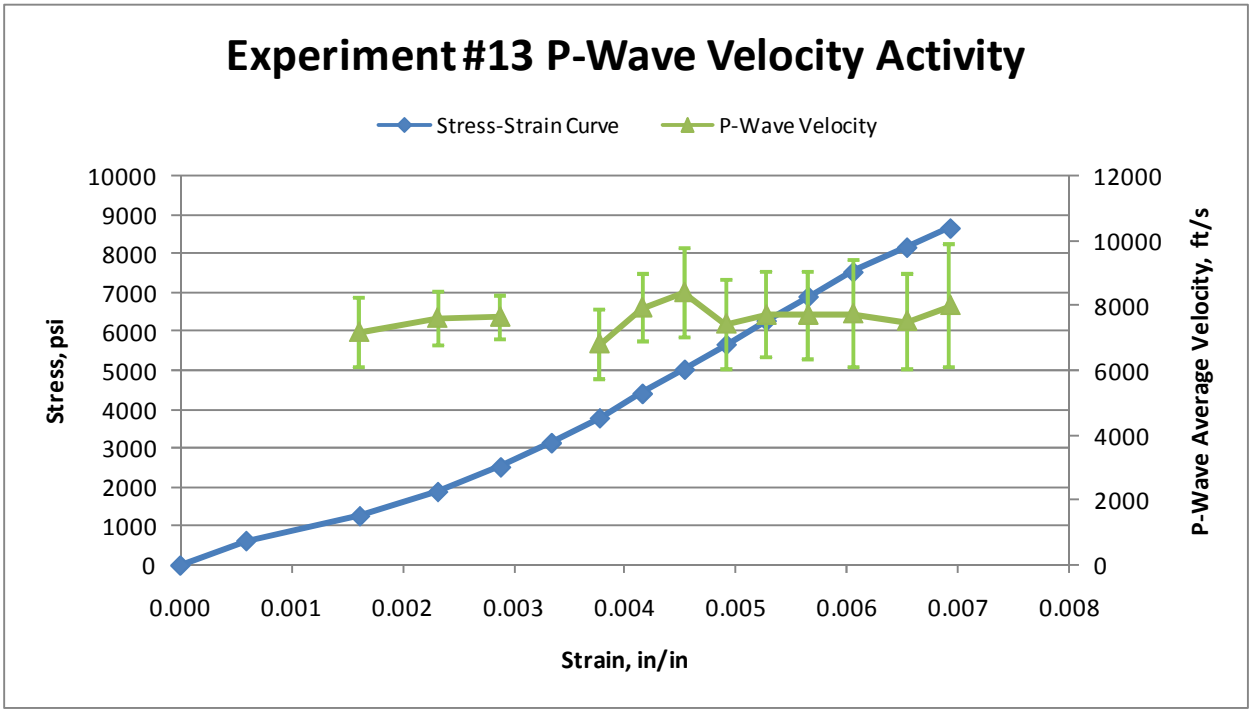

Figure B.26: Plot of Stress-Strain Curve & P-Wave Velocity for Experiment #13

Table B.14: Experiment #14 Acoustic Emission Activity & Loading Summary Statistics

Experiment #14									
Load Pause	Strain	Stress (psi)	Stress (MPa)	Number of Triggered Events	Number of Located Events	Thresh (mV)	Ave. Vel. (ft/s)	Std. Dev. (ft/s)	% Variation
0	0.00000	0	0.0	0	N/A	225	N/A	N/A	N/A
1	0.00071	629	4.3	0	N/A	225	N/A	N/A	N/A
2	0.00166	1258	8.7	1	N/A	225	N/A	N/A	N/A
3	0.00234	1893	13.1	1	1	225	7464	498	6.7
4	0.00290	2522	17.4	0	N/A	225	N/A	N/A	N/A
5	0.00336	3152	21.7	1	1	225	8380	466	5.6
6	0.00382	3825	26.4	1	1	225	7751	504	6.5
7	0.00417	4410	30.4	2	2	225	7511	1047	13.9
8	0.00456	5032	34.7	0	N/A	225	N/A	N/A	N/A
9	0.00493	5674	39.1	9	7	225	7498	1432	19.1
10	0.00530	6297	43.4	38	19	275	7853	1499	19.1
11	0.00568	6926	47.8	23	15	275	7794	1594	20.4
12	0.00608	7549	52.0	27	15	275	7269	1429	19.7
13	0.00658	8190	56.5	73	41	325	7491	1633	21.8
14	0.00705	8594	59.3	137	40	325	7511	1787	23.8

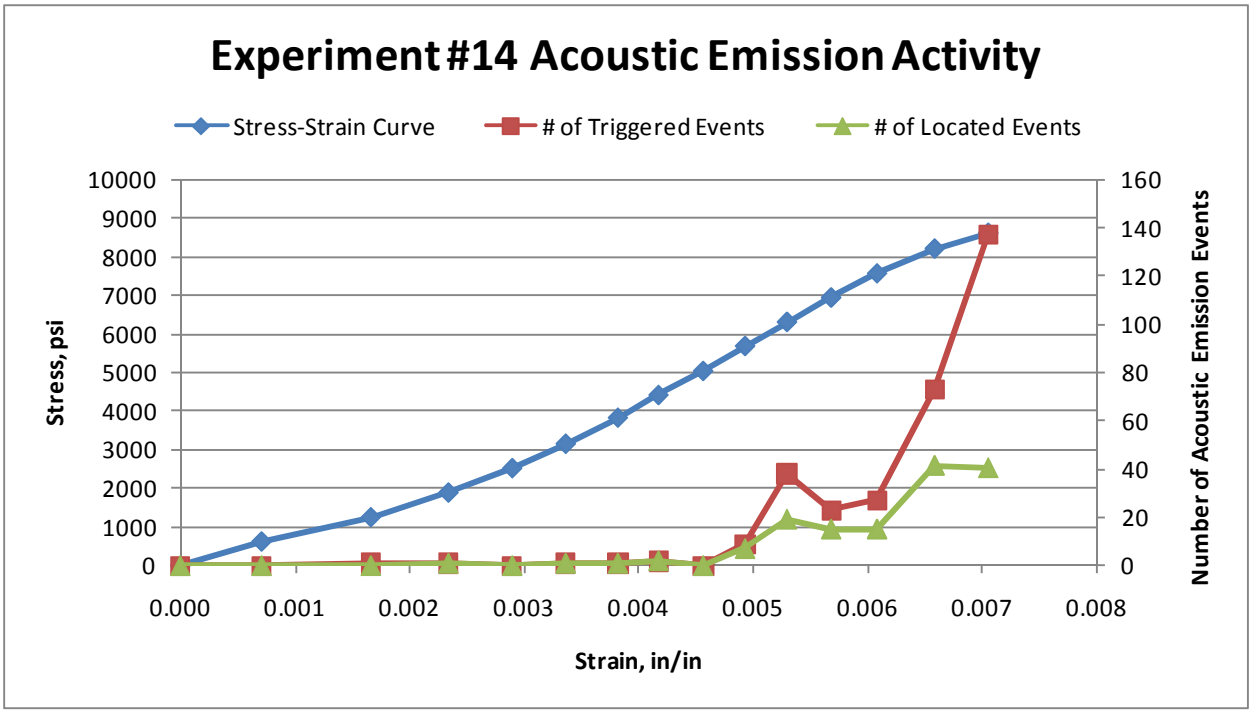

Figure B.27: Plot of Stress-Strain Curve & Acoustic Emission Activity for Experiment #14

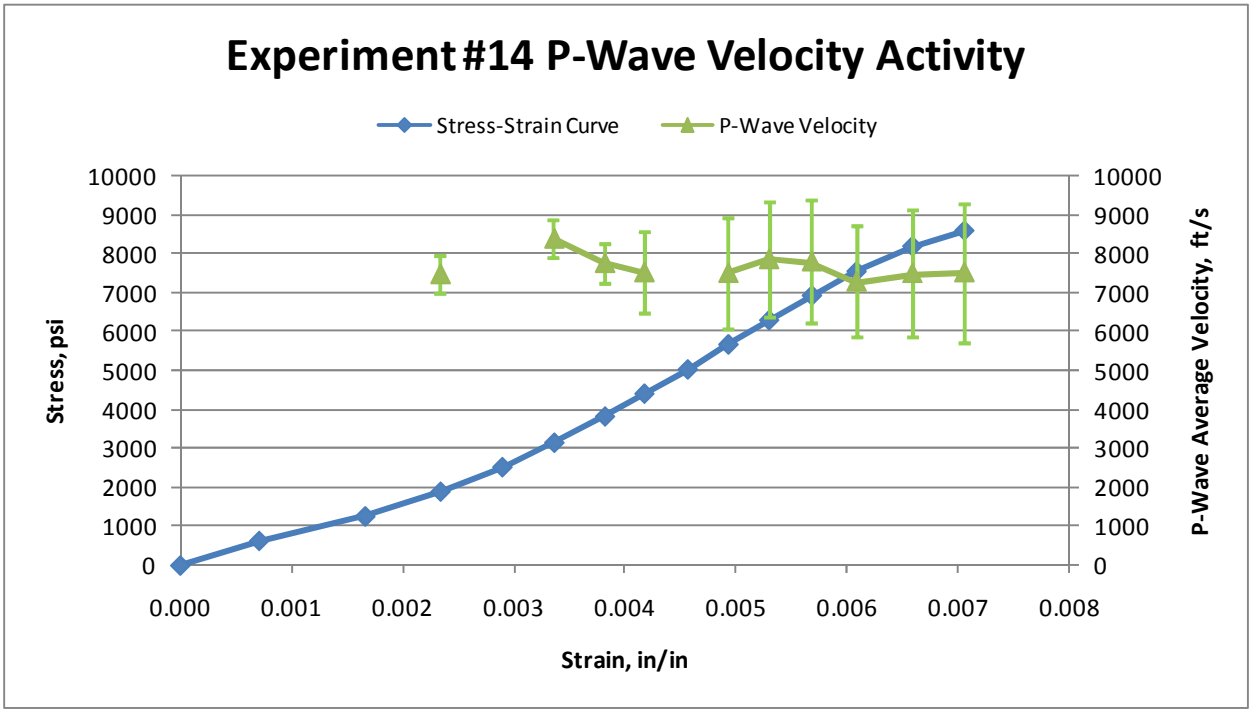

Figure B.28: Plot of Stress-Strain Curve & P-Wave Velocity for Experiment #14

Table B.15: Experiment #15 Acoustic Emission Activity & Loading Summary Statistics

Experiment #15									
Load Pause	Strain	Stress (psi)	Stress (MPa)	Number of Triggered Events	Number of Located Events	Thresh (mV)	Ave. Vel. (ft/s)	Std. Dev. (ft/s)	% Variation
0	0.00000	0	0.0	0	N/A	225	N/A	N/A	N/A
1	0.00127	629	4.3	0	N/A	225	N/A	N/A	N/A
2	0.00204	1258	8.7	0	N/A	225	N/A	N/A	N/A
3	0.00270	1893	13.1	0	N/A	225	N/A	N/A	N/A
4	0.00324	2535	17.5	1	1	225	7745	411	5.3
5	0.00370	3158	21.8	1	1	225	8001	1012	12.6
6	0.00411	3781	26.1	1	1	225	8268	1098	13.3
7	0.00451	4416	30.4	3	3	225	7509	1103	14.7
8	0.00489	5045	34.8	1	1	225	8306	1013	12.2
9	0.00526	5680	39.2	8	5	225	7532	1254	16.6
10	0.00562	6290	43.4	16	14	300	7576	1706	22.5
11	0.00602	6926	47.8	11	7	300	7227	1336	18.5
12	0.00641	7561	52.1	12	8	300	7316	1243	17.0
13	0.00687	8184	56.4	26	21	300	7634	1560	20.4
14	0.00754	8671	59.8	238	126	300	7183	1571	21.9

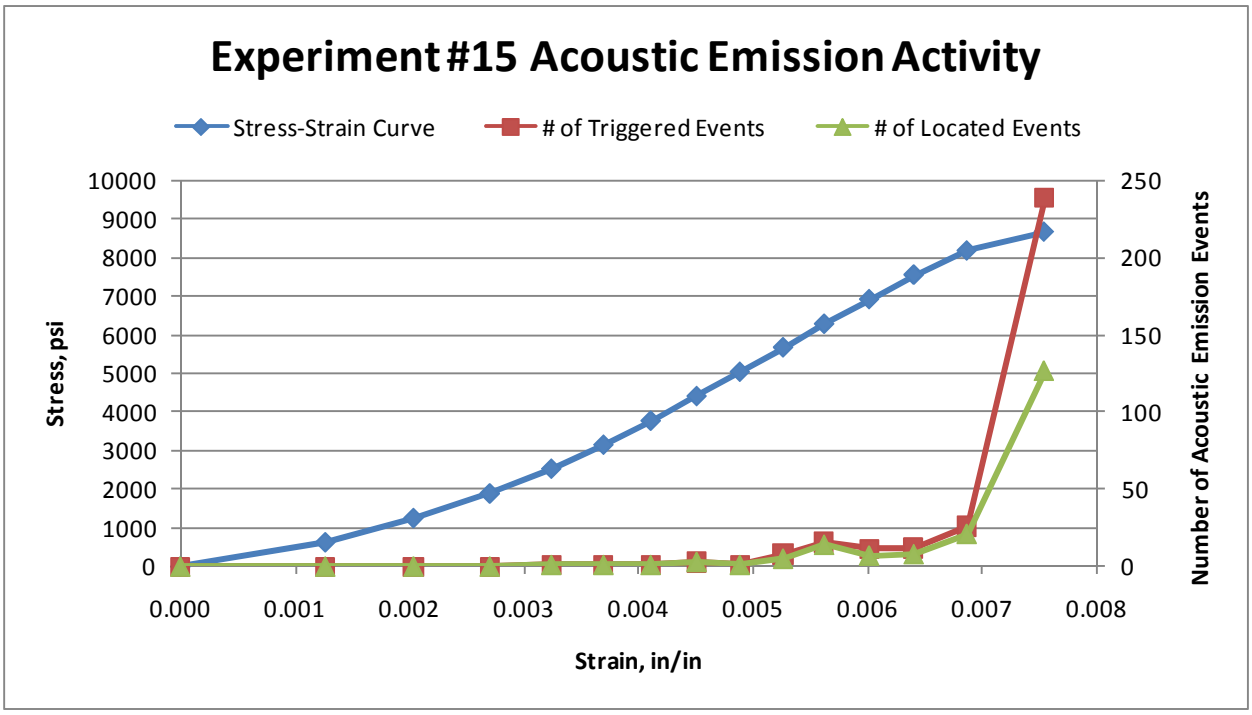

Figure B.29: Plot of Stress-Strain Curve & Acoustic Emission Activity for Experiment #15

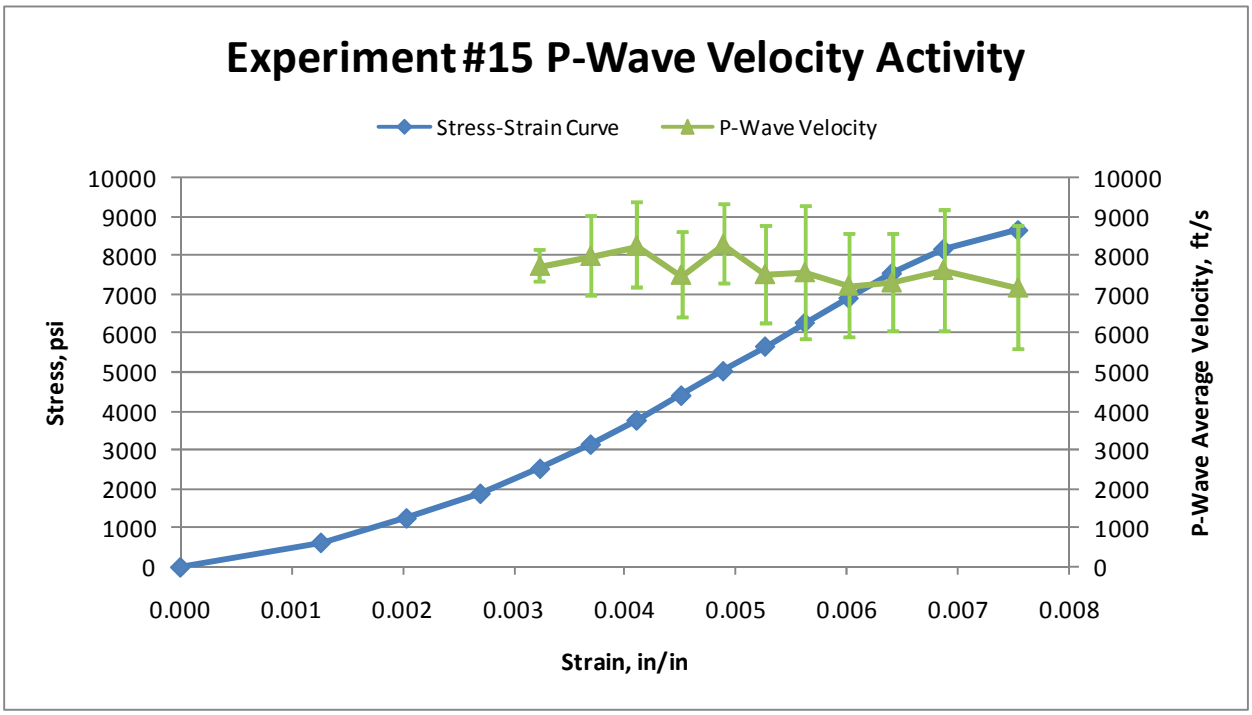

Figure B.30: Plot of Stress-Strain Curve & P-Wave Velocity for Experiment #15

Table B.16: Experiment #16 Acoustic Emission Activity & Loading Summary Statistics

Experiment #16									
Load Pause	Strain	Stress (psi)	Stress (MPa)	Number of Triggered Events	Number of Located Events	Thresh (mV)	Ave. Vel. (ft/s)	Std. Dev. (ft/s)	% Variation
0	0.00000	0	0.0	0	N/A	225	N/A	N/A	N/A
1	0.00231	630	4.3	40	N/A	225	N/A	N/A	N/A
2	0.00321	1266	8.7	0	N/A	225	N/A	N/A	N/A
3	0.00387	1902	13.1	0	N/A	225	N/A	N/A	N/A
4	0.00439	2519	17.4	0	N/A	225	N/A	N/A	N/A
5	0.00486	3155	21.8	2	2	225	7851	674	8.6
6	0.00529	3791	26.1	1	1	225	7506	654	8.7
7	0.00568	4414	30.4	1	1	225	7528	628	8.3
8	0.00607	5050	34.8	3	3	225	7507	1081	14.4
9	0.00645	5680	39.2	8	6	225	7581	1209	15.9
10	0.00682	6297	43.4	36	21	225	7522	1094	14.5
11	0.00721	6933	47.8	15	15	300	7459	1082	14.5
12	0.00763	7562	52.1	28	21	300	7469	1412	18.9
13	0.00815	8186	56.4	61	44	300	7891	1598	20.2
14	0.00841	8476	58.4	107	43	300	8363	1860	22.2

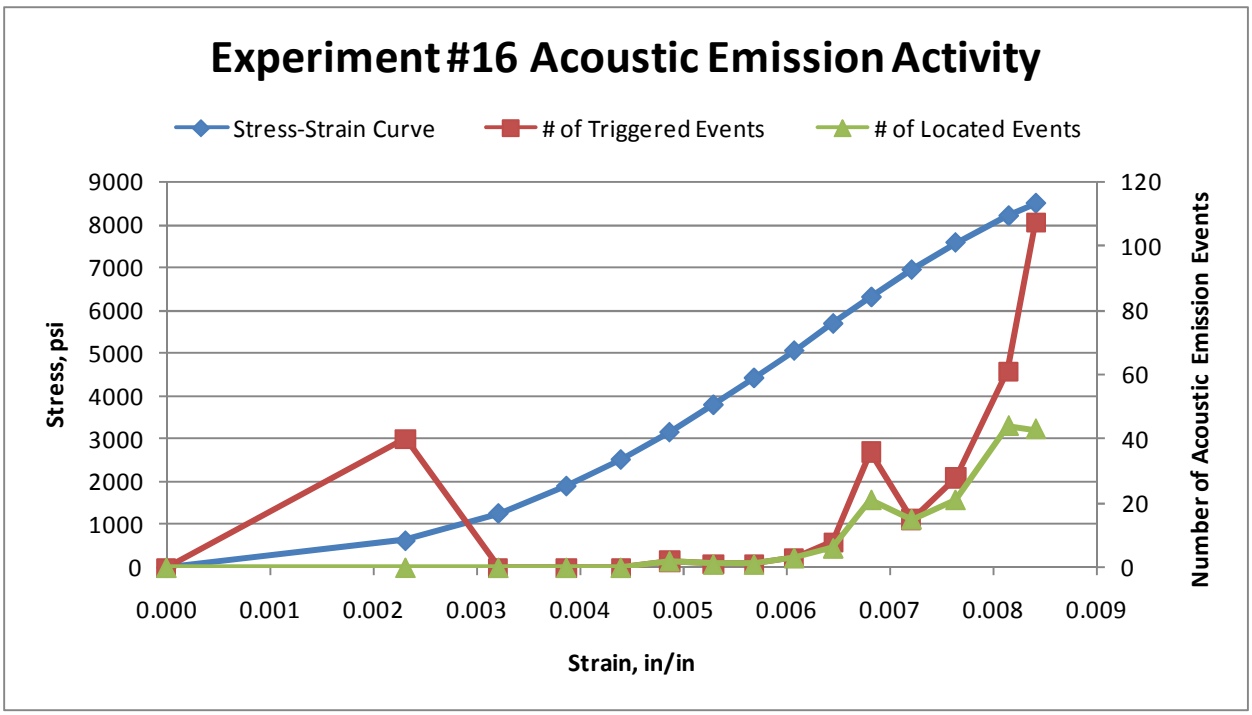

Figure B.31: Plot of Stress-Strain Curve & Acoustic Emission Activity for Experiment #16

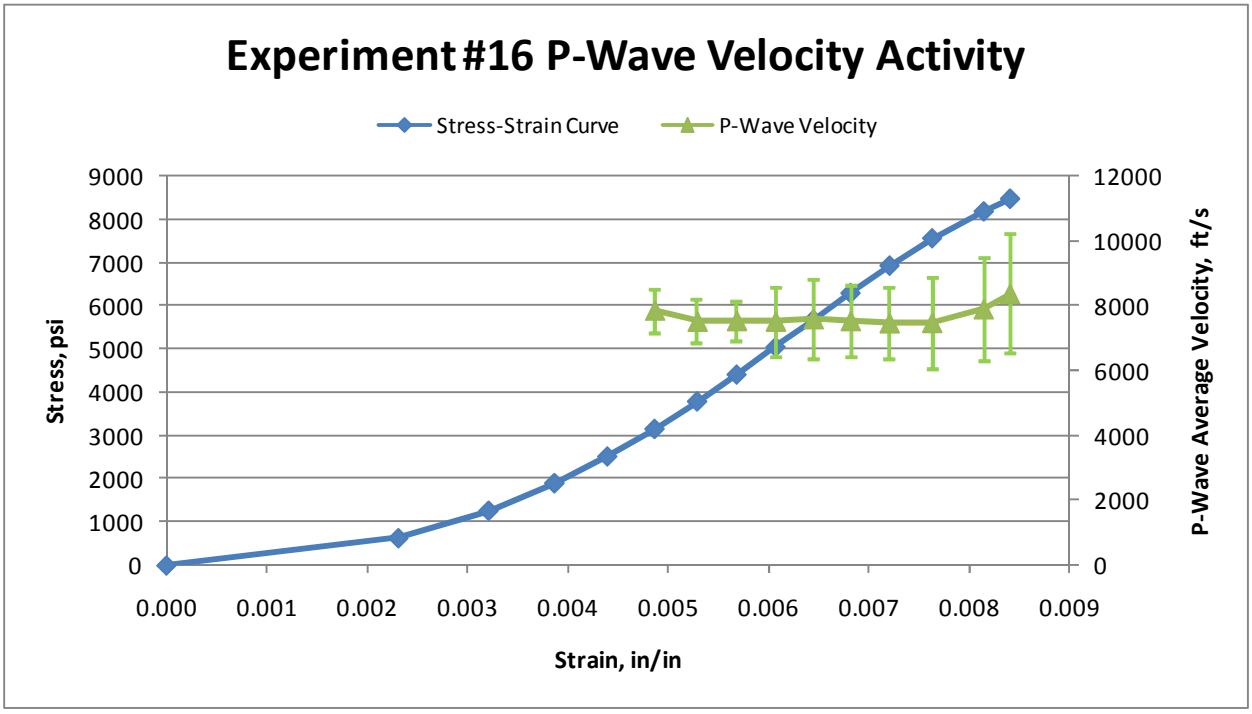

Figure B.32: Plot of Stress-Strain Curve & P-Wave Velocity for Experiment #16

Table B.17: Experiment #17 Acoustic Emission Activity & Loading Summary Statistics

Experiment #17									
Load Pause	Strain	Stress (psi)	Stress (MPa)	Number of Triggered Events	Number of Located Events	Thresh (mV)	Ave. Vel. (ft/s)	Std. Dev. (ft/s)	% Variation
0	0.00000	0	0.0	0	N/A	225	N/A	N/A	N/A
1	0.00210	629	4.3	4	N/A	225	N/A	N/A	N/A
2	0.00308	1264	8.7	4	2	225	7741	497	6.4
3	0.00381	1893	13.1	0	N/A	225	N/A	N/A	N/A
4	0.00440	2516	17.3	2	2	225	7404	928	12.5
5	0.00494	3152	21.7	4	4	225	7316	907	12.4
6	0.00542	3787	26.1	1	N/A	225	N/A	N/A	N/A
7	0.00584	4416	30.4	3	2	225	8391	1997	23.8
8	0.00631	5058	34.9	8	8	225	7364	1345	18.3
9	0.00670	5674	39.1	17	14	225	7079	1174	16.6
10	0.00712	6297	43.4	83	58	275	7399	1429	19.3
11	0.00773	6938	47.8	126	109	275	7736	1663	21.5
12	0.00775	7070	48.7	109	69	325	7705	1565	20.3

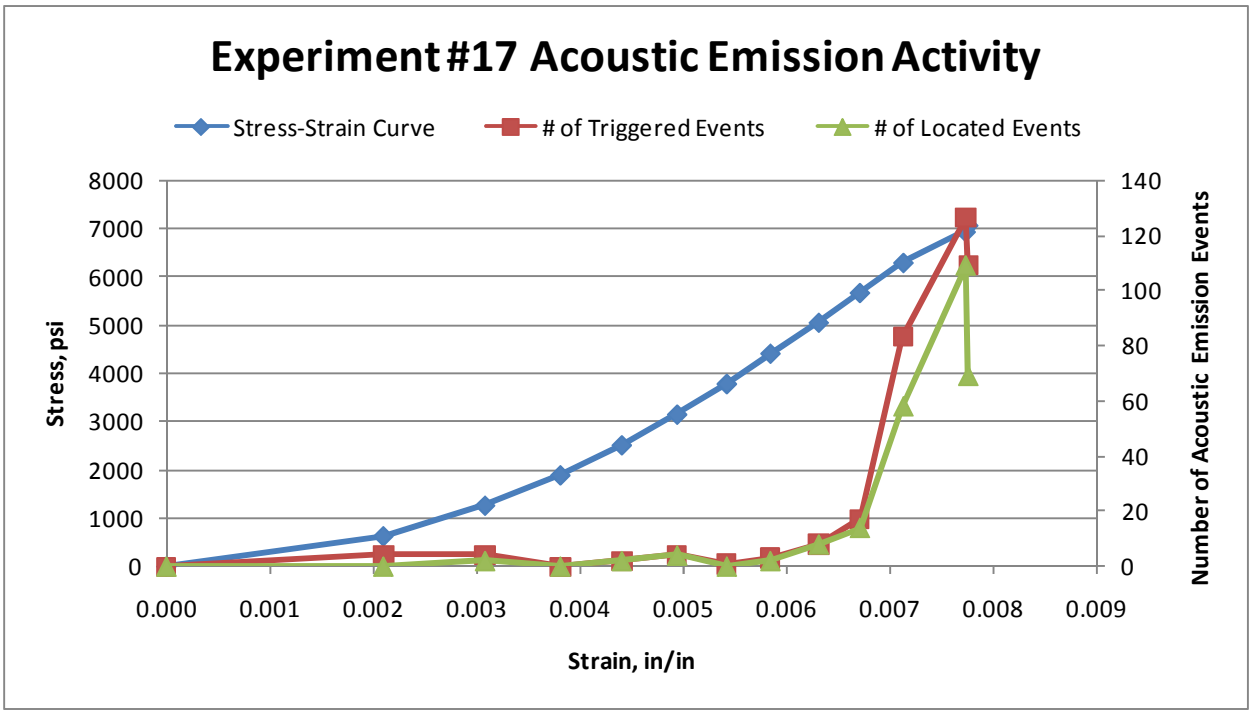

Figure B.33: Plot of Stress-Strain Curve & Acoustic Emission Activity for Experiment #17

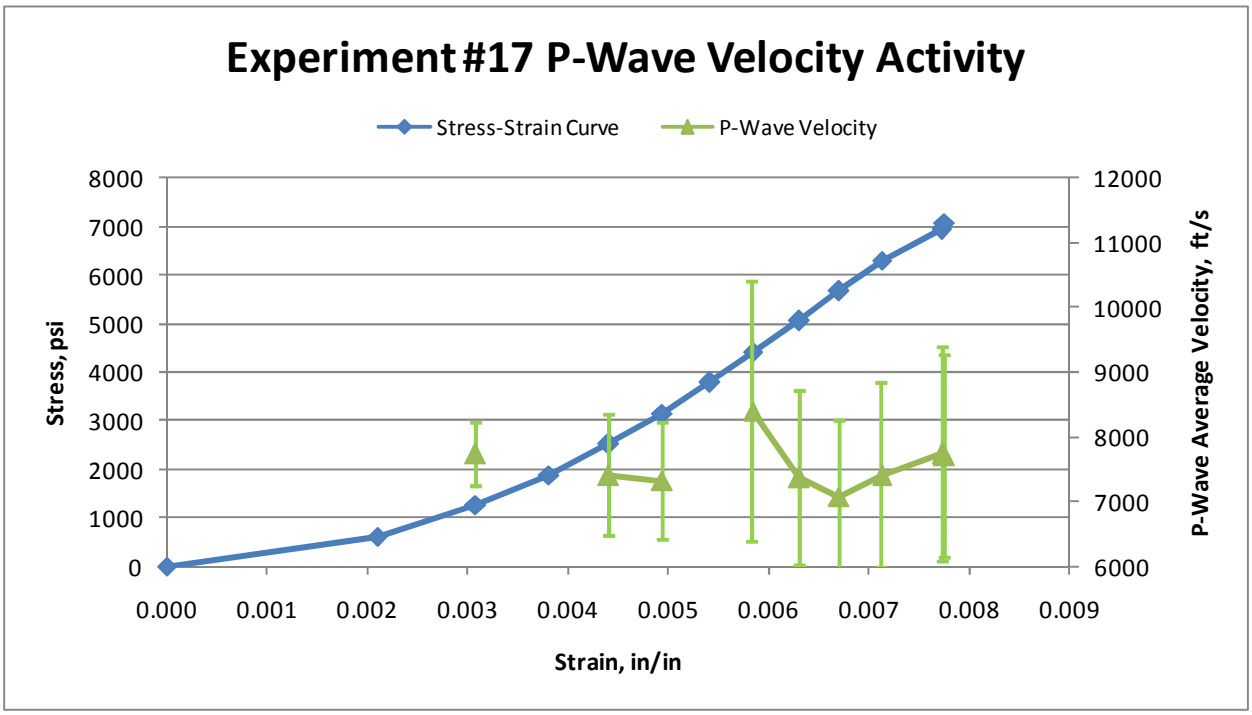

Figure B.34: Plot of Stress-Strain Curve & P-Wave Velocity for Experiment #17

Table B.18: Experiment #18 Acoustic Emission Activity & Loading Summary Statistics

Experiment #18									
Load Pause	Strain	Stress (psi)	Stress (MPa)	Number of Triggered Events	Number of Located Events	Thresh (mV)	Ave. Vel. (ft/s)	Std. Dev. (ft/s)	% Variation
0	0.00000	0	0.0	0	N/A	225	N/A	N/A	N/A
1	0.00219	635	4.4	22	N/A	225	N/A	N/A	N/A
2	0.00314	1271	8.8	2	1	225	7598	336	4.4
3	0.00379	1900	13.1	1	N/A	225	N/A	N/A	N/A
4	0.00432	2522	17.4	4	4	225	7585	723	9.5
5	0.00478	3177	21.9	4	4	225	7372	833	11.3
6	0.00519	3781	26.1	3	3	225	7159	811	11.3
7	0.00560	4429	30.5	3	3	225	8347	1180	14.1
8	0.00597	5051	34.8	4	4	225	7963	1726	21.7
9	0.00634	5674	39.1	15	12	225	7892	1193	15.1
10	0.00672	6297	43.4	11	8	300	7939	1034	13.0
11	0.00710	6926	47.8	6	5	300	7938	1163	14.6
12	0.00754	7561	52.1	122	78	300	8059	1734	21.5
13	0.00817	8190	56.5	75	38	300	7814	2298	29.4

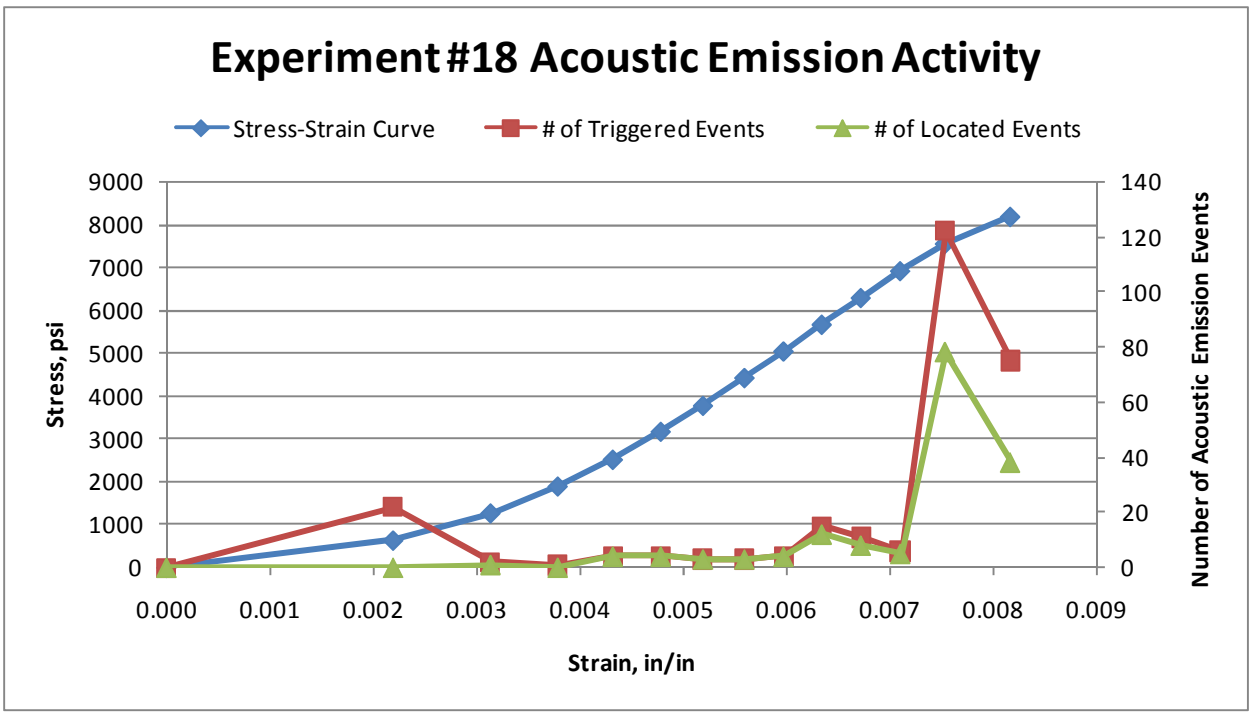

Figure B.35: Plot of Stress-Strain Curve & Acoustic Emission Activity for Experiment #18

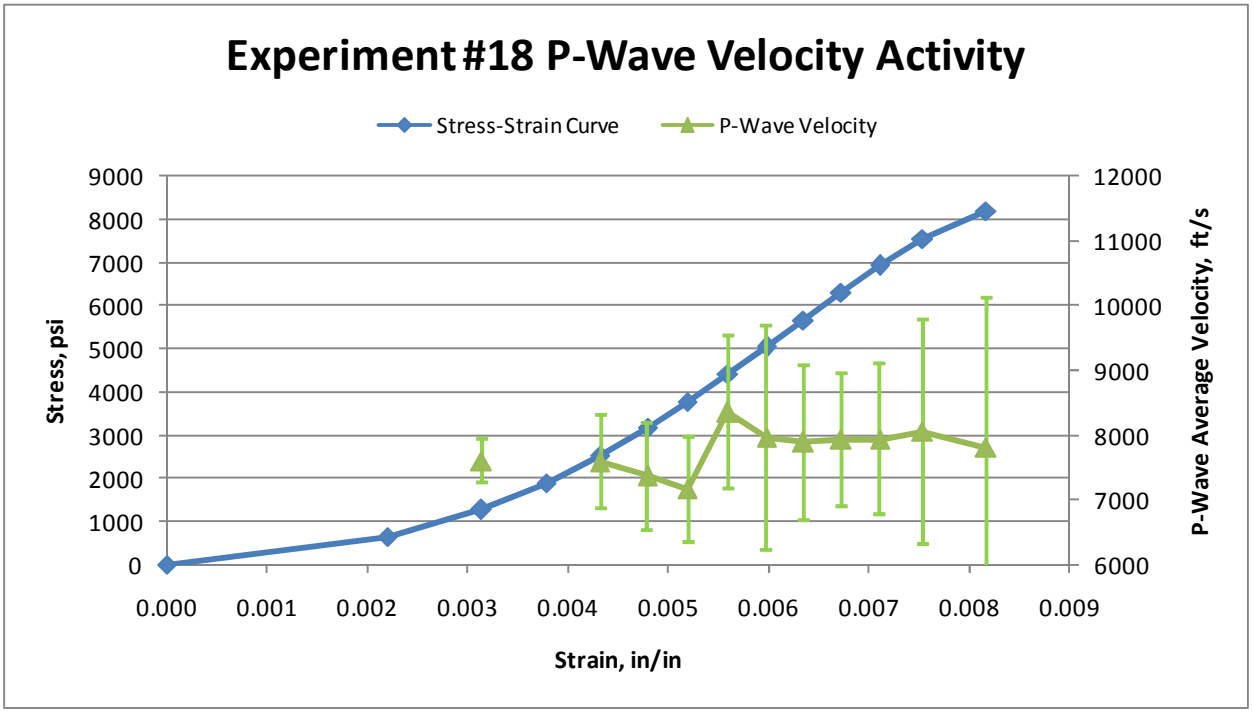

Figure B.36: Plot of Stress-Strain Curve & P-Wave Velocity for Experiment #18

Table B.19: Experiment #19 Acoustic Emission Activity & Loading Summary Statistics

Experiment #19									
Load Pause	Strain	Stress (psi)	Stress (MPa)	Number of Triggered Events	Number of Located Events	Thresh (mV)	Ave. Vel. (ft/s)	Std. Dev. (ft/s)	% Variation
0	0.00000	0	0.0	0	N/A	225	N/A	N/A	N/A
1	0.00094	636	4.4	0	N/A	225	N/A	N/A	N/A
2	0.00192	1272	8.8	0	N/A	225	N/A	N/A	N/A
3	0.00260	1902	13.1	0	N/A	225	N/A	N/A	N/A
4	0.00317	2519	17.4	0	N/A	200	N/A	N/A	N/A
5	0.00362	3155	21.8	2	2	200	7860	936	11.9
6	0.00408	3778	26.0	1	1	225	7624	1095	14.4
7	0.00449	4433	30.6	5	5	225	7974	1266	15.9
8	0.00492	5044	34.8	16	10	225	7597	1709	22.5
9	0.00532	5673	39.1	9	5	250	7819	1238	15.8
10	0.00571	6309	43.5	11	10	275	7384	1182	16.0
11	0.00617	6926	47.8	44	26	275	8040	2097	26.1
12	0.00667	7562	52.1	58	37	300	7738	1529	19.8
13	0.00715	8186	56.4	115	63	300	7701	1561	20.3
14	0.00729	8259	56.9	116	27	350	8004	2050	25.6

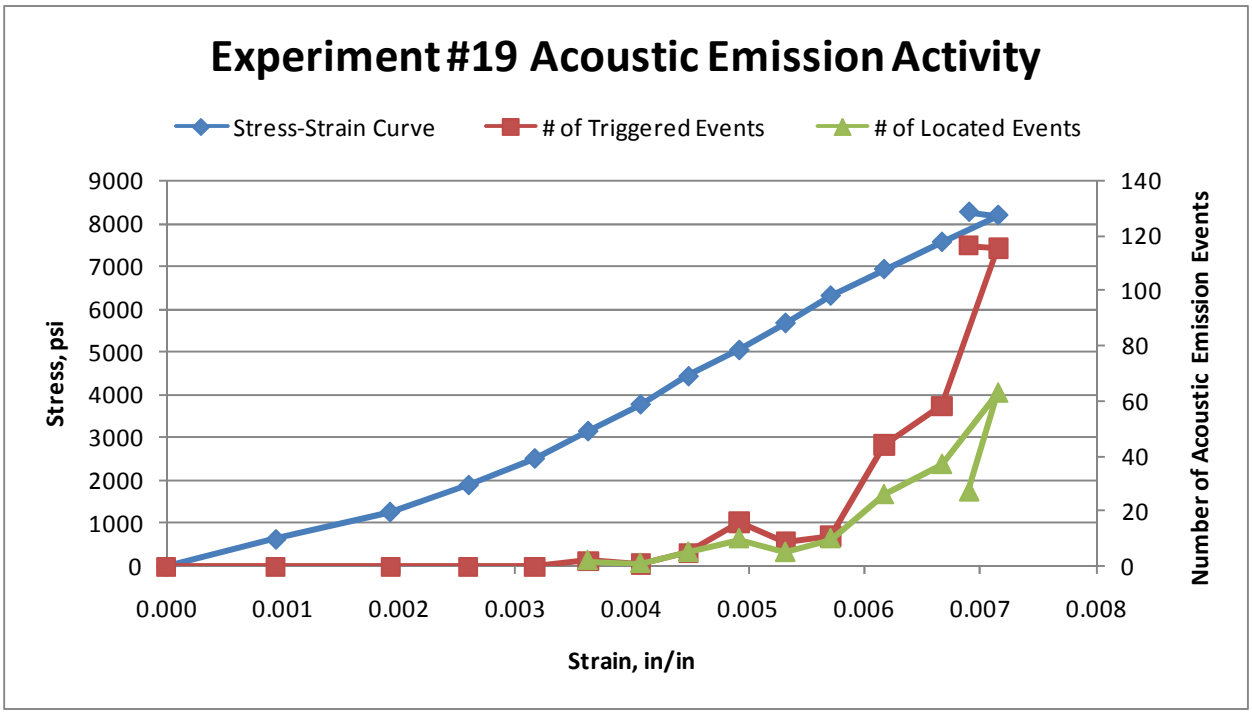

Figure B.37: Plot of Stress-Strain Curve & Acoustic Emission Activity for Experiment #19

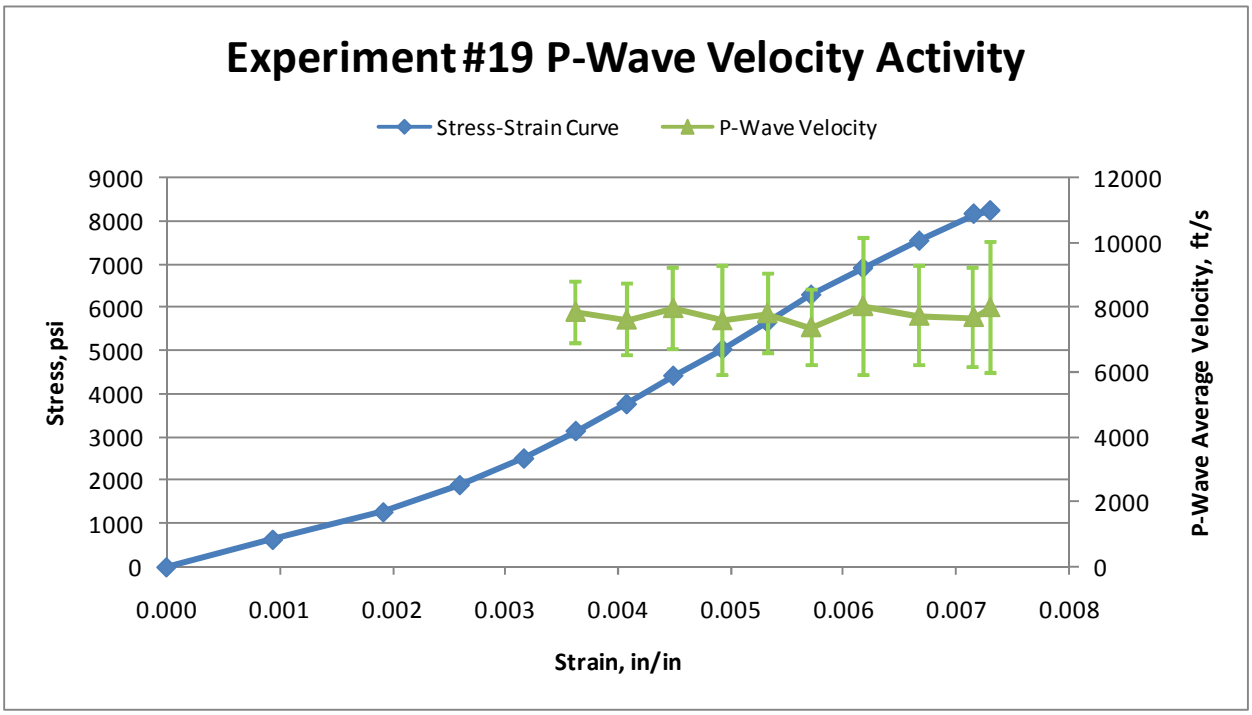

Figure B.38: Plot of Stress-Strain Curve & P-Wave Velocity for Experiment #19

Appendix C: Velocity Tomograms

Experiment #1 Tomograms

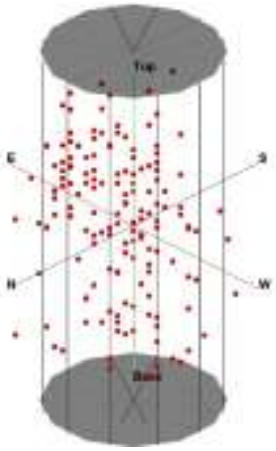

Acoustic Emission Locations

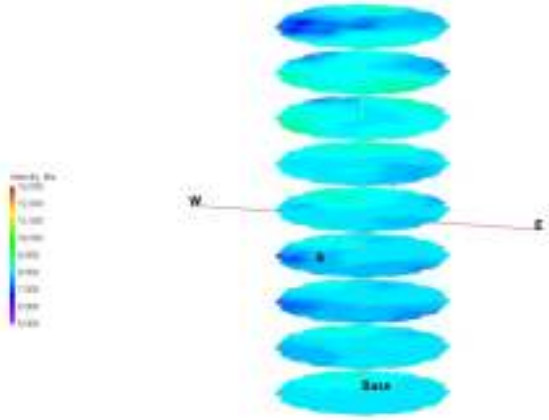

4.4 MPa of Load

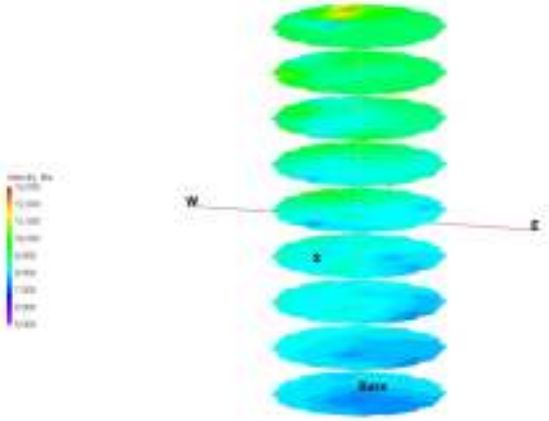

8.7 MPa of Load

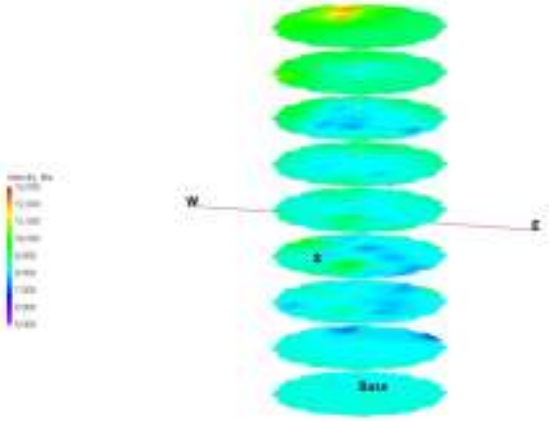

17.4 MPa of Load

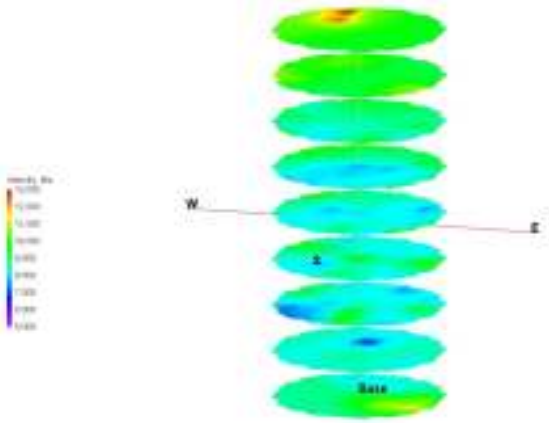

26.1 MPa of Load

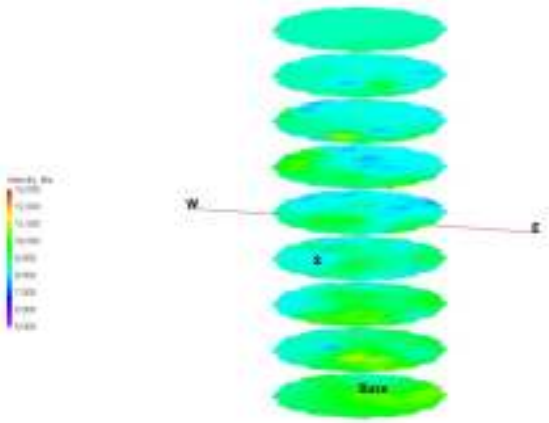

30.3 MPa of Load

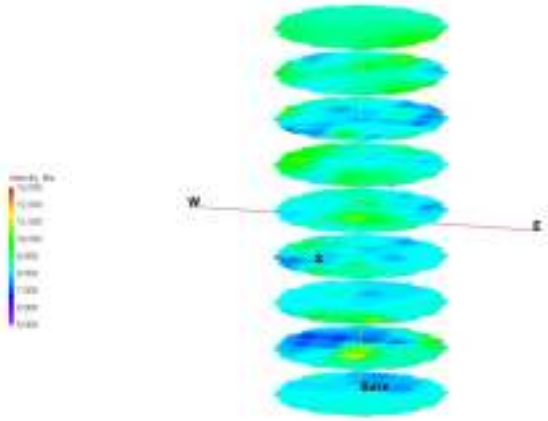

34.8 MPa of Load

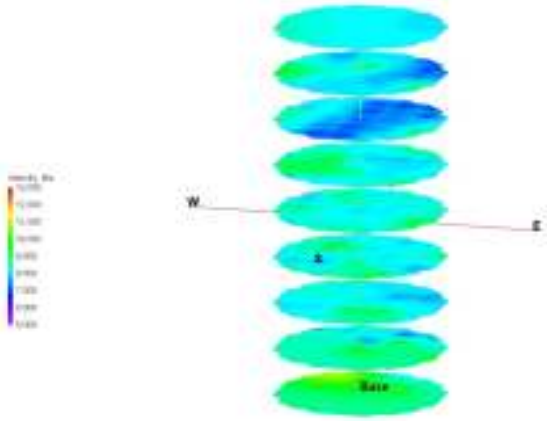

39.0 MPa of Load

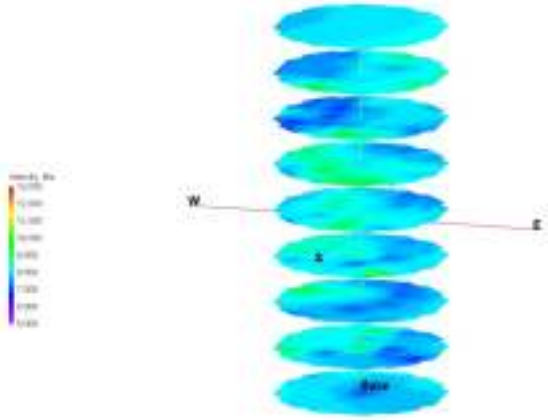

43.3 MPa of Load

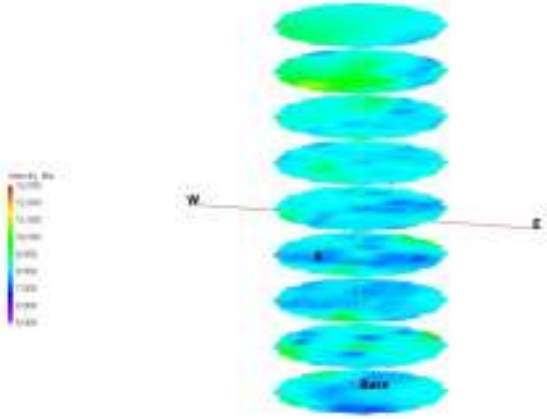

47.7 MPa of Load

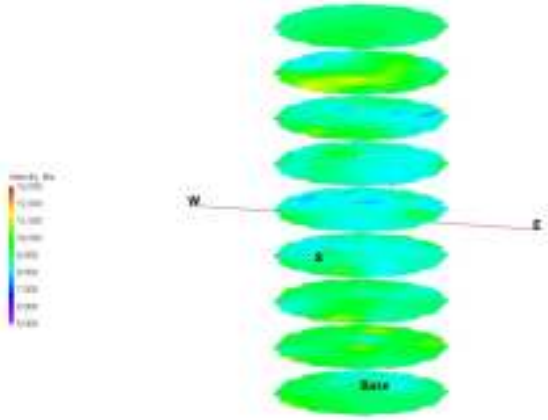

52.0 MPa of Load

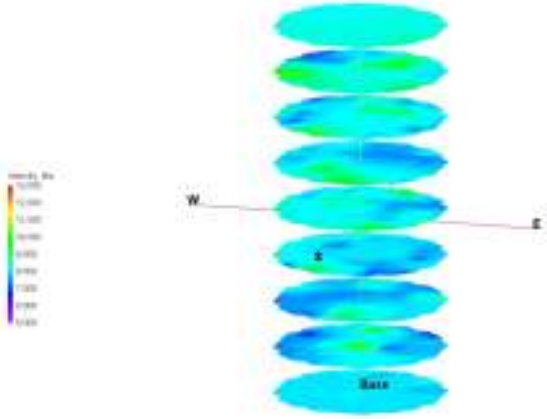

54.3 MPa of Load

Picture of Failed Sample from Experiment #1

Experiment #2 Tomograms

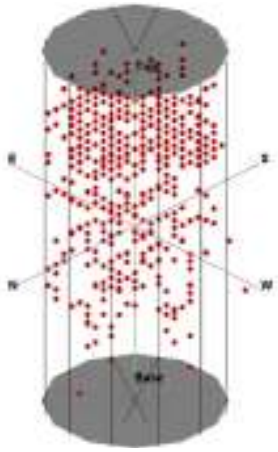

Acoustic Emission Locations

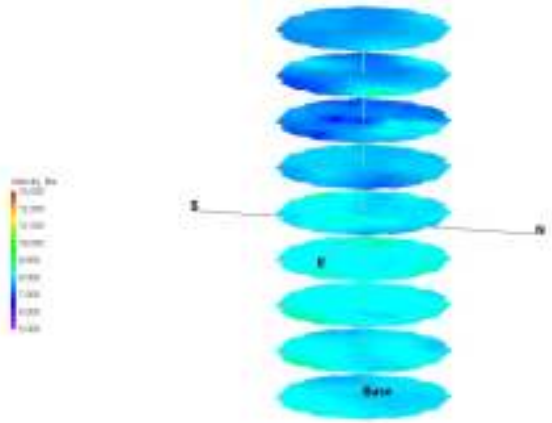

4.3 MPa of Load

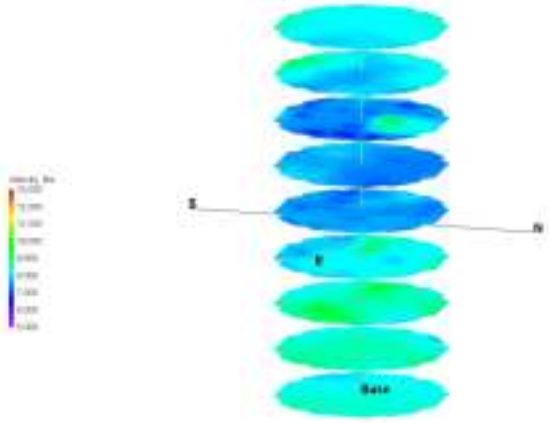

8.7 MPa of Load

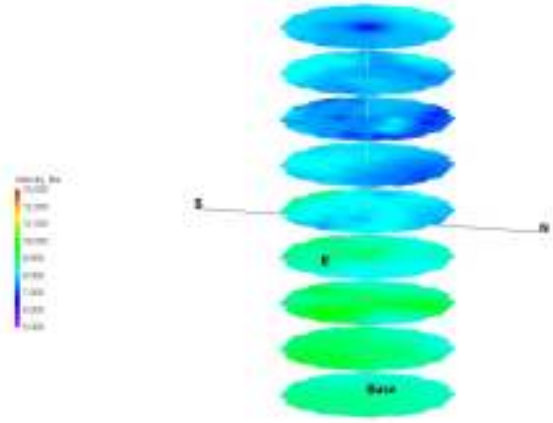

13.0 MPa of Load

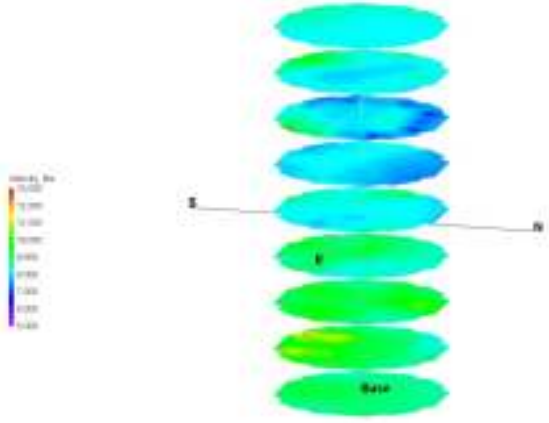

17.3 MPa of Load

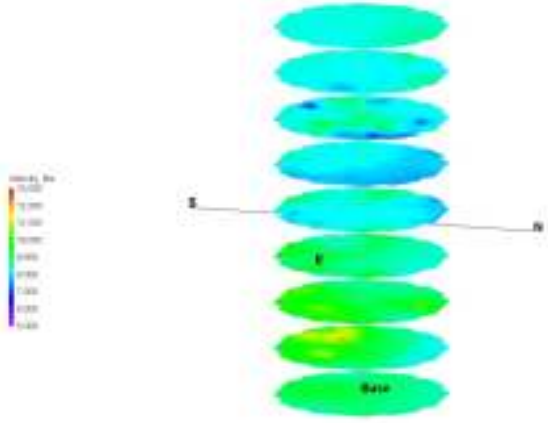

21.7 MPa of Load

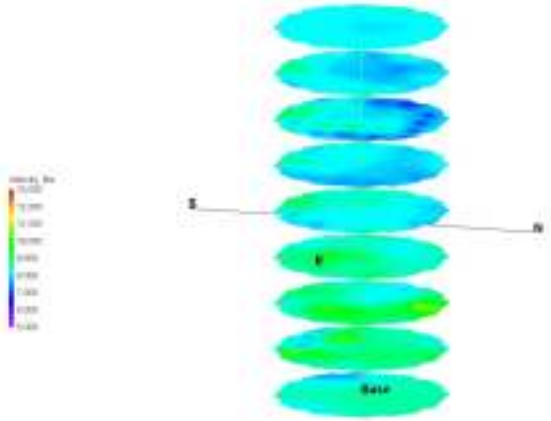

26.0 MPa of Load

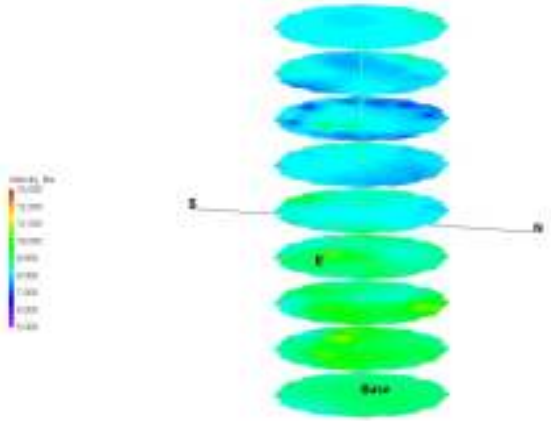

30.4 MPa of Load

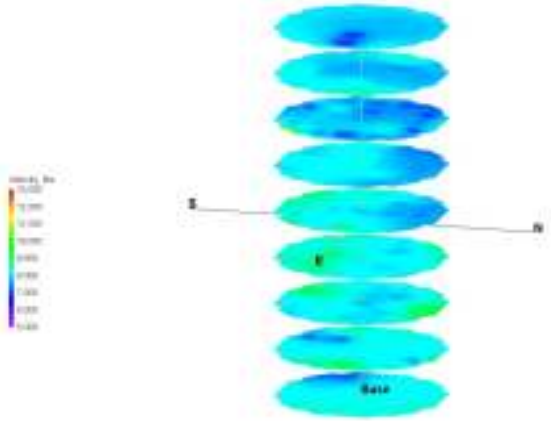

34.6 MPa of Load

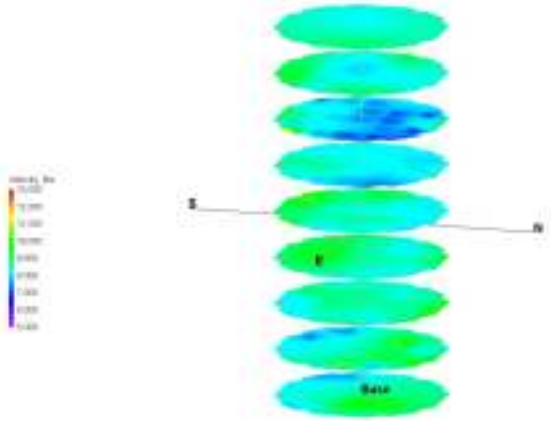

39.0 MPa of Load

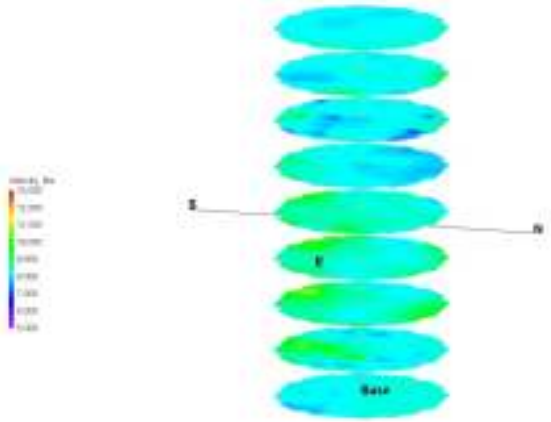

43.3 MPa of Load

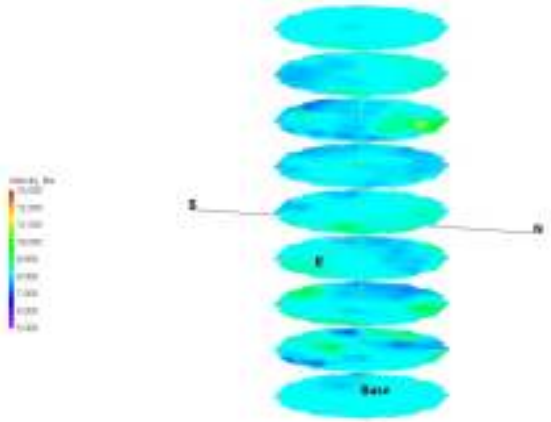

47.7 MPa of Load

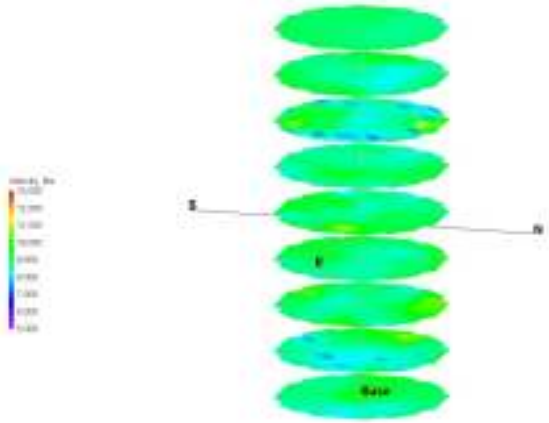

52.0 MPa of Load

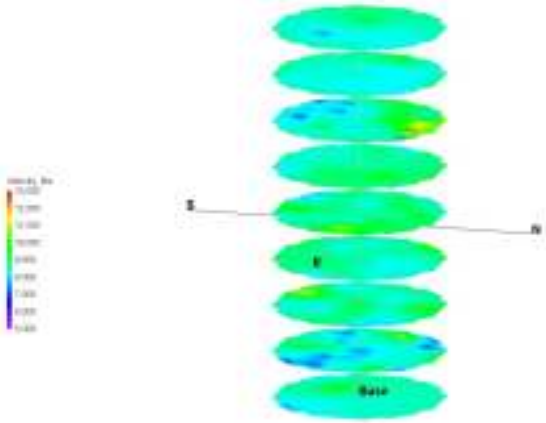

56.2 MPa of Load

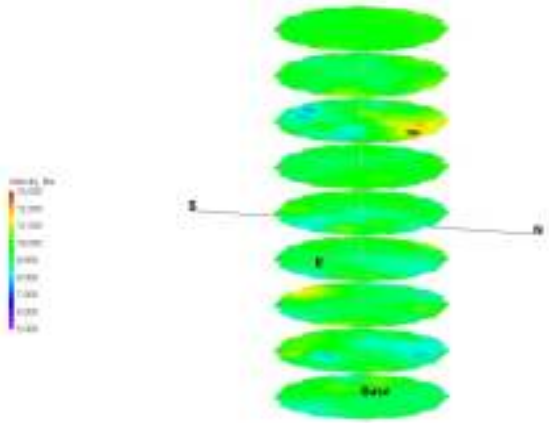

56.4 MPa of Load

Picture of Failed Sample from Experiment #2

Experiment #3 Tomograms

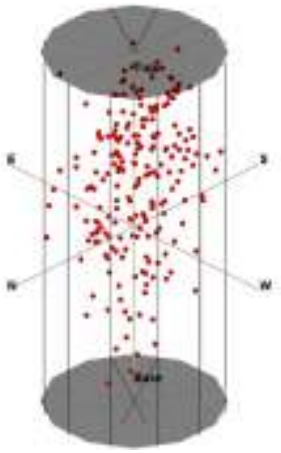

Acoustic Emission Locations

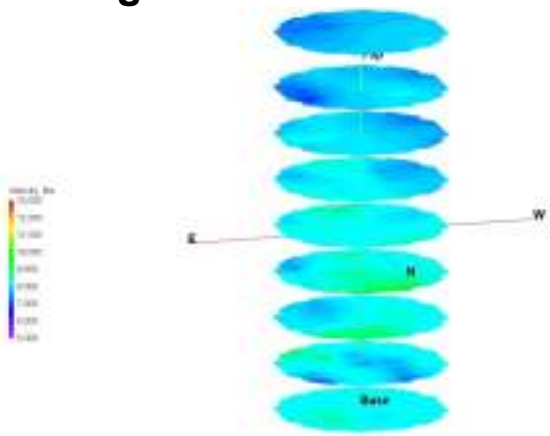

4.5 MPa of Load

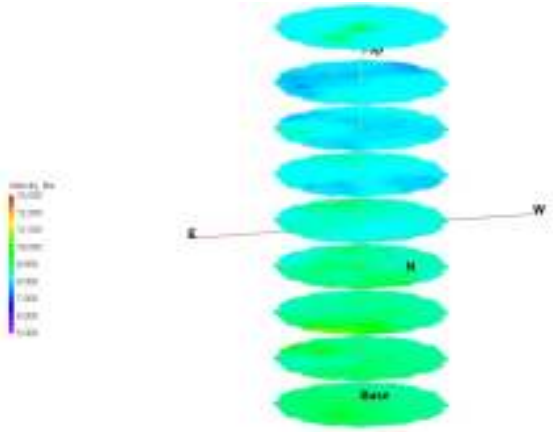

9.1 MPa of Load

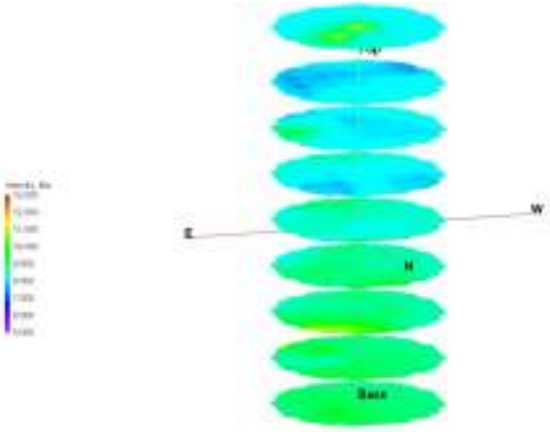

13.5 MPa of Load

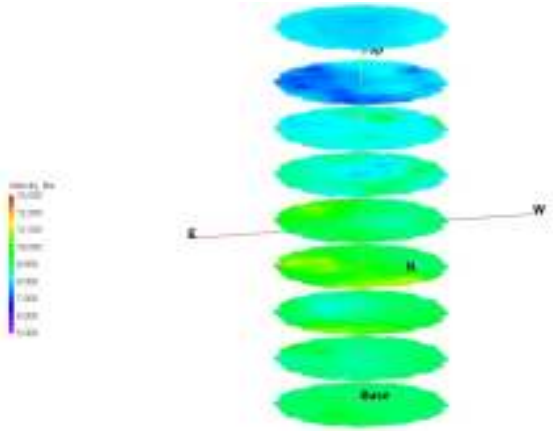

26.9 MPa of Load

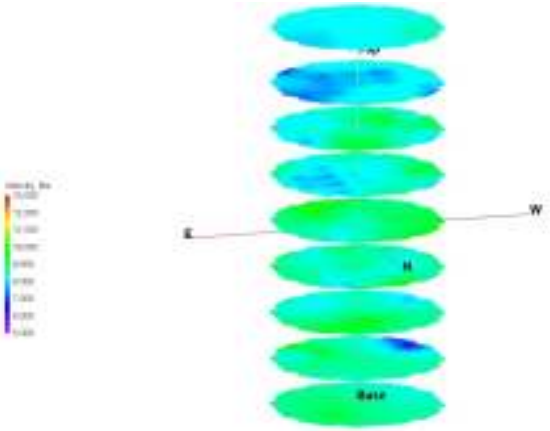

31.3 MPa of Load

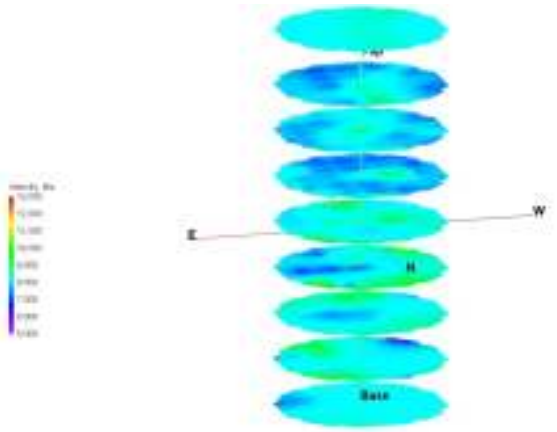

35.8 MPa of Load

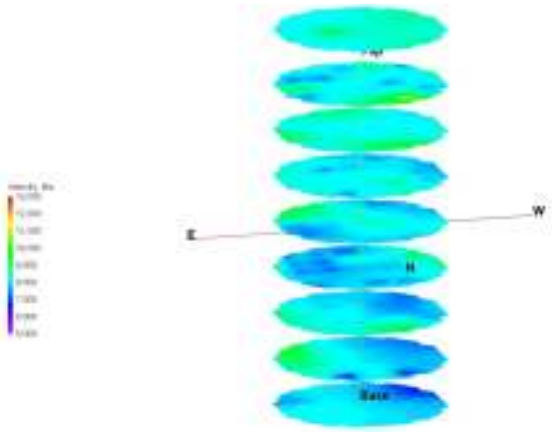

40.3 MPa of Load

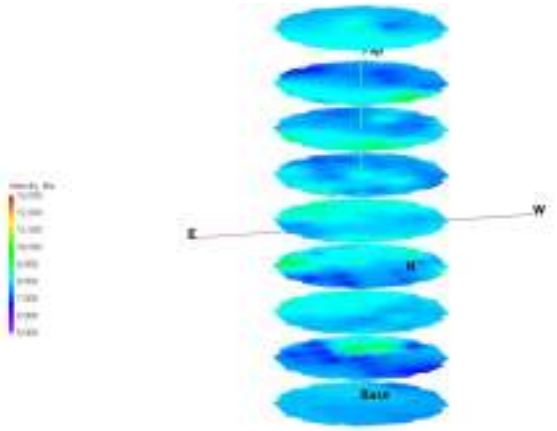

44.7 MPa of Load

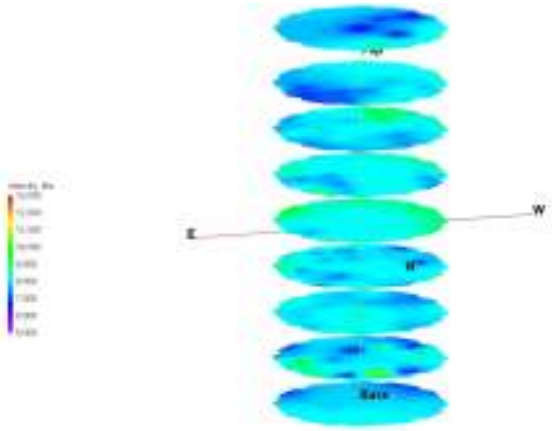

49.3 MPa of Load

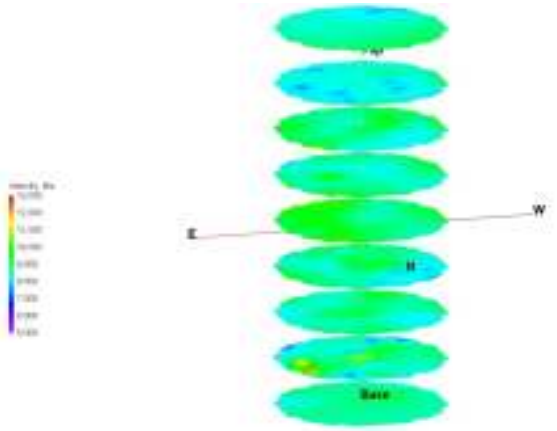

51.3 MPa of Load

Picture of Failed Sample from Experiment #3

Experiment #4 Tomograms

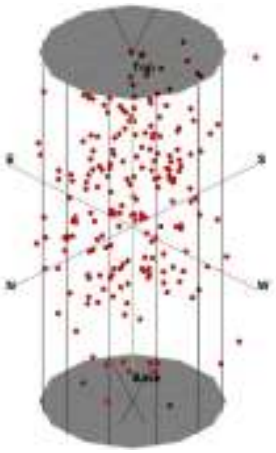

Acoustic Emission Locations

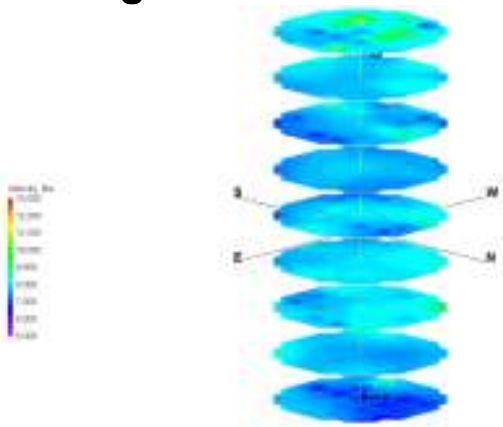

4.5 MPa of Load

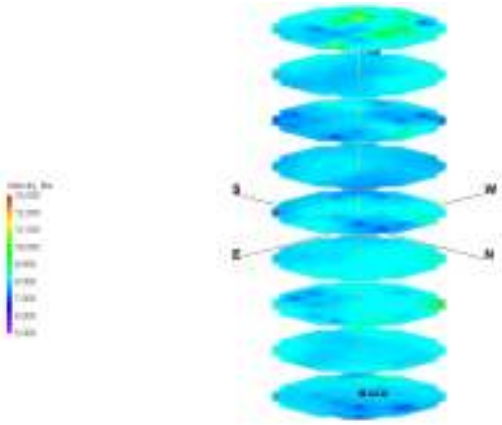

9.0 MPa of Load

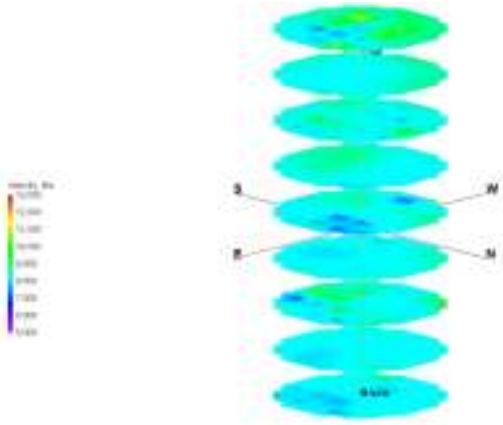

31.3 MPa of Load

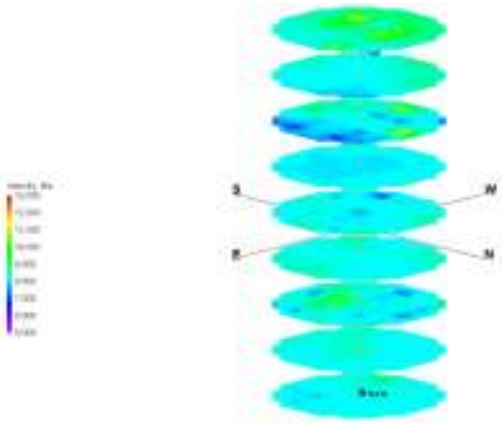

35.9 MPa of Load

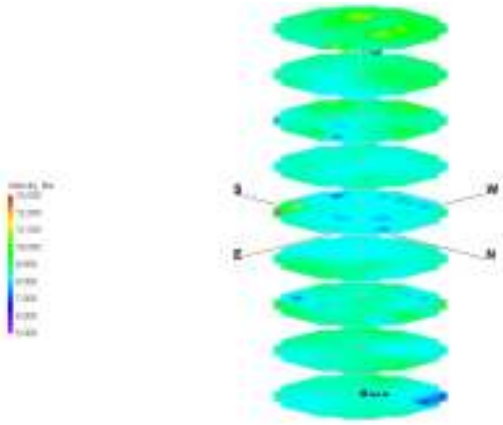

40.2 MPa of Load

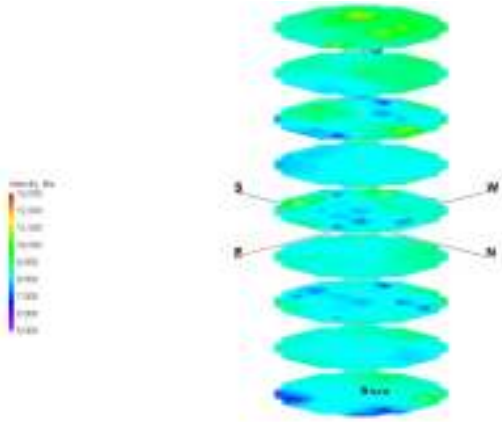

44.7 MPa of Load

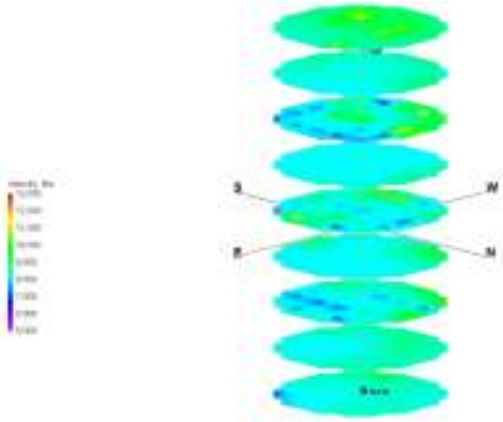

49.1 MPa of Load

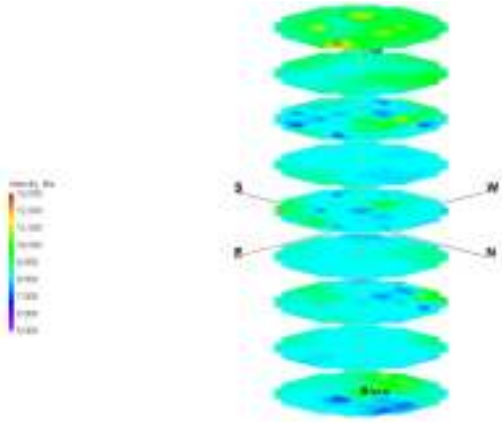

53.6 MPa of Load

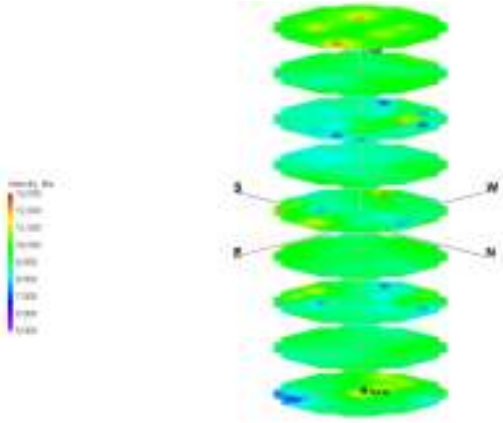

56.0 MPa of Load

Picture of Failed Sample from Experiment #4

Experiment #5 Tomograms

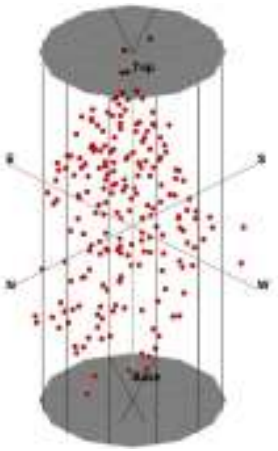

Acoustic Emission Locations

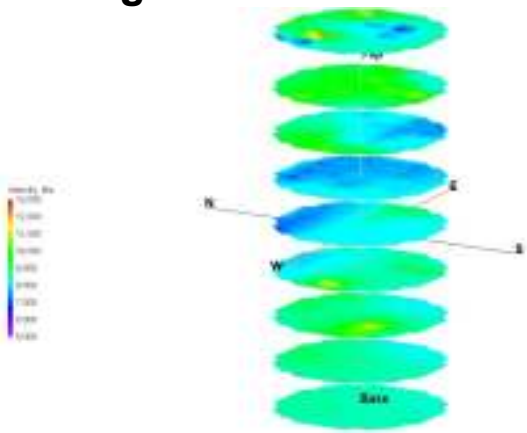

8.8 MPa of Load

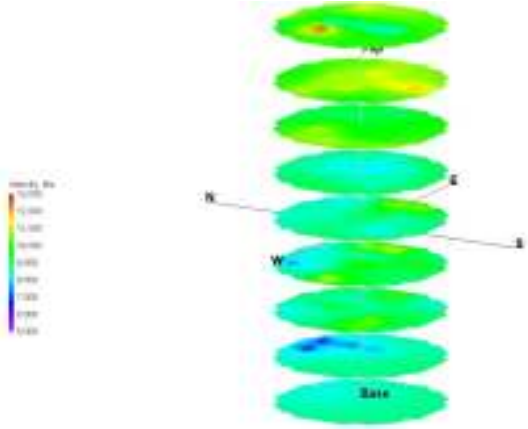

13.1 MPa of Load

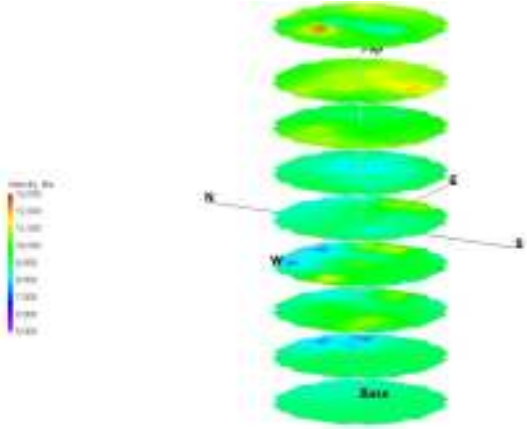

17.5 MPa of Load

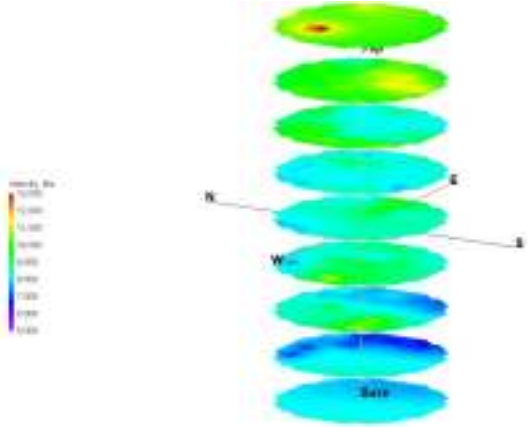

21.8 MPa of Load

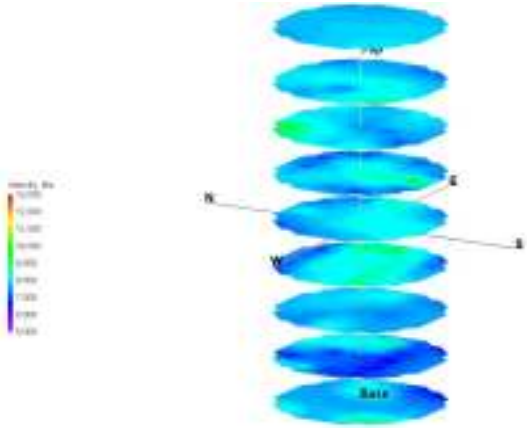

26.2 MPa of Load

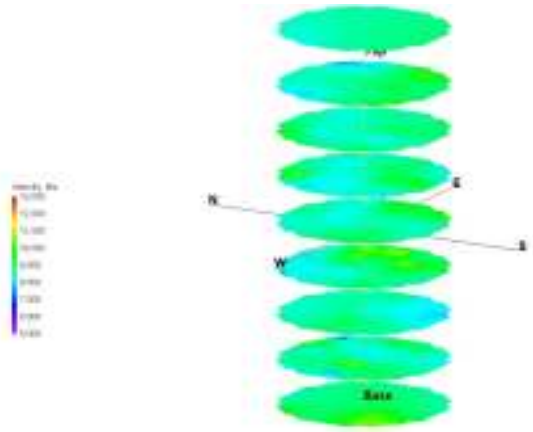

30.5 MPa of Load

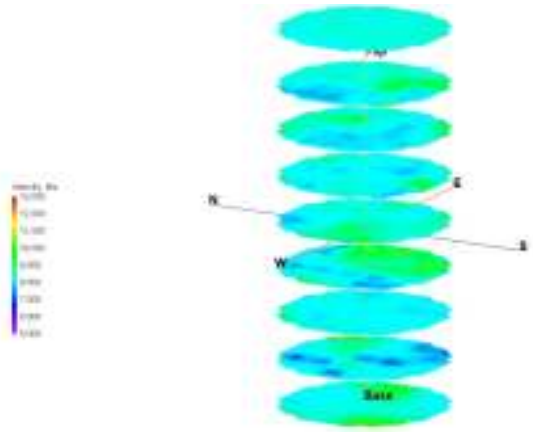

34.7 MPa of Load

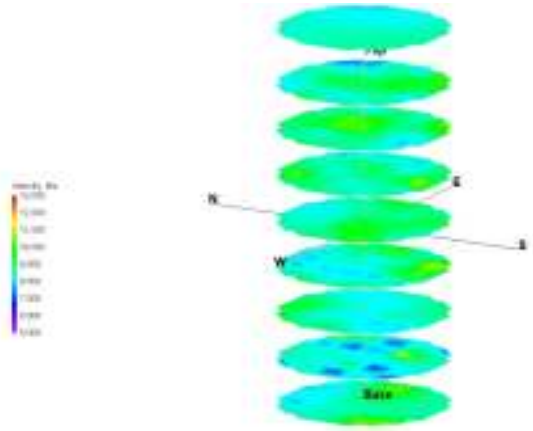

39.2 MPa of Load

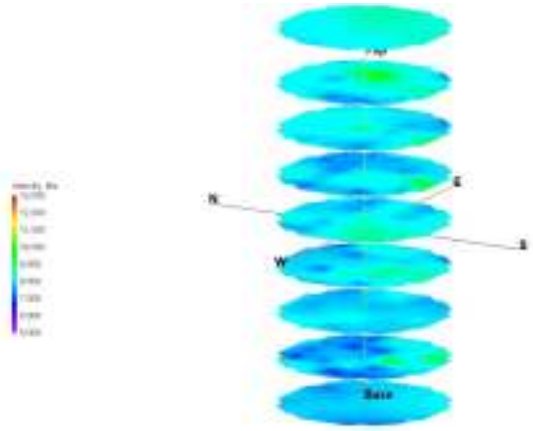

43.5 MPa of Load

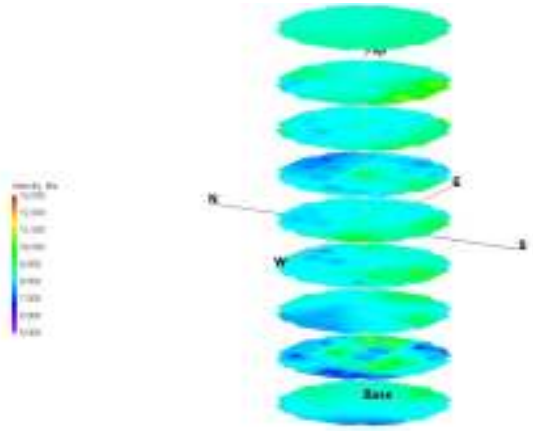

47.8 MPa of Load

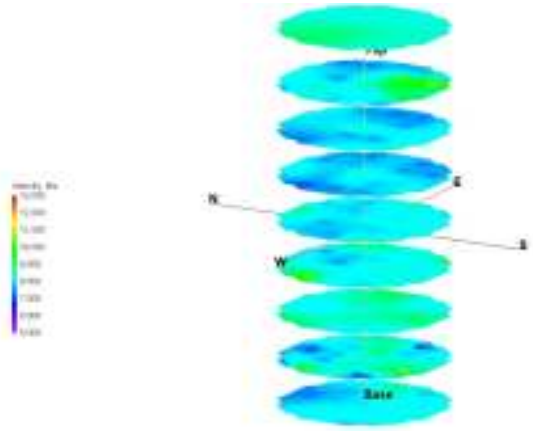

52.1 MPa of Load

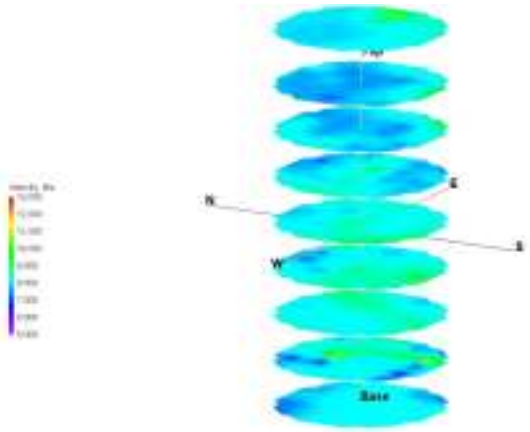

56.5 MPa of Load

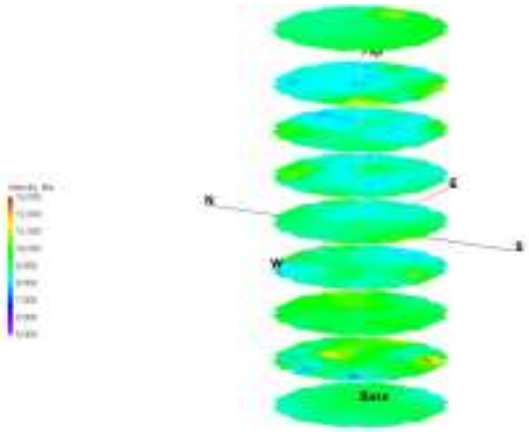

57.1 MPa of Load

Picture of Failed Sample from Experiment #5

Experiment #6 Tomograms

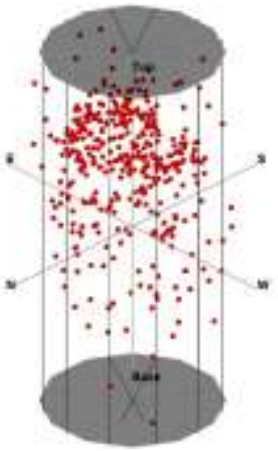

Acoustic Emission Locations

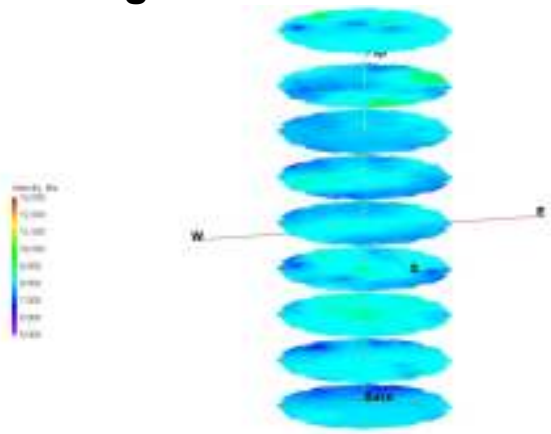

8.7 MPa of Load

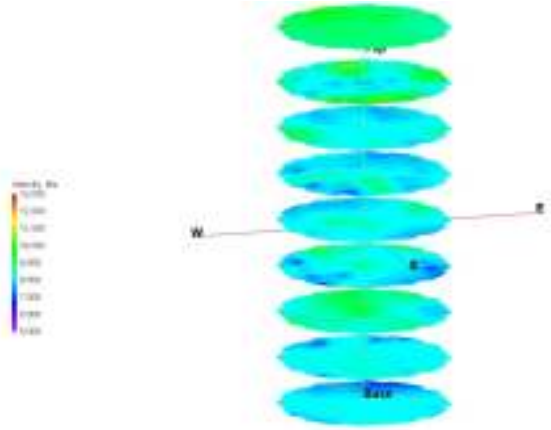

13.0 MPa of Load

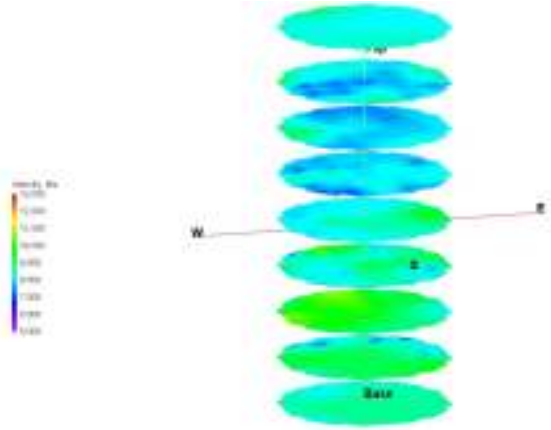

17.4 MPa of Load

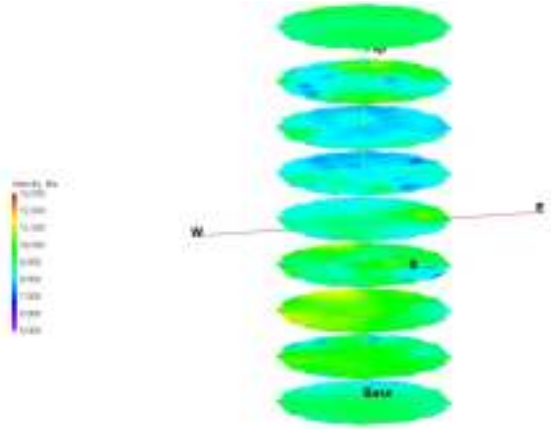

21.6 MPa of Load

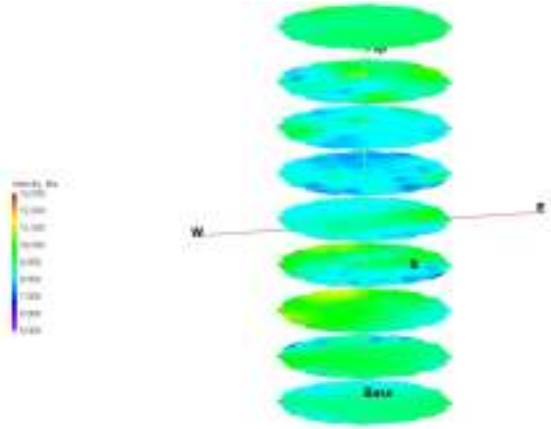

26.0 MPa of Load

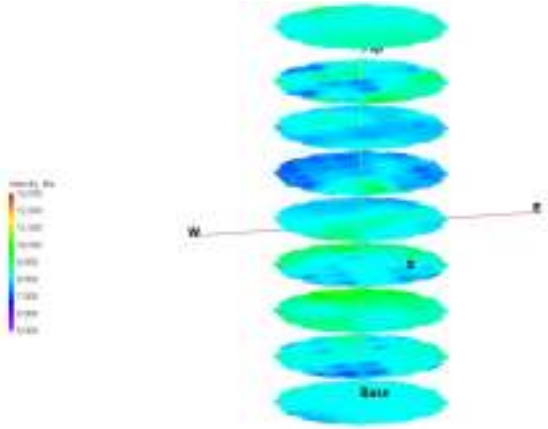

30.4 MPa of Load

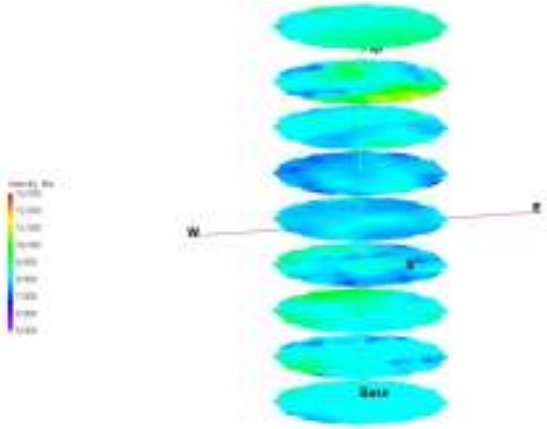

34.7 MPa of Load

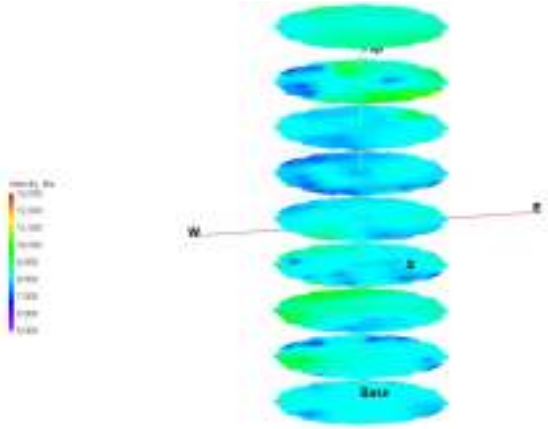

39.0 MPa of Load

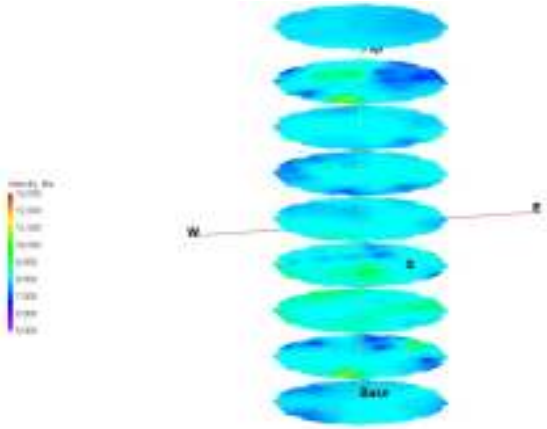

43.4 MPa of Load

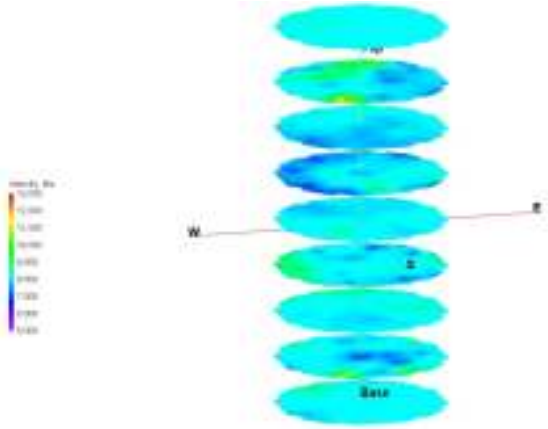

47.8 MPa of Load

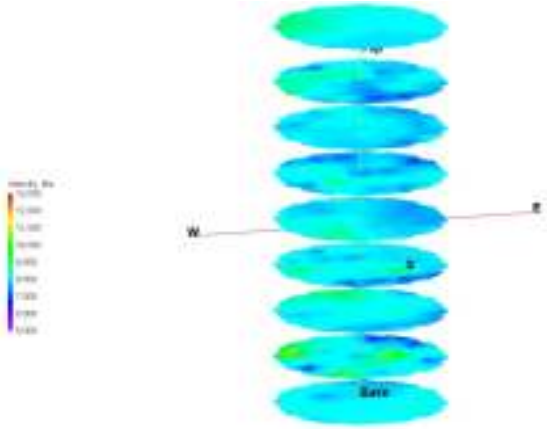

52.0 MPa of Load

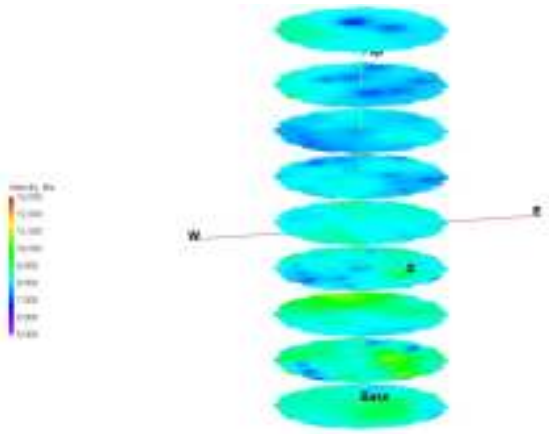

56.4 MPa of Load

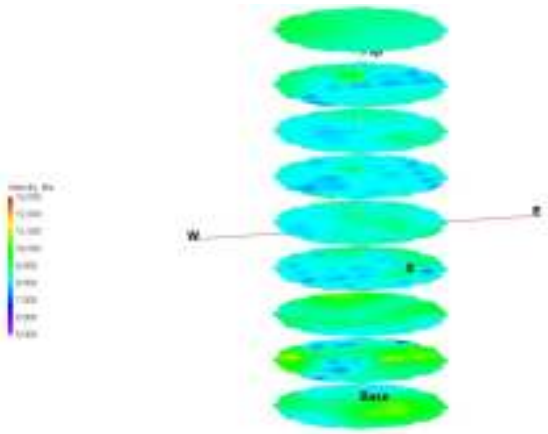

58.2 MPa of Load

Picture of Failed Sample from Experiment #6

Experiment #7 Tomograms

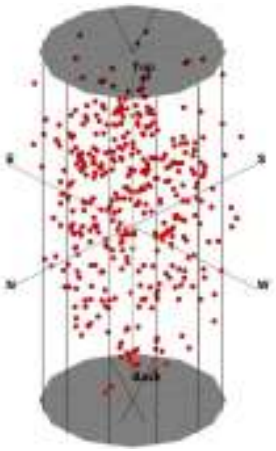

Acoustic Emission Locations

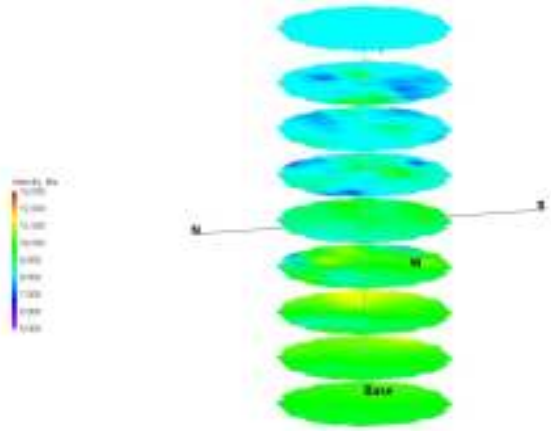

13.1 MPa of Load

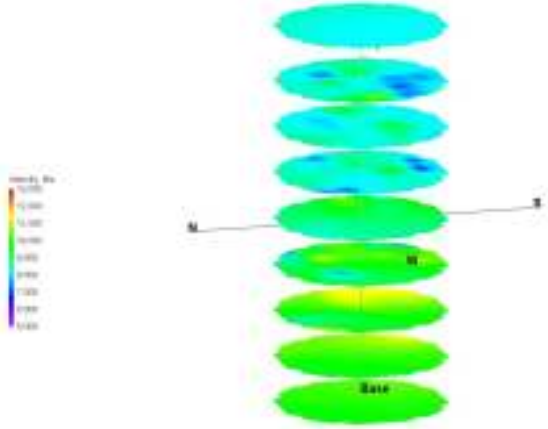

17.5 MPa of Load

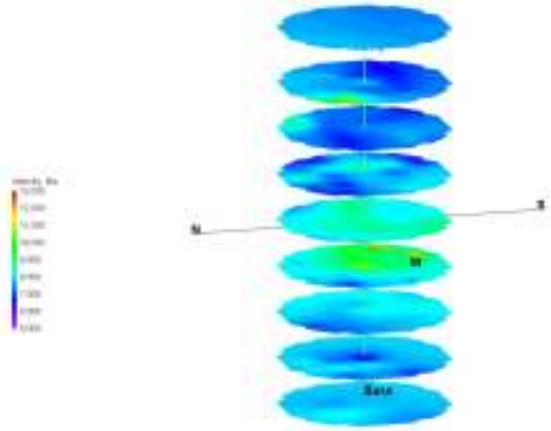

21.9 MPa of Load

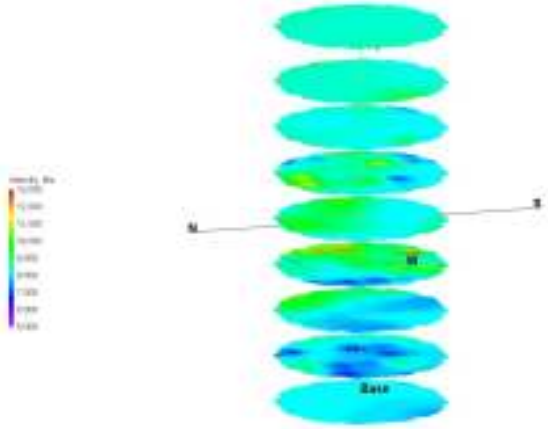

30.5 MPa of Load

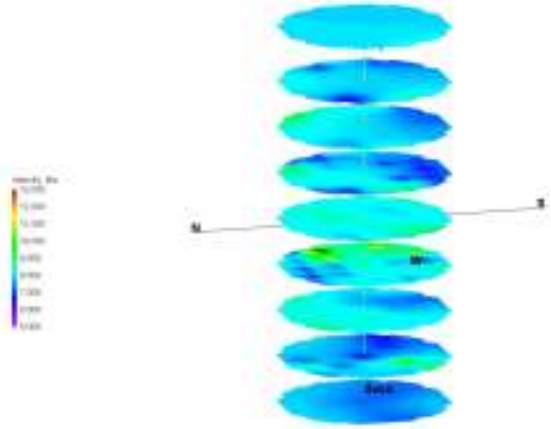

34.8 MPa of Load

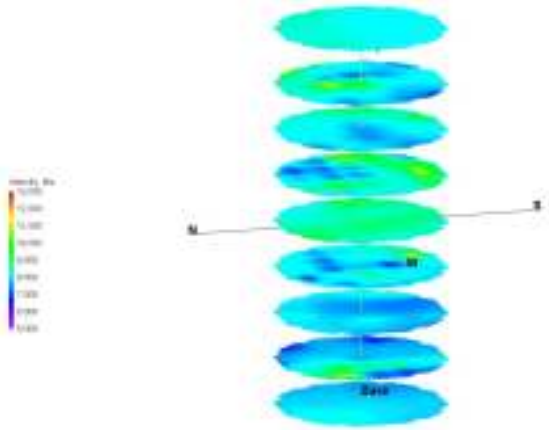

39.2 MPa of Load

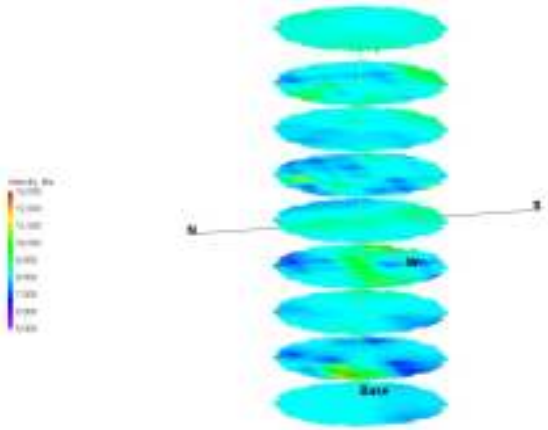

43.5 MPa of Load

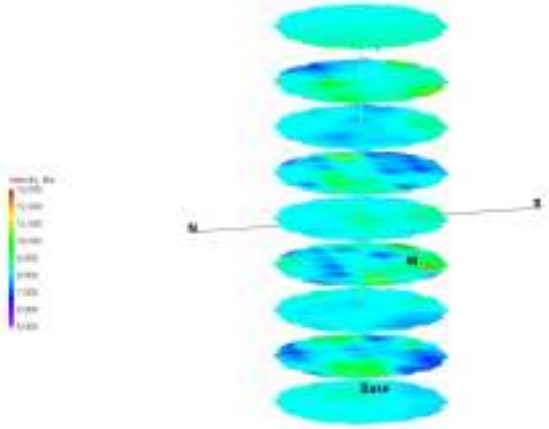

47.8 MPa of Load

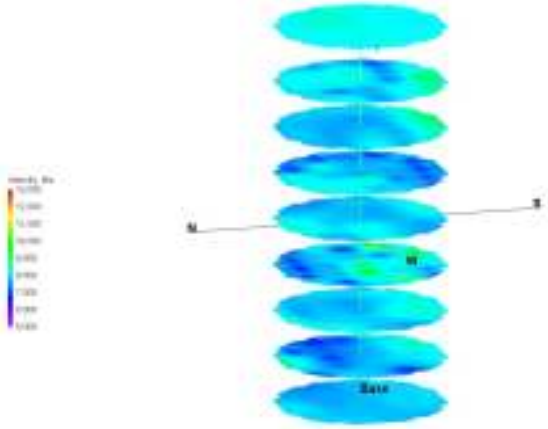

52.2 MPa of Load

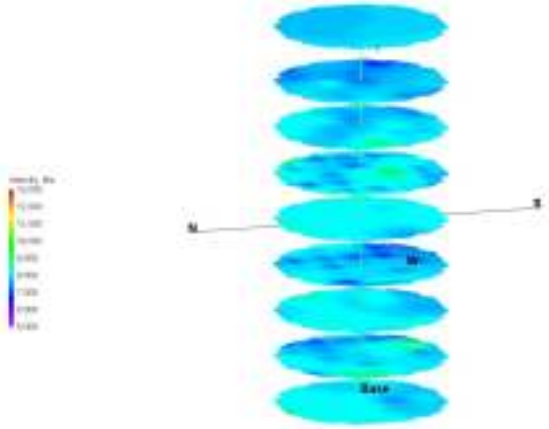

56.5 MPa of Load

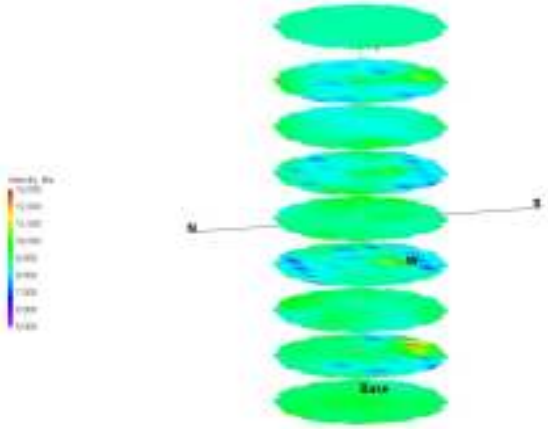

58.9 MPa of Load

Picture of Failed Sample from Experiment #7

Experiment #8 Tomograms

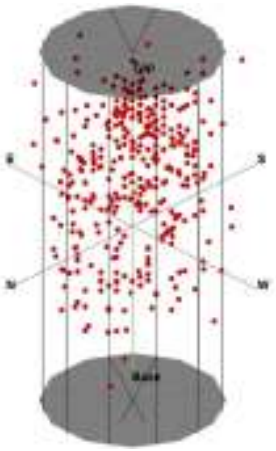

Acoustic Emission Locations

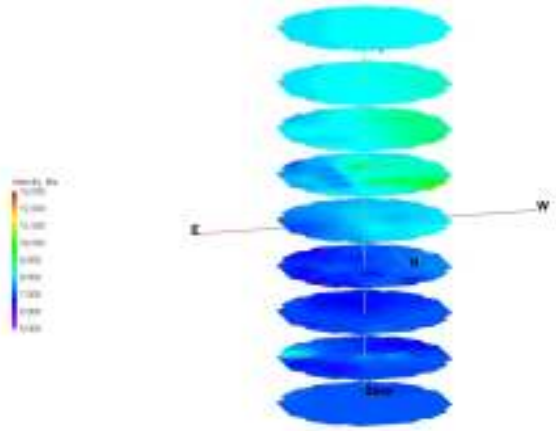

30.4 MPa of Load

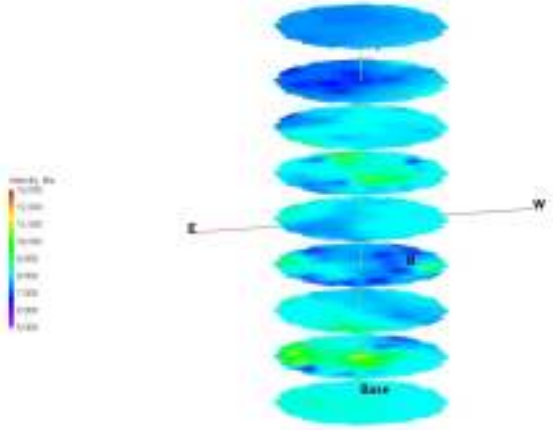

34.8 MPa of Load

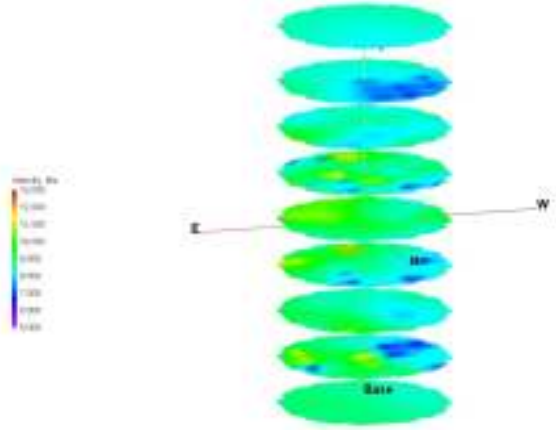

39.1 MPa of Load

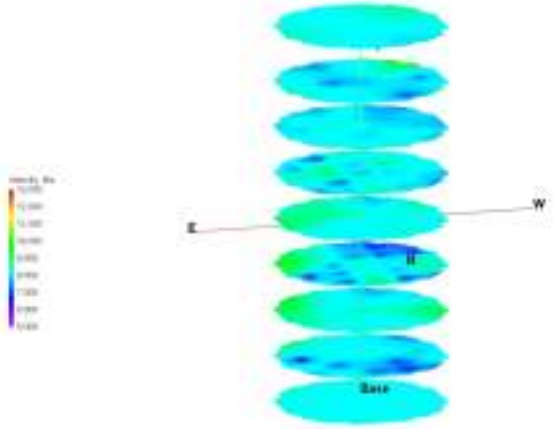

43.5 MPa of Load

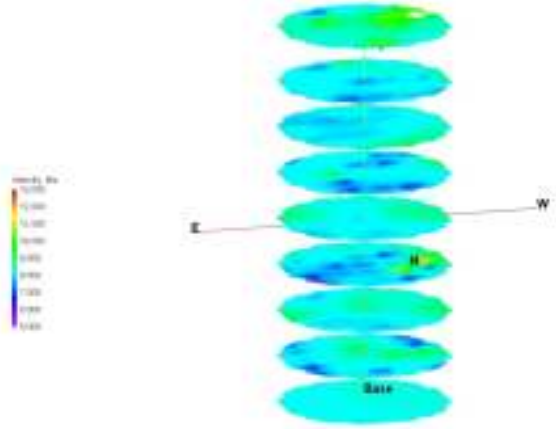

47.8 MPa of Load

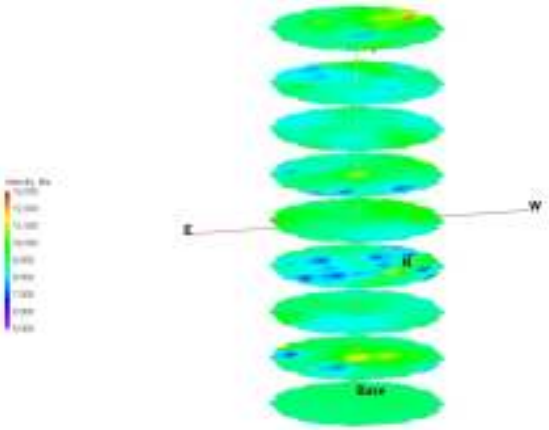

48.8 MPa of Load

Picture of Failed Sample from Experiment #8

Experiment #9 Tomograms

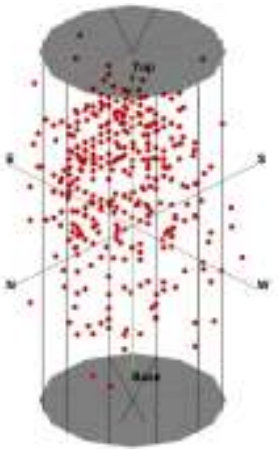

Acoustic Emission Locations

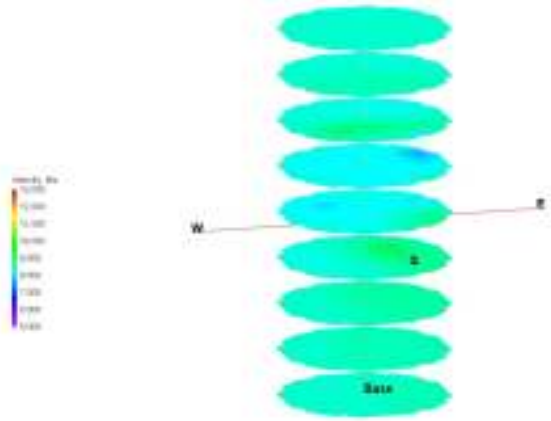

26.2 MPa of Load

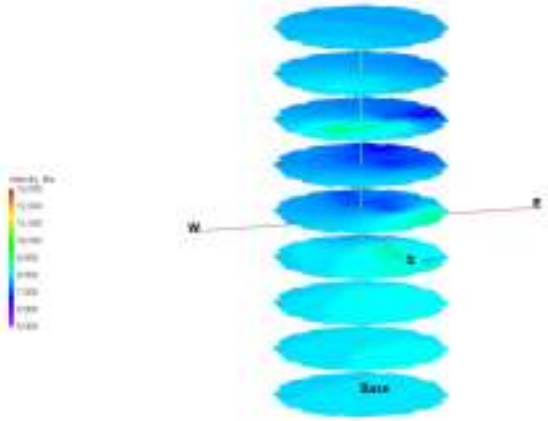

30.5 MPa of Load

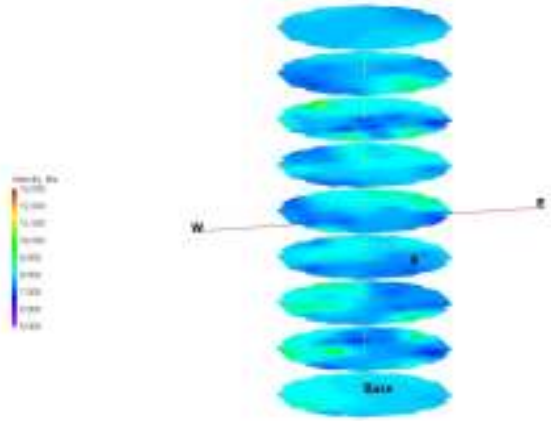

34.8 MPa of Load

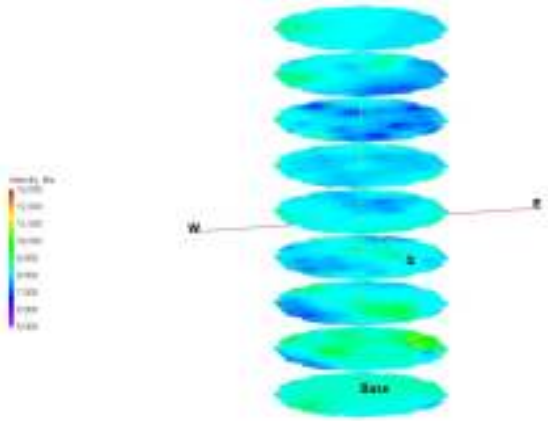

39.1 MPa of Load

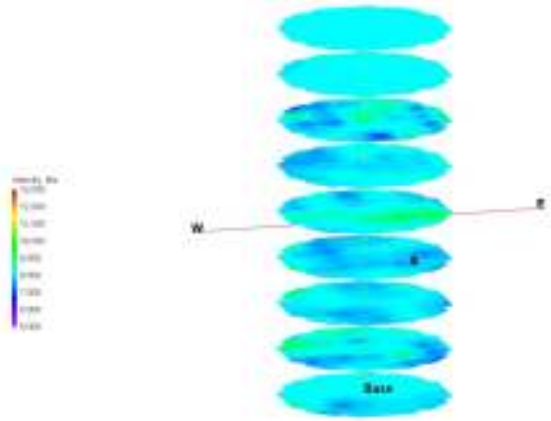

43.4 MPa of Load

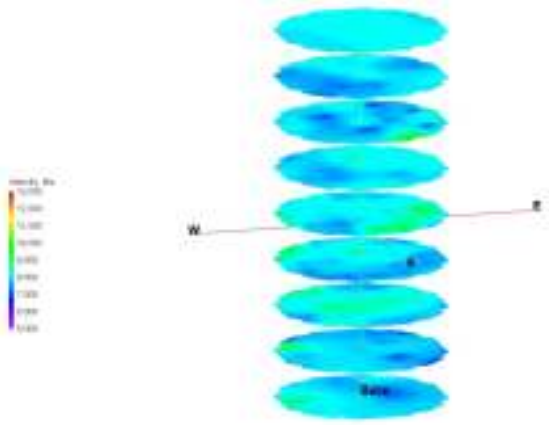

47.7 MPa of Load

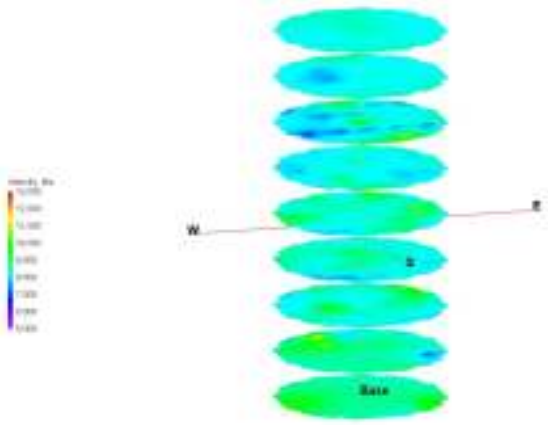

51.5 MPa of Load

Picture of Failed Sample from Experiment #9

Experiment #10 Tomograms

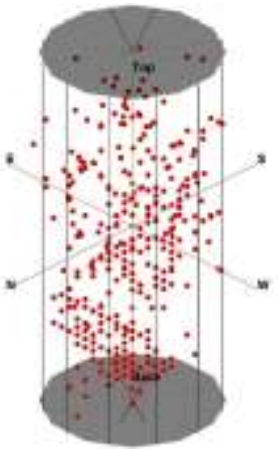

Acoustic Emission Locations

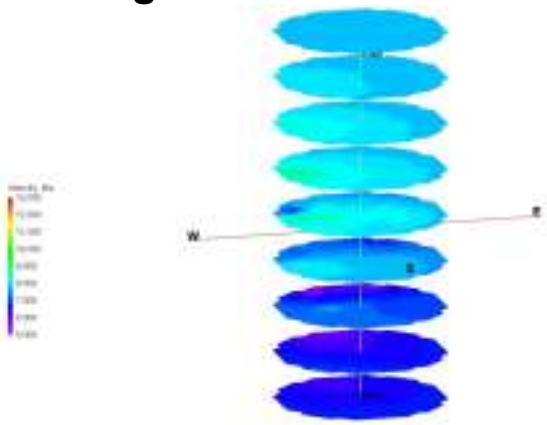

17.4 MPa of Load

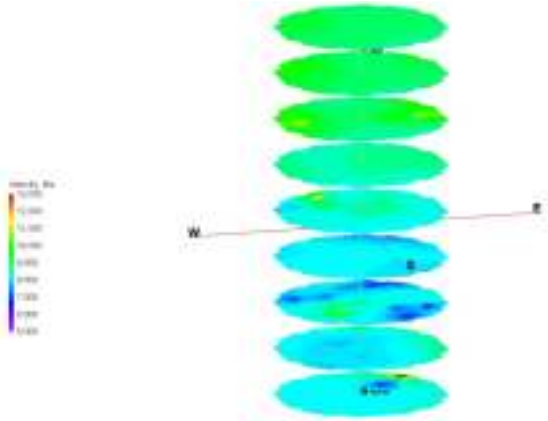

21.8 MPa of Load

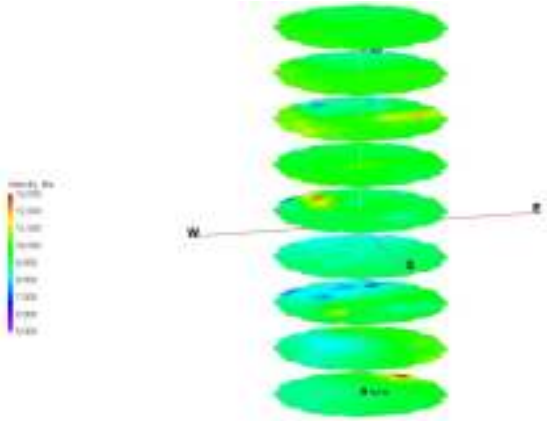

26.1 MPa of Load

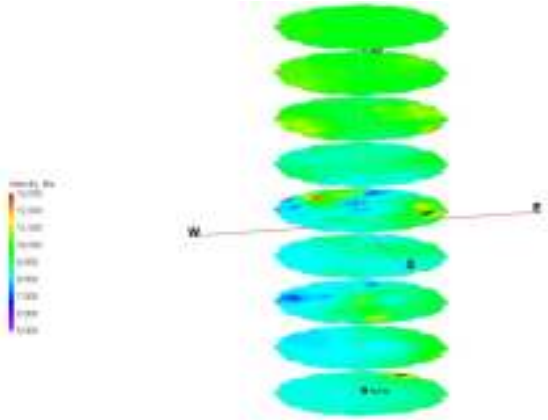

30.4 MPa of Load

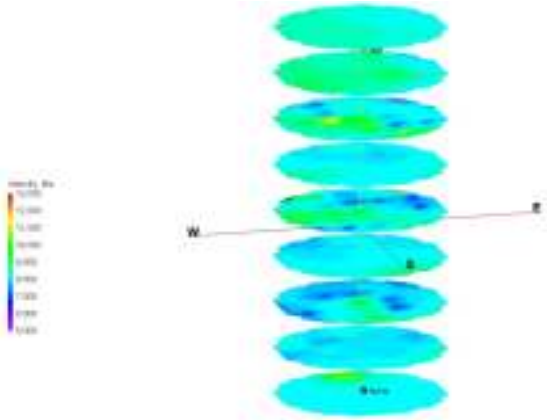

34.8 MPa of Load

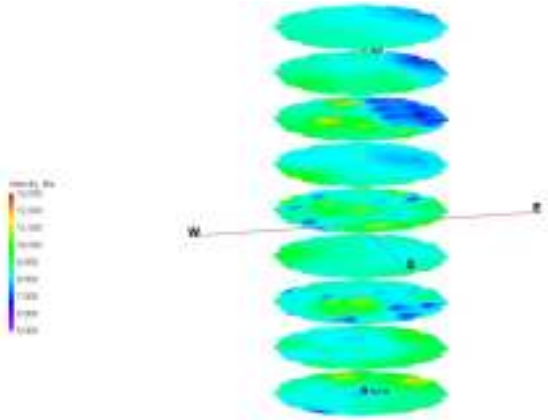

39.1 MPa of Load

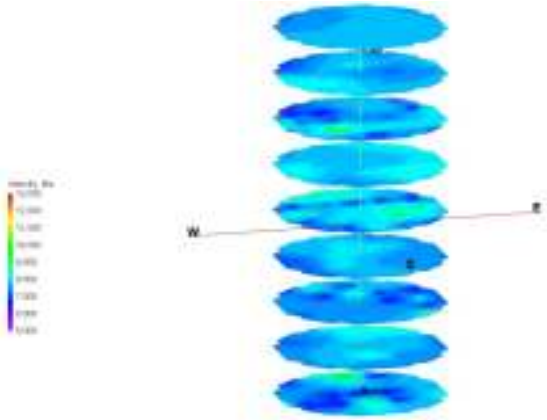

43.5 MPa of Load

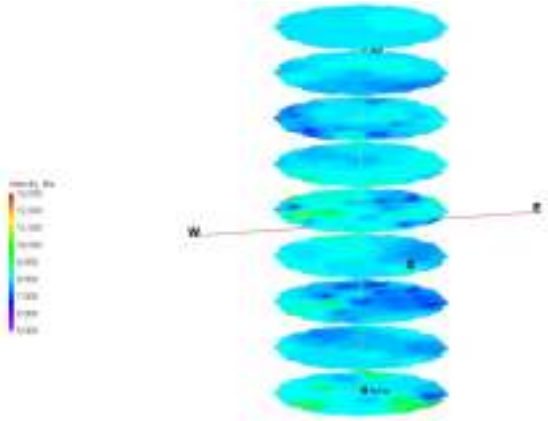

48.0 MPa of Load

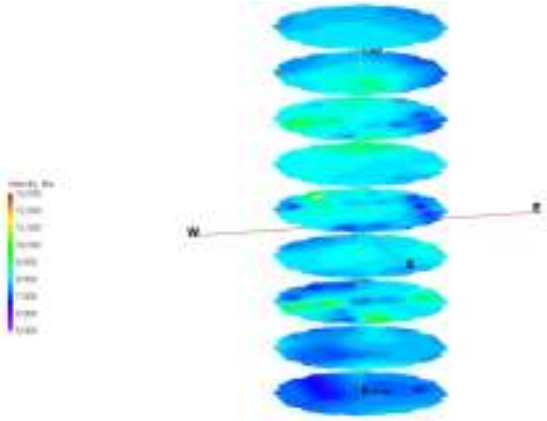

52.1 MPa of Load

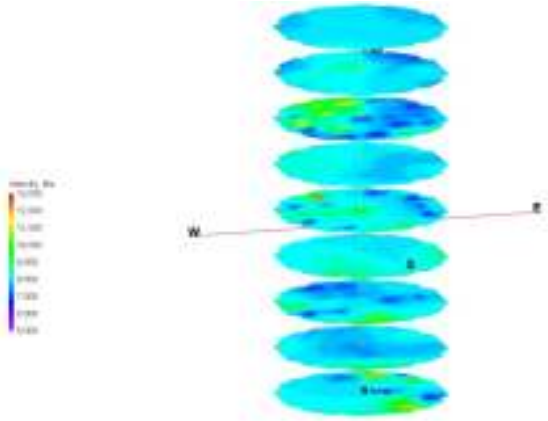

56.5 MPa of Load

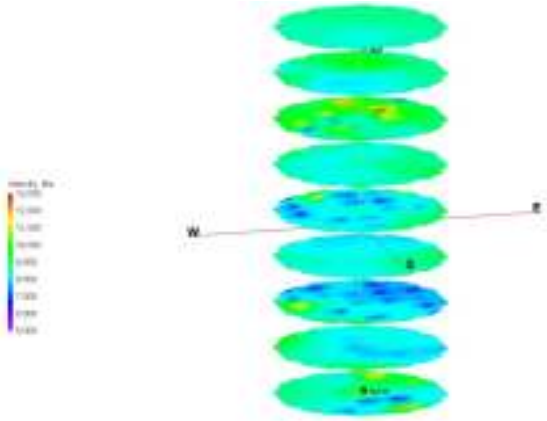

58.3 MPa of Load

Picture of Failed Sample from Experiment #10

Experiment #11 Tomograms

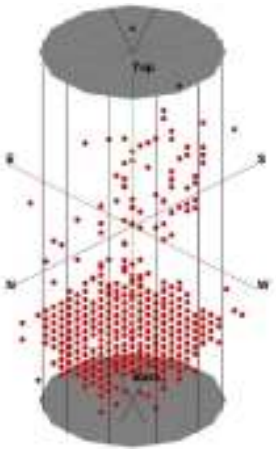

Acoustic Emission Locations

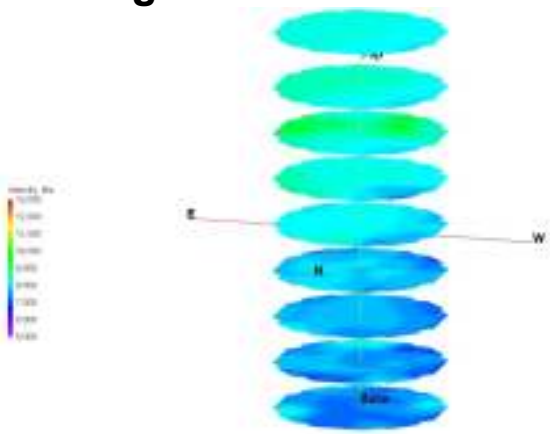

8.7 MPa of Load

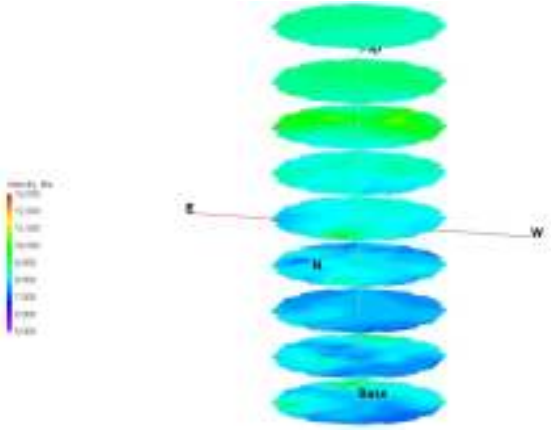

13.0 MPa of Load

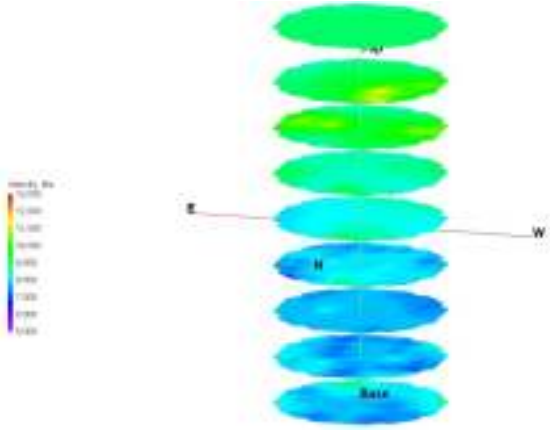

17.4 MPa of Load

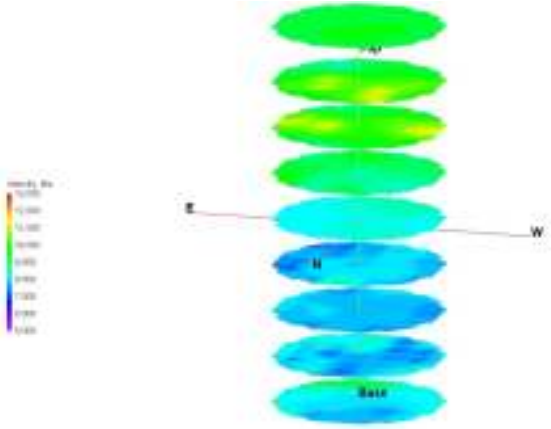

21.7 MPa of Load

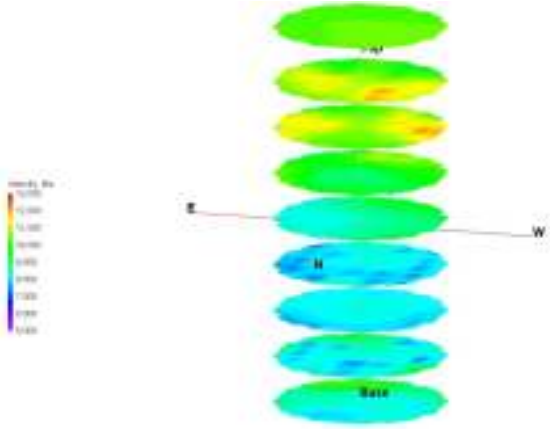

26.1 MPa of Load

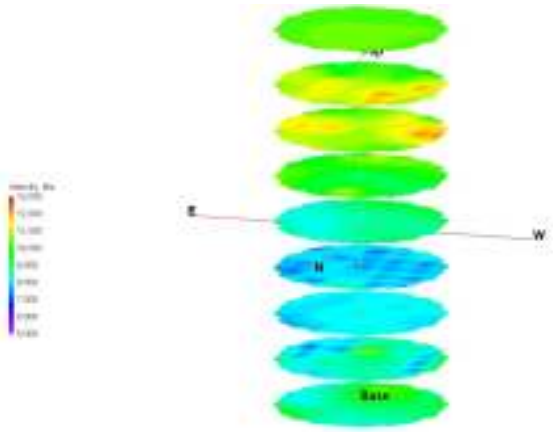

30.5 MPa of Load

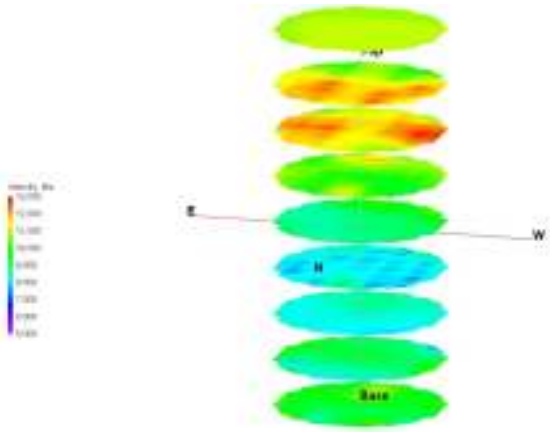

34.7 MPa of Load

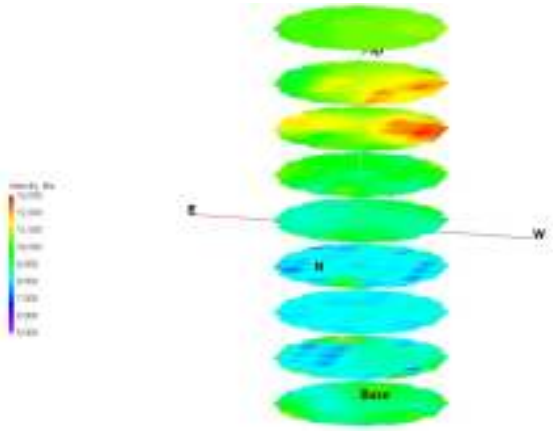

39.0 MPa of Load

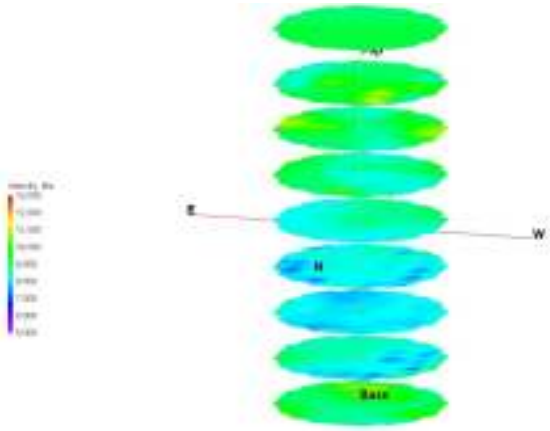

43.5 MPa of Load

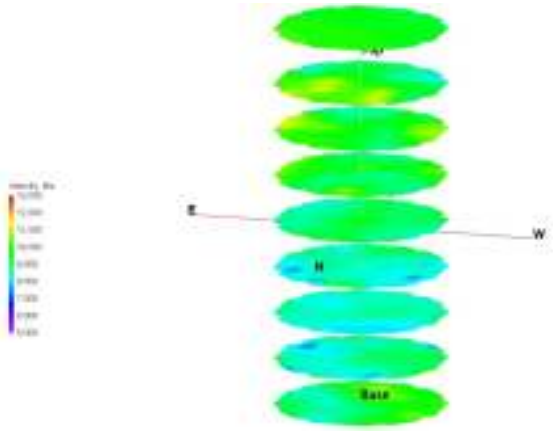

47.7 MPa of Load

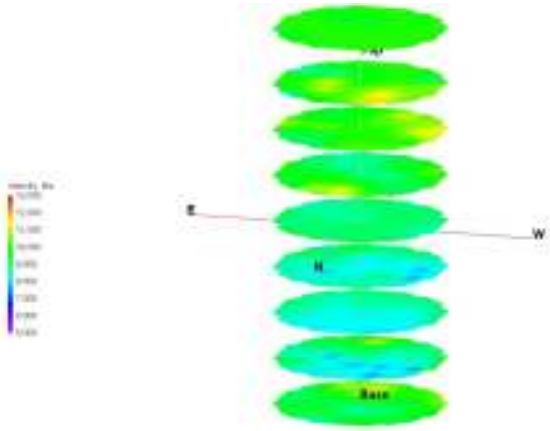

52.1 MPa of Load

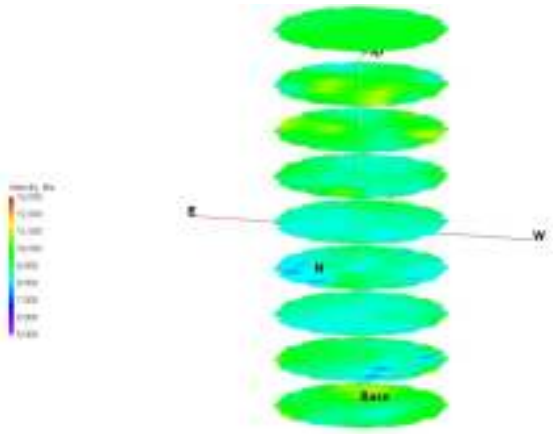

56.4 MPa of Load

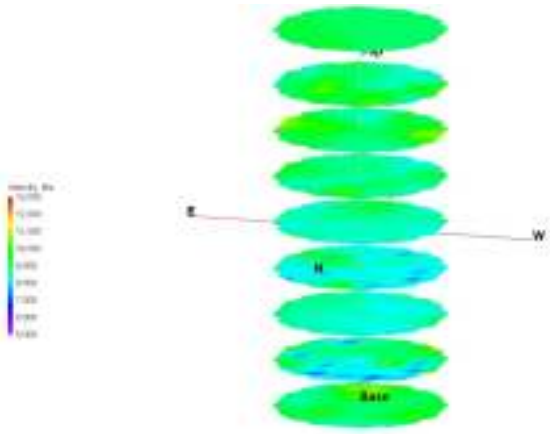

60.0 MPa of Load

Picture of Failed Sample from Experiment #11

Experiment #12 Tomograms

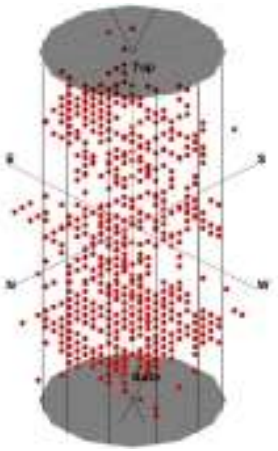

Acoustic Emission Locations

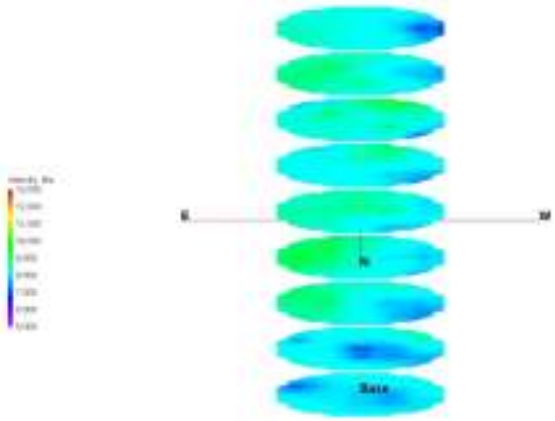

13.0 MPa of Load

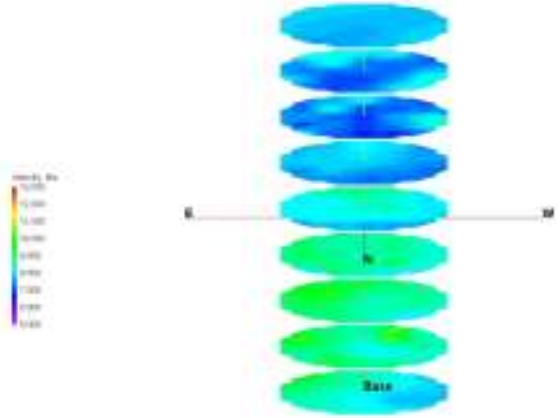

17.4 MPa of Load

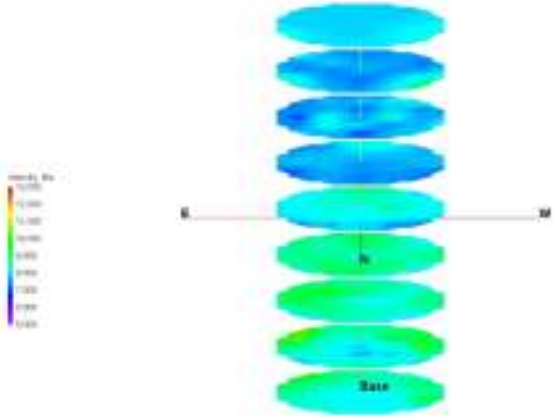

21.8 MPa of Load

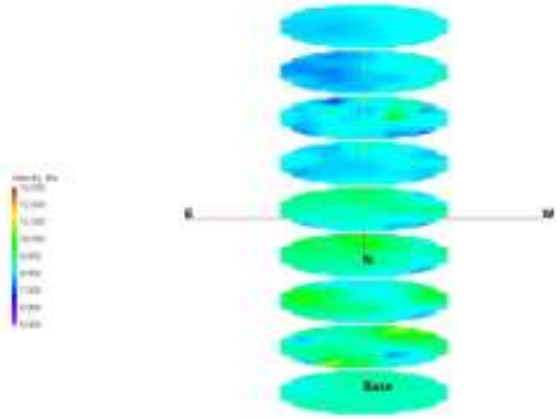

26.3 MPa of Load

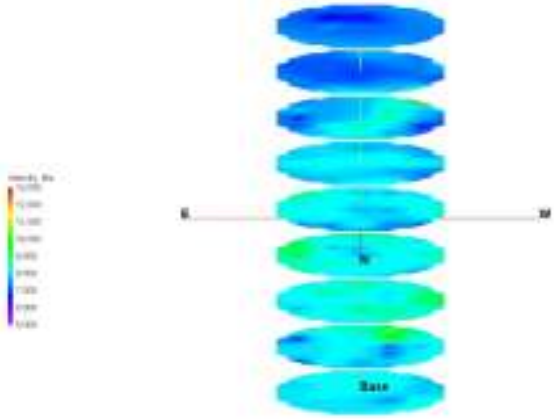

30.4 MPa of Load

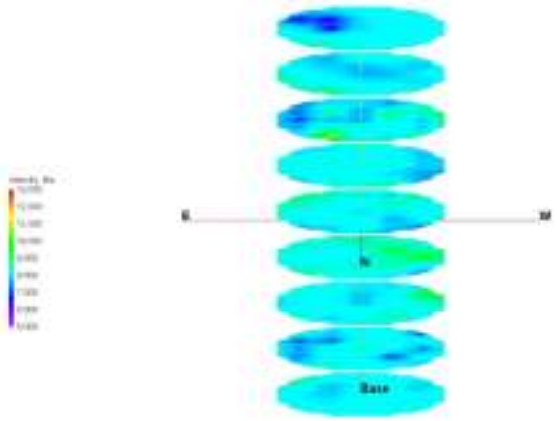

34.7 MPa of Load

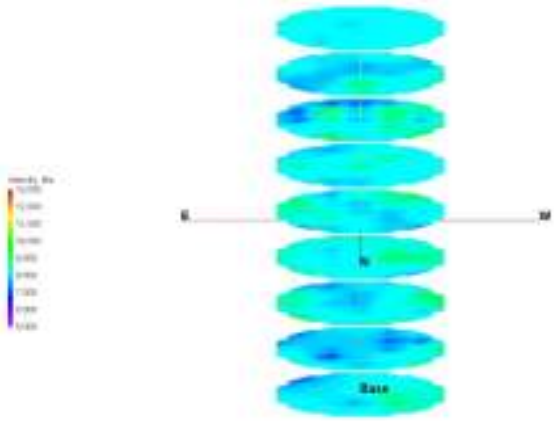

39.1 MPa of Load

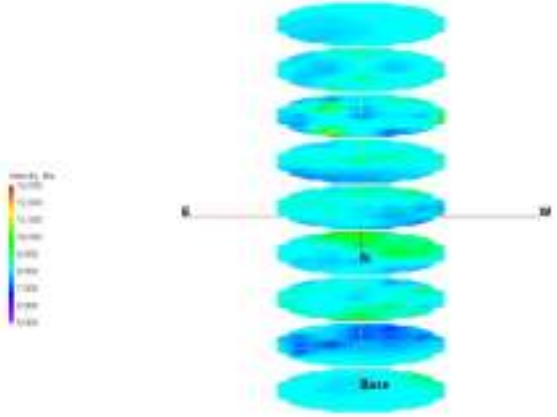

43.4 MPa of Load

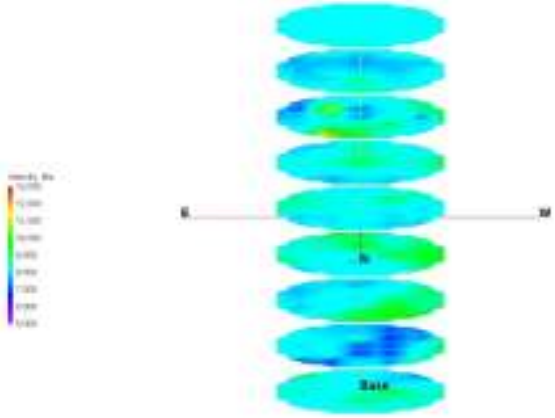

47.8 MPa of Load

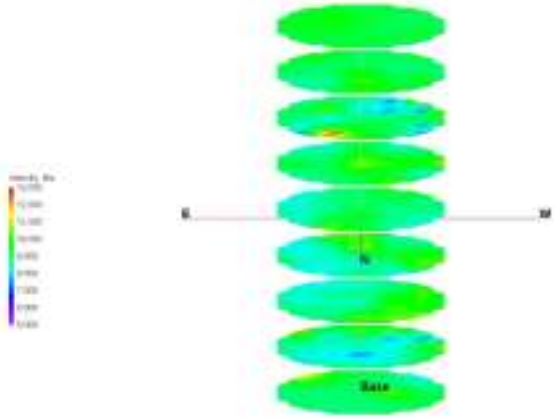

49.3 MPa of Load

Picture of Failed Sample from Experiment #12

Experiment #13 Tomograms

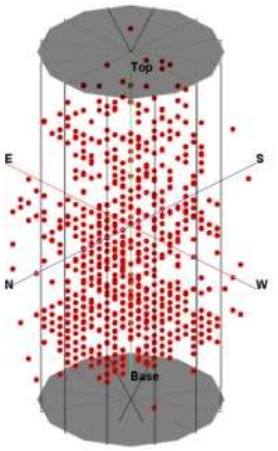

Acoustic Emission Locations

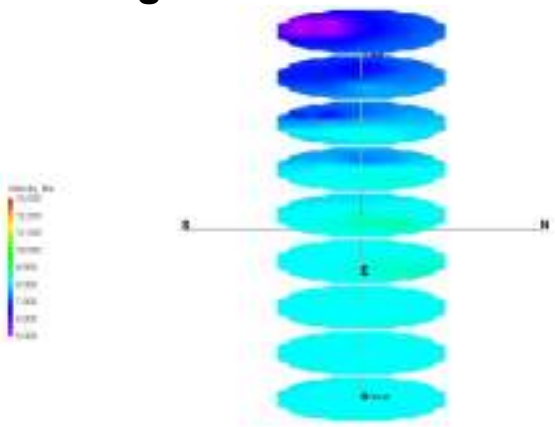

8.8 MPa of Load

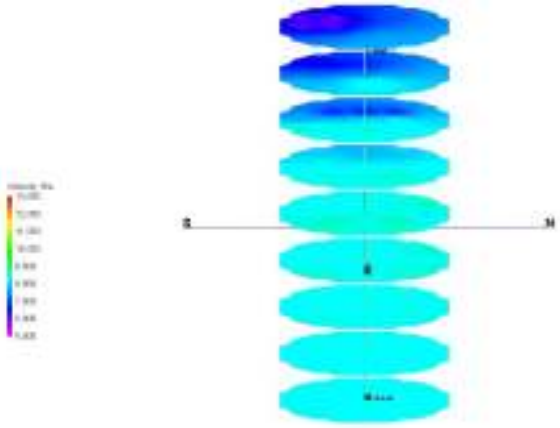

13.1 MPa of Load

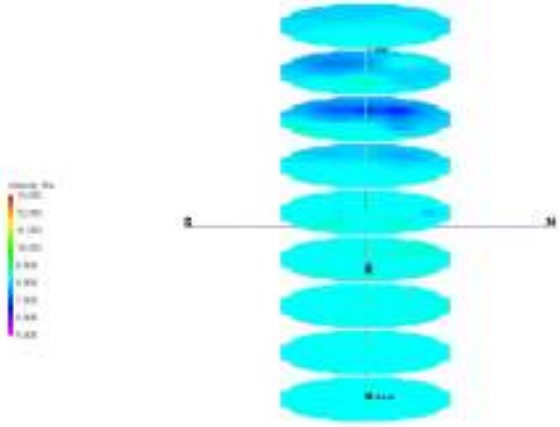

17.4 MPa of Load

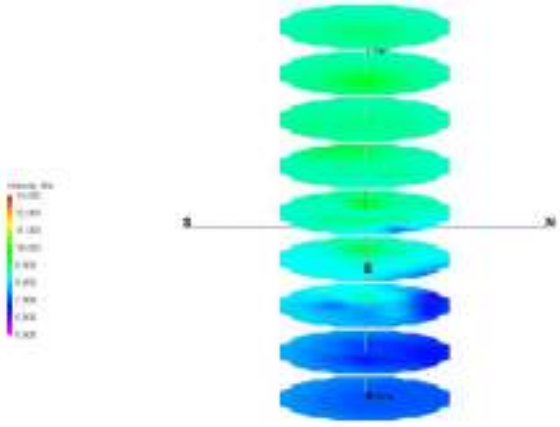

26.2 MPa of Load

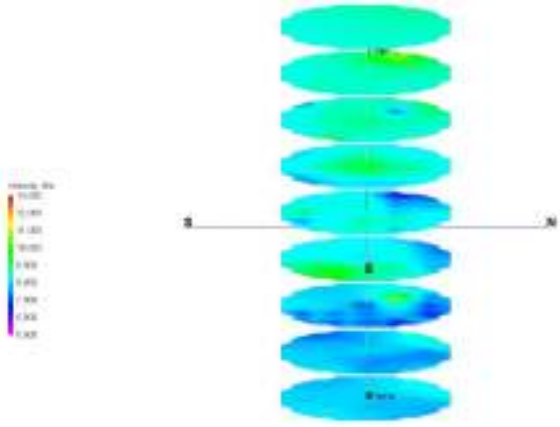

30.5 MPa of Load

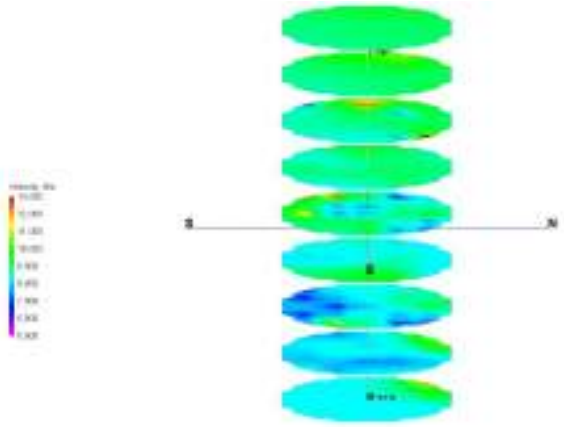

34.8 MPa of Load

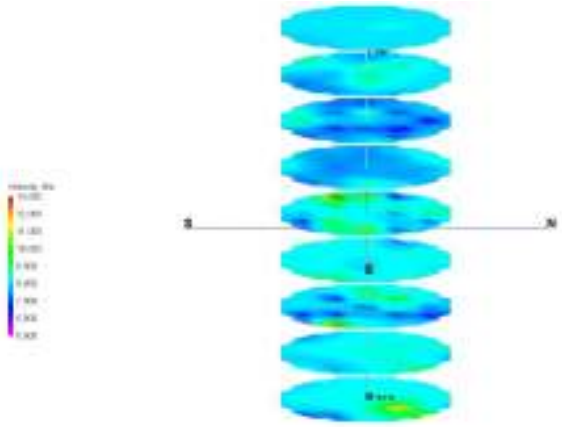

39.2 MPa of Load

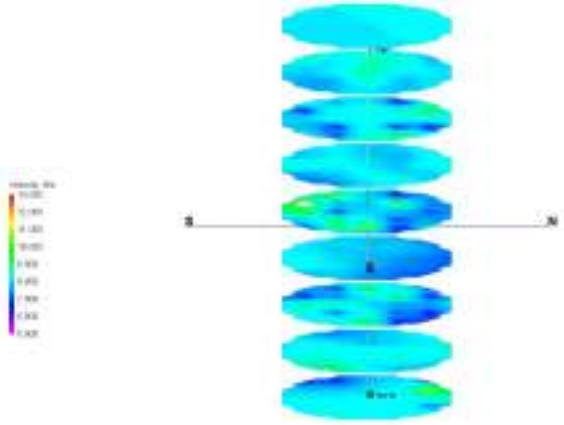

43.4 MPa of Load

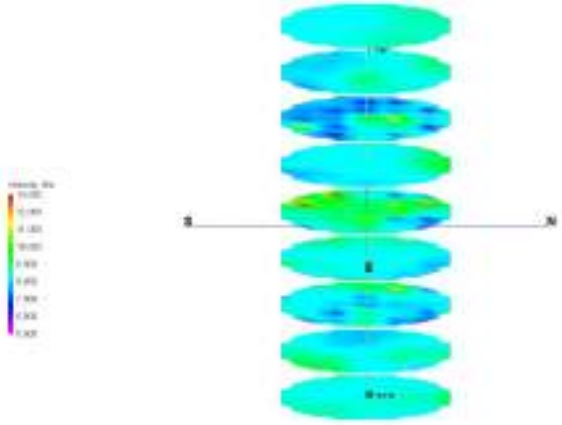

47.7 MPa of Load

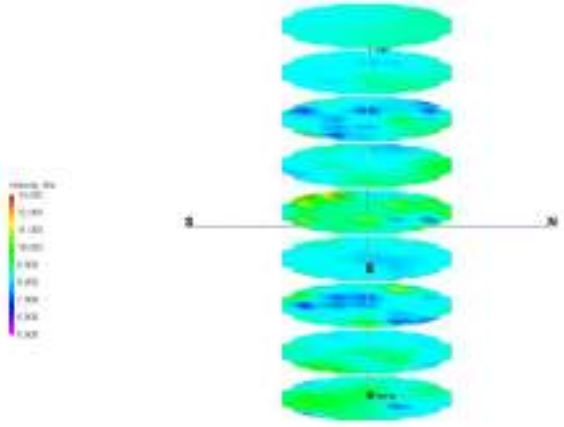

52.1 MPa of Load

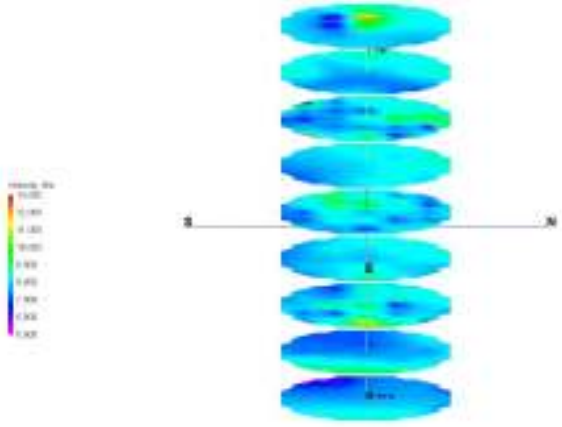

56.5 MPa of Load

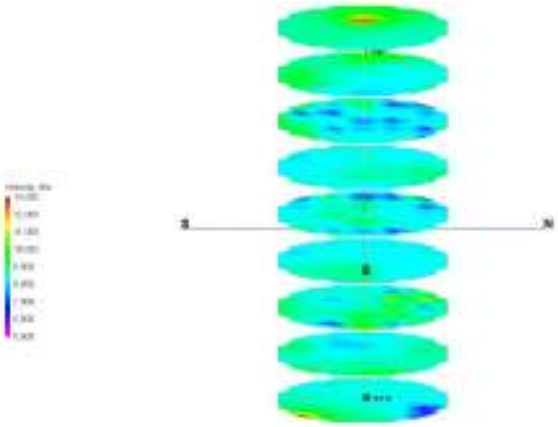

59.9 MPa of Load

Picture of Failed Sample from Experiment #13

Experiment #14 Tomograms

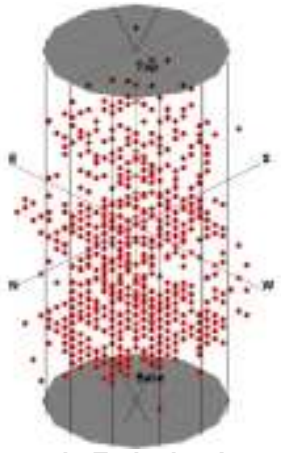

Acoustic Emission Locations

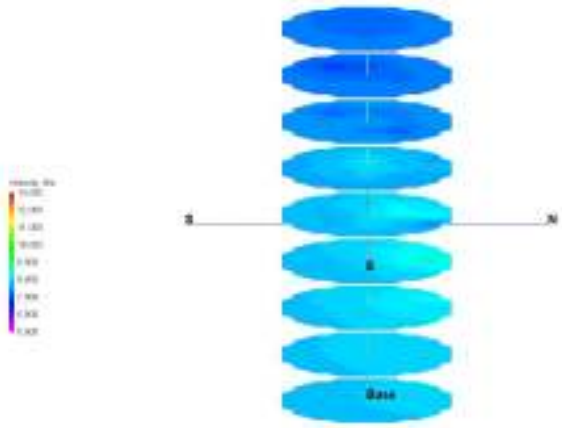

13.1 MPa of Load

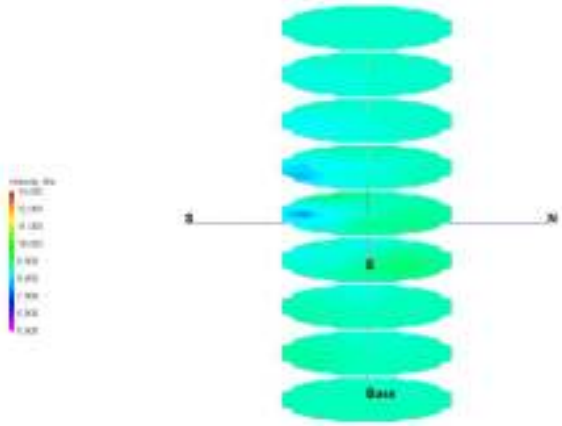

21.7 MPa of Load

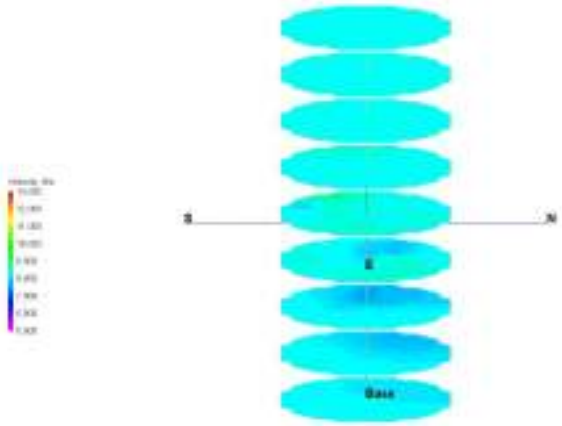

26.4 MPa of Load

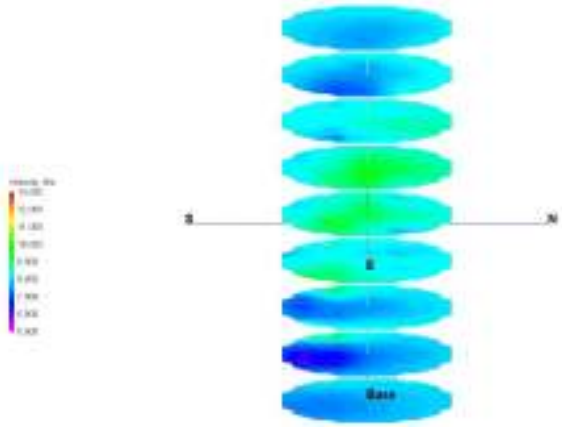

30.4 MPa of Load

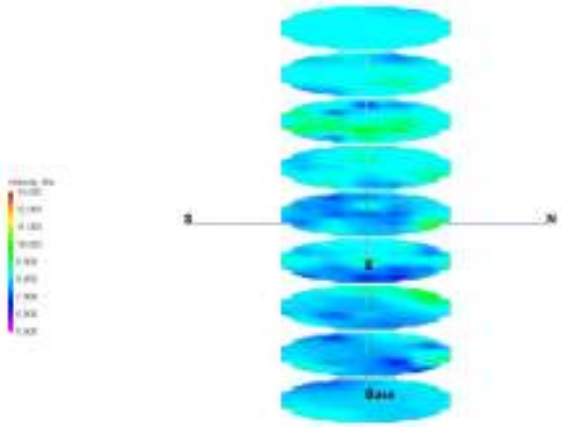

39.1 MPa of Load

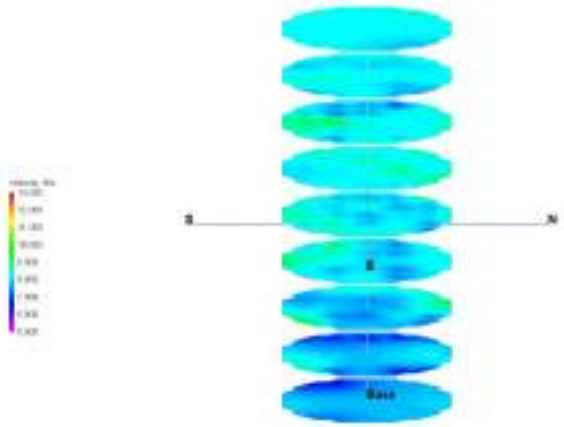

43.4 MPa of Load

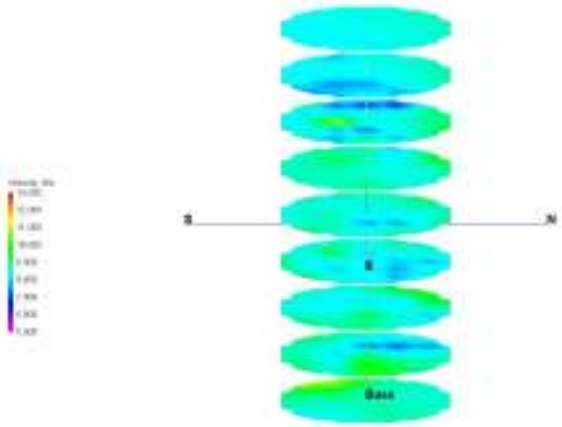

47.8 MPa of Load

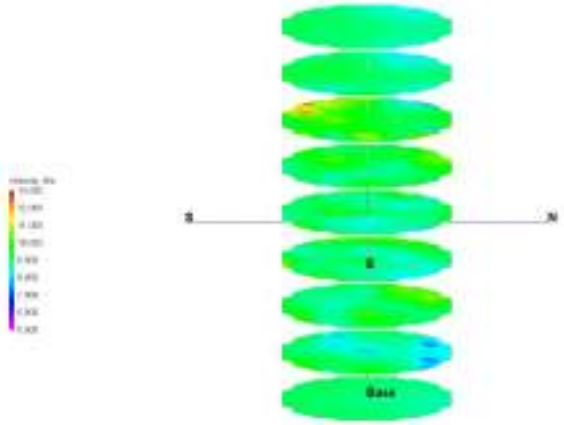

52.0 MPa of Load

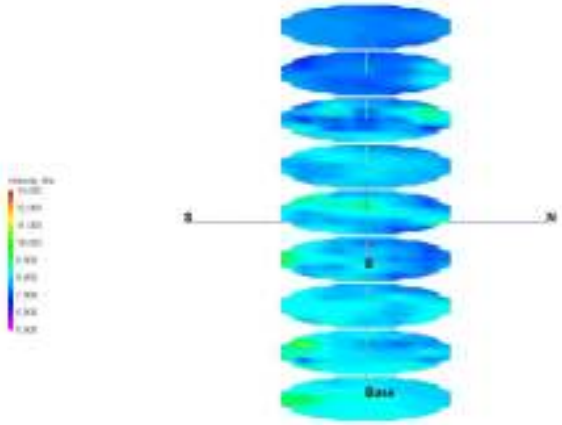

56.5 MPa of Load

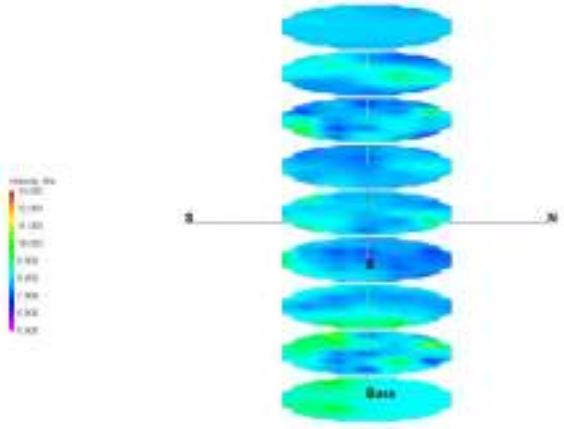

59.3 MPa of Load

Picture of Failed Sample from Experiment #14

Experiment #15 Tomograms

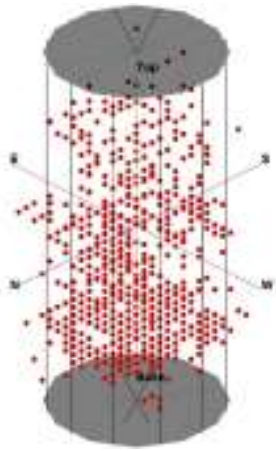

Acoustic Emission Locations

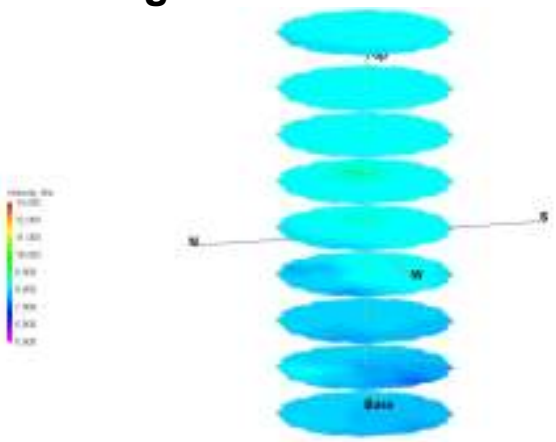

17.5 MPa of Load

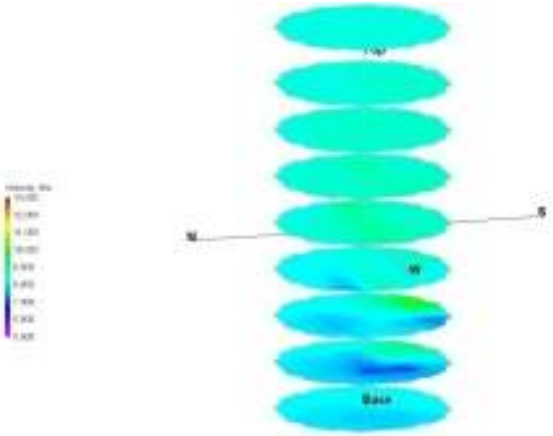

21.8 MPa of Load

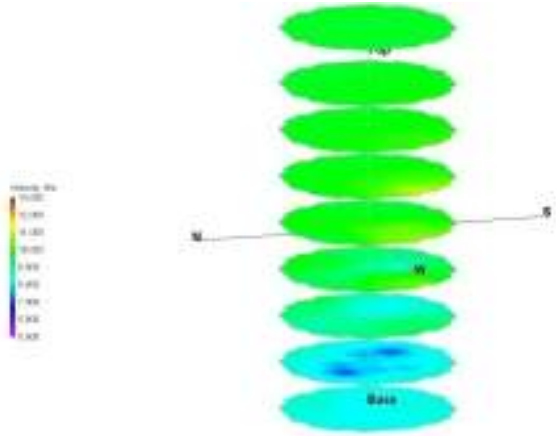

26.1 MPa of Load

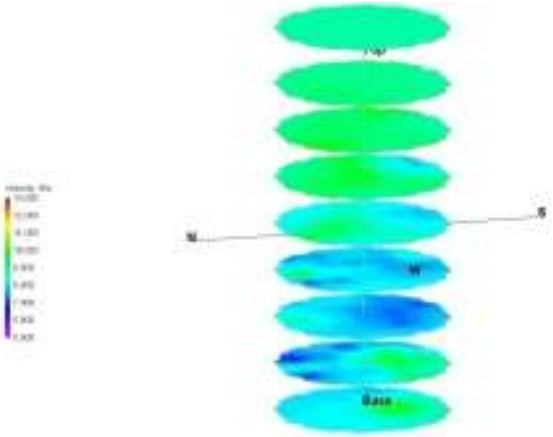

30.4 MPa of Load

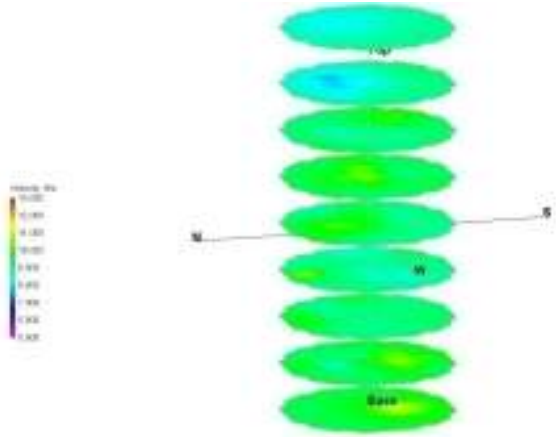

34.8 MPa of Load

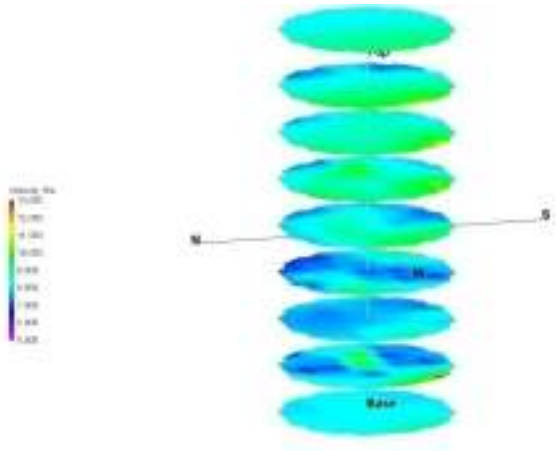

39.2 MPa of Load

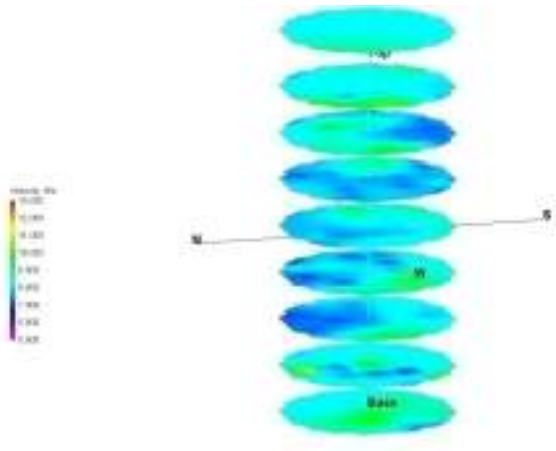

43.4 MPa of Load

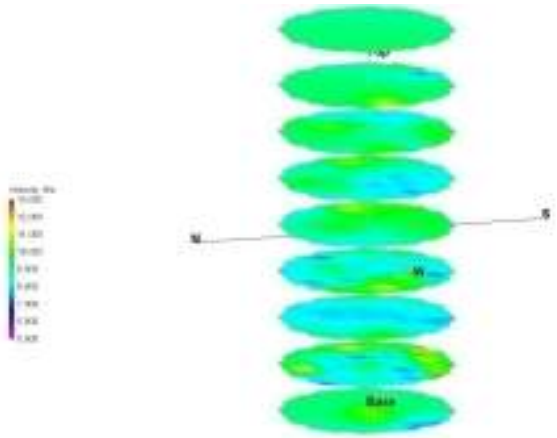

47.8 MPa of Load

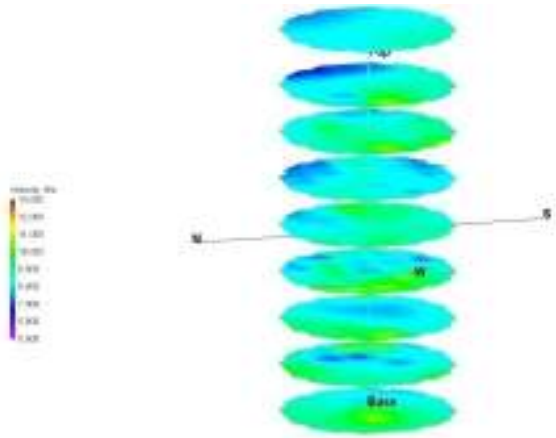

52.1 MPa of Load

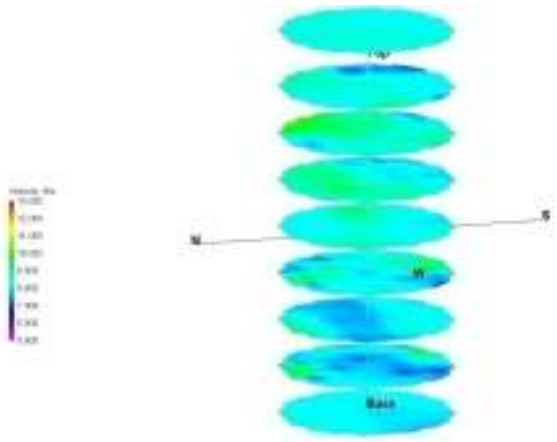

56.4 MPa of Load

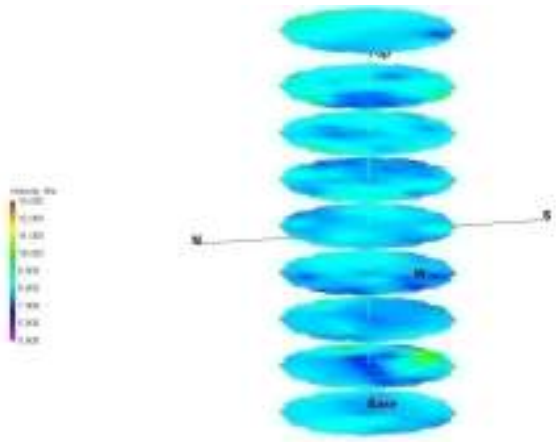

59.8 MPa of Load

Picture of Failed Sample from Experiment #15

Experiment #16 Tomograms

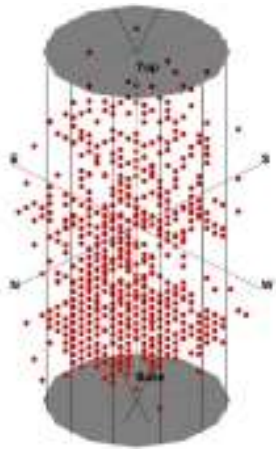

Acoustic Emission Locations

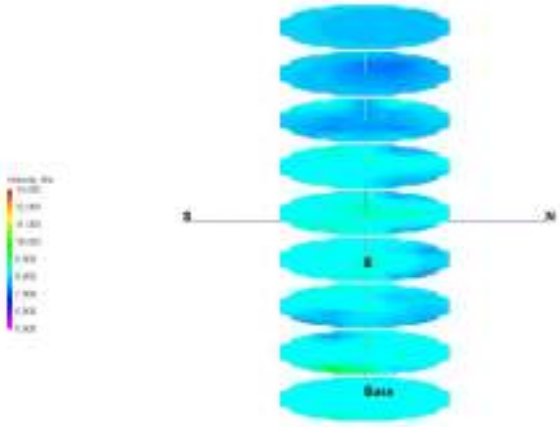

21.8 MPa of Load

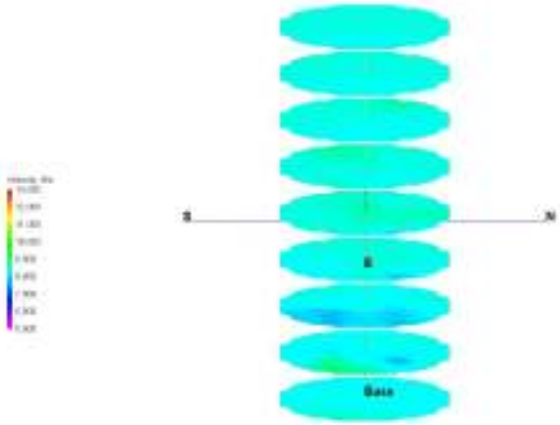

26.1 MPa of Load

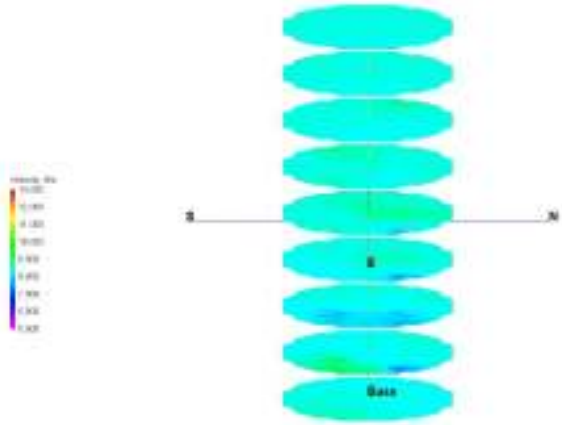

30.4 MPa of Load

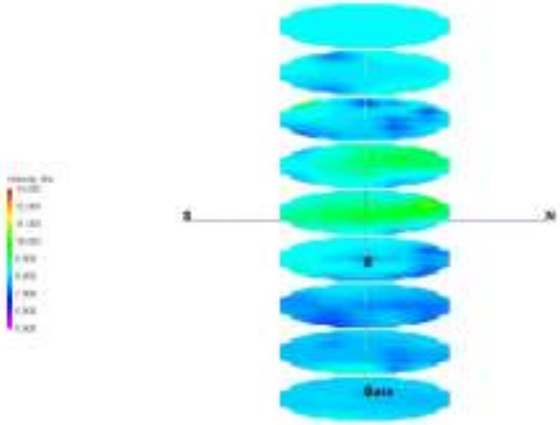

34.8 MPa of Load

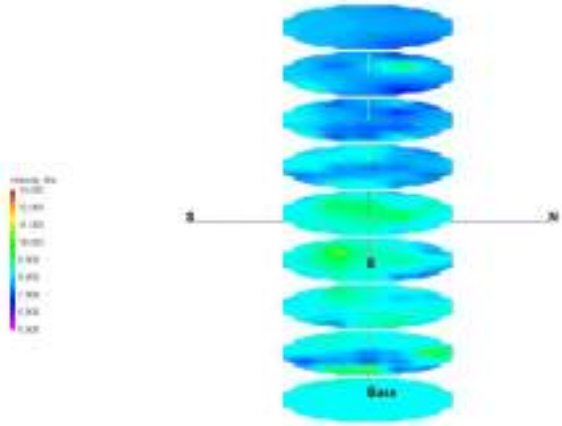

39.2 MPa of Load

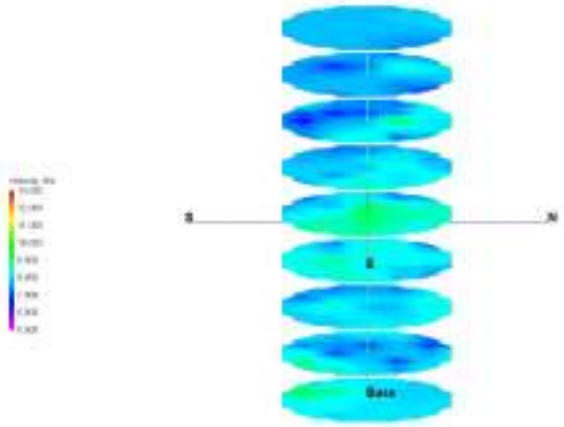

43.4 MPa of Load

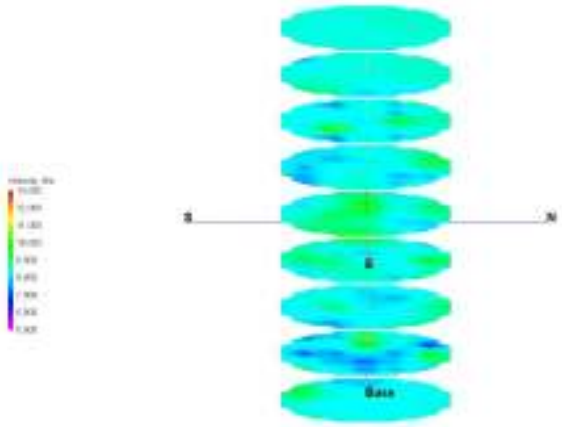

47.8 MPa of Load

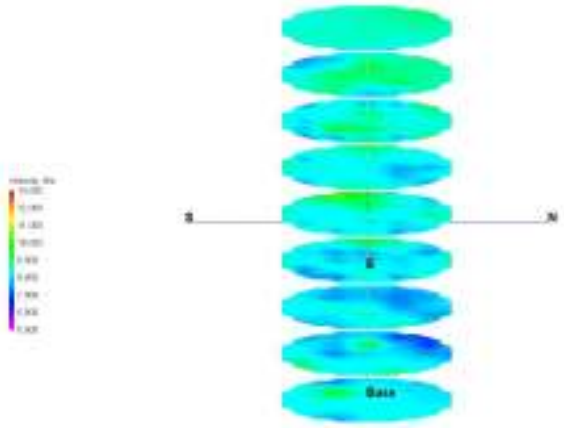

52.1 MPa of Load

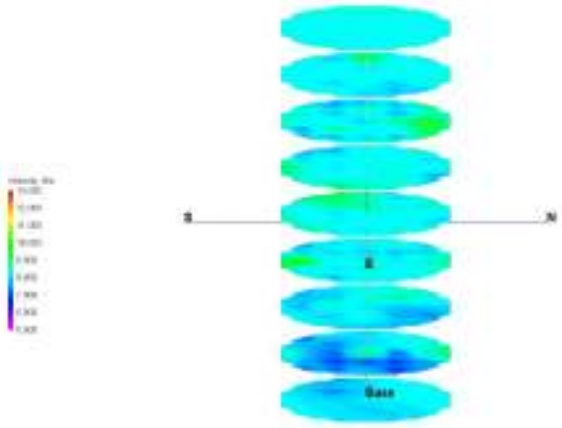

56.4 MPa of Load

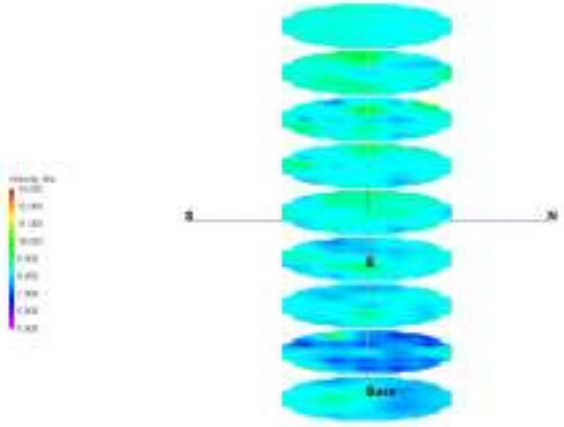

58.4 MPa of Load

Picture of Failed Sample from Experiment #16

Experiment #17 Tomograms

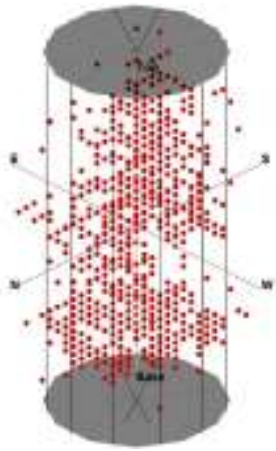

Acoustic Emission Locations

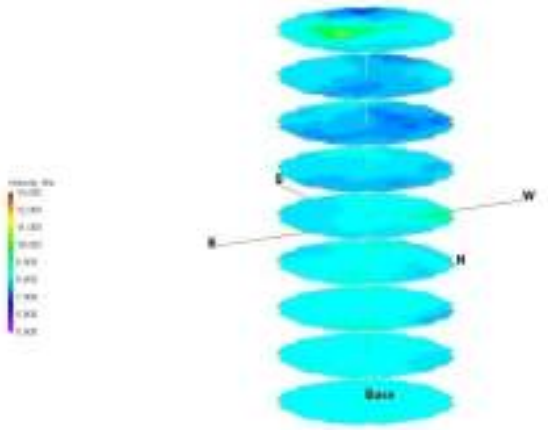

8.7 MPa of Load

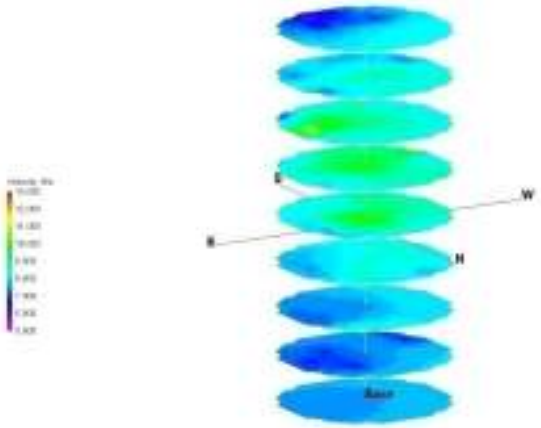

17.3 MPa of Load

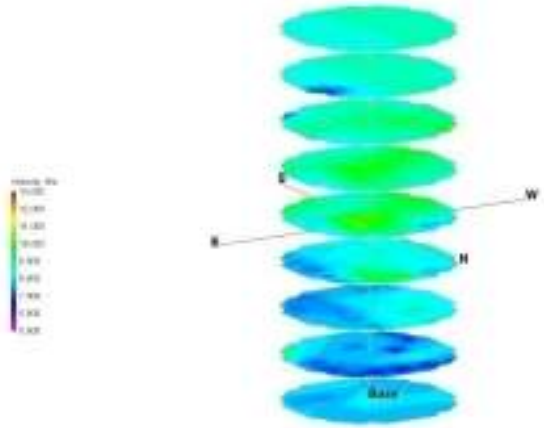

21.7 MPa of Load

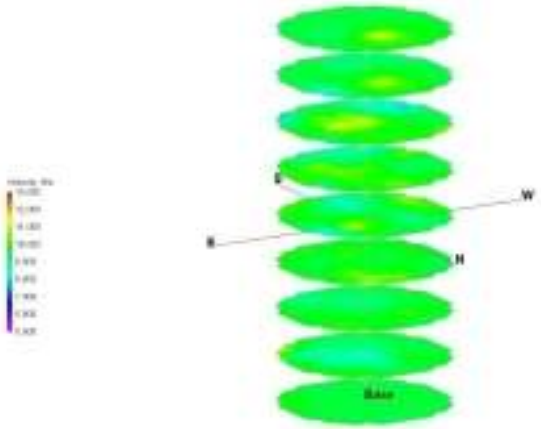

30.4 MPa of Load

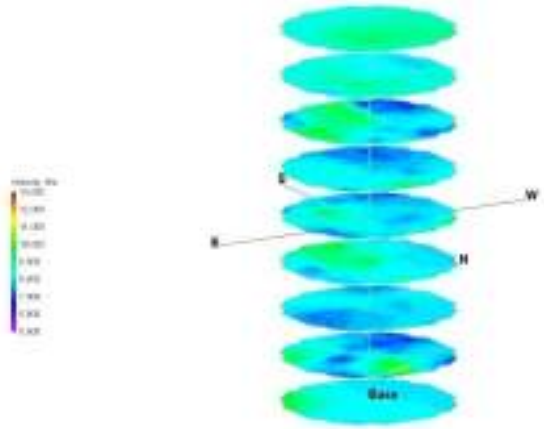

34.9 MPa of Load

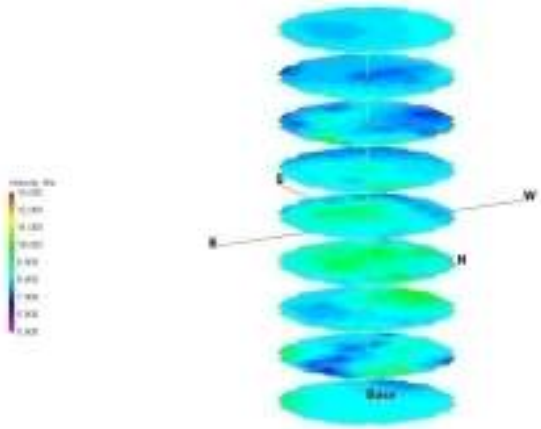

39.1 MPa of Load

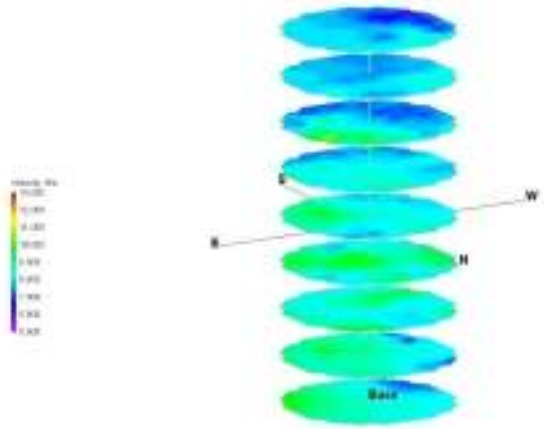

43.4 MPa of Load

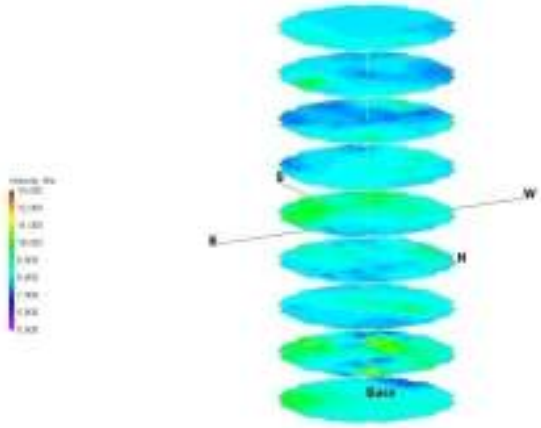

47.8 MPa of Load

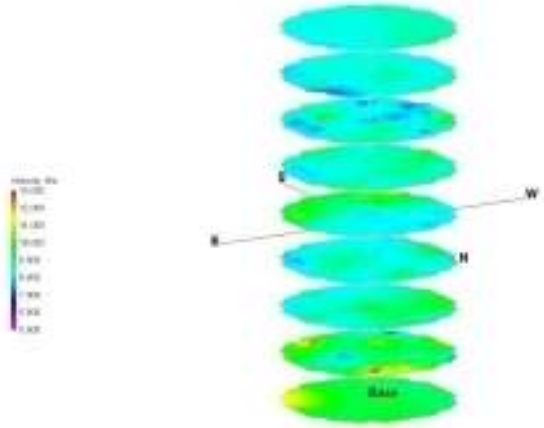

48.7 MPa of Load

Picture of Failed Sample from Experiment #17

Experiment #18 Tomograms

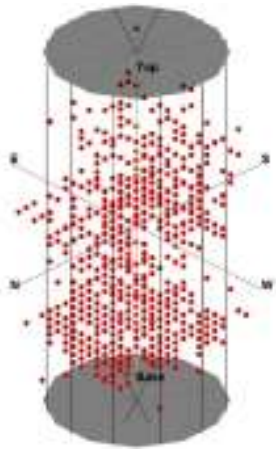

Acoustic Emission Locations

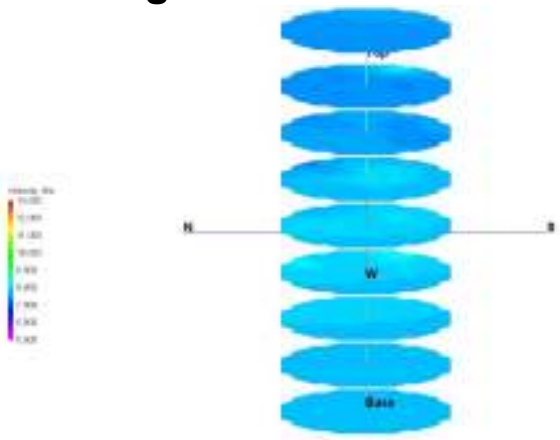

8.8 MPa of Load

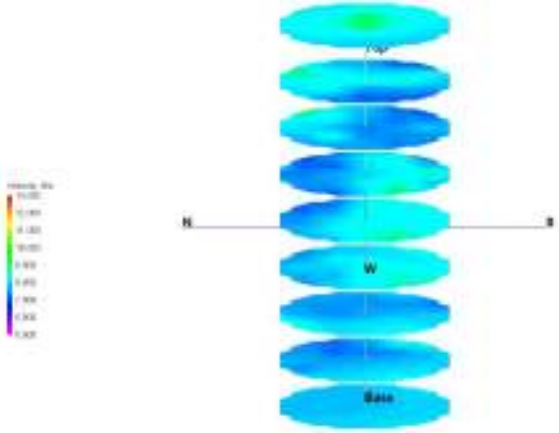

17.4 MPa of Load

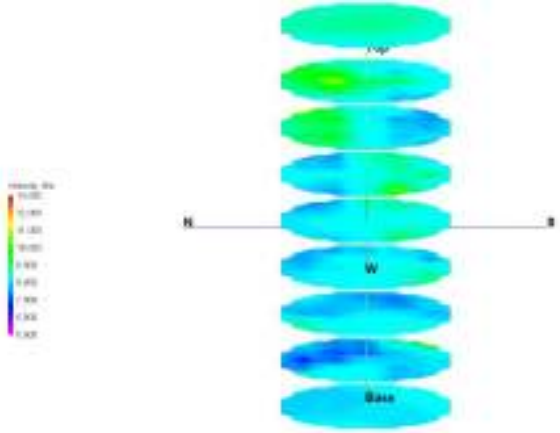

21.9 MPa of Load

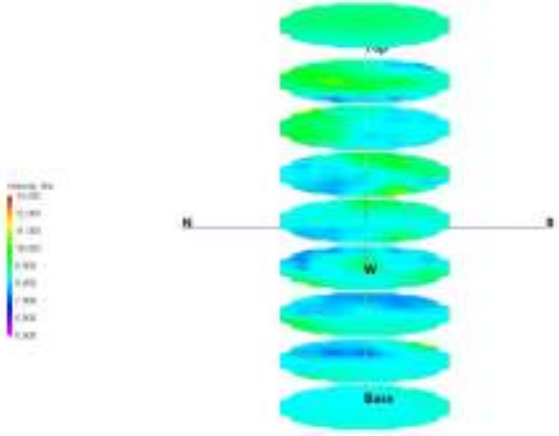

26.1 MPa of Load

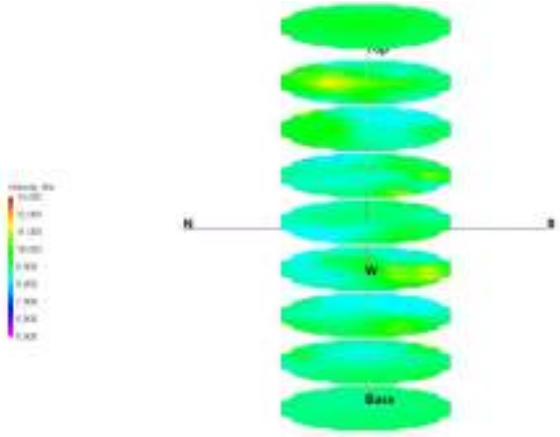

30.5 MPa of Load

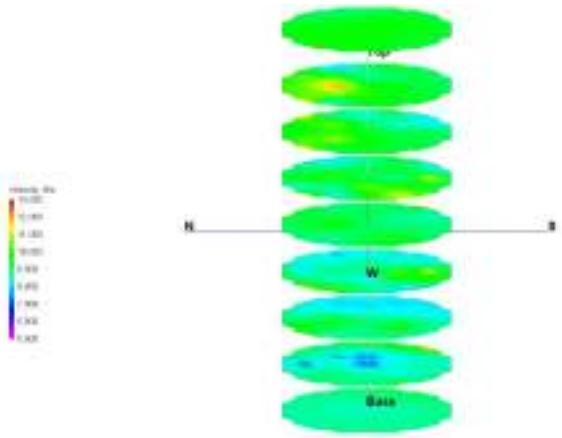

34.8 MPa of Load

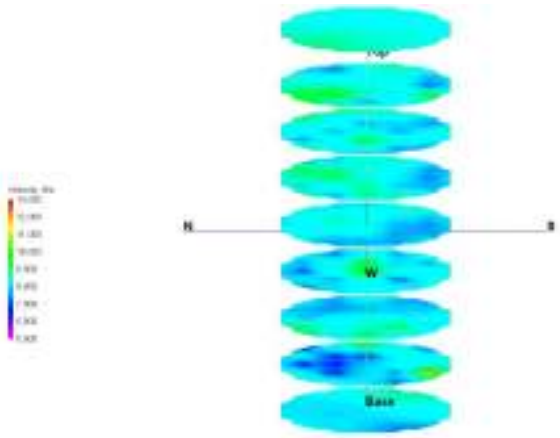

39.1 MPa of Load

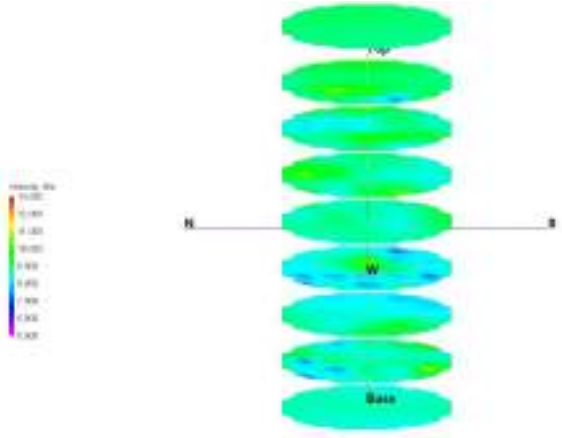

43.4 MPa of Load

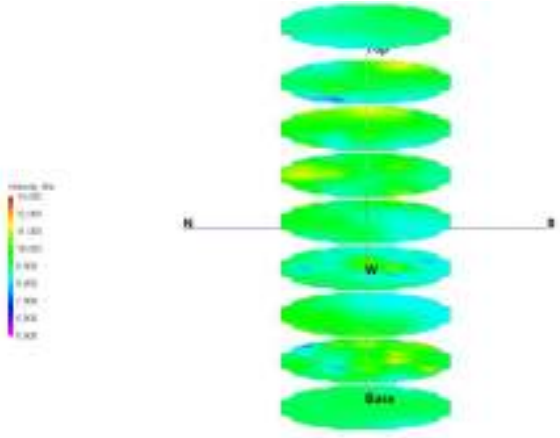

47.8 MPa of Load

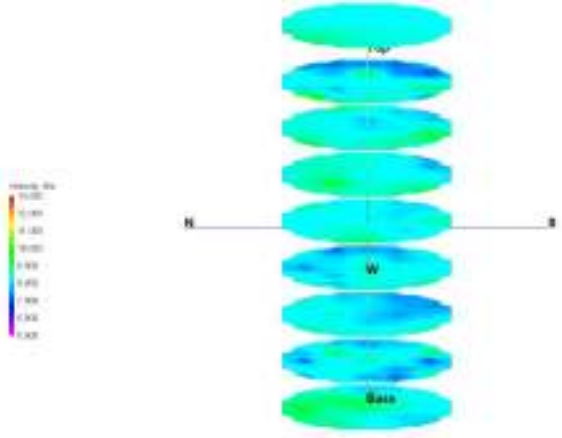

52.1 MPa of Load

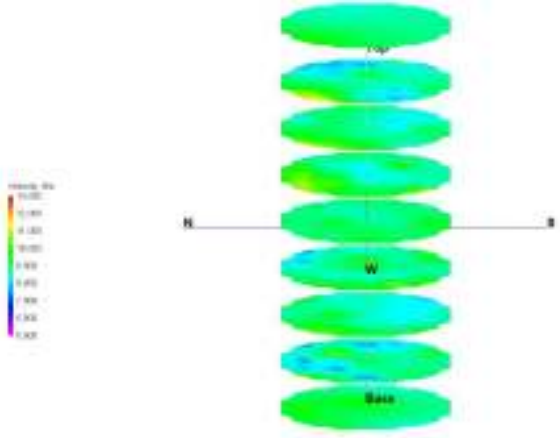

56.5 MPa of Load

Picture of Failed Sample from Experiment #18

Experiment #19 Tomograms

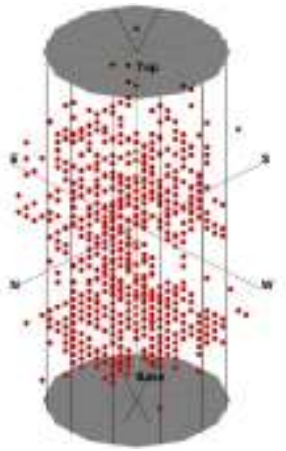

Acoustic Emission Locations

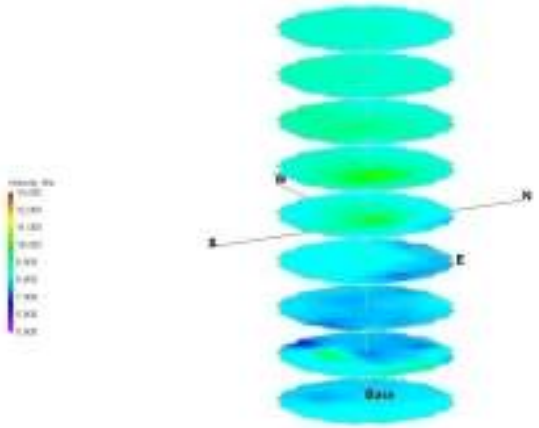

21.8 MPa of Load

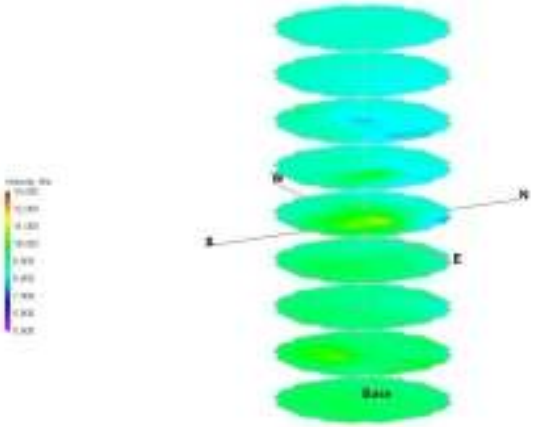

26.0 MPa of Load

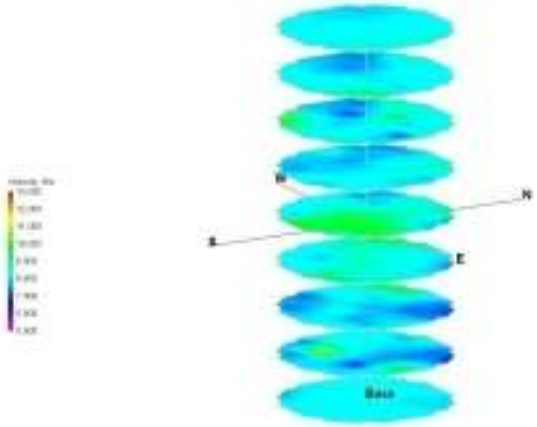

30.6 MPa of Load

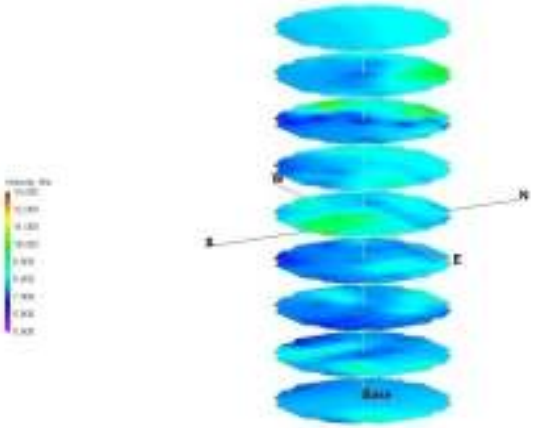

34.8 MPa of Load

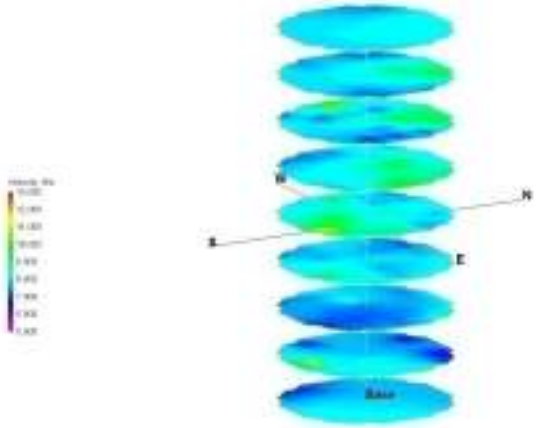

39.1 MPa of Load

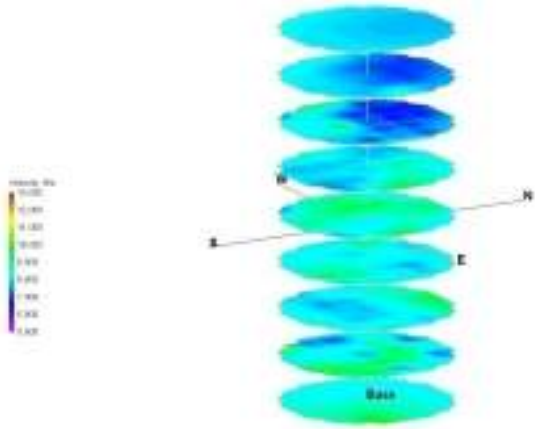

43.5 MPa of Load

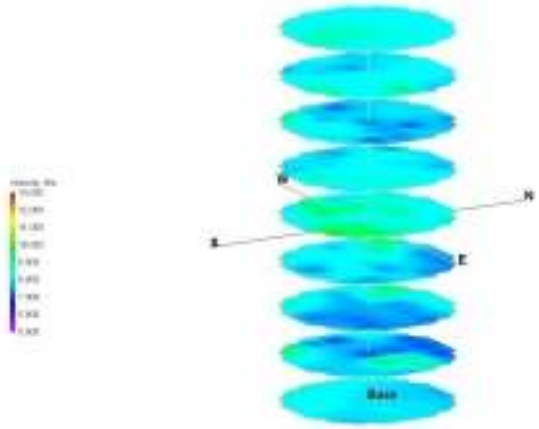

47.8 MPa of Load

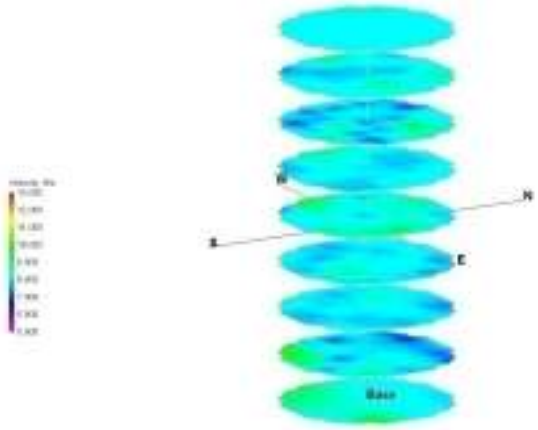

52.1 MPa of Load

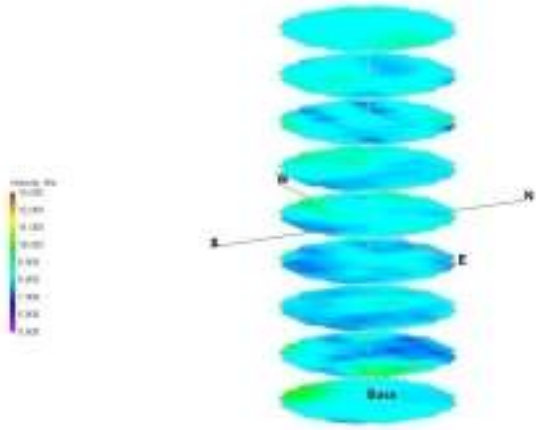

56.4 MPa of Load

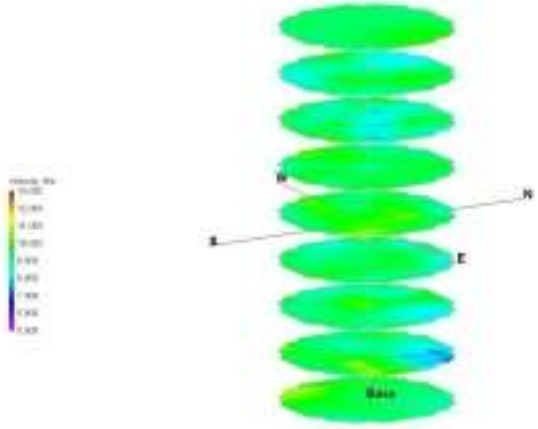

56.9 MPa of Load

Picture of Failed Sample from Experiment #19